NATIONAL AERONAUTICS AND SPACE ADMINISTRATION

Technical Report 32-1526

Volume III

The Deep Space Network

Progress Report For March and April 1971

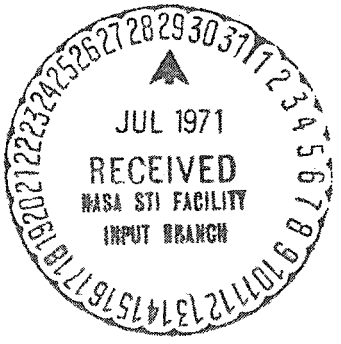

JET PROPULSION LABORATORY
CALIFORNIA INSTITUTE OF TECHNOLOGY
PASADENA, CALIFORNIA

June 15, 1971

NATIONAL AERONAUTICS AND SPACE ADMINISTRATION

Technical Report 32-1526

Volume III

The Deep Space Network

Progress Report
For March and April 1971

JET PROPULSION LABORATORY
CALIFORNIA INSTITUTE OF TECHNOLOGY
PASADENA, CALIFORNIA

June 15, 1971

Prepared Under Contract No. NAS 7-100
National Aeronautics and Space Administration

Preface

This report series presents progress on DSN supporting research and technology, advanced development and engineering, and implementation, and DSN operations which pertain to mission-independent or multiple-mission development as well as to support of flight projects. Each issue presents material in some, but not all, of the following categories in the order indicated.

Description of the DSN

Mission Support
- Interplanetary Flight Projects
- Planetary Flight Projects
- Manned Space Flight Project
- Radio Science Experiments
- Advanced Flight Projects

Advanced Engineering
- Tracking and Navigational Accuracy Analysis
- Communications Systems Research
- Communications Elements Research
- Supporting Research and Technology

Development and Implementation
- Space Flight Operations Facility Development
- Ground Communications Facility Development
- Deep Space Instrumentation Facility Development
- DSN Projects and Systems Development

Operations and Facilities
- DSN Operations
- Space Flight Operations Facility Operations
- Ground Communications Facility Operations
- Deep Space Instrumentation Facility Operations
- Facility Engineering

In each issue, the part entitled "Description of the DSN" describes the functions and facilities of the DSN and may report the current configuration of one of the six DSN systems (tracking, telemetry, command, monitoring, simulation, and operations control).

The work described in this report series is either performed or managed by the Tracking and Data Acquisition organization of JPL for NASA.

Contents

Contents (contd)

Communications Systems Research

Communications Elements Research

Supporting Research and Technology

DEVELOPMENT AND IMPLEMENTATION

SFOF Development

Contents (contd)

GCF Development

DSIF Development

DSN Projects and Systems Development

OPERATIONS AND FACILITIES

DSN Operations

Contents (contd)

SFOF Operations

Facility Engineering

DSN Functions and Facilities

N. A. Renzetti
Mission Support Office

The objectives, functions, and organization of the Deep Space Network are summarized. The Deep Space Instrumentation Facility, the Ground Communications Facility, and the Space Flight Operations Facility are described.

The Deep Space Network (DSN), established by the NASA Office of Tracking and Data Acquisition under the system management and technical direction of JPL, is designed for two-way communications with unmanned spacecraft traveling approximately 16,000 km (10,000 mi) from earth to planetary distances. It supports, or has supported, the following NASA deep space exploration projects: *Ranger, Surveyor, Mariner* Venus 1962, *Mariner* Mars 1964, *Mariner* Venus 67, *Mariner* Mars 1969, *Mariner* Mars 1971 (JPL); *Lunar Orbiter* and *Viking* (Langley Research Center); *Pioneer* (Ames Research Center); *Helios* (West Germany); and *Apollo* (Manned Spacecraft Center), to supplement the Manned Space Flight Network (MSFN).

The DSN is distinct from other NASA networks such as the MSFN, which has primary responsibility for tracking the manned spacecraft of the *Apollo* Project, and the Space Tracking and Data Acquisition Network (STADAN), which tracks earth-orbiting scientific and communications satellites. With no future unmanned lunar spacecraft presently planned, the primary objective of the DSN is to continue its support of planetary and interplanetary flight projects.

To support flight projects, the DSN simultaneously performs advanced engineering on components and systems, integrates proven equipment and methods into the network,[1] and provides direct support of each project through that project's Tracking and Data System. This management element and the project's Mission Operations personnel are responsible for the design and operation of the data, software, and operations systems required for the conduct of flight operations. The organization and procedures necessary to carry out these activities are described in Ref. 1.

[1]When a new piece of equipment or new method has been accepted for integration into the network, it is classed as Goldstone duplicate standard (GSDS), thus standardizing the design and operation of identical items throughout the network.

By tracking the spacecraft, the DSN is involved in the following data types:

(1) *Radio Metric:* generate angles, one- and two-way doppler, and range.

(2) *Telemetry:* receive, record, and retransmit engineering and scientific data.

(3) *Command:* send coded signals to the spacecraft to activate equipment to initiate spacecraft functions.

The DSN operation is characterized by six DSN systems: (1) tracking, (2) telemetry, (3) command, (4) monitoring, (5) simulation, and (6) operations control.

The DSN can be characterized as being comprised of three facilities: the Deep Space Instrumentation Facility (DSIF), the Ground Communications Facility (GCF), and the Space Flight Operations Facility (SFOF).

I. Deep Space Instrumentation Facility

A. Tracking and Data Acquisition Facilities

A world-wide set of deep space stations (DSSs) with large antennas, low-noise phase-lock receiving systems, and high-power transmitters provide radio communications with spacecraft. The DSSs and the deep space communications complexes (DSCCs) they comprise are given in Table 1.

Radio contact with a spacecraft usually begins when the spacecraft is on the launch vehicle at Cape Kennedy, and it is maintained throughout the mission. The early part of the trajectory is covered by selected network stations of the Air Force Eastern Test Range (AFETR) and the MSFN of the Goddard Space Flight Center.[2] Normally, two-way communications are established between the spacecraft and the DSN within 30 min after the spacecraft has been injected into lunar, planetary, or interplanetary flight. A compatibility test station at Cape Kennedy (discussed later) monitors the spacecraft continuously during the launch phase until it passes over the local horizon. The deep space phase begins with acquisition by either DSS 51, 41, or 42. These and the remaining DSSs given in Table 1 provide radio communications to the end of the flight.

To enable continuous radio contact with spacecraft, the DSSs are located approximately 120 deg apart in longitude; thus, a spacecraft in deep space flight is always

[2]The 9-m (30-ft) diam antenna station established by the DSN on Ascension Island during 1965 to act in conjunction with the MSFN orbital support 9-m (30-ft) diam antenna station was transferred to the MSFN in July 1968.

Table 1. Tracking and data acquisition stations of the DSN

DSCC	Location	DSS	DSS serial designation	Antenna		Year of initial operation
				Diameter, m (ft)	Type of mounting	
Goldstone	California	Pioneer	11	26 (85)	Polar	1958
		Echo	12	26 (85)	Polar	1962
		(Venus)[a]	13	26 (85)	Az–El	1962
		Mars	14	64 (210)	Az–El	1966
—	Australia	Woomera[b]	41	26 (85)	Polar	1960
Tidbinbilla	Australia	Weemala (formerly Tidbinbilla)[b]	42	26 (85)	Polar	1965
		Ballima[b] (formerly Booroomba)	43	64 (210)	Az–El	Under construction
—	South Africa	Johannesburg[b]	51	26 (85)	Polar	1961
Madrid	Spain	Robledo[b]	61	26 (85)	Polar	1965
		Cebreros[b]	62	26 (85)	Polar	1967
		Robledo	63	64 (210)	Az–El	Under construction

[a]A research-and-development facility used to demonstrate the feasibility of new equipment and methods to be integrated into the operational network. Besides the 26-m (85-ft) diam az–el-mounted antenna, DSS 13 has a 9-m (30-ft) diam az–el-mounted antenna that is used for testing the design of new equipment and support of ground-based radio science.

[b]Normally staffed and operated by government agencies of the respective countries (except for a temporary staff of the Madrid DSCC), with some assistance of U.S. support personnel.

within the field-of-view of at least one DSS, and for several hours each day may be seen by two DSSs. Furthermore, since most spacecraft on deep space missions travel within 30 deg of the equatorial plane, the DSSs are located within latitudes of 45 deg north or south of the equator. All DSSs operate at S-band frequencies: 2110–2120 MHz for earth-to-spacecraft transmission and 2290–2300 MHz for spacecraft-to-earth transmission.

To provide sufficient tracking capability to enable useful data returns from around the planets and from the edge of the solar system, a 64-m (210-ft) diam antenna network will be required. Two additional 64-m (210-ft) diam antenna DSSs are under construction at Madrid and Canberra, which will operate in conjunction with DSS 14 to provide this capability. These stations are scheduled to be operational by the middle of 1973.

B. Compatibility Test Facilities

In 1959, a mobile L-band compatibility test station was established at Cape Kennedy to verify flight–spacecraft–DSN compatibility prior to the launch of the *Ranger* and *Mariner* Venus 1962 spacecraft. Experience revealed the need for a permanent facility at Cape Kennedy for this function. An S-band compatibility test station with a 1.2-m (4-ft) diam antenna became operational in 1965. In addition to supporting the preflight compatibility tests, this station monitors the spacecraft continuously during the launch phase until it passes over the local horizon.

Spacecraft telecommunications compatibility in the design and prototype development phases was formerly verified by tests at the Goldstone DSCC. To provide a more economical means for conducting such work and because of the increasing use of multiple-mission telemetry and command equipment by the DSN, a compatibility test area (CTA) was established at JPL in 1968. In all essential characteristics, the configuration of this facility is identical to that of the 26-m (85-ft) and 64-m (210-ft) diam antenna stations.

The JPL CTA is used during spacecraft system tests to establish the compatibility with the DSN of the proof test model and development models of spacecraft, and the Cape Kennedy compatibility test station is used for final flight spacecraft compatibility validation testing prior to launch.

II. Ground Communications Facility

The GCF provides voice, high-speed data, wideband data, and teletype communications between the SFOF and the DSSs. In providing these capabilities, the GCF uses the facilities of the worldwide NASA Communications Network (NASCOM)[3] for all long distance circuits, except those between the SFOF and the Goldstone DSCC. Communications between the Goldstone DSCC and the SFOF are provided by a microwave link directly leased by the DSN from a common carrier.

Early missions were supported by voice and teletype circuits only, but increased data rates necessitated the use of high-speed circuits for all DSSs, plus wideband circuits for some stations.

III. Space Flight Operations Facility

Network and mission control functions are performed at the SFOF at JPL. The SFOF receives data from all DSSs and processes that information required by the flight project to conduct mission operations. The following functions are carried out: (1) real-time processing and display of radio metric data; (2) real-time and non-real-time processing and display of telemetry data; (3) simulation of flight operations; (4) near-real-time evaluation of DSN performance; (5) operations control, and status and operational data display; and (6) general support such as internal communications by telephone, intercom, public address, closed-circuit TV, documentation, and reproduction of data packages. Master data records of science data received from spacecraft are generated. Technical areas are provided for flight project personnel who analyze spacecraft performance, trajectories, and generation of commands.

[3]Managed and directed by the Goddard Space Flight Center.

Reference

1. *The Deep Space Network*, Space Programs Summary 37-50, Vol. II, pp. 15–17. Jet Propulsion Laboratory, Pasadena, Calif., Mar. 31, 1968.

DSN Multiple-Mission Command System

R. R. Rakunas and A. Schulze
DSN Engineering and Operations Office

This article describes the Deep Space Network (DSN) Multiple-Mission Command System and reflects the functions of the Deep Space Instrumentation Facility, Ground Communications Facility, and SFOF elements that support it.

I. Introduction

The purpose of the DSN Multiple-Mission Command System (MMCS) is to generate and transmit commands to one or two spacecraft simultaneously from a central location. All commands are originated at the Space Flight Operations Facility (SFOF) and can be sent to one or more Deep Space Stations (DSS) for storage or transmission to the spacecraft. The system also contains self checks to assure that improper commands are not processed and a verification system to confirm that proper data have been received by the DSS.

The MMCS is made up of three basic components: the SFOF, the Ground Communications Facility (GCF) and the Deep Space Instrumentation Facility (DSIF).

II. SFOF Operations

In the SFOF all command system data are processed by the 360/75 Central Processing System (CPS). Data which are sent to the DSS are formatted into data blocks and transmitted over high-speed data lines (HSDL) to the DSS. Data from the DSS or internal to SFOF are reformatted for display in the SFOF. A permanent record of command system activity is also generated by the CPS.

Command system data can originate from two areas of the SFOF. The Command System Operations Analysis Group Area (CAG) can generate command system control data or recall system data for display. Control messages, which include Standards and Limits and Configuration Messages, are stored at the DSS and are used to control the operation of the MMCS. DSN or project supplied standards and limits are used to permit automatic monitoring of certain functions of the MMCS by the DSIF. Violation of these values results in an Alarm Message being returned to the SFOF. Standards include maximum time of execution, frequency shift limits, symbol rates, exciter frequency, spacecraft number, etc. The command instruction configuration table automatically configures the DSS equipment for a particular mission. Another type of control message is a Command Recall Request

Message, which is used to check the status of system data such as standards and limits, configuration, or commands stored at the DSS. The station responds to this message with a Recall Response Message, which is displayed at the SFOF.

The Mission Support Area (MSA) can generate Command Messages, Enable or Disable Messages, or recall system data for display. During a mission, this area is manned by project personnel. At the present time all commands are input at the SFOF MSA; however, future models of the MMCS will have the capability of receiving inputs from remote MSAs. This will enable commands to be originated at locations remote to the SFOF, sent over HSDLs, and processed at the SFOF for transmission to the DSS.

Command data that must be entered each time a command is sent include type of command (priority, timed, or free), enable status (immediate, automatic, or manual), time of transmission (if timed), and the command. Other data included in the Command Message, such as DSS number, spacecraft number, day of year, message number, etc., are automatically entered in the HSD message by the CPS.

When the Command Message reaches the DSS, a Verify Message is returned to the SFOF where it is checked bit-by-bit against the transmitted message. The Verify Message is identical to the original message except that the source and destination codes are reversed. The Verify Message also contains an alarm word (synchronous alarm) to indicate whether the received HSD command block contained an error. If no Verify Message is received at the SFOF, the Command Message will automatically be retransmitted every five seconds up to seven more times or until it is verified. If the DSS does not accept the message after eight transmissions, this information will be displayed at the SFOF.

Once the command is accepted and is in the command stack, it cannot be removed for transmission to the spacecraft until it is enabled from the SFOF. This can be done in one of three ways. An "immediate enable" command has the enable included in the command message block, and is immediately enabled upon acceptance by the DSS. When an "automatic enable" command is sent and a Verify Message is returned, the CPS automatically sends the enable in an Enable Message for that command. When a "manual enable" command is sent, the operator in the MSA must manually send an Enable Message after the verification has been received. Once a command has been enabled, it will automatically be removed from the command stack at the proper time for transmission to the spacecraft.

Any command can be deleted from the stack by sending a Disable Message from the MSA. When a command has been deleted, it cannot be processed further. A timed command can be deleted from the stack by sending a duplicate Command Message (one with the same message number and subnumber) from the MSA. Since the new command will replace the original command in the stack, this can be used to change the time of a command without first sending a Disable Message.

Certain predefined commands may be categorized as critical commands. These commands cannot be transmitted to the DSS until an interlock key is entered at the MSA.

Data may be entered into the system in one of two formats: alpha-numeric or pseudo-octal. A translate table in the CPS converts alpha-numeric or pseudo-octal inputs to binary form which is used in the HSD blocks. Data may be input from an IBM 2260 with keyboard or stored command data tables. The data tables are a set of commands constructed in the CPS from a card file or project software (COMGEN for *Mariner* Mars 1971) and activated by a 2260. Once the file has been enabled, the CPS extracts commands, constructs HSD blocks and sends them to the DSS. When the number of commands in the stack reaches a predetermined level, an Alarm Message to the CPS will inhibit any more blocks from being sent until there is enough room in the stack for one more block. This process will continue automatically until inhibited manually from the 2260 or the file is empty.

Each area also has output devices to monitor system performance. These include IBM 1443 line printers, IBM 2260, digital TV, and TTY typewriters. Input and output devices are assigned to appropriate areas by the Operations Chief (OC). Voice communications networks are also available in CAG, MSA, and Operations Control Area.

III. Ground Communications Facility

The GCF provides the communications networks for the MMCS. These include HSDLs between SFOF and the DSIF for transmission of high-speed data blocks and the voice communications between the SFOF and the DSIF.

IV. DSIF Operations

The DSIF is made up of ten Deep Space Stations around the world. The main function of the MMCS at the DSS is to automatically receive command data from the SFOF, convert these data to a form which can be recognized by the spacecraft and transmit the data to the spacecraft. The DSS also sends Verification Messages to the SFOF when HSD are received, sends Alarm Messages, and Confirm or Abort Messages. In addition to synchronous alarms, the DSS also generates non-synchronous alarms which are the result of a violation of certain predefined conditions and are sent to the SFOF in a separate Alarm Message. As a backup to the HSDL, the DSS has the capability to manually enter command data by means of typewriter based on verbal information from the SFOF over the Operational Voice Communications Subsystem. However, this procedure is only used as a last resort in the event of an SFOF or GCF failure, and only when the command transmission to the spacecraft is critical.

The DSS MMCS hardware consists of the Telemetry and Command Data Handling Subsystem (TCD) which is made up of the Telemetry and Command Processor (TCP) and the Command Modulator Assembly (CMA). The TCP accepts and stores control data, accepts and stores command data up to 24 hours or until enabled or disabled, sends Verification, Alarm and Confirmation Messages to the SFOF, configures the CMA, sends Command Messages to the CMA, and generates permanent records of command system activity.

The command stack, which is a section of the TCP, is divided into three sections containing priority (P-type), timed (T-type), or free (F-type) commands. When enabled, P-type commands are transmitted immediately and in order of their reception at the TCP. Enabled T-type commands are transmitted within one-tenth second (starting with *Pioneer F*) of their specified time of execution. If another command is in the process of transmission when a T-command transmission time is reached, the T-command is automatically aborted and deleted from the stack. Any other command which is aborted is stored in the TCP until it is re-enabled or disabled by the SFOF. When a series of timed commands are sent, the time of execution cannot be less than the time required to transmit the previous command. Enabled F-type commands are transmitted on a non-interference basis with the other commands.

There are 126 positions set aside in the TCP for the command stack. Each position can store 24 bits, or one HSD word. For *Mariner* Mars 1971, this means that the stack will hold a maximum of 42 P-commands (3 TCP positions are required for each P-command), or 24 T-commands plus 2 P-commands (5 TCP positions are required for each T-command). The TCP generates a "stack warning" alarm when more than 84 command stack positions are filled and a "stack full" alarm when all 126 command stack positions are filled.

The SFOF will normally send HSD Command Messages to the stations from a command file; however, this process is interrupted when the "stack warning" alarm is received at the SFOF. After this, the commands can only be input from the 2260 in the MSA. When a "stack warning" dealarm is generated (84 stack positions or less are filled), the SFOF will resume the automatic file procedure. When the SFOF receives the "stack full" alarm from a station, no more commands can be accepted into the stack.

If a command is executed without encountering an abort condition, the station sends a Confirm Message to the SFOF indicating the identity of the command, the time of transmission, and the actual transmitted bits. If an abort condition interrupts a command transmission, the station sends an Abort Message to the SFOF indicating the identity of the command, the time of transmission, the bit at which the abort ocurred, the actual bits that were transmitted, and the reason for the abort.

V. Command Data Records

The SFOF to station HSD command traffic is stored by the SFOF in the system data record (SDR). From this record, the SFOF generates the master data record (MDR) which is delivered to the project. The station stores the station to SFOF HSD command traffic in the original data record (ODR) for playback to the SFOF to fill in missing command data records at the SFOF. The station also makes an analog recording of the actual bit stream of each command at the output of the CMA.

Pioneer Mission Support

A. J. Siegmeth
Mission Support Office

This article continues the description of the Pioneer F and G missions. The tracking and data acquisition support requirements are correlated with the mission characteristics. A description of the spacecraft's telecommunications and antenna subsystems is given. The CONSCAN subsystem, which has an automatic Earth-homing capability, is also delineated. The typical characteristics of the S-band telecommunications link during Jupiter encounter are depicted.

I. Introduction

The first part of this report was published in TR 32-1526, Volume II. It contained a description of the *Pioneer F* and *G* mission profile, the spacecraft system, electrical power supply, thermal control, and the structure and attitude control subsystems. Special emphasis was given on the characteristics of these missions which interface with the tracking and data acquisition functions.

This article describes both the telecommunications subsystem and the antenna system of the *Pioneer F* and *G* spacecraft. In addition, a description of the CONSCAN subsystem is given. This automatic spacecraft capability will precess the spacecraft's spin axis toward the Earth to line up the spacecraft's high-gain antenna axis to assure optimum telecommunications link performance.

II. *Pioneer F* and G Telecommunications Subsystem

The telecommunications subsystem performs a two-way function. The receiver portion of this subsystem maintains the telecommunications uplink with the transmitter of an Earth-based Deep Space Station; the transmitter portion sends spacecraft-originated signals in the form of a downlink toward the receiver of a Deep Space Station. Both the spacecraft receiver and transmitter can operate in a cascaded, coherent mode, thus making the extraction of the two-way doppler frequency shift possible at a Deep Space Station. This doppler frequency shift is proportional with the radial velocity between the spacecraft and the Earth-based tracking station. The time varying doppler frequency information is used to determine the spacecraft's trajectory and its space position versus time. The same doppler information is also used to generate

a priori type frequency and antenna angle predictions necessary to make future spacecraft signal acquisition possible. The Automatic Gain Control (AGC) voltage output of the spacecraft receiver is used for spacecraft spin axis and high-gain antenna axis orientation determination and control. The rotational motion of the spin stabilized spacecraft is used to generate a conical scan AGC signal. In this mode the spacecraft antenna main lobe is offset from the antenna axis to generate a conical scan. Both *Pioneer F* and *G* spacecraft will use the standard DSN S-band carrier frequencies and will operate on channels 6 and 7 of the DSN frequency bands. The S-band Earth/spacecraft uplink will operate on the PCM/PSK/PM modulation format; the spacecraft/Earth downlink will use a single subcarrier PCM/PSK/PM modulation scheme.

Figure 1 shows a block diagram of the telecommunications subsystem. Redundant spacecraft receivers, transmitter drivers, and traveling-wave-tube amplifiers are used. In addition, redundant power supplies are also employed to ensure the highest reliability of this vital subsystem. Either spacecraft receiver or power amplifier can be connected through coaxial switches and diplexers to the spacecraft's two antenna subsystems. One of the spacecraft receivers is always connected to each of the two spacecraft antenna systems. Either receiver is automatically capable of providing a phase-coherent signal to one of the transmitter drivers whenever a spacecraft receiver is locked to an uplink signal. This coherent mode can be inhibited by command. The transmitter frequency is controlled by an auxiliary oscillator whenever the spacecraft receiver is not locked to a DSN uplink signal. The redundant traveling-wave-tube amplifiers deliver 8 watts total power to the antennas. During the early part of the mission and during maneuvers, a medium-gain/omni antenna combination is used. The omni antenna is located aft of the spacecraft and is connected via a coupler to a medium-gain antenna mounted on the antenna feed tripod of the high-gain antenna. A 2.75-meter-diameter solid parabolic antenna dish which fits into the shroud of the launch vehicle is the reflector of the high-gain antenna. This dish is illuminated with a circular polarized antenna feed. The high-gain antenna produces a maximum gain of approximately 33 dB and the half-power beamwidth is about 3.5 degrees. The forward-facing medium-gain cone antenna provides a maximum effective gain of about 12 dB and a beamwidth of 32 degrees at the half-power point. The rearward-facing omni antenna is a logarithmic conical spiral having an effective gain greater than -5 dB over the aft hemisphere of the spacecraft. Since the medium-gain and omni antennas are fed from the same power source using a coupler, an interference zone exists between the forward and aft patterns.

The spacecraft/antenna configuration is displayed in Fig. 2. The medium-gain antenna located on the top of the high-gain antenna tripod is mechanically offset from the spin axis by approximately 9 deg. This offset is necessary to generate in the spacecraft receiver an AGC voltage variation which has a somewhat distorted sinusoidal pattern if the spacecraft axis is not in line with the direction of an Earth-based Deep Space Station. The conical scan offset of the medium-gain horn antenna is mechanically fixed and cannot be changed during the flight. In contrast, the feed mechanism of the high-gain spacecraft antenna can be moved mechanically by means of an electro-thermal actuator. This device can place the antenna feed in two extreme positions. In the so-called offset position, the feed is moved out from the center of the antenna, and, therefore, the main lobe of the high-gain subsystem has an angular offset against the antenna axis and spacecraft spin axis. It should be noted that because of certain thermal equilibrium constraints of the antenna feed, the high-gain antenna of the spacecraft will operate during the first 90 days of the flight in the conical scan type offset position and the antenna feed actuator can only be commanded in to the center position after this time. Therefore, the spacecraft high-gain antenna signal (both ways) will be exposed for the first 90 days to a variation of the signal amplitude during each spacecraft revolution and at each 12-second period when the spacecraft spin axis is not lined up completely in the direction of the Earth.

There is an approximate 20-cm (8-inch) offset between the electrical axis of the high-gain antenna and the spin axis of the spacecraft. During launch operations the two RTGs, including their supporting rods, are moved toward the center of the spacecraft below the high-gain antenna, and the magnetometer boom is also folded up and located at the opposite of the two RTGs. In this configuration the spacecraft is fully balanced toward the Z-axis and will rotate during the first stage burning for stabilization purposes at about 60 rev/min. After spacecraft separation, an automatic on-board sequencer releases the magnetometer boom, and the supports of the RTGs, which move out from the spacecraft by means of centrifugal force, are applied upon them. After the RTGs are deployed, the spacecraft spin axis line moves away from the original center point of the high-gain antenna system toward the minus X-axis. The spin axis will remain approximately 20 cm (8 inches) from the high-gain antenna

axis during the flight. This distance can vary slightly depending upon the fuel level in the hydrazine tank.

The polar radiation patterns of the medium-gain/omni and high-gain antenna are shown in Fig. 3. This radiation pattern indicates that there is a fringe zone between the omni and medium-gain antenna patterns because both antennas are fed from the same transmitter. Since the fringe patterns have a tilt toward the spin axis, it is expected that, during so-called spacecraft turn-around maneuvers, DSN will have difficulty in maintaining a useful telecommunications link between the spacecraft and the Deep Space Stations. The high-gain antenna pattern also shows the first order side lobes which are approximately 9 degrees from the main lobe.

III. CONSCAN Subsystem

The CONSCAN subsystem logic is a signal processor which conditions the amplitude-modulated AGC signal produced in the spacecraft receiver by the scanning motion of the offset antenna pattern, and extracts a phase reference for generation of a thruster firing signal. Figure 4 shows that the antenna lobe gain varies during the spin between positions A and B. During one 12-second spin period, the amplitude-modulated AGC signal describes one cycle of a sinewave. The positive going zero crossing of the sinewave is determined by a phase estimator which automatically fires two precession thrusters. A signal-to-noise ratio threshold detector, which is part of the CONSCAN processor, terminates the automatic thruster firing. This occurs when the amplitude modulation index of the CONSCAN signal has dropped to a point where the phase estimator cannot determine the positive going zero crossing to an acceptable accuracy. The spacecraft precession thrusters fire once per three revolutions. The integration time within the phase estimator is two revolutions. The automatic CONSCAN precession is generally initiated by a command sent from the *Pioneer F* Mission Support Area by the *Pioneer* Missions Operations Team.

Looking from the spacecraft, Earth will appear on the star sphere as a bright star. The spacecraft spin axis trajectory will describe a random walk-type spiral when the following conditions are exemplified (Fig. 5): The high-gain antenna together with the spacecraft spin axis points away from the Earth by 2.2 degrees, and the phase estimation has a constant 30-degree phase error and a signal-to-noise ratio of 10 dB. In this homing mode, the spin and antenna axes will move up to the 0.3-degree target dead zone. At this zone, the signal-to-noise ratio of the phase estimator will degrade to a level where the phase determination is not now possible. The small circles shown on the spin axis trajectory will be caused by circular movement of the spacecraft spin axis wobble. As the spacecraft spin axis reaches the CONSCAN dead zone, the threshold detector disconnects the automatic operation and the automatic CONSCAN maneuver is completed. Because of the continuous changes between the Earth and the spacecraft's relative locations, this maneuver must be repeated approximately every 3 to 4 days during the early part of the mission and every week during the time that the spacecraft travels at a Jupiter distance.

Because of signal amplitude versus noise constraints of the spacecraft's CONSCAN subsystem, the *Pioneer* Project requires that the amplitude stability of the effective radiated power transmitted by the Deep Space Stations should be within 0.1 dB peak-to-peak about the spacecraft's spin frequency.

DSN has already developed techniques to check the amplitude stability of the effective radiated power of the uplink signal, and has verified that the capability exists as required by the *Pioneer* Project for CONSCAN support. Development work in this area was conducted at DSS 71 and the verification tests were performed at DSSs 11 and 12. The best technique applied provided an upper bound measurement of the RF amplitude instability due to the combined effects of the transmitter power variations and antenna pointing errors. Using this technique, no new station hardware is required. The outputs of software analysis programs will give the assurance that the Deep Space Stations are ready for *Pioneer F* CONSCAN operations.

It should be mentioned that the spacecraft's CONSCAN processor cannot distinguish between RF amplitude variations due to the spacecraft's aiming errors and those due to fluctuations in the DSIF effective radiated power. Therefore, the use of the DSN uplink signal as a beacon signal required the re-evaluation of the ERP variations at the Deep Space Stations.

The small amplitude variations of the transmitter power were monitored with a crystal detector and with the aid of a frequency translator and the DSIF S-band receiver. The antenna pointing was evaluated using a DSS ground receiver's AGC output while tracking ALSEP 1, the Lunar Scientific Package. The assumption

was made that the instability of the uplink signal amplitude due to antenna pointing errors is almost identical to that of the downlink signal.

The ERP variations detected by a synchronous AGC detector were recorded on a digital tape and analyzed off line. In addition, a power spectrum type frequency analysis was also made to obtain the data in the frequency domain.

The analysis of the data shows that the ERP variation of the DSS 11 uplink was in the vicinity of 0.0355 dB rms within the frequency response of CONSCAN. No periodic component was observable in this bandpass.

IV. CONSCAN Backup Modes

To obtain near optimum data return from the *Pioneer F* and *G* spacecraft, the Mission Operations Team of the flight project is required to make continuous plans to assure that the high-gain antenna points toward Earth during all phases of the mission. Since the CONSCAN subsystem developed for these third generation *Pioneer* missions is the first space application of an Earth-seeking automatic device, the flight project elected to develop backup modes to be used in the case of a possible degradation of the CONSCAN subsystem. Four basic backup modes are planned and certain specific requirements were generated in order to assure a successful backup operational capability.

A. Ground-Processed Uplink CONSCAN

The first of the CONSCAN backup modes is the ground-processed uplink CONSCAN. If the CONSCAN processor is inoperable, but the Sun or star sensor and the high-gain antenna offset mechanism is working, the Project plans to obtain the telemetered amplitude and phase information of the spacecraft's CONSCAN signal relative to the roll index pulse generated by the Sun or star sensor. In this mode DSN will furnish real-time spacecraft telemetry to the Missions Operations Team, and the Project will compute the roll index pulse versus CONSCAN zero crossing angle. This information will be transmitted via commands to the spacecraft and stored in the Program Storage and Execution module. The module will then fire the precession thrusters. The spin axis of the spacecraft will precess in this mode on a rhumb line. Figure 6 shows that if an Earth-based vehicle moves between two points, using a constant bearing angle versus north, the vehicle's trajectory will describe a rhumb line.

B. Ground-Processed Downlink CONSCAN

The second CONSCAN backup mode is the ground-precessed downlink CONSCAN. The spacecraft spin axis can be precessed in this mode in case the star and Sun sensors are inoperative and the high-gain antenna is in the CONSCAN offset mode. To assist the Project team in firing the precession thrusters in the proper time, DSN is required to assist the Project in the measurement of the light round-trip time. The Project will send a command to switch the telemetry format of the spacecraft. After the format change has been received by DSN, the light round-trip time can be established to an accuracy of 0.1 second. DSN plans to hold the command and telemetry systems timing accurate to 10 ms GMT. To make the ground precessed downlink CONSCAN possible, DSN also plans to transmit, via the TCD of the DSS, ten DSN S-band receiver AGC samples per second to the SFOF. This information will be used by the Project to establish a downlink CONSCAN signal in the Mission Support Area. DSN will also provide a capability to transmit command words to a transmission execution accuracy of 0.1 second in Greenwich Mean Time. With DSN's assistance the Project will have a capability to fire spin axis torquing thrusters at a predetermined roll position of the spacecraft. The roll angle position uncertainty will be in the vicinity of 3 degrees, equivalent to a thruster firing timing error of 0.1 second. The success of such a maneuver will be verified by the downlink carrier power level measurements made at the DSS and comparing them with the predicted values.

C. Dead Reckoning

Dead reckoning can also be used as a CONSCAN backup. This method can be applied if the CONSCAN precessor of the spacecraft and the high-gain antenna offset are inoperable, and if the Programmed Storage and Execution board is still working. In this backup mode, the Project plans to follow the following procedure: The spacecraft's spin axis will be torqued in an open-loop mode in a transfer plane to detect and validate the peak of the antenna main lobe. In addition, once this peak is established the spin axis will also be torqued in a new plane perpendicular to the previous plane to detect and validate the improved peak of the antenna main lobe. If necessary, the spin axis can be torqued further to arrive at the opposite -3 dB point. To make a dead-reckoning maneuver possible, the Project requires that the relative downlink carrier power (AGC) measurements do not drift more than 0.125 dB. These AGC measurements will be transferred from the Deep Space Stations to the Mission Support Area at the SFOF.

Project plans to plot the resultant antenna pattern using display devices provided by DSN. Figure 7 depicts the correlation of spin axis pointing versus high-gain antenna patterns observed during a typical dead-reckoning maneuver.

D. Search Mode

The fourth CONSCAN backup mode is the search mode. If the star and Sun sensor, the Programmed Storage and Execution board, and the Antenna Offset are inoperable, the search mode maneuver can be applied to point the spacecraft high-gain antenna toward Earth. To make this possible, DSN will have a timed command capability accurate to 0.1 second in GMT. To operate the search mode, the Project will establish and verify the two-way light round-trip time by sending a timed command to the spacecraft and receive a telemetry format change. After the spin period is also established, the Project will send real-time thruster commands in a search pattern. The plotting of a high-gain antenna pattern will be used to determine the peak of the pattern, thus analyzing the results of the torquing precession maneuvers. It should be noted that the hydrazine fuel consumption in a search mode can be four times as high as the fuel needed to operate in the automatic CONSCAN mode.

V. Signatures of the Telecommunications Link

Since *Pioneers F* and *G* are using the telecommunications link for spacecraft spin axis attitude determination and control, the rotating antennas can add amplitude and phase signatures to the telecommunications downlink. The amplitude signatures are caused by the following factors:

(1) The rotating antennas in the offset CONSCAN mode can vary the S-band downlink amplitude from zero up to 10 dB during every 12-second period. The amplitude of this variation is a function of the antenna axis attitude toward Earth. If the antenna axis points exactly toward the Earth, the amplitude variation is almost zero, but, if the spacecraft high-gain antenna axis is off from the Earth direction by 2 degrees, the amplitude of the downlink can vary from zero to 10 dB during each spacecraft revolution.

(2) The spacecraft and DSN antennas are circularly polarized. The mutual polarization ellipticity between the *Pioneer F* spacecraft high-gain antenna and the DSN Earth-based antenna can cause an amplitude variation of 0.5 dB. This variation can be detected by DSN as a periodic ripple of the downlink signal amplitude. This variation occurs at the double value of the spacecraft spin rate and has a period of approximately 6 seconds.

(3) An additional amplitude variation is also caused by spacecraft wobble. Every torquing pulse causes a wobble motion of the spacecraft spin axis which is gradually damped out by special devices carried on board the spacecraft. The signal amplitude variations caused by wobble can be as high as 0.5 dB. This variation occurs at the resultant wobble frequency.

Besides the amplitude signatures, certain phase signatures are also the by products of rotating spacecraft antennas. The phase signatures can be described in two groups:

(1) The S-band downlink carrier can be exposed to phase variations caused by the spacecraft antenna spin axis offset of approximately 8″ and by antenna alignment uncertainties. Radial movements from $\pm 0.01''$ up to $\pm 1.4''$ can be expected. These variations continuously affect the downlink doppler frequency, but because of their periodic nature, they can be filtered out from the doppler solution and will not upset the accuracy of trajectory determination.

(2) Because of the mechanical rotation of the spacecraft antenna versus the fixed Earth-based DSS antenna, the two-way precision doppler counter of DSN loses approximately 2.1 doppler cycles during each spacecraft revolution. The loss of these doppler cycles can adversely affect the accuracy of trajectory determination. The Project plans to determine the spin rate history of the spacecraft using telemetry data and will generate a time history of the lost doppler cycles for trajectory determination corrections.

It should be pointed out that the described amplitude and phase signatures will not affect the performance or efficiency of ground-based hardware or software of the DSN, but will affect the operational capabilities of the spacecraft downlink especially when the amplitude variations are above 1 dB.

The *Pioneer* utilization of the two-way S-band telecommunications link can be summarized as follows: The

coherent S-band carrier uplink radiated by DSN will be used in the PCM/PSK/PM mode for commanding purposes. The uplink signal will also be used by the spacecraft for automatic CONSCAN operation, thus making possible an automatic spin axis attitude control. Further use of the uplink will be the transmitting of Project-initiated timed commands in the CONSCAN backup modes. These commands will torque the spin axis attitude by ground-based control. The S-band coherent downlink signal transmitted by the spacecraft will be received by DSN. Ground-based equipment will detect the downlink carrier in a synchronous mode and one subcarrier operating in a PCM/PSK/PM mode will transfer telemetry data from the spacecraft to DSN. This function is necessary to provide the Project science and engineering telemetry data collected from the spacecraft. DSN will also provide means for the Project control team to determine the antenna pattern of the spacecraft and by detecting the downlink amplitude variations caused by spacecraft spin modulation. Both measurements will be used by the Project for spacecraft spin attitude control. Since the S-band uplink and downlink carrier is coherent, DSN extracts the doppler frequency shift which is proportional to the range rate between the ground-based station and the spacecraft. This radiometric tracking information will be used by the Project for spacecraft trajector determination.

Figures 8, 9, and 10 show typical power budgets of the S-band downlink carrier, subcarrier and uplink carrier during *Pioneer F* Jupiter encounter. The downlink carrier power performance margin referenced to a 6-dB signal-to-noise ratio threshold in the carrier tracking loop is 11.1 dB. If the spacecraft would operate in the uncoded mode at Jupiter, the telemetry bit rate would be 512 bps; the telemetry bit error rate would be one error in a thousand detected bits. Since the Project plans to operate these spacecraft most of the time in the convolutional coded mode, an error-free bit rate of 1,024 bps can be predicted assuming a coding gain of 3.8 dB. If the 64-meter DSN antenna is used with a nominal 20-kW output in the uplink, a 26-dB performance margin to threshold can be expected in the spacecraft receiver. The given performance is based upon the assumption that the spacecraft high-gain antenna points to the Earth and that the spacecraft telecommunications subsystem would operate from the Earth to Jupiter for almost two years without any detectable deterioration. With the 26-meter antenna Deep Space Stations, a Jupiter flyby telemetry rate would be 64 bps in the convolutional coded mode.

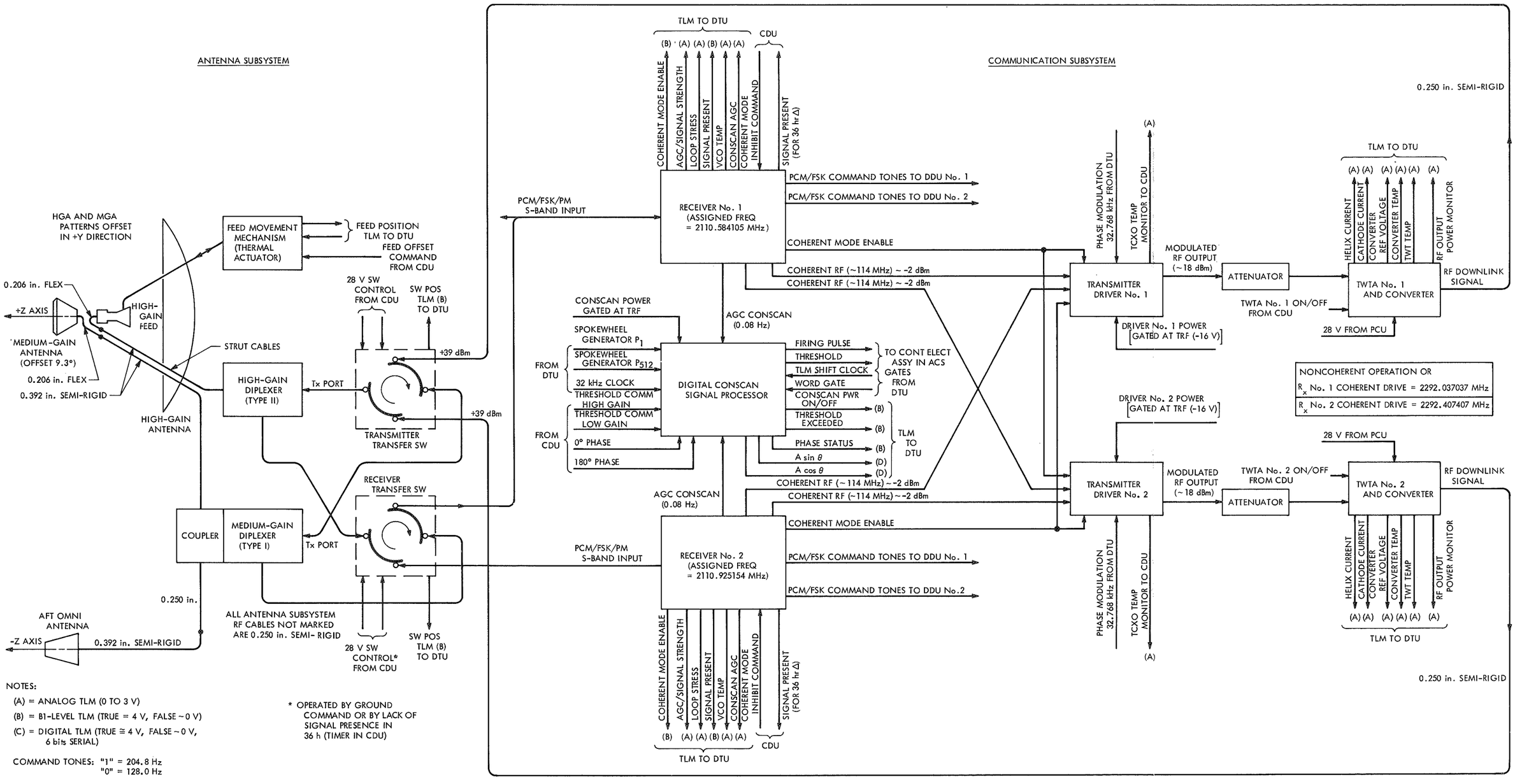

Fig. 1. *Pioneer F* and *G* antenna and communication subsystems

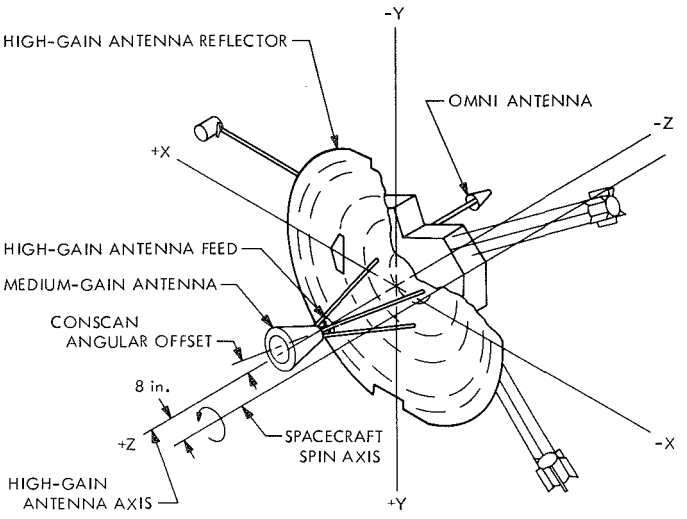

Fig. 2. *Pioneer F* and G spacecraft/antenna configuration

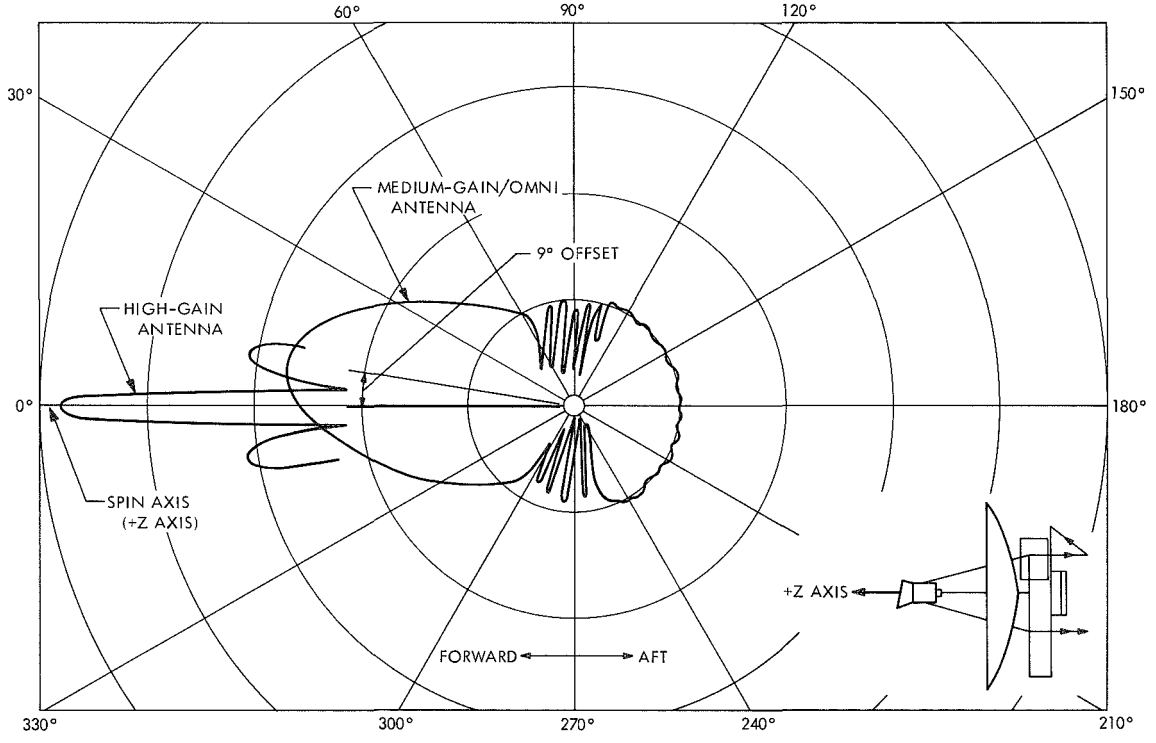

Fig. 3. Polar radiation patterns for medium-gain/omni and high-gain antennas

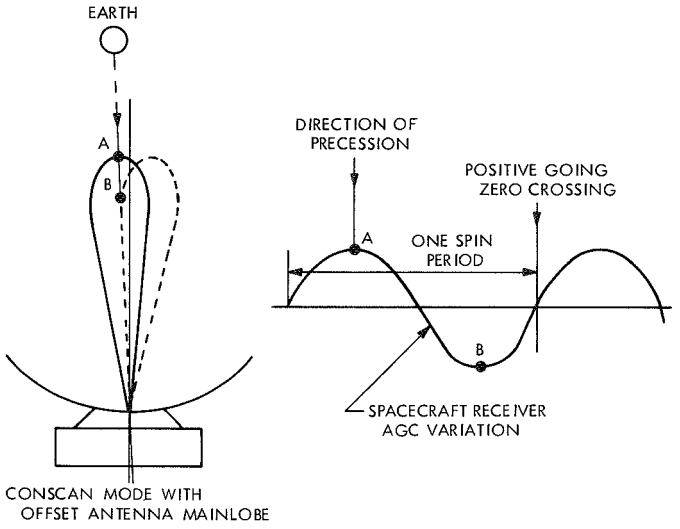

Fig. 4. CONSCAN

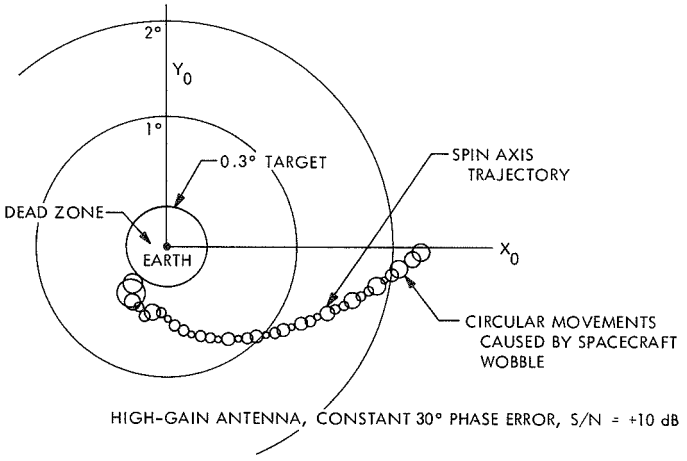

Fig. 5. CONSCAN closed-loop precession maneuver

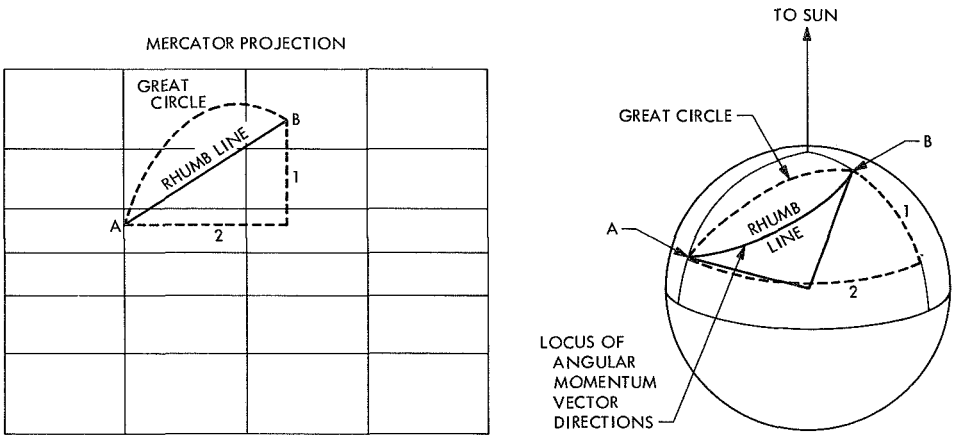

Fig. 6. Open-loop precession maneuver

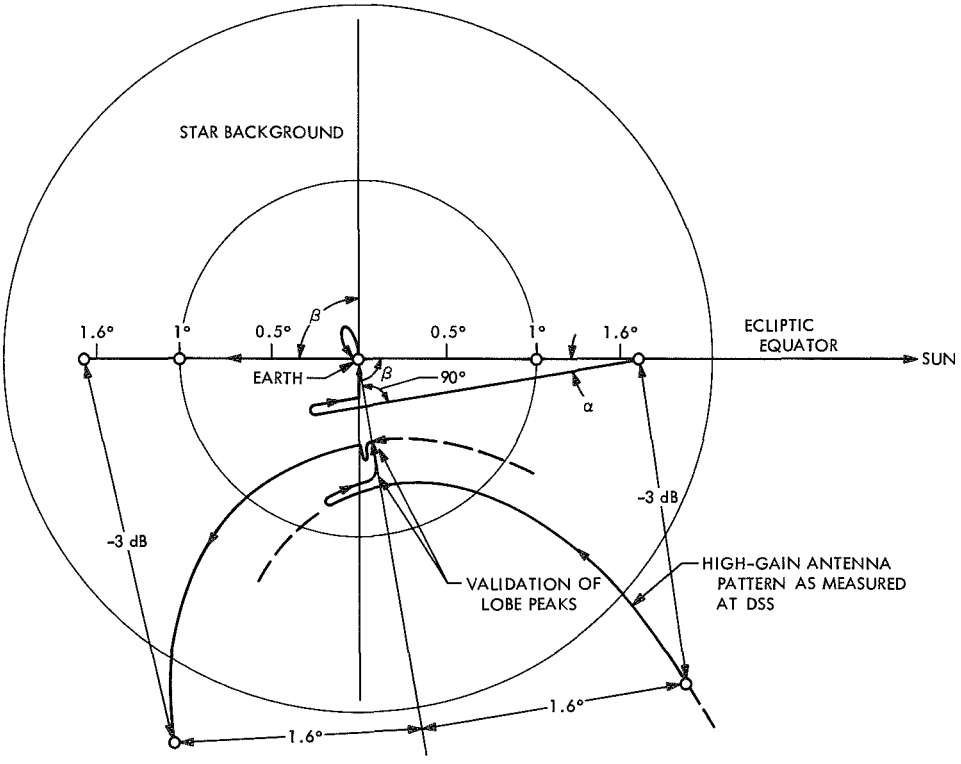

α = CONSTANT ANGLE BETWEEN ROLL INDEX PULSE AND PRECESSION PLANE
SPACECRAFT SPIN AXIS WILL MOVE ON A RHUMB LINE

Fig. 7. Dead-reckoning type torquing maneuver using high-gain spacecraft antenna

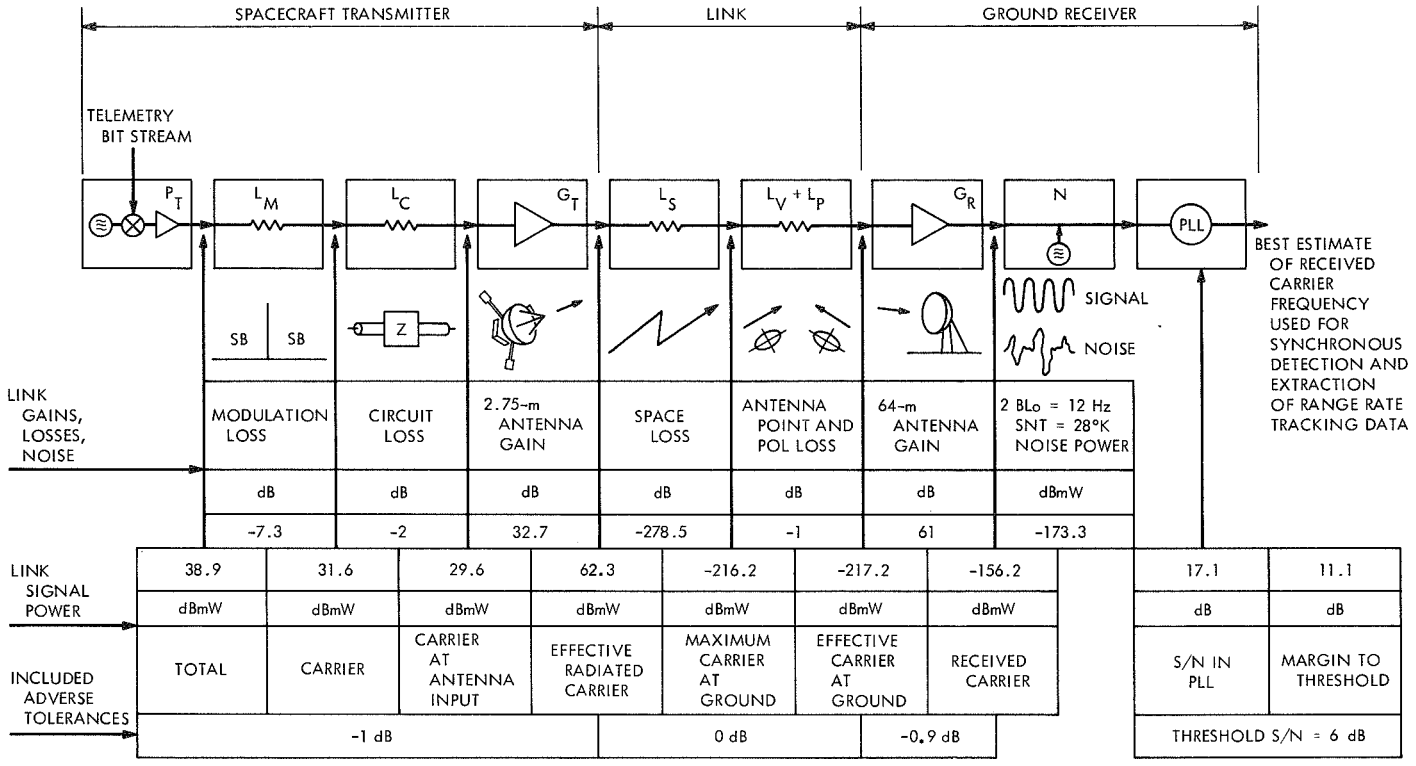

Fig. 8. *Pioneer F* Jupiter encounter downlink carrier power budget for tracking system

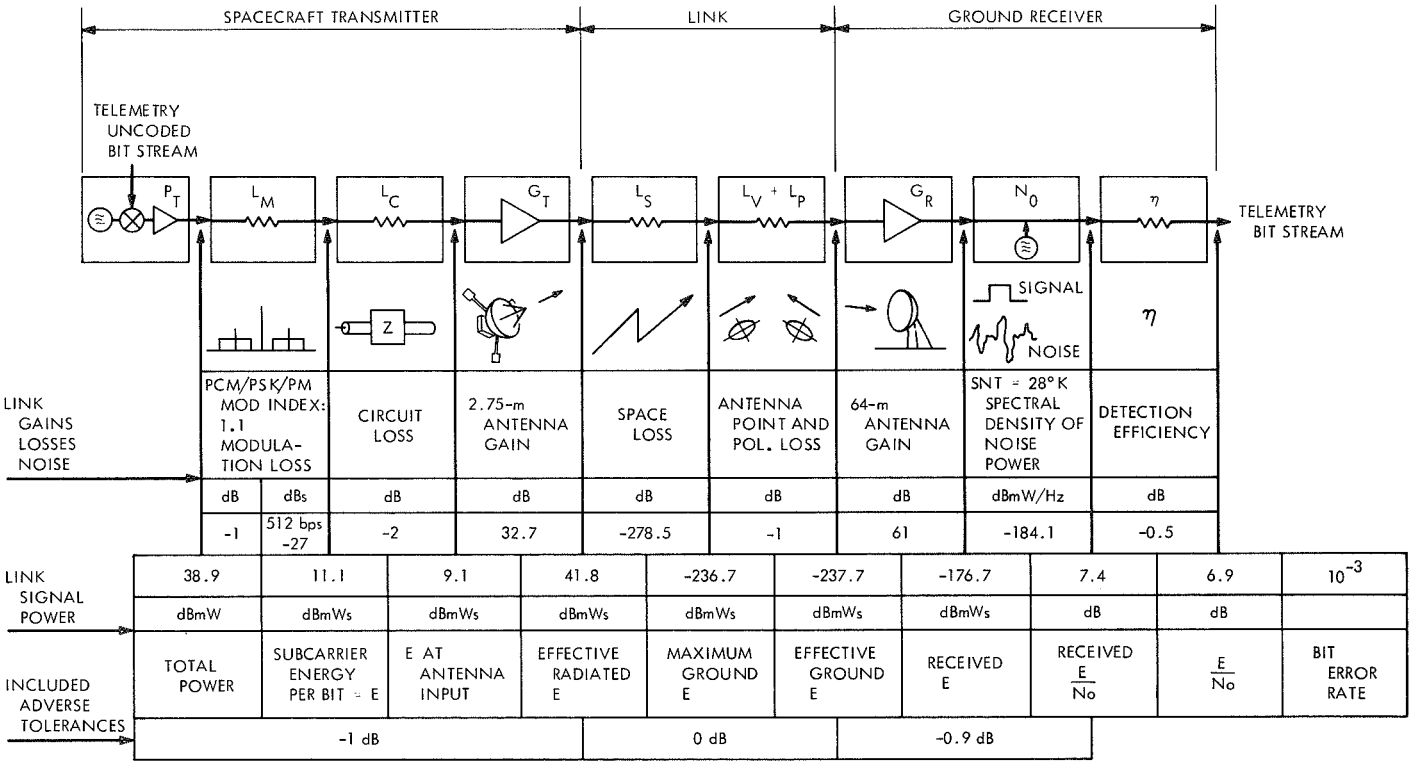

Fig. 9. *Pioneer F* Jupiter encounter downlink subcarrier power budget for telemetry system

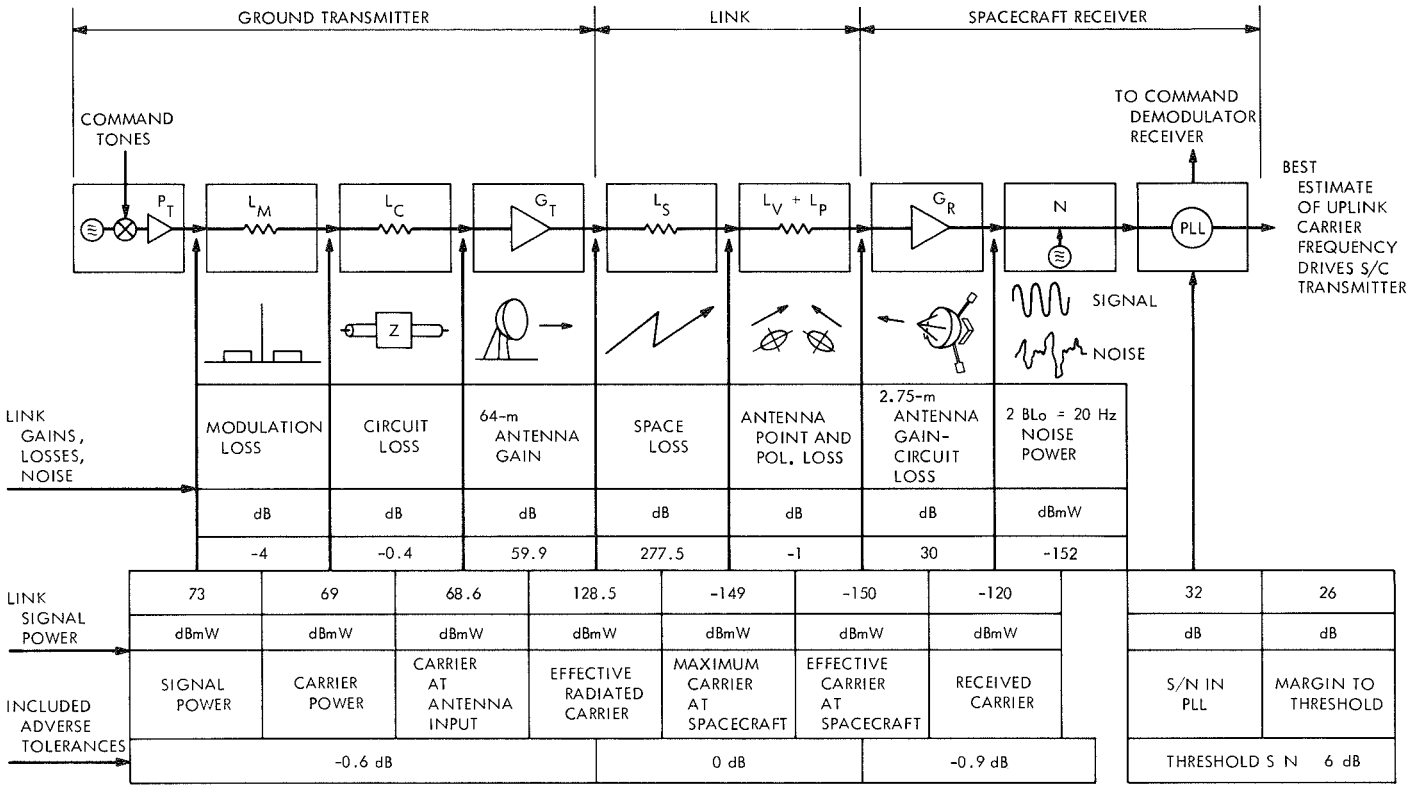

Fig. 10. *Pioneer F* Jupiter encounter uplink carrier power budget for command and tracking systems

Helios Mission Support

P. S. Goodwin
Mission Support Office

This is the second in a series of articles relating to Project Helios which, when used in conjunction with the first article, will give the reader an overall view of the Project, its objectives and organization, and the support to be provided by the Deep Space Network (DSN). This article treats, in particular, the contemplated Helios trajectories. Both the near-earth phase and the deep space phase of the mission are discussed, with particular emphasis being placed upon the tracking and data acquisition aspects.

I. Introduction

The previous article (Ref. 1) provided the historical background of Project *Helios,* a cooperative U.S.–West German deep space effort to send a spacecraft closer to the sun than any currently planned, free-world space program to date. Two launches are planned: the first in mid-1974 and the second in late 1975. In addition, Ref. 1 described the physical configuration of the spin-stabilized *Helios* spacecraft and provided the reader with an overview of the spacecraft radio and antenna subsystems. This article will be devoted to the contemplated *Helios* trajectories and their associated tracking and data acquisition support requirements. For convenience, the discussion will be divided into two parts: the near-earth phase and the deep space phase of the mission.

II. *Helios* Near-Earth Phase Trajectory and Support

During the planning and early design stages of any new flight project, it is important to investigate a few typical spacecraft trajectories to ascertain whether or not the spacecraft design, the mission objectives, and the necessary tracking and data system support can be molded into a viable total concept. For *Helios,* an initial effort started in 1968 and was culminated by the publication of the "Mission Definition Group Report" in April 1969. This initial effort proved the feasibility of the basic *Helios* concept. Subsequently, the West German *Helios* Project Office has selected a spacecraft prime contractor — Messerschmitt-Boelkow-Blohm (MBB), Ottobrun (near Munich), West Germany — who has now made a

preliminary design of the spool-shaped spacecraft (see Ref. 1). It was, therefore, appropriate to evaluate this preliminary spacecraft design with respect to not only the planned trajectory, but also to ascertain whether or not the post-launch mission sequences could be performed in an operationally efficient manner. Toward this end, a special *Helios* Near-Earth Phase Study Group was established during the Third *Helios* Joint Working Group Meeting in Bonn, October 5–9, 1970. In preparation for the Near-Earth Phase Study Group Meeting (which occurred the week following the Joint Working Group Meeting), the JPL/ETR organization developed a set of near-earth phase station coverage data for each of the tentative *Helios* trajectories developed by the NASA Lewis Research Center. These data, together with information provided by the *Helios* experimenters, provided a better knowledge of the spacecraft and launch vehicle performance characteristics, and a refined knowledge of the *Helios* Program mission objectives permitted the Near-Earth Phase Study Group to develop a tentative mission sequence following launch up through completion of the spacecraft's orientation maneuvers. In developing their recommendations for the near-earth sequence of mission events, the Near-Earth Phase Study Group considered both direct-ascent and parking-orbit trajectories. Typical "earth tracks" for these two classes of trajectories are shown in Figs. 1 and 2. The Near-Earth Phase Study Group concluded that the parking-orbit trajectory case provided only a moderate increase in launch window opportunities over that provided by the direct-ascent trajectory case, while at the same time presented a more difficult tracking and data acquisition problem due to the lack of sufficient tracking facilities in the South Atlantic and Indian Oceans. Therefore, the *Helios* Project Office accepted the Study Group's recommendation that for present planning purposes the nominal *Helios* mission design should be based upon a direct-ascent trajectory—but with the Project Office restriction that the spacecraft itself must be designed to be compatible with a parking-orbit trajectory in case the latter should become necessary sometime in the future.

Once the foregoing decision was made, the Lewis Research Center produced a formal set of *Helios* direct-ascent launch trajectories covering both the *Titan/Centaur* and *Atlas/Centaur* launch vehicle combinations (see Ref. 1). Subsequently, the JPL/ETR organization developed tracking and telemetry station coverage data for these upgraded trajectories. This material will be used during the second meeting of the Near-Earth Phase Study Group to be held in conjunction with the Fourth *Helios* Joint Working Group Meeting, Goddard Space Flight Center, April 28–May 5, 1971, to establish a formal mission sequence for the near-earth phase of the *Helios* mission. It is anticipated that this updated mission sequence will become the baseline design for the near-earth phase of the *Helios* mission, and that it will probably not undergo significant refinement until final spacecraft weights, etc., and launch vehicle performance data become available approximately a year prior to launch.

III. Deep Space Phase

A. DSN Initial Acquisition Phase

The exact definition of the completion of the near-earth phase and the beginning of the deep space phase of a particular mission is individually negotiated with each flight project; however, it is usually considered to be the point at which the spacecraft altitude is such that the Deep Space Network will have continuous (i.e., 24-hour/day) coverage of the spacecraft. For direct-ascent *Helios* trajectories, this would occur fairly soon after launch using one of the 0-degree longitude DSN stations, depending upon the launch azimuth. Figure 1 depicts two launch azimuth corridors for the *Helios* direct-ascent, *Titan/Centaur* launch vehicle. The upper corridor, between 50- and 60-degree launch azimuth, passes over the Madrid Deep Space Station while the lower corridor, 80- to 90-degree launch azimuth, passes over the Johannesburg, South Africa, DSN station. The gap between these two corridors represents an Eastern Test Range safety restriction to protect the island of Bermuda from possible launch vehicle impact. Of the two permissible *Helios* direct-ascent launch corridors, the one between 50- and 60-degree launch azimuth presents a slightly more difficult initial DSN acquisition problem due to high angular tracking rates, but at the same time affords the *Helios* Project the possibility of obtaining earlier communication with the spacecraft following separation. Figure 1 shows that for *Helios Titan/Centaur* direct-ascent trajectories, spacecraft injection occurs at approximately 15 degrees west longitude. Using the upper corridor, this would place spacecraft injection very close to spacecraft rise at the Madrid Deep Space Station. Since the spacecraft is still very close to the earth at that time, the angular tracking rates at Madrid can conceivably reach as high as 5 to 10 degrees per second immediately following injection. However, at the same time, the spacecraft is rapidly gaining altitude in its departure from the earth. This in turn causes the effective angular tracking rates to drop rather rapidly so

that after 5 to 15 minutes following injection, the tracking rates should fall within the capabilities of the Deep Space Station. During this initial high-rate period, the DSN will probably request cross-support from the Manned Space Flight Network (MSFN) stations at Madrid or Canary Island because they have the capability of tracking at 3 degrees per second as opposed to the approximately 1-degree per second capability of the Madrid Deep Space Station. Handover from the MSFN station to the DSN station would then occur as soon as the angular tracking rates fall within the Deep Space Station capabilities. Once the latter is accomplished, the trajectory is such that the Deep Space Network would have continuous spacecraft coverage capability.

The situation with respect to the lower direct-ascent launch trajectory is not quite so acute from an angular tracking rate point of view, but increases the time delay to initial DSN acquisition. However, it is not necessary to wait until the spacecraft reaches the vicinity of Johannesburg, South Africa, to achieve initial DSN acquisition. This is because the spacecraft altitude is rising very rapidly following injection so that, depending upon the actual launch azimuth within the lower corridor, initial acquisition can occur at either or both the DSN Madrid and/or Johannesburg stations while the spacecraft is crossing the region of 0 to 10 degrees east longitude for the first time. Further, this initial acquisition can be enhanced by cross-support from the MSFN Canary Island and/or Ascension Island stations. Again, the *Helios* trajectory is such that once initial acquisition has occurred in the lower launch corridor of Fig. 1, the DSN would have continuous spacecraft visibility from then on to the end of the primary mission.

The DSN initial acquisition situation with respect to the *Helios* parking-orbit trajectories is quite different. Though not part of the present *Helios* mission nominal design, the parking-orbit trajectory must be considered in case it is necessary to return to the *Atlas/Centaur* launch vehicle combination. In this event, the trajectory would be as shown in Fig. 2. The spacecraft is inserted into a nominal 160-km (100-mile) parking orbit at launch vehicle main engine cutoff (MECO). It remains in the 160-km (100-mile) parking orbit until third-stage burnout east of Johannesburg, South Africa, at which time it is injected into its heliocentric orbit. During the parking-orbit arc, only relatively short (3 to 8 minutes) tracking periods are possible from the Ascension Island station and/or any ships that might be deployed in the South Atlantic. Due to the high angular rates when a spacecraft is in earth orbit, it will probably not be possible to track the spacecraft from the Johannesburg Deep Space Station during its initial overhead pass, but rather await the time that the spacecraft has gained sufficient altitude following injection for it to re-rise over the station's eastern horizon. Depending upon the particular trajectory flown, the initial DSN acquisition could occur at either or both the Johannesburg and/or Canberra Deep Space Stations. However, this would occur a considerable number of minutes following injection and separation. Due to the criticality of these latter two events, the Project Office would probably request the TDS to deploy a ship into the Indian Ocean to cover this sequence. In such an event, the tracking ship would be considered part of the near-earth phase network, mentioned in *Section II*.

B. Spacecraft Orientation Maneuvers and Near-Earth Science Phase

As mentioned briefly in Ref. 1, the first of two spacecraft orientation maneuvers occurs shortly after spacecraft injection. The first maneuver, which normally occurs automatically, orients the spacecraft's solar panels until they are fully illuminated by the sun in order to relieve the load on the spacecraft's batteries. During this maneuver, the spacecraft's spin axis remains basically in the plane of the ecliptic with the result that the DSN's communication with the spacecraft is via the latter's omni-directional antenna system. Since the latter has not yet been completely designed, it is possible that there may be some antenna pattern nulls which could cause momentary communications dropouts following the initial DSN acquisition. However, the frequency of such dropouts should diminish as the spacecraft assumes a stable position and departs the vicinity of the earth. Once the spacecraft has completed its first (Step I) orientation maneuver, selected onboard science experiments are activated to measure the various shock fronts that surround the earth. This initiates the near-earth science phase of the mission which continues until the spacecraft has reached a distance equivalent to lunar range from earth. Due to the spacecraft's high-departure velocity from earth, it reaches lunar distance in approximately nine hours following injection (direct-ascent case). During this time, the spacecraft is still over the Madrid/Johannesburg Deep Space Stations (Fig. 1). The spacecraft's initial Goldstone rise occurs approximately 7 hours after injection—at which time the vehicle sub-earth point is slightly west of Ascension Island in Fig. 1. Following handover to the Goldstone Deep Space Station, the spacecraft is commanded to turn off the science instruments and then to execute the second (Step II) of

the two planned maneuvers. Using the procedures described in Ref. 1, Step II maneuver orients the spacecraft's spin axis to the pole of the ecliptic. This in turn permits the first use of the spacecraft's medium- and high-gain antenna systems. Following completion of the Step II maneuver and the orientation of the spacecraft's high-gain antenna, the onboard science instruments are reactivated to initiate the Cruise-Science Phase of the mission, which continues to the end of the primary mission.

The foregoing description depicted the case for the direct-ascent trajectory. The situation for the parking-orbit trajectory would be roughly similar except that the initial DSN acquisition and subsequent handover to Goldstone would be delayed in time over the direct-ascent trajectory case. This would mean that the spacecraft would be automatically performing its Step I maneuver during the time the DSN was attempting its initial acquisition. This might accentuate the problem associated with nulls in the spacecraft omni-directional antenna pattern, but at the same time, the acquiring Deep Space Station (either Johannesburg or Canberra) would be experiencing much lower angular tracking rates (and smaller general changes in azimuth pointing direction) than experienced in the direct-ascent case over Madrid. The degree to which these two factors might offset each other has not yet been determined. The parking-orbit trajectory does offer a slight advantage for early orbit determination purposes in that it is possible to get a two-station, different longitude orbit determination solution slightly sooner than in the direct-ascent case. However, since *Helios* spacecraft does not have a midcourse correction capability, there is no primary requirement for early orbit determination. These factors, combined with the somewhat delayed first acquisition at Goldstone, make the parking-orbit trajectories slightly less attractive than the direct-ascent trajectories using the *Titan/Centaur* launch vehicle. However, studies to date have indicated that a meaningful *Helios* mission can be flown using the *Atlas/Centaur* launch vehicle using the parking-orbit trajectory approach.

C. Primary Mission Phase

The primary phase of the *Helios* mission encompasses that time period from launch through first perihelion and up to the first solar occultation of the *Helios* spacecraft. (This encompasses Phase I and Phase II described in Ref. 1, i.e., Phase I covering the first several weeks where Mission Operations are conducted from the SFOF, and Phase II where Mission Operations are conducted from the remote terminal at Oberpfaffenhofen, West Germany.) The Deep Space trajectory for the *Helios* 0.25 AU perihelion case (*Titan/Centaur* launch vehicle) is shown in Fig. 3, and for the 0.3 AU case (*Atlas/Centaur* launch vehicle) is shown in Fig. 4. By current definition, the primary mission phase of *Helios* ends at first solar occultation—which in the case of the 0.25 AU mission occurs at approximately 110 days after launch, and in the case of the 0.3 AU mission occurs at approximately 120 days after launch. The region of greatest scientific interest occurs around perihelion (90 and 100 days, respectively, in Figs. 3 and 4), since this will be the previously unexplored region of our solar system. Therefore, continuous DSN coverage during this time period is a primary requirement. As mentioned in Ref. 1, the telecommunications link is being designed to provide useful scientific data rates back to the DSN 26-meter network during this time period, with the possibility of enhanced mission data return through supplemental use of the DSN 64-meter subnet and/or the West German 100-meter Effelsberg antenna station. While the perihelion phase has the greatest scientific interest, other important scientific objectives have created a requirement for the DSN to provide continuous (i.e., 24-hour/day) coverage to the *Helios* spacecraft from initial acquisition through first solar occultation. In the region from earth to first perihelion, the primary responsibility for providing continuous coverage will be placed upon the DSN 26-meter subnet, while in the region from perihelion to first solar occultation, the primary responsibility for *Helios* support will probably fall upon selected DSN 64-meter antenna stations in order to obtain planetary ranging data in support of the celestial mechanics experiment. During this same time period, the West German 100-meter Effelsberg station will be supporting the onboard scientific experiments at telemetry data rates in excess of those possible into the DSN 64-meter antennas. Since the Effelsberg antenna is a receive-only station, it will not be able to obtain planetary ranging data for the celestial mechanics experiment. However, the combination of the 100-meter Effelsberg station and selected DSN 64-meter stations will provide extremely valuable scientific data to the project in the region from perihelion to first solar occultation. This will be the first time that these large aperture antennas will be combined in the support of a flight project, and as such is an example of one of the benefits derived from this international cooperative project between the U.S. and the Federal Republic of West Germany.

D. Extended Mission Phase

Officially, there are no project requirements for DSN support to the extended phase of the *Helios* mission. In

fact, it would be very premature for the project to place such requirements on the DSN at the present time. Nonetheless, the contemplated *Helios* trajectories (Figs. 3 and 4) suggest some very interesting scientific rationale for continued tracking support to the *Helios* spacecraft during the extended mission portion of the trajectory. For one, the retrograde loop behind the sun offers the opportunity for three solar occultations rather than just one; and, for another, the spacecraft will experience a second perihelion pass prior to returning to the vicinity of the earth. The trajectory, therefore, offers multiple opportunities to obtain the same type of data as obtained during the primary mission but at later points in time—provided, of course, that the spacecraft is still functioning properly. It is, therefore, plausible to expect that at some future time, requirements could develop for DSN support to the extended mission phase of the *Helios* Project.

Of the three possible *Helios* trajectories under current discussion (0.3 AU, 0.25 AU, and 0.2 AU), the 0.25 AU trajectory has the additional characteristic that it is harmonically synchronous with the earth's orbit. Theoretically, the trajectory could be retraced several times if the spacecraft's orbital parameters were not perturbed by the earth's gravity when it returned after each year's traverse. However, such an ideal case would be difficult to achieve, so in practice it is expected that the *Helios* orbit will become skewed with each return pass near earth so that the retrograde loop in the trajectory would cease to occur behind the sun. Earth's gravity would also influence the next perihelion distance—it could be closer to or farther from the sun depending upon whether the spacecraft passed behind or in front of the earth on its return trajectory.

Considering the above, it is understandable why there are no official requirements for extended mission support at the present time. However, it is just as important to recognize that many scientific possibilities exist for such an extended mission should it materialize sometime in the future.

IV. Concurrent DSN Flight Project Support

During the *Helios* time period, the DSN will also be providing support to other flight projects as depicted in Fig. 5. By plotting the various spacecraft viewperiods with respect to "station local meridian time," it is possible to make Fig. 5 apply to any station in the world—if one ignores the effects of station latitude or local terrain. 1200 hours is "local station noon-time," i.e., the time the sun crosses the station's local meridian. Similarly, 0000 hours is station local midnight. For approximation purposes, one can consider sunrise to occur at 0600 hours and sunset to occur at 1800 hours local meridian time.

Inspecting *Helios-A* in Fig. 5, one notes that it is launched near sunset in mid-CY 1974. This is in agreement with Fig. 3, which shows the spacecraft departing the vicinity of the earth in a direction retrograde to earth's orbit around the sun. However, as time progresses from launch, the spacecraft viewperiods approach closer and closer to the sun with the first hump in the curve denoting the first perihelion pass shown in Fig. 3. Past perihelion, the spacecraft viewperiod returns closer to the sun as it goes through the several occultations noted in Fig. 3. For obvious reasons, this type of presentation has been nicknamed a "worm chart." The fat part of the *Helios* "worm" denotes the primary mission phase while the dotted worm portion represents a possible extended mission support for the *Helios* celestial mechanics experiment. The subsequent large excursions of the *Helios* viewperiod curve denote that portion of the trajectory when the spacecraft returns to the vicinity of the earth and then possibly repeats the cycle.

With the foregoing explanation in mind, it is now possible to compare the *Helios* viewperiods with those of other spacecraft that will be operational and requiring support during the *Helios* time period. The "fat worm" portions of the other spacecraft trajectories denote the time span associated with their respective planetary encounters. It is seen that, if one considers only the primary mission objectives of all of these space flight projects, there is a very minimum viewperiod conflict between them and that, if the DSN stations were operated on a 24-hour/day basis, it should be able to support all of the noted flight projects without conflict—especially when one remembers that the DSN has both 26- and 64-meter subnetworks at its disposal during this time period. However, conflicts can occur if any of these flight projects develop tracking requirements into their extended mission time periods or if their planetary encounter dates shift significantly. Since neither of the latter can be accurately predicted at the present time, the DSN is only making firm commitments for the primary phase of these respective missions. This does not preclude possible extended mission coverage for any of the flight projects, but the exact amount of additional coverage possible will probably not be known until these spacecraft have been launched and their trajectories accurately determined.

V. Conclusion

This article and Ref. 1 complete the general description of the *Helios* Program—its international management, its mission objectives, its spacecraft and launch vehicle configuration, the spacecraft radio system, and the support requirements it places upon the Tracking and Data System. The treatment has been intentionally general in nature in order to provide the reader with a composite overview which he can use as a basis for understanding the more detailed radio subsystem discussions that will appear in future articles.

Reference

1. Goodwin, P. S., "*Helios* Mission Support," in *The Deep Space Network Progress Report,* Technical Report 32-1526, Vol. II, pp. 18–27. Jet Propulsion Laboratory, Pasadena, Calif., Apr. 15, 1971.

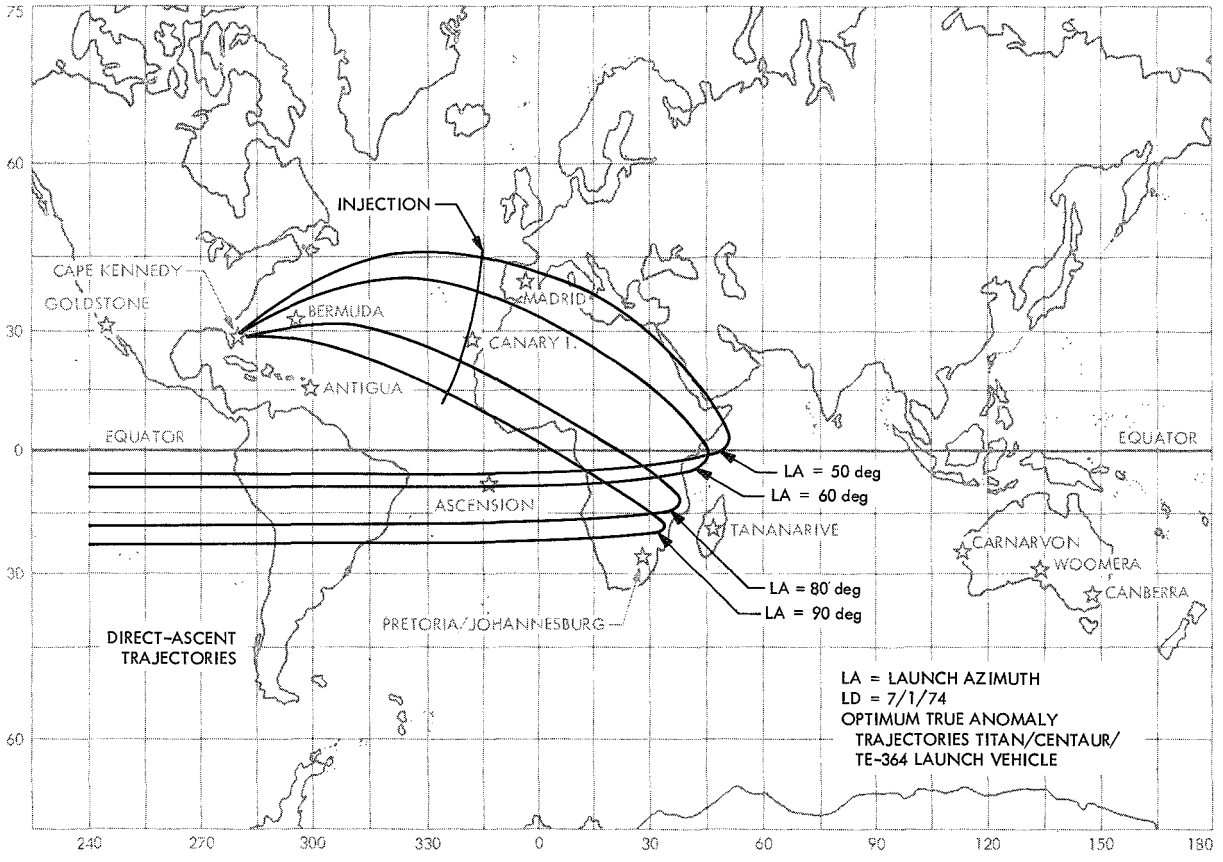

Fig. 1. *Helios* direct-ascent trajectories using a *Titan/Centaur*/TE-364 launch vehicle

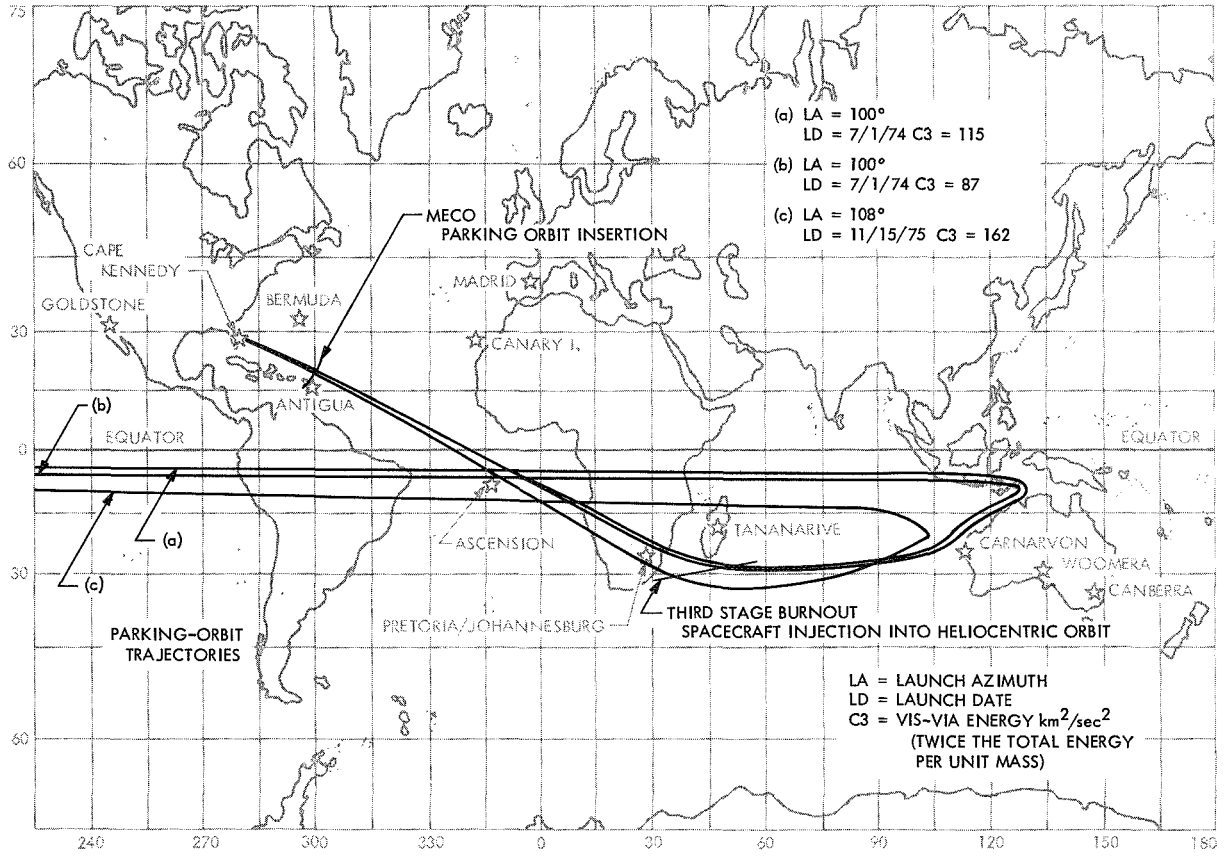

Fig. 2. *Helios* parking-orbit trajectories using an *Atlas/Centaur*/TE-364 launch vehicle

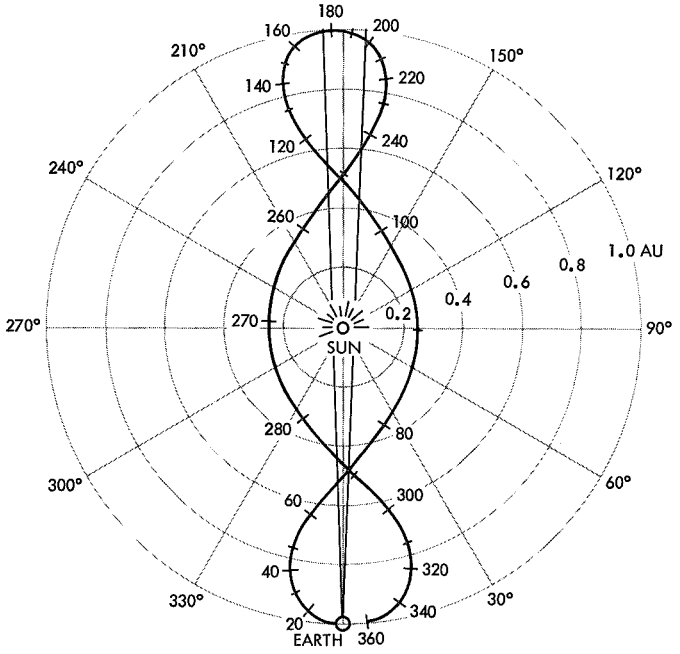

Fig. 3. Typical *Helios* trajectory at 0.25 AU

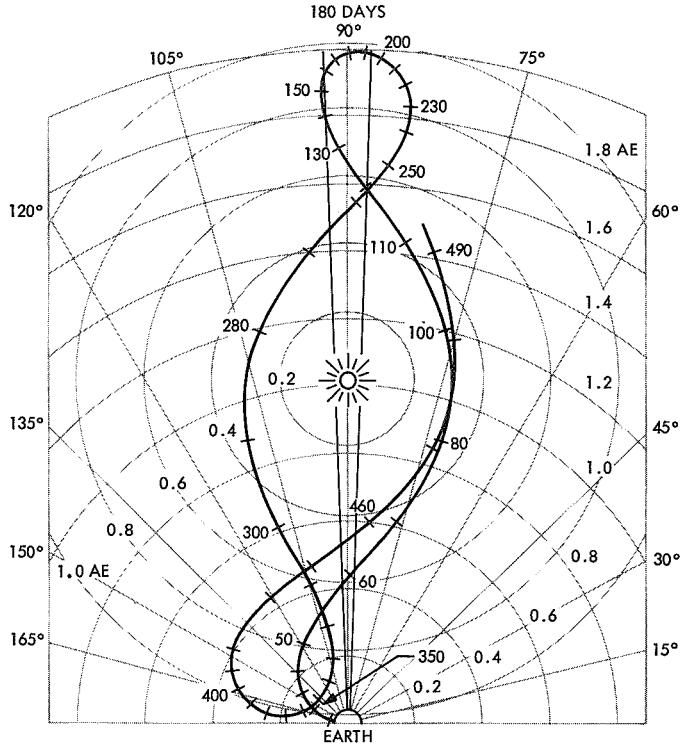

Fig. 4. Typical *Helios* trajectory at 0.3 AU

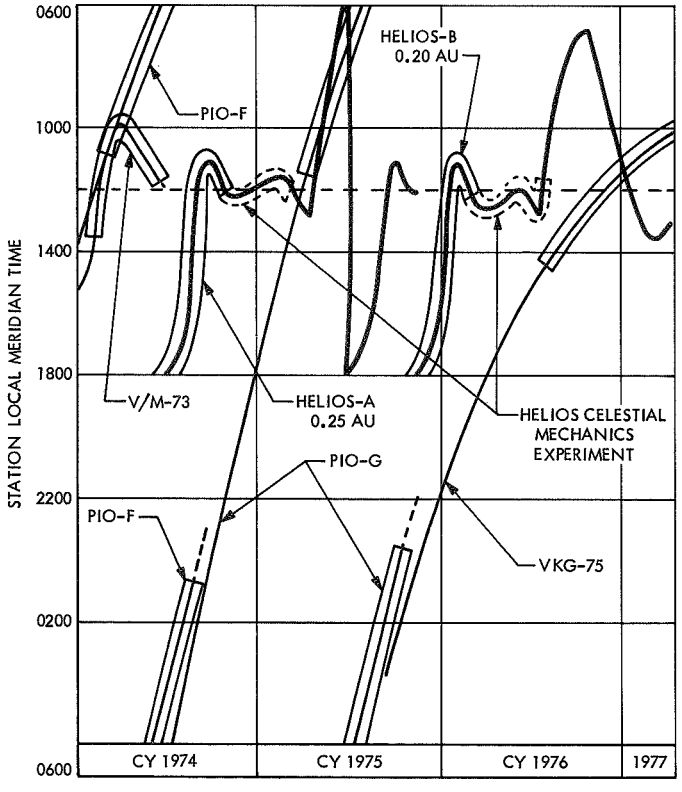

Fig. 5. Spacecraft viewperiods for 1974–1977 era

Mariner Mars 1971 Mission Support

R. P. Laeser
Mission Support Office

Implementation schedule tradeoffs caused the actual DSN configuration for support of Mariner *Mars 1971 launch/midcourse/cruise to be significantly different from the original plans. This article describes the actual configuration by network system.*

In previous articles, the configuration of the six DSN systems for support of the *Mariner* Mars 1971 Mission were described. Confronted with the realities of implementation problems, slipped schedules, and launch dates, a reduced set of the most critical capabilities and a corresponding configuration were defined and are included here. Table 1 and Figs. 1 and 2 apply to the telemetry system; Table 2 and Fig. 3 to the command system; Table 3 and Figs. 4 and 5 to the tracking system; Table 4 and Fig. 6 to the monitor system; and Table 5 and Fig. 7 to the operations control system. The simulation system is not covered, because it plays no role in operations support. For each capability listed in a table, a figure reference is given to the corresponding element on the cross-referenced figure; in some cases the blocks on a figure are numbered and the figure reference 2-(1) is interpreted as Fig. 2, Block (1).

Table 1. Telemetry system

Launch/cruise capabilities	Figure reference
A. DSIF	
1. Multi-mission telemetry hardware (including receiver (RCV), subcarrier demodulation assembly (SDA), symbol synchronizer assembly (SSA), and Telemetry and Command Processor (TCP) with its GCF interface and interface with the receiver for (AGC)	1
a. At DSS 12, 41, and 51	1
b. At DSS 71	1
2. TCP telemetry software operating at DSS 12, 41, and 51:	
a. Acquire engineering or CC&S telemetry from SDA and perform bit sync at 8⅓ or 33⅓ bps	1-TCP
b. Format telemetry and output on high speed data line to SFOF	1-TCP
c. Frame sync engineering telemetry, decommutate and output to SFOF on TTY	1-TCP
d. Acquire ground AGC and SNR, convert to db, and transmit to SFOF via high speed	1-TCP
e. Acquire receiver, subcarrier demodulation, and bit sync lock status and transmit to SFOF via high speed	1-TCP
f. Acquire and send to station Monitor computer; spacecraft AGC and SPE, configuration changes, alarms and SNR in db	1-TCP
g. Record all received data on a digital Original Data Record	1-TCP
h. Playback portions of ODR to SFOF via high speed	1-TCP
i. a through h at DSS 71	1-TCP
j. Operate simultaneously with TCP command capabilities	1-TCP
3. Provide analog recording of receiver and subcarrier demodulation assembly outputs	1
B. GCF	
1. High speed data (4800 bps) system to SFOF from DSS 12, 41, and 51	1-HSD
2. Teletype to SFOF from DSS 12, 41, and 51	1-TTY 1
3. Internal SFOF teletype distribution of 360/75 formatted data	1-TTY 2
4. Closed circuit TV distribution of DTV formatted telemetry	1-CCTV
5. 1 and 2 for DSS 71 and 2 for MSFN stations	1
C. SFOF	
1. Hardware	
a. 360/75 computer and GCF interface	1
b. Digital TV and its 360/75 interface	1-DTV
c. 2260 (manual input, CRT display)	1-2260
d. Digital TV format request box	1-FRB
e. 1443 line printer	1-1443
f. 2501 card readers	1-2501
2. 360/75 telemetry software for engineering and CC&S data:	
a. Receive high speed data blocks, log, extract bit stream and status information, and frame sync data	2-(1)
b. Automatic selection of best data stream	2-(2)
c. Generate system data record (SDR)	2-(6)
d. Decommutate	2-(3)
e. Perform conversion to engineering units	2-(4)
f. Alarm on supplied alarm limits	2-(4)
g. Perform data suppressions and suppression tolerance tests	2-(4)
h. Perform data averaging	2-(4)
i. Format for 1443 display	2-(5)
j. Format for digital TV display—alphanumeric	2-(5)
k. Format for teletype character printer display	2-(6)
l. Recall data from SDR for display—limited to last 24 hours	2
m. Execute format request box inputs	1-FBB
n. Perform COMGEN mask/CC&S data comparison	1-360
3. Digital TV software	1-DTV
4. Operate simultaneous with other Systems in same 360/75	1-360

Table 2. Command system

Launch/cruise capabilities	Figure reference
A. DSIF	
1. Multi-mission command hardware (including all TCP and GCF interface hardware)	
a. At DSSs 12, 41, and 51	3
b. At DSS 71	3
2. TCP command software operating at DSSs 12, 41, and 51	
a. Configure multi-mission command hardware according to message from SFOF via high speed	3-TCP
b. Locally configure multi-mission command hardware	3-TCP
c. Accept message and transmit verification via high speed	3-TCP
d. Accept and act on enable/disable high speed messages	3-TCP
e. Transmit command at appropriate times to spacecraft	3-TCP
f. Bit-by-bit check for abort	3-TCP
g. Transmit to SFOF confirm or abort message via high speed	3-TCP
h. Local display of alarms and confirm/abort messages	3-TCP
i. Transmit alarms to SFOF	3-TCP
j. Command stack recall	3-TCP
k. Generate Original Data Record (ODR)	3-TCP
l. a through k at DSS 71	3-TCP
m. Local entry of command message and enable/disable message	3-TCP
n. Configuration and standards and limits recall to SFOF	3-TCP
o. Compare status with standards and limits and alarm/abort as specified	3-TCP
3. Analog recording of command modulation waveform	3
4. Command capability at Ascension MSFN using RWV	—

Launch/cruise capabilities	Figure reference
B. GCF	
1. High speed data (4800 bps) system between SFOF and DSSs 12, 41, and 51	3
2. Teletype between SFOF and DSSs 12, 41, 51, and ACN	3
3. *Internal SFOF teletype distribution of 360/75* formatted data	1-TTY
4. Voice between SFOF and DSSs 12, 41, 51, and ACN	—
5. 1 through 4 at DSS 71	3
C. SFOF	
1. Hardware	
a. 360/75 computer and GCF interface	3-360
b. Digital TV and its 360/75 interface	3-DTV
c. 2260 (manual input, CRT display)	3-2260
d. 2501 (card readers)	3-2501
2. 360/75 command software	
a. Accept and transmit manually input commands—pseudo-octal	3-360
b. Accept and transmit manually input commands—alphanumeric	3-360
c. Accept and transmit files of commands from COMGEN or card entry	3-360
d. Display verification—TTY	3-360
e. Display verification—DTV	3-360
f. Automatic verification and enable	3-360
g. Accept and transmit enable/disable	3-360
h. Display confirm/abort—TTY	3-360
i. Display confirm/abort—DTV	3-360
j. Display alarms	3-360
k. TCP command stack recall and display	3-360
l. Recall DSS configuration and standards and limits, and display	3-360
m. Accept and transmit DSS configuration and standards and limits	3-360
n. Generate system data record (SDR)	3-360
3. Digital TV software	3-DTV

Table 3. Tracking system

Launch/cruise capabilities	Figure reference
A. DSIF	
1. Acquire doppler, angles, and (lunar distance) range data; format and transmit to SFOF from DSSs 12, 41, and 51 via teletype	4-TDH
2. Acquire doppler, (planetary distance) range, and DRVID data at DSS 14; format for teletype and transmit to SFOF	4-TDH
3. Provide 20 μsec inter-station time synchronization	—
B. GCF	
1. Teletype between SFOF and DSSs 12, 41, 51, 14	4-TTY
2. Teletype between SFOF and MSFN ACN	—
3. Closed circuit TV distribution of tracking DTV formats	4-CCTV
C. SFOF	
1. Hardware	
a. 360/75 computer and GCF teletype interfaces	4-360
b. Digital TV and its 360/75 interface	4-DTV
c. 1443 line printer	4-1443
2. 360/75 tracking software	
a. Acquire tracking data from DSIF via GCF and create SDR	5-(1)
b. Same as for MSFN data	5-(1)
c. Transfer SDR to 1108 via tape	5
d. Acquire spacecraft ephemeris from 1108 via tape	5
e. Generate predictions of DSS observables and format for high speed or TTY transmission to DSS for local printout, and for pseudo-residual use (predicts)	5-(3)
f. Difference predictions with actual data as it is received and displayed (pseudo-residuals)	5-(2)
g. Provide real-time accountability of received data	5-(1)
3. Digital TV software	4-DTV

Table 4. Monitor system

Launch/cruise capabilities	Figure reference
A. DSIF (DSS 12, 41, 51)	
1. Acquire hardware/software status in real-time from other DSIF subsystems	6-DIS
2. Compare status with standards and limits, and alarm if necessary	6-DIS
3. Provide local display of DSS status and alarms	6-DIS
4. Transmit required subset of DSS status to SFOF	6-DIS
5. Encode accounting and status data from the GCF station communications terminal, and transmit to SFOF	6-DIS
6. Accept tracking predicts and generate pseudo-residuals as part of 2	6-DIS
7. 1 through 4 for DSS 71 and 1 through 5 for DSS 14	6-DIS
B. GCF	
1. High-speed data between SFOF and DSS 12, 41, 51	6-HSD_1
2. Transmit high-speed data blocks to 360/75 containing high-speed data accounting and status	6-HSD_2
3. 1 and 2 for DSS 71 and 14	6
4. Automatically display GCF accounting and status on closed-circuit TV	6
5. Provide 360/75 driven character printer for alarms	6-CP
C. SFOF	
1. Hardware	
a. 360/75 computer and GCF interface	6-360
b. Digital TV, its 360/75 interface, and format request boxes	6-DTV
c. 1443 Line printer	6-1443
d. 2260 (manual input, CRT display)	6-2260
2. 360/75 SFOF monitor software	
a. Accept status data from SFOF telemetry, command, and tracking software	6-360
3. 360/75 DSN monitor software	
a. Accept DSIF and GCF monitor data via high speed, and data from SFOF monitor software	6-360
b. Assemble monitor criteria data and use to generate alarms	6-360
c. Display alarms on digital TV and character printer	6-360
d. Provide real-time network status/configuration on digital TV	6-360
4. Digital TV software	6-DTV

Table 5. Operations control system

Launch/cruise capabilities	Figure reference
A. DSIF	
1. Display on line printer sequences of events, schedules, and predictions received from SFOF via high speed (DSSs 12, 41, 51)	7-DIS
2. Display on TTY character printer schedules and predictions received from SFOF via teletype (DSSs 12, 41, 51)	7
3. 1 and 2 for DSSs 71 and 14	7
B. GCF	
1. High-speed data between SFOF and DSS 12, 41, 51	7
2. Same for DSSs 71, 14	7
3. Teletype between SFOF and DSS 12, 41, 51	7
4. Same for DSSs 71, 14	7
C. SFOF	
1. Hardware	
a. 360/75 computer and GCF interface	7-360
2. 360/75 Operations Control software	
a. Sequence of events generation program, real-time (launch/cruise version with limited capabilities)	7-360
b. Control output routing of sequence of events, schedules, and predictions to DSS via high-speed data	7-360
c. Control output routing of schedules and predictions via teletype	7-360
3. Rapid recovery from failures	7-360

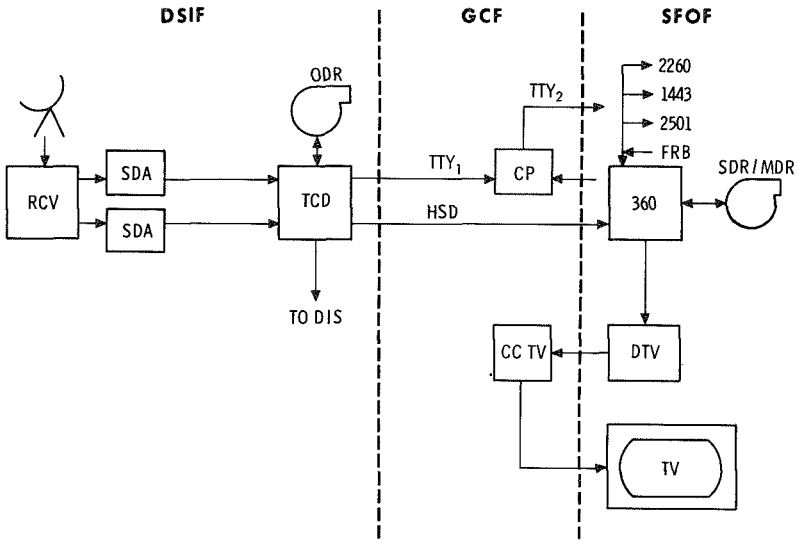

Fig. 1. Telemetry system

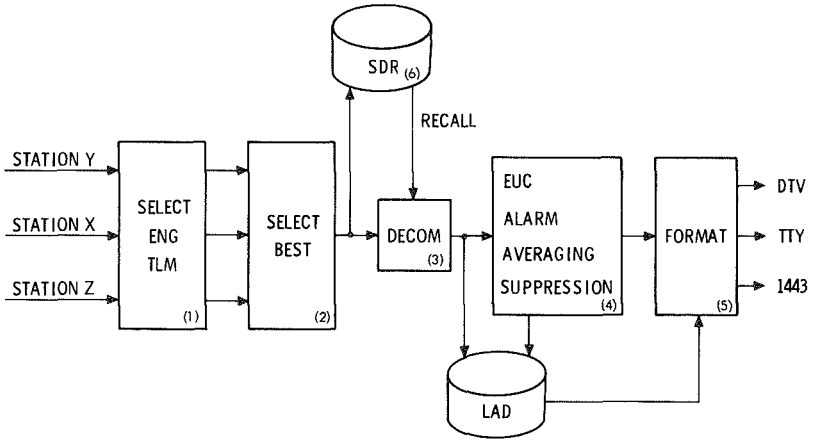

Fig. 2. Telemetry inside the 360 computer

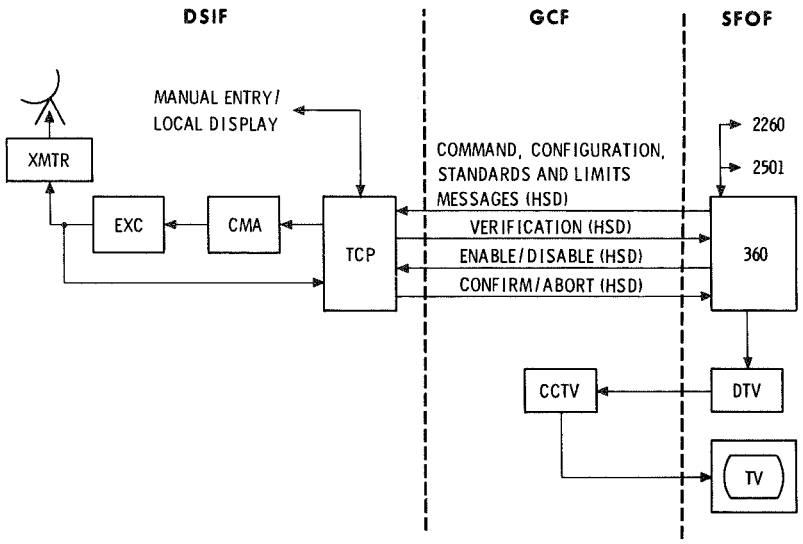

Fig. 3. Command system

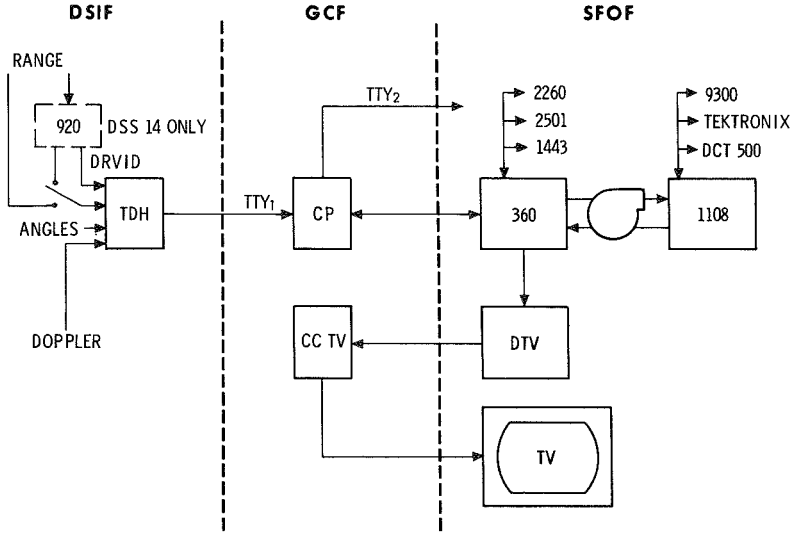

Fig. 4. Tracking system

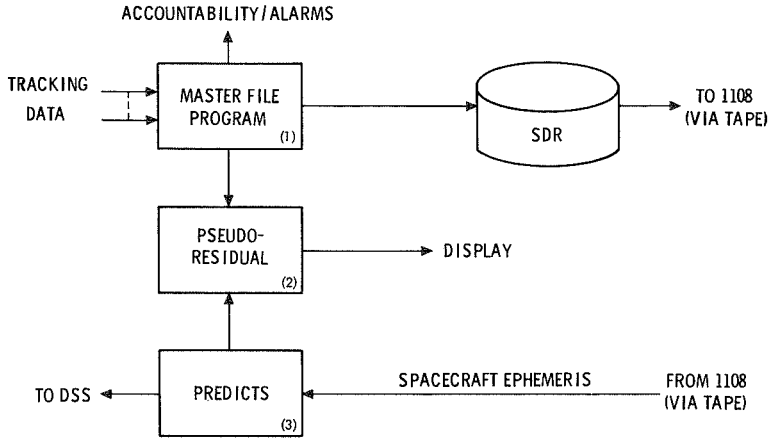

Fig. 5. Tracking inside the 360 computer

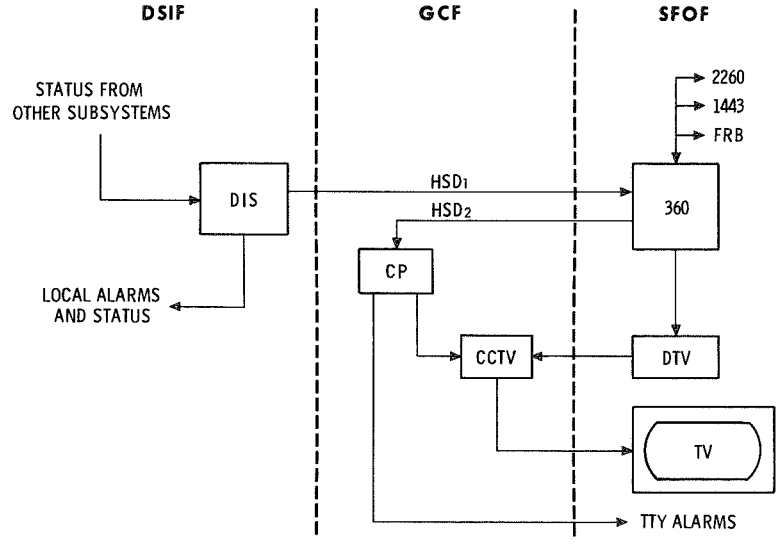

Fig. 6. Monitor system

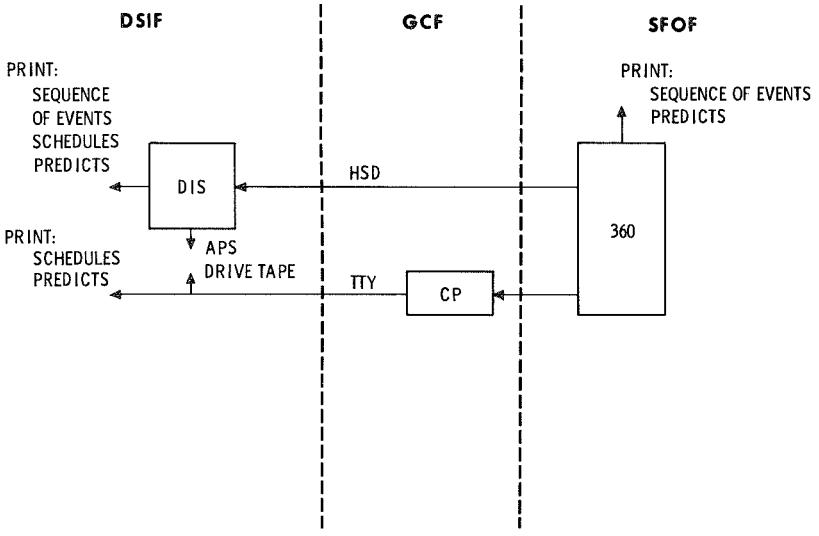

Fig. 7. Operations control system

Viking Mission Support

D. J. Mudgway
Mission Support Office

This article discusses the capabilities of the Deep Space Network (DSN) as a factor in the design of the Viking telecommunications system. The problem of accommodating simultaneous downlinks from two orbiters and one lander with dual uplinks to one orbiter and one lander or two orbiters is discussed.

Because the Viking encounter and subsequent orbital and landed operations take place near maximum earth–Mars separation (approximately 400 × 10^6 km), the signal-to-noise ratios on both up and downlinks are minimal to support the extensive command and data retrieval requirements.

The tradeoffs between DSN capabilities and project requirements such as these are described in the context of the mission design.

I. Introduction

Continuing the series of articles on DSN support for the *Viking* Mission, this article discusses the capabilities of the DSN as a factor in the design of the *Viking* telecommunications system.

An earth-to-spacecraft telecommunications link must provide telemetry, command, and metric data for navigation and scientific purposes. It must be almost totally reliable and must have sufficient performance margin to permit the achievement of basic mission objectives in the event of anomalous conditions in spacecraft or ground data systems.

A multiple space vehicle mission of this kind poses significant problems for the DSIF in accommodating simultaneous downlinks from two orbiters and one lander with dual uplinks to one orbiter and one lander or two orbiters.

Unlike most of the orbital flyby missions we have supported in the past, the *Viking* encounter and subsequent orbital and landed operations take place near maximum earth-Mars separation (approximately 400 × 10^6 km).

As a consequence, signal-to-noise ratios on both up and downlinks are minimal to support the very extensive command and data retrieval requirements of the project.

The tradeoffs between DSN capabilities and Project requirements such as these are described in the context of the mission design as it stands at this time.

II. Telemetry

Each *Viking* orbiter has three telemetry channels as shown in Table 1. Each *Viking* lander has two telemetry data channels as shown in Table 2. Each *Viking* orbiter may transmit the following combinations of channels: B only, A and B, B and C. Each lander will transmit A and B simultaneously during most of the mission. The DSN must be capable of receiving telemetry data simultaneously from two orbiters and one lander at one DSS and providing that data (along with metric data streams from two of the vehicles) in real time for processing and display at the SFOF. Table 3 illustrates the combinations of telemetry data which must be handled.

The baseline functional configuration with which the DSIF expects to support these combinations of data streams is given in Fig. 1. This diagram covers representative 26- and 64-m deep space stations in the multiple-mission telemetry and command configuration.

All data streams pass through the subcarrier demodulator assemblies (SDA). The uncoded low-rate data goes directly to the telemetry and command processors (TCP) for formatting and transmission to the SFOF. The medium-rate block-coded data is symbol synchronized in the symbol synchronizer assembly (SSA) and decoded in the data decoding assemblies (DDA) before passing to the TCP for formatting and transmission to the SFOF via high-speed data lines (HSDL). The high-rate block-coded data is similarly processed except that the DDA outputs this data directly to a wideband buffer for driving the 50 kbps wideband data system (WBS).

The functional arrangement of the entire DSN telemetry system for *Viking* is given in Ref. 1, Fig. 6, p. 13.

The DSN telecommunications parameters with which the *Viking* Project must work in designing its telecommunications links are given in Ref. 2. Preliminary performance studies that result from an orbiter design including a 20-W TWT are shown in Figs. 2 and 3. Preliminary performance estimates for the lander are shown in Figs. 4 and 5. Many options exist to improve the margins shown in these figures and these are continually under evaluation as the design of the mission proceeds.

Both the orbiter and lander telecommunications links are significantly degraded by the noise and spectral spreading effects around the period of solar conjunction as is shown in Figs. 2, 3, and 4. Unfortunately, very little data exists on which to base theoretical estimates of the magnitude of these effects, and the DSN is attempting to collect as much data as possible on missions prior to *Viking* to permit a better analytical understanding of the problem.

III. Command

The DSN multiple-mission command system will be used to support *Viking*, using a single bit rate of 4 bps. Because of the multiple spacecraft nature of this mission, the Project requires a capability in the 64-m subnet for two simultaneous uplinks on different frequencies.

This allows the project to simultaneously command one orbiter and one lander, or two orbiters. Lander and orbiter telecommunication link designs are such that simultaneous carriers of 10 kW each are needed at DSSs 43 and 63 and carrier levels of 40 kW each at DSS 14. The DSN plans to meet these requirements with 100-kW transmitters at DSSs 43 and 63 and a 400-kW transmitter at DSS 14. At all three stations dual exciters and command modulation assemblies (CMA) permit dual carrier operation with separate carrier frequencies, separate subcarrier frequencies, and separate command modulation.

The standard DSN command system facilities for command verification, confirmation, enable/disable and abort are available on each individual command data stream. The functional configuration of the DSN command system for *Viking* is given in Ref. 1, Fig. 6, p. 14.

The command links to the orbiter and lander are affected by the solar degradation mentioned above in the same way as downlinks, and a much better understanding of the degradation process is needed to be able to adequately predict the effect on the mission.

IV. Tracking

The spacecraft tracking function performed by the DSN yields, among other things, the radiometric data (range, doppler, time) required by the project to carry out its navigation function. The telecommunication link performance constitutes a major constraint on amount and quality of the data that can be provided.

A. Doppler

To satisfy the requirements of a multiple-spacecraft mission it is planned to provide two doppler extractors at each 64-m antenna and one doppler extractor at each 26-m antenna. Together with the dual uplinks at the 64-m stations, this will provide two simultaneous coherent two-way doppler streams at these stations. The 26-m stations will support one two-way doppler stream. Adequate carrier margin appears to be available to support the two-way doppler requirements, although more attention is required on expected doppler tracking rates as the mission details become more clearly identified.

B. Planetary Ranging

There are two requirements for planetary ranging, one for lander science purposes and the other for improving the quality of the doppler data by means of the differenced range versus integrated doppler (DRVID) technique. In both cases, the maximum communications range presents difficulty in meeting the required acquisition time because of marginal signal-to-noise ratios. This is particularly acute in the case of the lander, where the daily lander *on* time is limited by thermal and power considerations to approximately 2 hr, and SNR conditions preclude simultaneous ranging and telemetry transmissions. The project's requirement for lander ranging acquisition time is 4 min, and this requirement is under evaluation to find an acceptable solution under the link conditions described above.

C. X-Band

In addition to its S-band transponder, the *Viking* orbiter will carry a small (100 mW) X-band transponder to be used for radio science dispersive measurements of electron content in the Mars and interplanetary environment. The X-band downlink carrier will be coherent with the S-band uplink carrier and will be modulated with the planetary ranging code only.

The performance margins in the X-band downlink are being developed at this time but do not appear to present a problem. Of much more concern is the multiplication of phase instability effects from the S-band uplink into the X-band downlink.

The DSN plans to support the X-band experiment with X-band ranging receivers at each 64-m station in addition to the standard S-band ranging receivers. These receivers will also provide the DSN with an alternative to DRVID techniques for calibration of charged particle effects in the doppler data. The configuration of the entire DSN tracking system for *Viking* is described in Ref. 1.

References

1. Mudgway, D. J., "Viking Mission Support," in *The Deep Space Network,* Space Programs Summary 37-62, Vol. II, pp. 12–22. Jet Propulsion Laboratory, Pasadena, Calif., Mar. 31, 1970.
2. Jet Propulsion Laboratory Document 810-5, Rev. A, DSN Standard Practice, Deep Space Network/Flight Project Interface Design Handbook, Pasadena, Calif., Dec. 15, 1970.

Table 1. Orbiter telemetry channels

Telemetry Channel	Description	Bit rate	Subcarrier frequency, kHz
A	Uncoded science data	1, 2, or 4 kbps	240
B	Engineering data	8⅓ or 33⅓ bps	24
C	Coded (32, 6) science data	1, 2, 4, 8, or 16 kbps	240

Table 2. Lander telemetry channels

Telemetry Channel	Description	Bit rate	Subcarrier frequency, kHz
A	Uncoded engineering data	8⅓ bps	23.3
B	Coded (32, 6) science data	250 or 500 bps	144.0

Table 3. Orbiter and lander telemetry combinations

Combination No.	Lander data	Orbiter A	Orbiter B
1	A and B	B	B
2	A and B	B	A and B
3	A and B	B	B and C
4	A and B	A and B	A and B
5	A and B	A and B	B and C
6	A and B	B and C	B and C

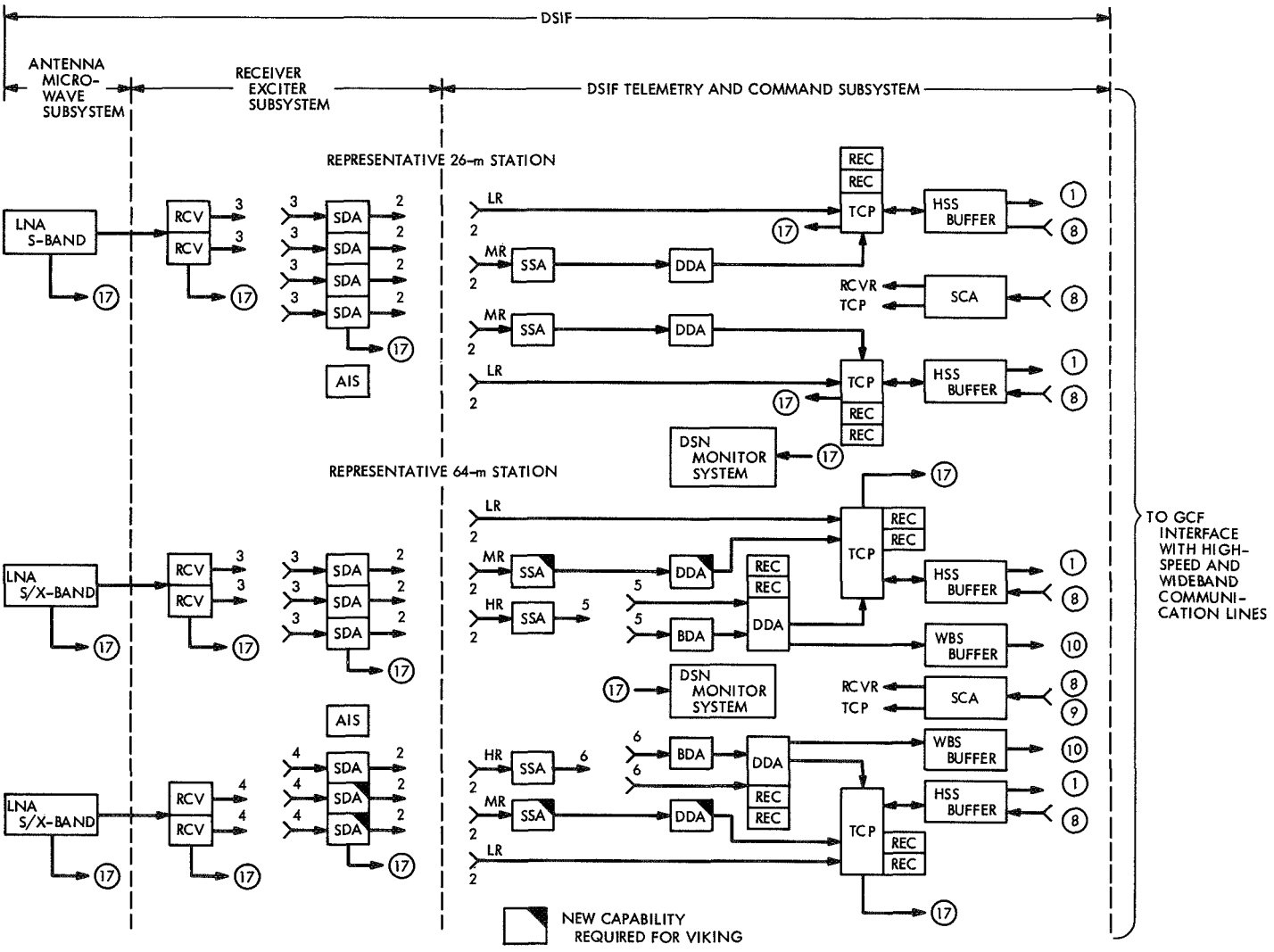

Fig. 1. DSIF telemetry configuration for *Viking*

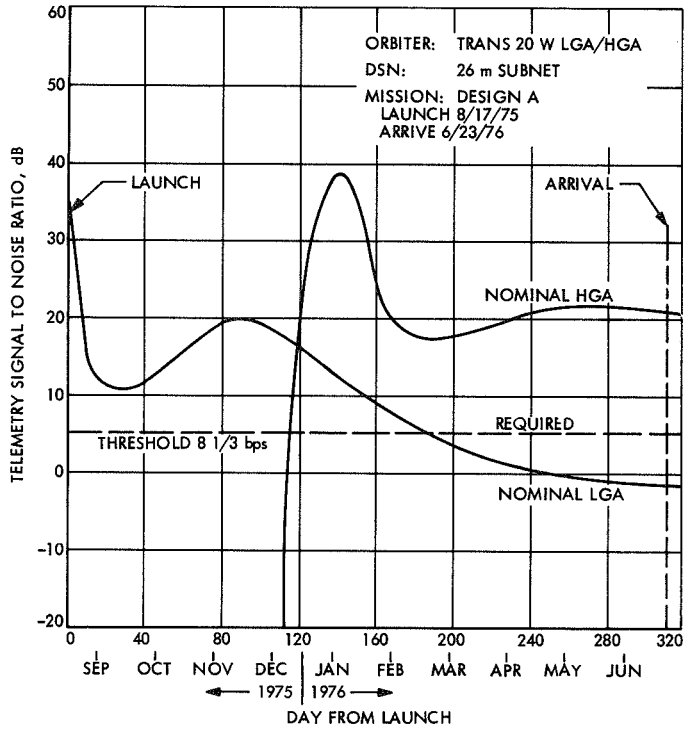

Fig. 2. Orbiter low-rate telemetry. Nominal performance during cruise operations

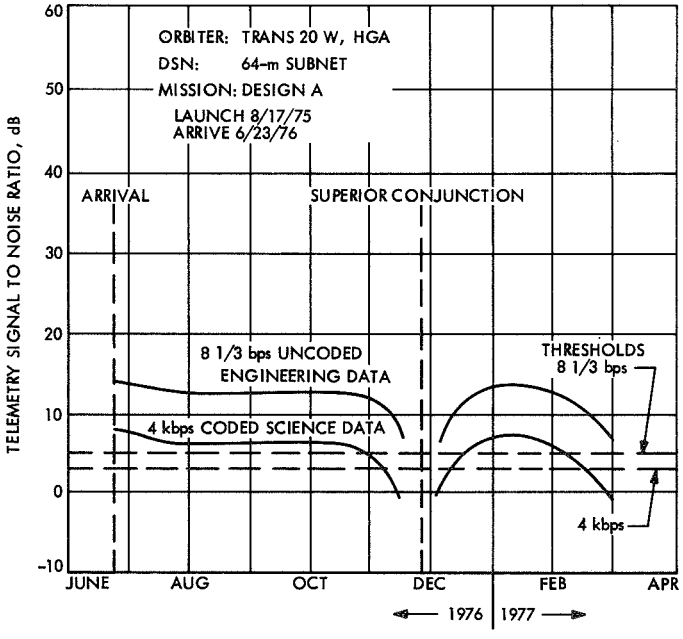

Fig. 3. Orbiter low-rate and high-rate telemetry. Nominal performance with sun effects during orbital operations

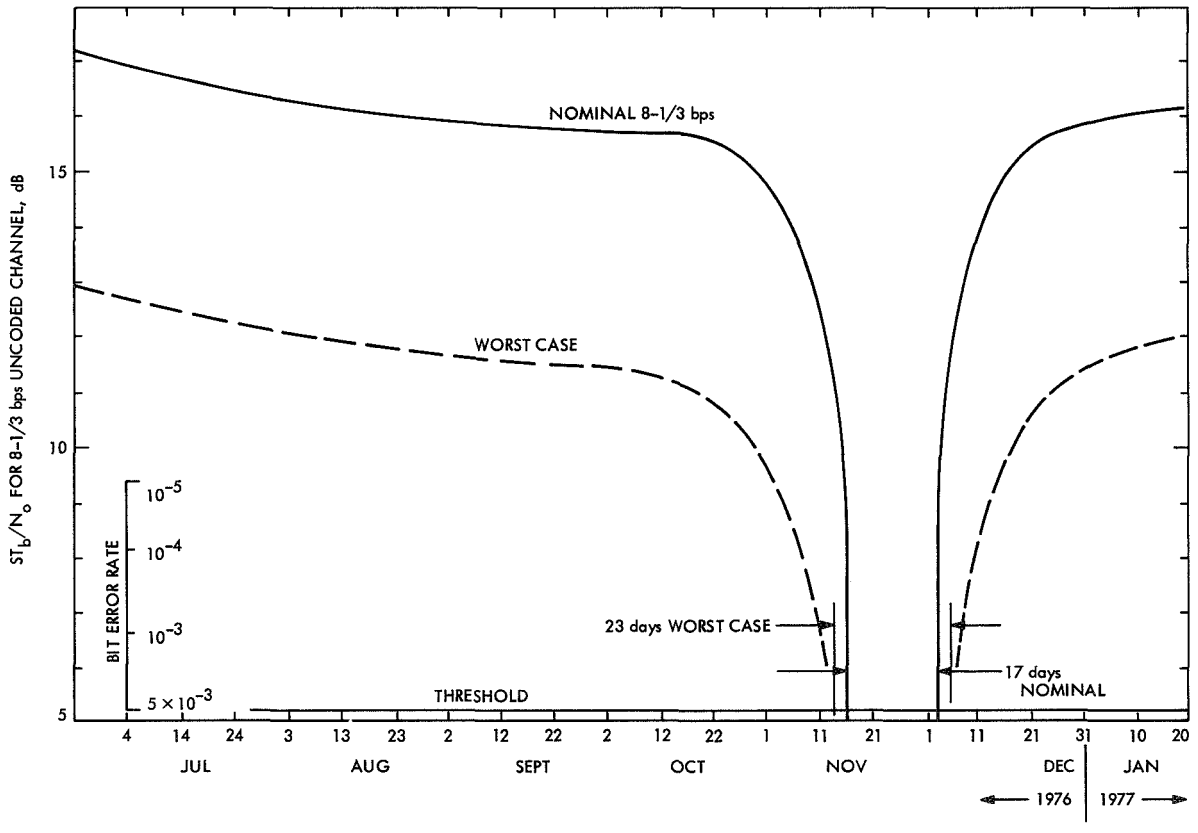

Fig. 4. Lander engineering data channel performance with sun effects

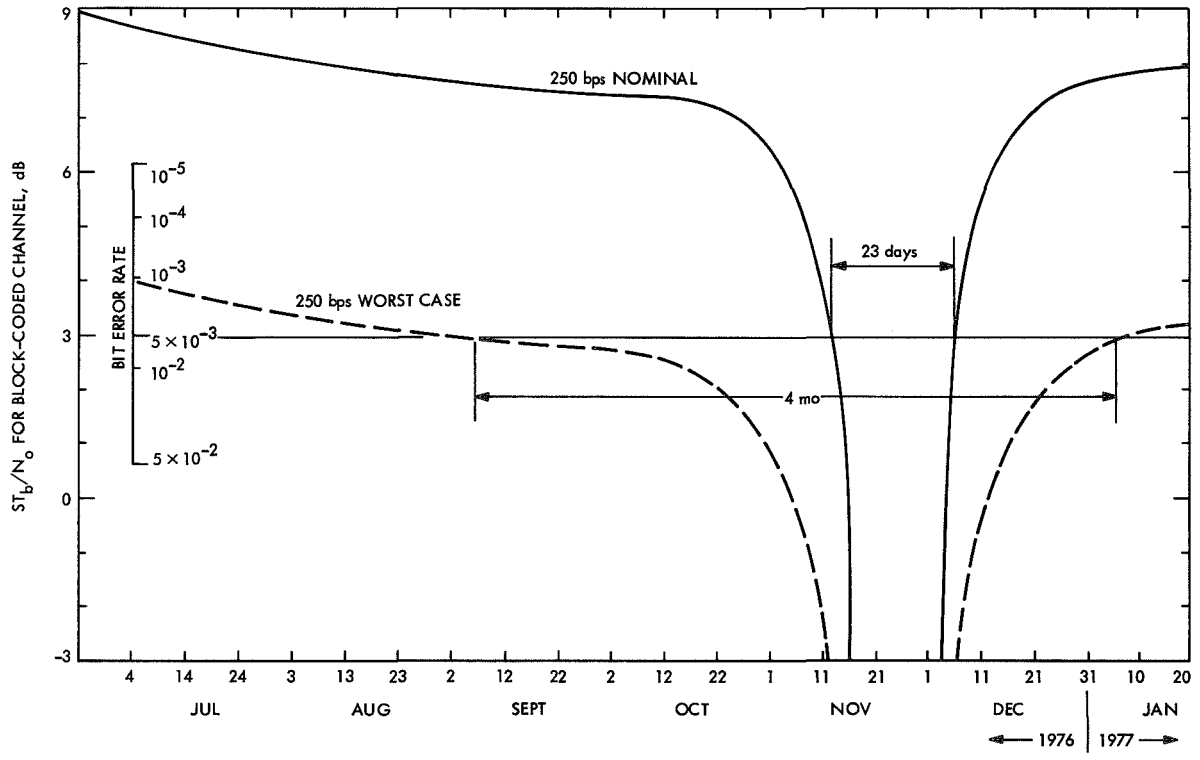

Fig. 5. Lander science data channel performance with sun effects

Radio Science Support

K. W. Linnes
Mission Support Office
T. Sato
Communications Elements Research Section
D. Spitzmesser
DSIF Operations Section

Since 1967, radio scientists have used the DSN 26- and 64-m antenna stations to investigate pulsars, the effects of the solar corona on radio signals, to observe radio emissions of X-ray sources, and have used very long baseline interferometry techniques for high-resolution studies of quasars. The various experiments are identified and summarized, and the published results are indicated.

I. Introduction

The 26- and 64-m antenna stations of the DSN have been used for several years to support radio science experiments (Ref. 1). NASA, JPL, and university scientists have used key DSN facilities whose particular and unique capabilities were required for the performance of the experiments. In order to formalize the method of selecting experiments and experimenters, a Radio Astronomy Experiment Selection (RAES) Panel was formed in 1969 (Ref. 2). Notice of the availability of these facilities was placed in professional journals to inform the scientific community that they were available for limited use by qualified radio scientists. No charge is made for use of the standard DSN facilities and equipment; special equipment, however, must be provided by the experimenters (Ref. 3). A number of experiments have since been proposed, evaluated, selected and performed (Refs. 4, 5 and 6). A summary of the experiments conducted, both before and since formation of the panel, is shown in Table 1.

II. Radio Science Operations

Activities through October 31, 1970, have been reported in Refs. 1 through 6. The scientific results of these experiments that have been published in the open literature are shown in Refs. 7 through 20.

The character of the experiments being conducted indicates the unique DSN capabilities being employed. The very long baseline interferometry (VLBI) experiments depend upon the widely separated stations to achieve high angular resolution. The X-band VLBI and the earth physics VLBI at S-band depend in addition on the extreme stability provided by hydrogen maser frequency standards. The X-band pulsar measurements are made possible by the very low system noise temperature and high

sensitivity of the 64-m antenna station. Both the stability and sensitivity are necessary to conduct the general relativity experiment by VLBI techniques.

As indicated in Refs. 15, and 17 through 20, the extremely high angular resolution of the VLBI technique (milliseconds of arc) along with high sensitivity, gives the DSN a unique capability which has been used to resolve the fine structure of quasars. This data has provided fresh material for discussions of the character and origin of these sources (Ref. 20).

III. RAES Panel Activities

A summary of recently approved experiments is shown in Table 2.

References

1. Hall, J. R., "Radio Science Support," in *The Deep Space Network*, Space Programs Summary 37-56, Vol. II, p. 148. Jet Propulsion Laboratory, Pasadena, Calif., March 31, 1969.

2. Sato, T., et al., "Radio Science Support," in *The Deep Space Network*, Space Programs Summary 37-61, Vol. II, p. 153. Jet Propulsion Laboratory, Pasadena, Calif., Jan. 31, 1970.

3. *Bulletin of the American Astronomical Society*, Vol. 2, No. 1, p. 177, 1970.

4. Sato, T., et al., "Radio Science Support," in *The Deep Space Network*, Space Programs Summary 37-63, Vol. II, p. 98. Jet Propulsion Laboratory, Pasadena, Calif., May 31, 1970.

5. Sato, T., et al., "Radio Science Support," in *The Deep Space Network*, Space Programs Summary 37-65, Vol. II, p. 132. Jet Propulsion Laboratory, Pasadena, Calif., Sept. 30, 1970.

6. Sato, T., et al., "Radio Science Support," in *The Deep Space Network*, Space Programs Summary 37-66, Vol. II, p. 151. Jet Propulsion Laboratory, Pasadena, Calif., Nov. 30, 1970.

7. Moffet, A. T., and Ekers, R. D., "Detection of the Pulsed Radio Source CP 1919 at 13 cm Wave Length," *Nature*, Vol. 218, No. 5138, pp. 227–229, April 20, 1968.

8. Moffet, A. T., and Ekers, R. D., "Further Observations of Pulsating Radio Sources at 13 cm," *Nature*, Vol. 220, No. 5169, pp. 756–761, Nov. 23, 1968.

References (contd)

9. Ekers, R. D., and Moffet, A. T., "Polarization of Pulsating Radio Sources," *Astrophys. J.*, Vol. 158, No. 1, Part 2, pp. L1–L8, Oct. 1969.

10. Maxwell, A., and Taylor, J. H., "Lunar Occultation of the Radio Source Sagittarius A," *Astrophys. Lett.*, Vol. 2, pp. 191–194, Dec. 2, 1968.

11. Gubbay, J., et al., "Trans-Pacific Interferometer Measurements at 2300 MHz," *Nature*, Vol. 222, No. 5195, p. 730, May 24, 1969.

12. Gubbay, J., et al., "Variations of Small Quasar Components at 2300 MHz," *Nature*, Vol. 224, No. 5224, pp. 1094–1095, Dec. 13, 1969.

13. Klein, M. J., and Gulkis, S., "Measurements of Jupiter in the Spectral Range 20–24 GHz," *Bulletin of the American Astronomical Society*, Vol. 3, p. 276, 1971.

14. Gary, B., and Gulkis, S., "New Circular Polarization Measurements of Jupiter's Decimeter Radiation," *Astrophys. J.*, Vol. 158, No. 3, pp. 193–195, December 1969.

15. Cohen, M. H., et al., "Compact Radio Source in the Nucleus of M87," *Astrophys. J.*, Vol. 158, No. 2, Part 2, pp. L83–L85, November 1969.

16. Muhleman, D. O., et al., "Radio Interferometric Test of General Relativistic Light Bending Near the Sun," *Phys. Rev. Lett.*, Vol 24, No. 24, p. 1377, June 15, 1970.

17. Gubbay, J., et al., "The Structure of P1934-63," *Astrophys. J.* (in publication).

18. Lampton, M., et al., "Simultaneous Radio and Optical Measurements of Scorpius XR-1," *Astrophys. J.*, Vol. 164, p. L-61, March 1, 1971.

19. Shapiro, I., et al., "Quasars: Millisec of Arc Structure Revealed by Very Long Baseline Interferometry," *Science*, Vol. 172, p. 52, April 2, 1971.

20. Sullivan, W., "Scientists Puzzled by a Space 'Impossibility': Objects Moving at 10 Times Speed of Light," *New York Times*, April 15, 1971.

Table 1. Radio science experiments involving 64- and 26-meter antenna facilities

Experiment	Purpose	Experimenter	DSN facility	Date	Published findings
Pulsar measurements (2295 MHz)	To study pulse characteristics	A. Moffet (Caltech) R. D. Ekers (Caltech)	DSS 14	May 1967 April 1967 May 1967 March 1969	Ref. 7 Ref. 8 Ref. 9
Lunar occultation of radio sources (2295 MHz)	To determine intensity and angular size of radio sources	A. Maxwell (Harvard) J. H. Taylor (Harvard)	DSS 14 DSS 11	July 1967 Oct. 1967 Jan. 1968 April 1968	Ref. 10
Very long baseline interferometer (narrow data bandwidth, S-band)	To determine angular size of radio sources using trans-Pacific baseline	J. Gubbay (Univ. of Adelaide) A. Legg (Space Research Group, WRE) D. Robertson (Space Research Group, WRE) A. Moffet (Caltech) B. Seidel (JPL)	DSS 14 DSS 11 DSS 12 DSS 41 DSS 42	Sept. 1967 Nov. 1967 May 1968 June 1969	Ref. 11 Ref. 12
Study characteristics of radio source signals after passage through solar corona (2295 MHz)	To determine angular size of radio sources	R. Ekers (Caltech)	DSS 11	Oct. 1967	
Planetary radiometric observations	Continuing survey	S. Gulkis (JPL) D. Jones (JPL) B. Gary (JPL)	9-meter antenna at DSS 13	Continuing from 1967	Ref. 13
Jupiter occultation of radio sources (2295 MHz)	To investigate structure of Jupiter magnetosphere	B. Gary (JPL) D. Nicolson (South African Scientific Institute for Research)	DSS 51	Sept. 1968	
X-band pulsar	To study X-band emission of pulsar	A. Moffet (Caltech)	DSS 14	July 1970	
General relativity VLBI (X-band)	To test the theory of general relativity using VLBI techniques to observe 3C273 and 3C279 near solar occultation of the latter	B. Burke (MIT) T. Clark (GSFC) R. Goldstein (JPL) A. Rogers (Haystack Radio Observatory) I. Shapiro (MIT)	DSS 14 (and MIT Haystack antenna)	Oct. 1970 Feb. 1971	Ref. 19 Ref. 20
Pulsar polarization measurements	To study polarization characteristics of five pulsating radio sources at 2295 MHz	A. Moffet (Caltech) R. D. Ekers (Caltech)	DSS 14	Oct. 1970 April 1971	
Indian Ocean VLBI (narrow data bandwidth, 2295 MHz)	To observe southern hemisphere radio sources	D. Robertson (Space Research Group, WRE) G. Nicholson (SA-CSIR)	DSS 41 DSS 51	Nov. 1970	Ref. 17
Very long baseline interferometry (2295 MHz, NRAO recording terminals)	High resolution studies of extra galactic radio sources	J. Broderick (NRAO) B. Clark (NRAO) M. Cohen (Caltech) D. Jauncey (Cornell) K. Kellermann (NRAO)	DSS 13 (and NRAO 140-ft antenna)	Nov. 1970	
Earth physics VLBI (S-band)	To demonstrate feasibility of DSN-VLBI for geophysical applications	P. MacDoran (JPL)	DSS 12 DSS 14	Jan. 1971	
X-band VLBI	To study structure of extra galactic sources with improved resolution	K. Kellermann (NRAO) M. Cohen (Caltech) B. Clark (NRAO) D. Jauncey (Cornell)	DSS 14 (and MIT Haystack antenna)	Feb. 1971	

Table 1 (contd)

Experiment	Purpose	Experimenter	DSN facility	Date	Published findings
Jupiter radiation belt study	To measure intensity of beamed radiation and its variation with Jupiter rotation	S. Gulkis (JPL)	DSS 14	March 1971	
Solar scintillation (2295 MHz)	To determine solar wind characteristics	R. Ekers (Caltech) L. Little (Caltech)	DSS 14 DSS 11 DSS 12 DSS 13	April 1969	
Jupiter polarization experiment (2295 MHz)	Circular polarization measurements of Jupiter at 13 cm	B. Gary (JPL) S. Gulkis (JPL)	DSS 14	April 1969 May 1969	Ref. 14
Very long baseline interferometer (NRAO wideband terminal, S-band)	To determine angular size of radio sources using trans-Pacific baseline and wideband system	M. Cohen (Caltech) A. Moffet (Caltech) D. Shaffer (Caltech) B. Clark (NRAO) K. Kellermann (NRAO) D. Jauncey (Cornell) S. Gulkis (JPL)	DSS 14 DSS 42	June 1969	Ref. 15
General relativity interferometer experiment	To measure apparent change in angular separation of two radio sources when one is occulted by sun	D. Muhlemann (Caltech) R. Ekers (Caltech) E. Fomalont (Caltech)	DSS 14 DSS 13	Oct. 1969	Ref. 16
Very long baseline interferometer (medium data bandwidth, S-band)	To determine angular size of radio sources	J. Gubbay (Univ. of Adelaide) A. Legg (Space Research Group, WRE) D. Robertson (Space Research Group, WRE) A. Moffet (Caltech) B. Seidel (JPL)	DSS 14 DSS 11 DSS 42	Dec. 1969 June 1970 Jan. 1971	Ref. 17
SCO-XR-1 Observations	To observe variability of 13 cm radio emissions and their correlation with observed optical variability	M. Lampton (UC-Berkeley) S. Boyer (UC-Berkeley) J. Welch (UC-Berkeley) G. Grasdalen (UC-Berkeley)	DSS 14	June 1970	Ref. 18

Table 2. Recently approved experiments

Experimenter	Objective	Comments
H. S. Zisk (MIT, Lincoln Laboratory) C. A. Knight M. A. Slade (MIT, Department of Earth and Planetary Sciences)	Precision VLBI Observations of *Apollo* ALSEP Transmitter	Approved 19 November 1970; support plans in process
J. Broderick (NRAO) B. Clark (NRAO) M. Cohen (Caltech) D. Jauncey (Cornell) K. Kellermann (NRAO) L. Matveenko (Institute for Cosmic Research, USSR) I. Moiseyev (Crimean Astrophysical Observatory, USSR) V. Vitkevitch (Institute for Cosmic Research, USSR)	High Resolution Studies of Extra Galactic Sources at 3 cm by VLBI	Scheduled for May and June 1971

Tracking System Analytic Calibration Support for the *Mariner* Mars 1971 Mission

G. A. Madrid
Tracking and Orbit Determination Section

The means by which calibrations for Deep Space Network (DSN) tracking data will be provided to the Mariner Mars 1971 project is described. The scope and accuracy of calibrations for distinct error source components is stated and a description of the software to compute and provide calibrations for transmission media and platform observable errors is furnished. Utilization of these calibrations will permit the DSN to satisfy the project's navigational accuracy requirements of 250 km at encounter minus 30 days.

I. Objectives

The tracking system analytic calibration (TSAC) activity has been initiated within the DSN to provide to the *Mariner* Mars 1971 Project, in a timely fashion, calibrations for platform observables and the transmission media effects. A breakdown of the error sources considered under these two classifications is shown in Table 1. Also shown in this table are the accuracy to which these error sources are expected to be calibrated during the *Mariner* Mars 1971 mission.

TSAC will utilize computer programs which will process the calibration inputs and provide calibration parameters. One program, called PLATO, will provide a table of functional values to permit corrections for variations in the earth's rotation rate (UT1) and the motion of the pole. The other program, MEDIA, will define range corrections for charged particles and tropospheric refraction as polynomial functions of time. The charged-particle corrections will be computed utilizing the newly developed Differenced Range Versus Integrated Doppler (DRVID) technique.[1]

[1]During the *Mariner* Mars 1969 Extended Mission, MacDoran and Martin (Ref. 1) demonstrated the practicability of obtaining DRVID as a measure of charged-particle effects on a doppler signal. During the *Mariner* Mars 1971 mission, the DSN will use DRVID to provide to the *Mariner* Mars 1971 Project a calibration for two-way doppler from DSS 14.

II. Plan

The performance of the TSAC function will depend on a reliable data collection process, certified software to process the data, and dependable operating plans and procedures.

A. Data Collection

The data required to be collected for the TSAC function consists of locations of the tracking stations, polar motion data, universal time (UT1) information, DRVID data from DSS 14, and data for tropospheric corrections.

DSS location information will be obtained through an analysis of selected data from prior missions (e.g., Mottinger, Ref. 2) and will be provided to the mission on punched cards prior to launch.

Polar motion information will be received for the Bureau International de l'Heure (BIH) and the International Polar Motion Service (IPMS) on a weekly basis during cruise and on a daily basis during encounter.

Time (UT1) information will be obtained from the U. S. Naval Observatory (USNO) and the BIH on a similar basis as polar motion data.

DRVID data will be taken at DSS 14 whenever the Tau ranging equipment is operated. The DSN will take DRVID data at least three times a week during cruise and four times a week just prior to encounter. These passes will be divided between the two *Mariner* Mars 1971 spacecraft. The DRVID data will be treated as an observable and transmitted to the SFOF on the tracking data stream.

Data for tropospheric corrections are based on past history of the temperature, pressure, and humidity profiles obtained from radiosonde balloon sites located near the tracking stations to be used for *Mariner* Mars 1971. These data will be prepared prior to launch and input to the TSAC software for computation of the calibration polynomials.

B. Data Processing

1. Software design. The computer software which will support the TSAC activity during the *Mariner* Mars 1971 mission will operate as an assembly under the SFOF Tracking Software Subsystem. This assembly (or program) will consist of two subassemblies (or subprograms).

The MEDIA Subassembly takes its name from its title, the Transmission Media Subassembly. Figure 1 illustrates how the two subassemblies will interact with the other SFOF tracking system software in the IBM 360/75 and the orbit determination software in the Univac 1108. DRVID data will come in from DSS 14 over the teletype or high-speed data lines and will be processed by a tracking data input processor assembly which will in turn place the deciphered data into a mass storage record, termed the system data record (SDR). Once in the SDR it becomes available to MEDIA, which operates in real time whenever tracking data are being processed. Troposphere inputs to MEDIA may be entered also during this time. A functional flow diagram of the MEDIA processing is given in Fig. 2.

PLATO, the other subassembly, will concern itself with producing calibration tables for UT1 and polar motion. Since these parameters may be considered as platform observables, the subassembly is named PLATO after Platform Observable Subassembly. This subassembly operates in a non-real-time (batch) mode in the IBM 360/75 processing card inputs containing raw timing (UT1) and polar motion data. Figure 3 outlines the processing function performed within PLATO. Output destined for orbit determination use is in punched cards.

2. Software accuracy. Both MEDIA and PLATO use least-squares fitting techniques to achieve their objectives. MEDIA fits a polynomial to the data as shown in Fig. 4. The error actually incurred in the doppler cannot be determined directly since the range correction is converted to a doppler correction in the orbit determination process. An approximate evaluation of the error can be obtained, in the case shown here, by merely comparing the derivatives of the original polynomial used for simulation and that of the polynomial fitted to the noisy data. The results of this comparison are shown in Fig. 5. The calibration of charged-particle effects will produce a polynomial for every pass of a spacecraft over DSS 14 where ranging is taken. The polynomial will define the range change error

$$\Delta\rho_\varepsilon(t) = \frac{C}{4}\,(\text{DRVID})$$

where C is the speed of electromagnetic propagation in a vacuum.

The data being fitted in the case shown in Fig. 4 are simulated data from a quadratic function with 1-nanosecond (ns) noise added. As we can see, the fitted polynomial approximates the original signal to within 1 ns.

Much of the difference is due, not to the noise, but to the fact that the least-significant unit in the received DRVID data is a nanosecond and therefore the values from the original polynomial appear truncated. As can be seen from Fig. 5, however, neither the noise nor the truncation affects the fit sufficiently to alter its derivative. The maximum error that would affect the doppler signal would be on the order of 0.5×10^{-4} Hz. Typical charged-particle effects on doppler due to the earth's ionosphere are of the order 2×10^{-2} Hz (private communication with B. D. Mulhall). Similar tests with noise levels of up to 20 ns have indicated that the fit can recover the original signal to within 3 ns.

Another segment of the error which cannot be eliminated completely is due to system drift. On the equipment used for the *Mariner* Mars 1969 Extended Mission, the range of this drift was established by Martin (Ref. 3) to be less than 10 ns for periods approximately equivalent to those of a tracking pass. Experience on the current equipment has been insufficient to establish the drift characteristics, but, assuming them to be similar to those of its precursor, errors can therefore be presumed to induce an uncertainty of about 10 ns.

Troposphere zenith range effects are computed by MEDIA using past time histories of surface pressure, temperature, and relative humidity at radiosonde balloon sites near the DSS site to be activated for the mission. Recent studies by Ondrasik and Thuleen (Ref. 4) have indicated that the total zenith tropospheric range effect on a radio beam seldom varies more than 5% from the yearly average. By using monthly averages of troposphere parameters from previous years, an estimate of the zenith range correction can be computed accurately to within 5%. The subassembly uses an expression by Berman (Ref. 5) to compute the total effect of the troposphere at the zenith. Mapping tables are provided in the orbit programs to calculate the effect at decreasing elevation angles. The error due to this mapping has not been clearly established but estimates place it somewhere in the order of 1 to 2%.

The PLATO subassembly was developed to replace the Timing Polynomial (TPOLY) program (Ref. 6) devised to support other JPL missions. PLATO utilizes the least-squares process to fit raw time and polar motion data and then to extrapolate to those periods for which time and polar motion corrections are required. Figure 6 illustrates how error enters the extrapolation process. In Fig. 6a an extrapolation is carried out by extending the tangent to the fitted curve out to a period of interest. Predictions for time are obtained by the linear extrapolation of UT1 and for the pole by a circular fit to the motion of the pole. In Fig. 6b it is evident that, as new data are admitted, the fitted polynomial begins to diverge from the predicted points. If the newly received data begins at time x and ends at time y, the difference between the actual and predicted values of A.1−UT1 at $t = y$ forms the main processing error to be committed. Chao (Ref. 7) found the total error including processing noise on the data by using these predictions in the orbit determination process to be on the order of 5 milliseconds (ms) on the average when weekly prediction intervals are taken. Polar motion is handled in much the same way. Chao and Fliegel (Ref. 8) have determined that the error on the raw polar motion data is on the order of 0.7 m in the x and y directions,[2] while the processing effects are on the order of 0.2 m. Thus, the combined effect for polar motion is expected to lie between 0.7 and 0.8 m.

C. Operations

Operation of the TSAC function involves personnel from the tracking station (DSS 14), the Tracking and Orbit Determination Section (391), and the DSN Operations and Engineering Section (401). Figure 7 diagrams the functions to be performed in the operations and identifies the personnel and groups responsible for them.

Current scheduling plans call for MEDIA to be operated within one hour after the receipt of each pass of data. Each pass can be processed in approximately 5 min. However a visual analysis of the results must be performed prior to certification. If there is any dissatisfaction with the results, the subassembly will be reinitiated until certification is possible. This process may take as much as an additional hour of time. Calibration data will be provided whenever DRVID is being taken during the mission and during the extended mission (orbital phase). Troposphere and station location data are prepared prior to launch and, although changes can be made in-flight, it is assumed that the data provided initially will satisfy the accuracy requirements.

The operation of PLATO does not represent a problem as it need only be run on the batch mode of the IBM 360/75 on a weekly basis during cruise and on a daily basis near encounter. Running time for PLATO is less than 2 min.

[2]The standard reference system for recording polar motion is an x and y orthogonal system centered at the pole at a specified epoch, viz, the 1903 BIH pole.

III. Expected Results

The *Mariner* Mars 1971 Project has placed a requirement of 250 km (3σ) in the $\hat{B}$ direction[3] on the navigation accuracy required at encounter minus 30 days. A low-order approximation of the effect the calibrated errors will have on navigation accuracy can be made by means of simple transformations. An estimate based on the values found in Table 1 indicates an expected 3-sigma value of 180 km in the $\hat{B}$ direction.

The effect of an overseas station, which is not calibrated for charged particles is about 540 km (3σ). However, because of the weight given to these data during the orbit determination process, the effect of two such stations will be diminished so that the overall effect approaches that of the station with the lowest uncertainty. Thus, the DSS 14 statistics will dominate the overall network effects.

[3]The unit vector $\hat{B}$ is a vector pointing from the spacecraft to the center of the target planet and perpendicular to the incoming asymptote.

Now, in addition to the tracking station errors, there are other errors which can also have a distinct influence on navigation. These are errors in the mass of Mars, the astronomical unit, spacecraft ephemeris, dynamical state of the spacecraft (gas leakages, uncoupled forces, radiation pressure, etc.), and the ephemeris of other astronomical bodies. Reynolds, Mottinger, and Ondrasik (Ref. 9) have indicated that the overall effect of these errors is approximately 75 km (3σ). Combining this with the 180 km (3σ) for the station errors, we obtain as a root-sum-square the total error estimate of approximately 195 km (3σ) which is well within the 250 km (3σ) constraint. Without the charged-particle calibration at DSS 14, the total estimated error in the B direction is 310 km (3σ).

We conclude that, if the DRVID calibration as well as the other pertinent media and platform calibrations are collected in a timely fashion and properly applied, the navigation error budget for *Mariner* Mars 1971 will be met, thus increasing the probability of attaining the orbital insertion goals set by the project.

References

1. MacDoran, P. F., and Martin, W. L., "DRVID Charged-Particle Measurement With a Binary-Coded Sequential Acquisition Ranging System," in *The Deep Space Network*, Space Programs Summary 37-62, Vol. II, pp. 34–41. Jet Propulsion Laboratory, Pasadena, Calif., Mar. 31, 1970.
2. Mottinger, N. A., "Status of DSS Location Solutions for Deep Space Probe Missions: Third-Generation Orbit Determination Program Solutions for *Mariner* Mars 1969 Mission," in *The Deep Space Network*, Space Programs Summary 37-60, Vol. II, pp. 77–89. Jet Propulsion Laboratory, Pasadena, Calif., Nov. 30, 1969.
3. Martin, W. L., "Information Systems: Performance of the Binary-Coded Sequential Acquisition Ranging System of DSS 14," in *The Deep Space Network*, Space Programs Summary 37-62, Vol. II, pp. 55–60. Jet Propulsion Laboratory, Pasadena, Calif., Mar. 31, 1970.
4. Ondrasik, V. J., and Thuleen, K. L., "Variations in the Zenith Tropospheric Range Effect Computed From Radiosonde Balloon Data," in *The Deep Space Network*, Space Programs Summary 37-65, Vol. II, pp. 25–35. Jet Propulsion Laboratory, Pasadena, Calif., Sept. 30, 1970.
5. Berman, A. L., "A New Tropospheric Range Refraction Model," in *The Deep Space Network*, Space Programs Summary 37-65, Vol. II, pp. 140–153. Jet Propulsion Laboratory, Pasadena, Calif., Sept. 30, 1970.

References (contd)

6. Muller, P. M., and Chao, C. C., "New Timing Polynomial Program and Data," in *The Deep Space Network*, Space Programs Summary 37-57, Vol. II, pp. 42–51. Jet Propulsion Laboratory, Pasadena, Calif., May 31, 1969.

7. Chao, C. C., "Perturbation in JPL-Adopted Timing Data Due to Newly Input Raw Data," in *The Deep Space Network*, Space Programs Summary 37-59, Vol. II, pp. 110–114. Jet Propulsion Laboratory, Pasadena, Calif., Sept. 30, 1969.

8. Chao, C. C., and Fliegel, H. F., "Polar Motion: Doppler Determinations Using Satellites Compared to Optical Results," in *The Deep Space Network*, Space Programs Summary 37-66, Vol. II, pp. 23–26. Jet Propulsion Laboratory, Pasadena, Calif., Nov. 30, 1970.

9. Reynolds, G. W., Mottinger, N. A., and Ondrasik, V. J., "An Example of the Space Plasma Effect on the *Mariner* Mars 1971 Encounter Accuracy," in *The Deep Space Network*, Space Programs Summary 37-62, Vol. II, pp. 24–28. Jet Propulsion Laboratory, Pasadena, Calif., Mar. 31, 1970.

Table 1. TSAC error sources and current calibration capability

Classification	Error source	Accuracy
Platform observables	DSS locations	
	Goldstone	$\sigma_{r_s} \leq 0.6$ m, $\sigma_\lambda \leq 2.0$ m
	Overseas	$\sigma_{r_s} \leq 1.1$ m, $\sigma_\lambda \leq 3.0$ m
	Timing (A.1—UTI)	4 ms $\leq \sigma_{UT1} \leq$ 5 ms
	Polar motion	0.7 m $\leq \sigma_x \leq$ 0.8 m, 0.7 m $\leq \sigma_y \leq$ 0.8 m
Transmission media	Charged particles[a]	$\sigma_{\Delta\rho}$/pass $\leq$ 0.75 m
	Troposphere (10° elevation cutoff)	$\sigma_{\Delta\rho}$/pass $\leq$ 0.5 m

[a]This calibration will only be applied to data from DSS 14 as this is the only site with DRVID

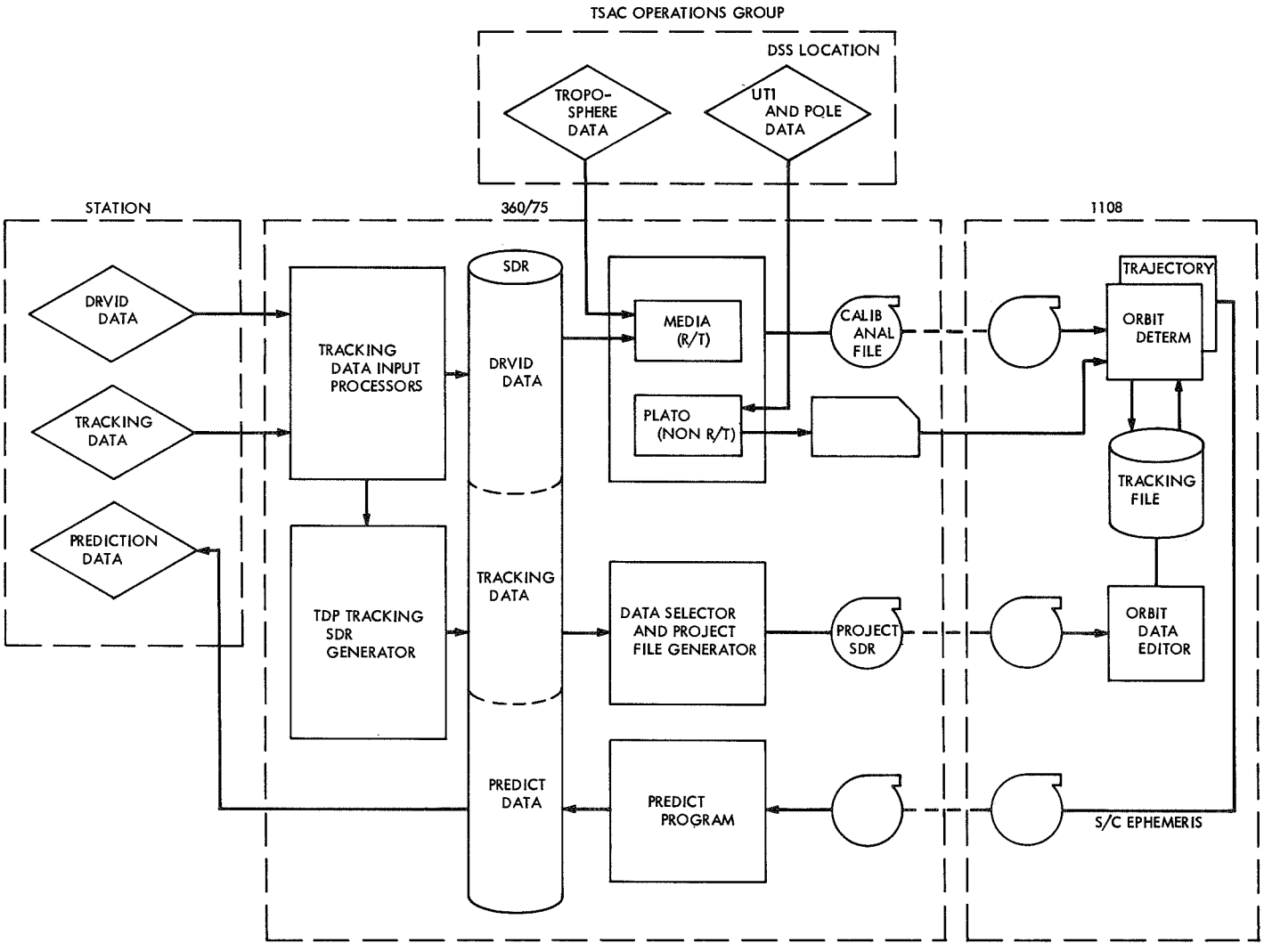

Fig. 1. Tracking system analytic calibration 360/1108 interface

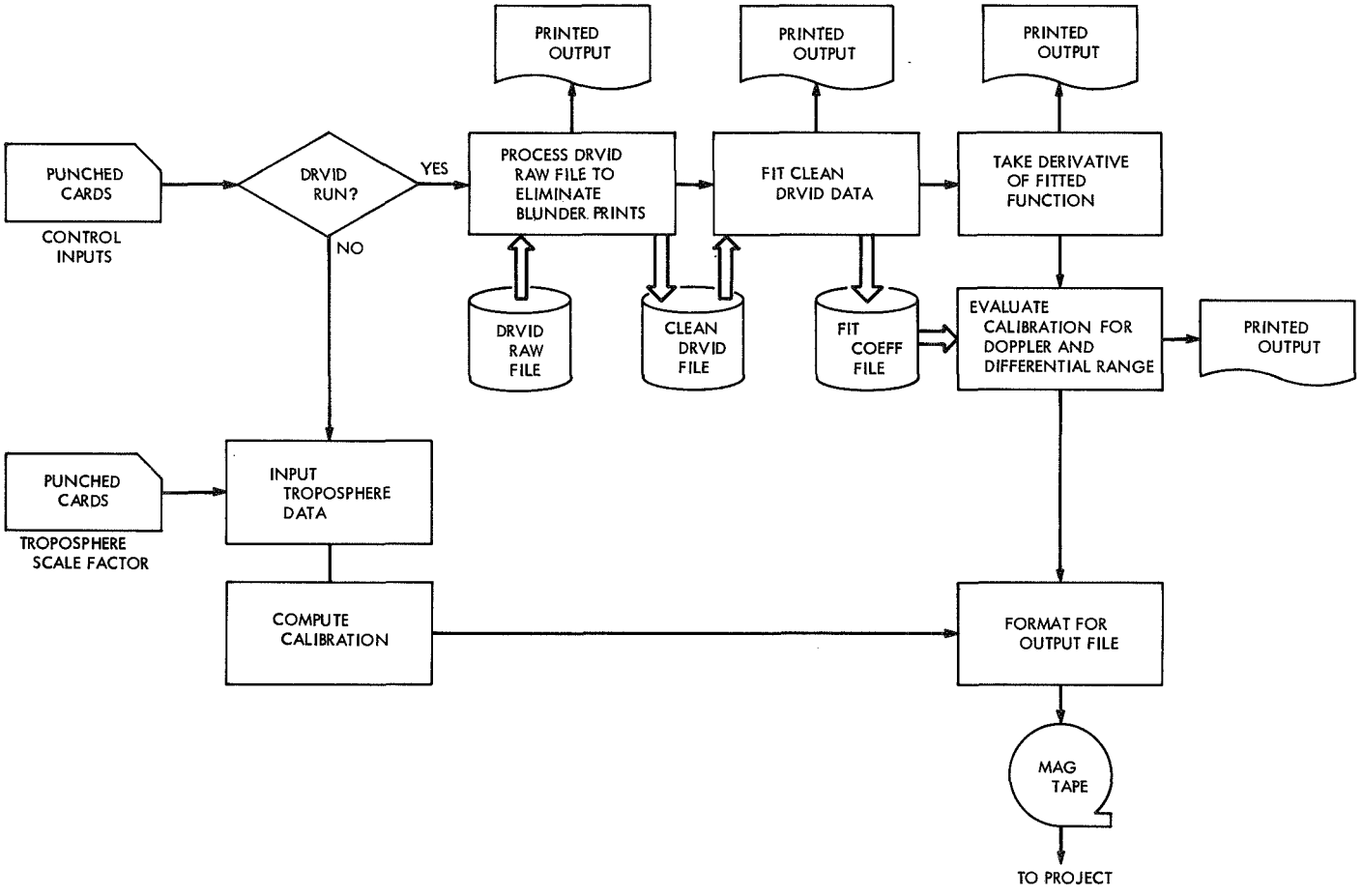

Fig. 2. MEDIA functional and data flow diagram

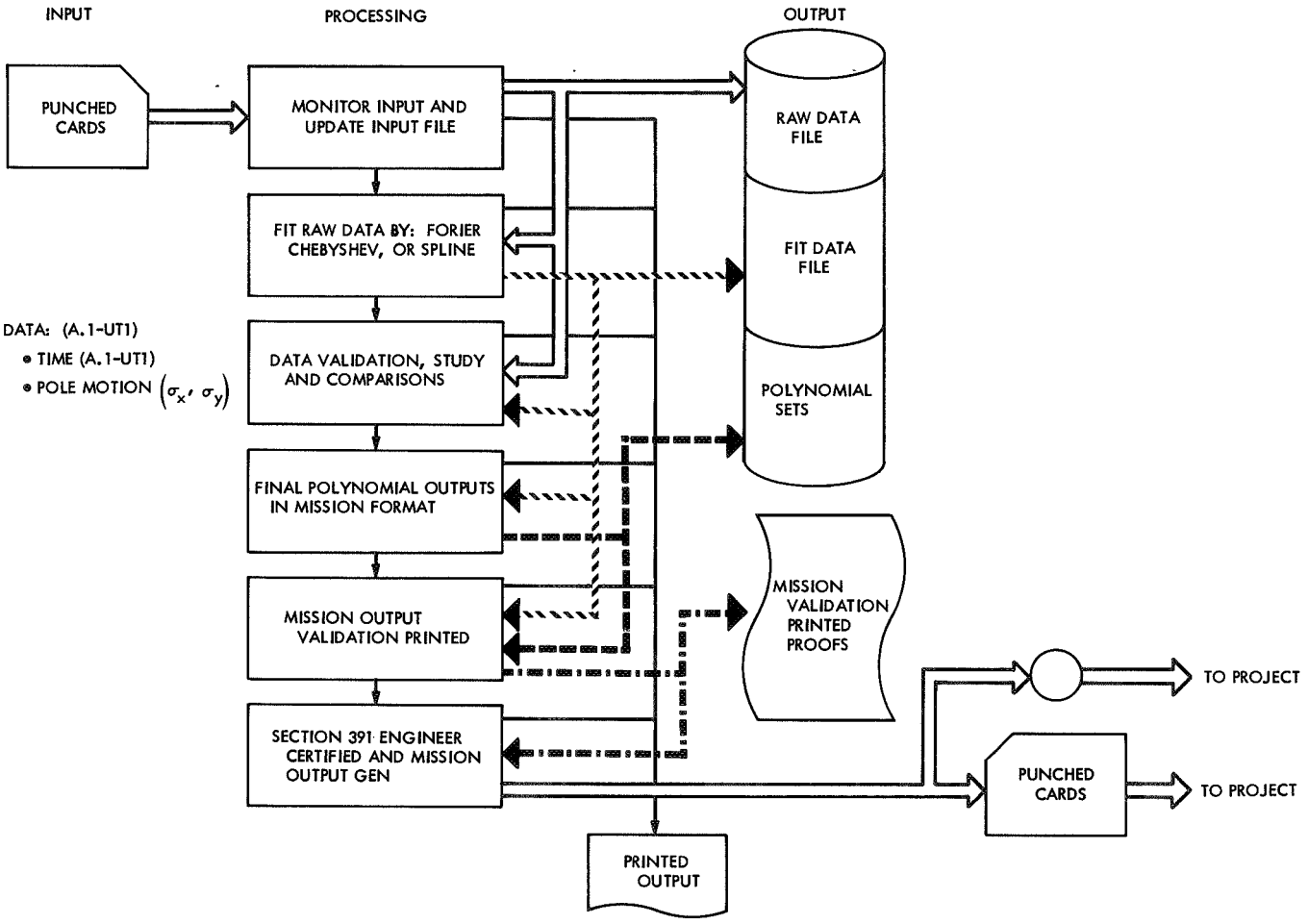

Fig. 3. PLATO functional and data flow diagram

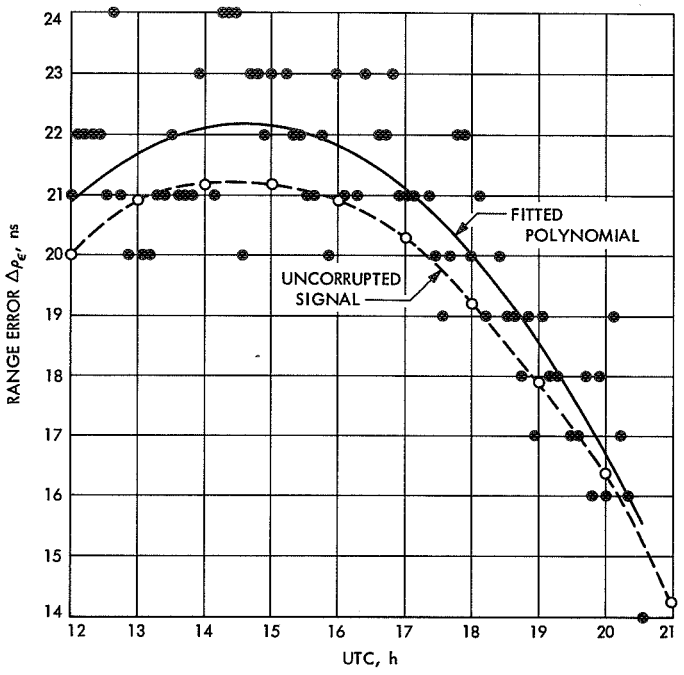

Fig. 4. MEDIA least-squares fit to simulated DRVID data

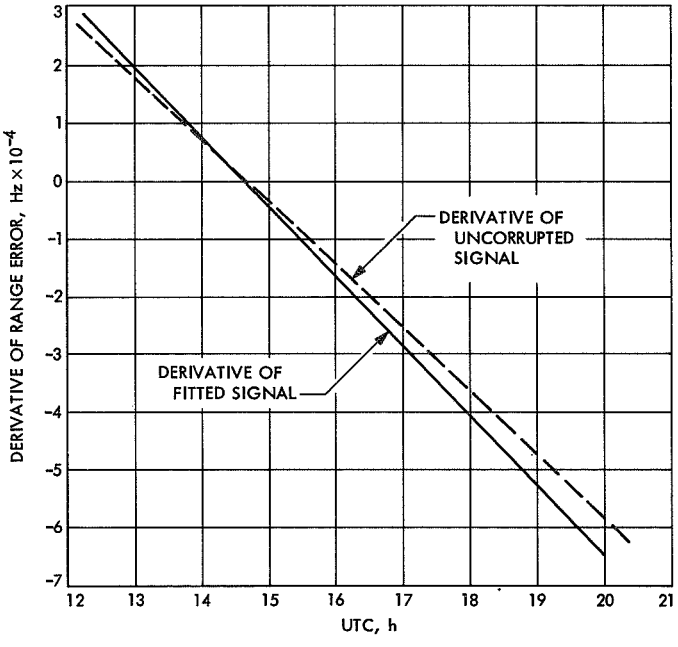

Fig. 5. Derivative of range error

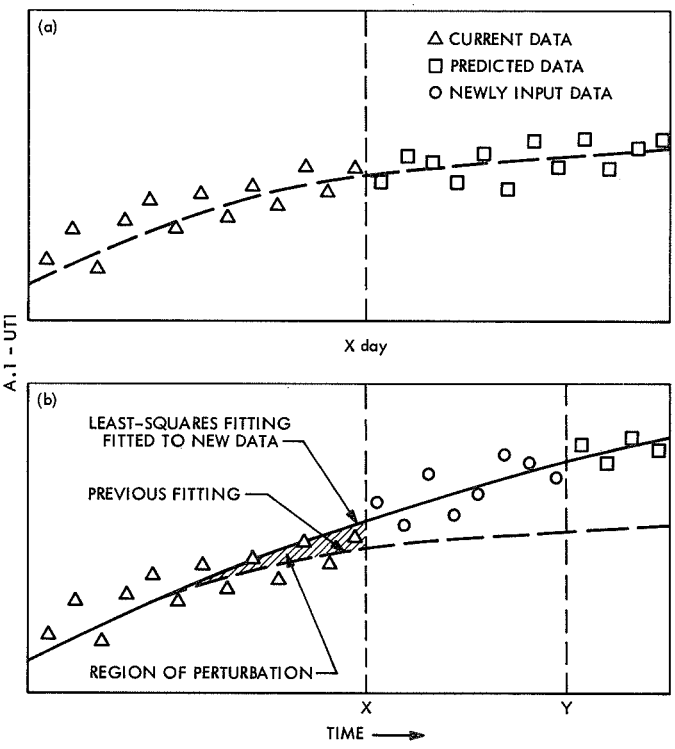

Fig. 6. Least-squares fit to raw timing data: (a) PLATO run made on *X* day, (b) PLATO run made on *Y* day

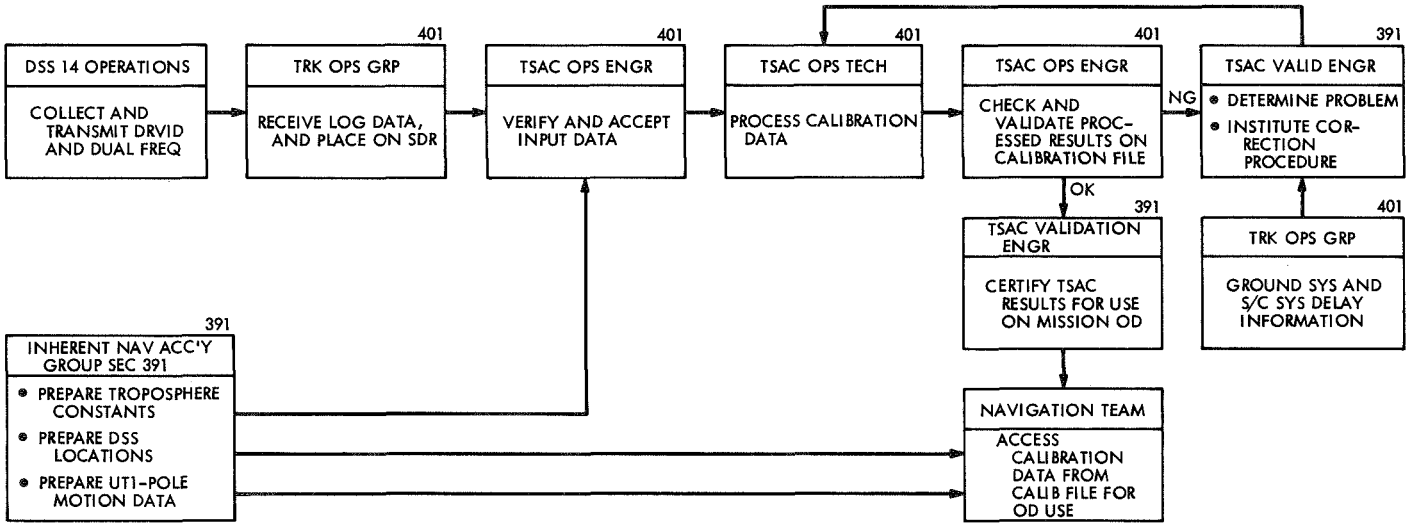

Fig. 7. TSAC operations design chart

An Additional Effect of Tropospheric Refraction on the Radio Tracking of Near-Earth Spacecraft at Low Elevation Angles

C. C. Chao and T. D. Moyer
Tracking and Orbit Determination Section

The current tropospheric calibration in DPODP assumes that the direction of the ray path after it exits from the troposphere is parallel to the true line-of-sight. Such an assumption will induce a sizable error for near earth tracking at low elevation angles. This report examines such effect and gives the additional corrections to the present tropospheric calibration for near-earth tracking.

I. Introduction

As an operational simplification, the tropospheric corrections employed in the JPL Double Precision Orbit Determination Program assume that the direction of the ray path after it exits from the troposphere is the same as it would be if there were no atmosphere. This assumption, for distant spacecraft, is consistent with the formulation of the current orbit determination software which had as one of its design goals the ability to compute range differences (obtained by counting doppler over a tracking pass, ~12 h for deep space probe) to an accuracy of 0.1 m. The error in the tropospheric range correction caused by the above approximation to the ray-path direction is shown to be less than this 0.1-m design goal for Earth-spacecraft distance greater than 5×10^4 km (8 earth radii). However, for low-orbiting earth satellites, failure to account for the true ray-path "exit" direction can cause errors exceeding 1 m in the differential tropospheric refraction correction applied during a tracking pass to the counted doppler at low elevation angles. An earlier paper (Ref. 1) indicated the similar effect for optical data.

Three types of trajectories were investigated, and the results indicated that such additional effect becomes insignificant when the range of the spacecraft is greater than 8 earth radii or when the elevation angle is greater than 10 deg.

II. Analysis

The current model of troposphere correction used in the JPL Double Precision Orbit Determination Program (DPODP) was derived under the assumption that the direction of the ray path after it exits from the troposphere is parallel to the true line-of-sight (Ref. 2). The range and range rate correction for either down leg or up leg is computed by the following empirical formulae:

$$\Delta\rho(\gamma) = \frac{N_{oi}}{340}\left[\frac{A}{(\sin\gamma + B)^{1.4}}\right] \tag{1}$$

$$\Delta\dot{\rho}(\gamma) = \left(\frac{N_{oi}}{340}\right)\left(\frac{A}{\tau}\right)\left[\frac{1}{(\sin F + B)^{1.4}} - \frac{1}{(\sin G + B)^{1.4}}\right] \tag{2}$$

where A and B are constants determined empirically, and

γ = elevation angle

N_{oi} = surface refractivity of station i

τ = doppler averaging time in seconds

$F = \gamma + (\tau/2)\dot{\gamma}$

$G = \gamma - (\tau/2)\dot{\gamma}$

$\dot{\gamma}$ = rate of elevation angle change

The range correction made by Eq. (1) can be explained geometrically from Fig. 1. For a spacecraft at S with an elevation angle γ and a distance ρ, away from the tracking station O, the range correction is the difference between the ray path OGS'[1] and the true range OS, where GS' is parallel to OS under the previous assumption. The line SS' is perpendicular to both OS and GS'. The range rate correction made by Eq. (2) is the rate of change of range correction from Eq. (1) for the given elevation angle. For deep-space spacecraft, the range becomes so large compared to the distance h that the true ray path OKS tends to coincide with the assumed ray path OGS' from the above formulae. For near-earth spacecraft, the exit-ray path direction becomes no longer parallel to the true line of sight OS and consequently, the range and range rate corrections made by the above formulae will induce an error which is a function of ρ and h. To account for such additional correction, the following analysis is made.

The true correction for range when the spacecraft is at S in Fig. 1 should be the difference between the ray path OKS[2] and the true range OS or ρ, which can be expressed as:

$$\begin{aligned}\Delta\rho_{\text{True}}(\gamma) &= OKS - OS \\ &= (OKS - OT) - (OS - OT)\end{aligned}$$

where OT is parallel to KS and ST is normal to both of them. Thus the quantity $OKS - OT$ is just the range correction by the current formula (Eq. 1) at a slightly different elevation angle γ_2 (Fig. 1).

$$\begin{aligned}\Delta\rho_{\text{True}}(\gamma) &= \Delta\rho(\gamma_2) - \rho(1 - \cos\Delta\alpha) \\ &= \Delta\rho(\gamma - \Delta\alpha) - \tfrac{1}{2}\rho(\Delta\alpha)^2 + \ldots .\end{aligned} \tag{3}$$

Since $\Delta\alpha$ is small, we can expand $\Delta\rho(\gamma - \Delta\alpha)$ in a Taylor series and neglect second-order terms:

$$\Delta\rho_{\text{True}}(\gamma) = \Delta\rho(\gamma) - \left.\frac{d\Delta\rho}{d\gamma}\right|_{\gamma}\Delta\alpha - \tfrac{1}{2}\rho\,(\Delta\alpha)^2 \tag{4}$$

The first term on the right hand side gives the range correction at γ when the spacecraft is assumed at infinity, and is the current DPODP correction (Eq. 1). The remaining two terms are the additional correction for near-earth spacecraft.

The range-rate correction, by definition, is the time derivative of the range correction. From Eq. (4) with $\Delta\alpha = h/\rho$ (Fig. 1) we have

$$\begin{aligned}\Delta\dot{\rho}_{\text{True}}(\gamma) = \Delta\dot{\rho}(\gamma) &- \frac{d^2\Delta\rho}{d\gamma^2}\dot{\gamma}\Delta\alpha - \frac{1}{h}\frac{d\Delta\rho}{d\gamma}\frac{dh}{d\gamma}\dot{\gamma}(\Delta\alpha) \\ &+ \frac{1}{h}\frac{d\Delta\rho}{d\gamma}\dot{\rho}(\Delta\alpha)^2 - \frac{dh}{d\gamma}\dot{\gamma}(\Delta\alpha) + \tfrac{1}{2}\dot{\rho}(\Delta\alpha)^2\end{aligned} \tag{5}$$

The first term corresponds to the DPODP correction by Eq. (2). The five remaining terms are additional corrections. Two terms among the five are of second order in $\Delta\alpha$. However, before we know the magnitude of $\dot{\rho}$ which is contained in the two terms, it is better to retain

[1]The propagation time along OGS' multiplied by the speed of light C.

[2]The propagation time along OKS multiplied by the speed of light C.

them for this analysis. Let us define these additional corrections for range and range-rate as $\delta\rho$ and $\delta\dot{\rho}$, respectively. One can rewrite them as:

$$\delta\rho(\gamma) = -\left(\frac{d\Delta\rho}{d\gamma} + \frac{h}{2}\right)\Delta\alpha \tag{6}$$

$$\delta\dot{\rho}(\gamma) = -\left[\frac{d^2\Delta\rho}{d\gamma^2} + \left(\frac{1}{h}\frac{d\Delta\rho}{d\gamma} + 1\right)\frac{dh}{d\gamma}\right]\dot{\gamma}\Delta\alpha + \left[\frac{1}{h}\frac{d\Delta\rho}{d\gamma} + \frac{1}{2}\right]\dot{\rho}(\Delta\alpha)^2 \tag{7}$$

The two derivatives, $d^2\Delta\rho/d\gamma^2$ and $d\Delta\rho/d\gamma$ can be obtained from the ray trace program (Ref. 3). An expression for the offset h is derived as follows.

From the triangle CBK in Fig. 1, we have

$$\frac{\sin\Psi}{CB} = \frac{\sin CBK}{CK} \tag{8}$$

which will lead to

$$h = OB\cos\gamma_2 = \left[\frac{R_T\sin\Psi}{\sin(\phi+\Psi)} - R_0\right]\cos\gamma_2 \tag{9}$$

Since

$$\gamma_2 = 90\text{ deg} - (\phi + \Psi)$$

$$h = R_T\sin\Psi - R_0\sin(\phi+\Psi) \tag{10}$$

The quantities R_0 and R_T are the distances from geocenter to the tracking station O, and the outer edge of the troposphere, respectively. The angles ϕ and Ψ are the results from the ray trace program.

III. Computed Results and Discussion

The derivatives in Eqs. (6) and (7) together with the distance of the ray path deflection h were computed by the ray trace program and plotted in Figs. 2 to 4 for low elevation angles where the additional effect $\delta\rho$, $\delta\dot{\rho}$ becomes important. A bi-exponential profile of refractivity ($N_D = 290$, $H_D = 7.0$ km, $N_w = 40$, $H_w = 2.0$ km) was assumed in the calculation.

The value of $\Delta\alpha$ depends on the elevation angle and the range of spacecraft ($\Delta\alpha = h/\rho$). For a given elevation angle, the additional range correction $\delta\rho$ (Eq. 6) is inversely proportional to the range ρ. The variation of $\delta\rho$ with elevation angle and range is plotted in Fig. 5. The solid curves are the equal $\delta\rho$ lines. For instance, at 1 deg of elevation the value of $\delta\rho$ decreases from 1 m at $\rho \approx 900$ km down to 0.1 m at $\rho \approx 9000$ km. The two broken lines represent the variation of range with elevation angle for two geocentric circular orbits of altitudes 200 and 1000 km. If we follow the circular orbit of 200 km altitude, the additional range error $\delta\rho$, is about 3 m at zero elevation angle and decreases below 0.1 m above 3 deg elevation.

When the range increases to the lunar distance, as seen from Fig. 5, the additional range error $\delta\rho$ reduces to about 0.01 m at zero elevation angle. For interplanetary distances, such error is vanishingly small.

Based on the above analysis this additional error needs correction for 0.1-m design goal only for near-Earth tracking ($\rho \leq 4.5 \times 10^4$ km) at low elevation angles ($\gamma < 10$ deg).

The additional range rate correction $\delta\dot{\rho}$ is a function of γ, ρ the time rate of elevation angle change $\dot{\gamma}$ and the range rate $\dot{\rho}$, all of which depend on the particular geometry of the orbit and the latitude of the tracking station. Three different types of trajectories were investigated: (1) Geos–C orbit (SMA = 7674.7 km, apogee = 7860 km, inclination 20 deg), (2) Lunar orbiter (*Surveyor*) and (3) close approach of *Mariner* Mars 1971 spacecraft. The values of these additional range rate effects $\delta\dot{\rho}$ were computed and tabulated in Table 1.

Although such additional effects become negligibly small for the radio tracking of deep-space probes, it is recommended that such effects should be considered or corrected when the DPODP is used for:

(1) Those deep space or lunar missions having low elevation angle tracking data during the launch phase ($\rho < 4.5 \times 10^4$ km) which is important for the orbit determination, i.e., the 0.1-m precision in integrated doppler is required in this period.

(2) The orbit determination of earth satellites with the same required precision and the data at low elevation angles are desirable.

References

1. Cain, D. L., and Mathews, C., "Secondary Refraction Correction for Optical Data," TM 311-275, Jet Propulsion Laboratory, Pasadena, Calif., February, 1963.

2. Liu, A., "Recent Changes to the Tropospheric Refraction Model Used in the Reduction of Radio Tracking Data From Deep Space Probes," in *The Deep Space Network*, Space Programs Summary 37-50, Vol. II. Jet Propulsion Laboratory, Pasadena, Calif., February, 1968.

3. Miller, L. F., Ondrasik, V. J., and Chao, C. C., "A Cursory Examination of the Sensitivity of the Tropospheric Range and Doppler Effects to the Shape of the Refractivity Profile," in *The Deep Space Network*, TR 32-1526, Vol. I, pp. 22–30. Jet Propulsion Laboratory, Pasadena, Calif., Feb. 15, 1971.

Table 1. Additional error in range rate due to troposphere $\delta\dot{\rho}$

Type of orbits range, km	Range rate, mm/sec			
	Elevation angle γ,			
	At 0 deg	At 0.5 deg	At 1 deg	At 5 deg
Geos C (Altitude $\approx$ 1300 km)	14	8.2	4.9	0.2
Lunar Orbiter (3.7×10^6)	1.2×10^{-2}	0.7×10^{-2}	0.4×10^{-2}	0.1×10^{-3}
Mariner Mars 1971 (0.8×10^8)	0.5×10^{-5}	0.3×10^{-5}	0.2×10^{-5}	0.005×10^{-5}

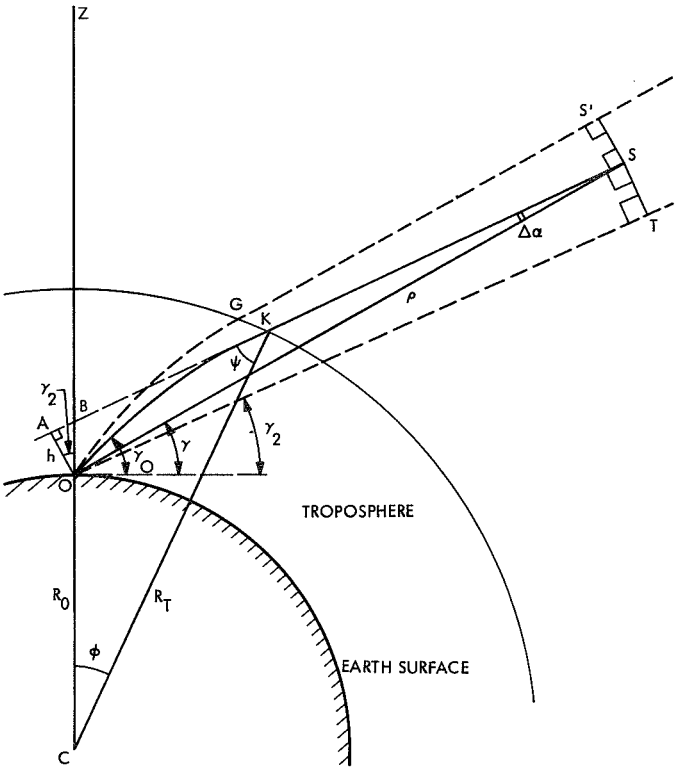

Fig. 1. Geometry for the additional tropospheric effect on radio tracking on near-earth probe

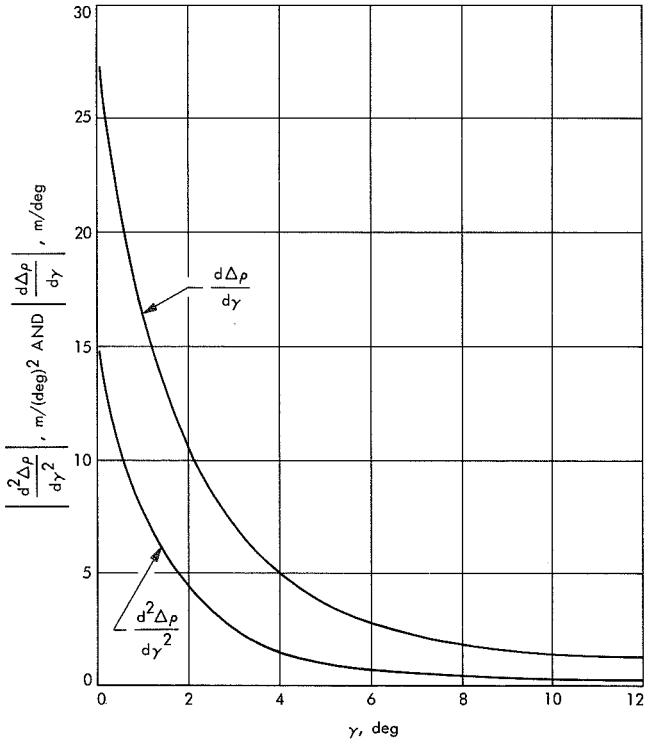

Fig. 2. Variations of the functions $d\Delta\rho/d\gamma$ and $d^2\Delta\rho/d\gamma^2$ with elevation angle

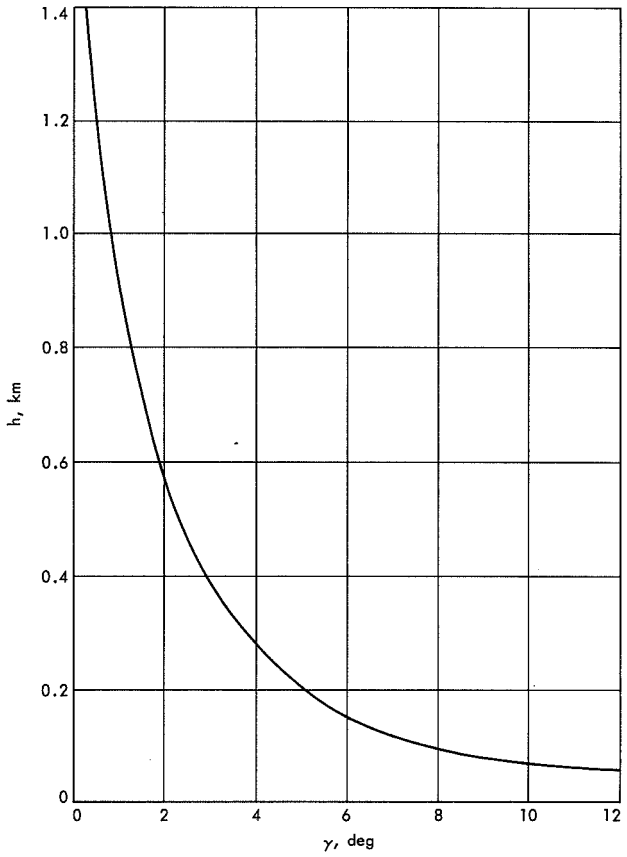

Fig. 3. Variation of h at low elevation angle

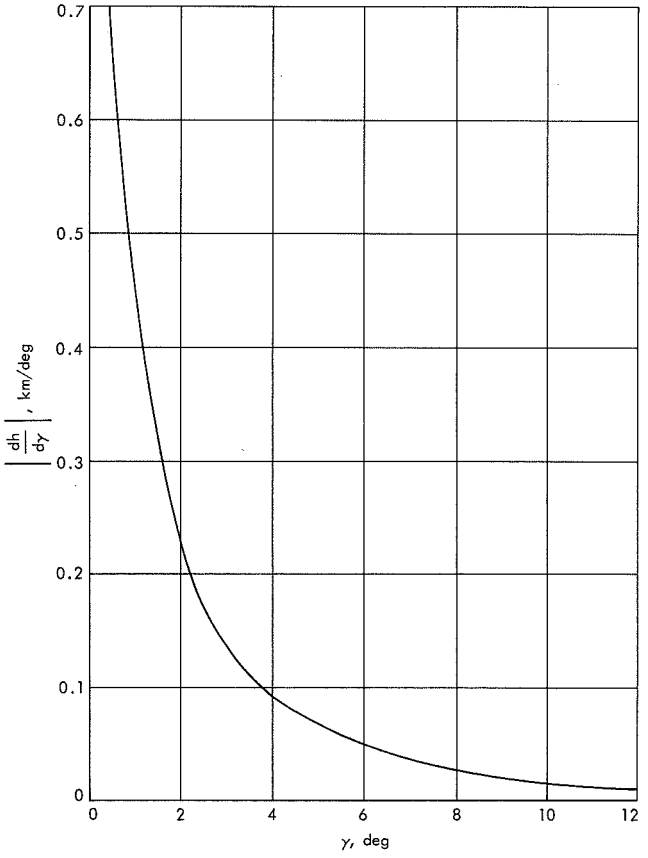

Fig. 4. Variations of the magnitude of $dh/d\gamma$ with elevation angle

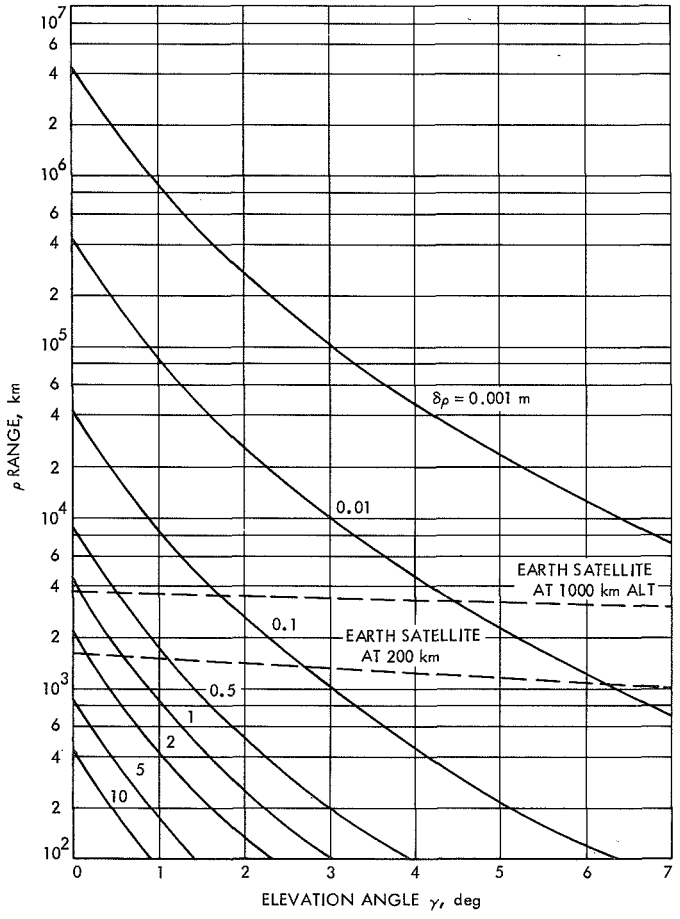

Fig. 5. Additional error in range at low elevation angle

Analysis of the DRVID and Dual Frequency Tracking Methods in the Presence of a Time-Varying Interplanetary Plasma

O. H. von Roos
Tracking and Orbit Determination Section

An analysis is made of two different methods for determining the total electron content of the plasma existing between a spacecraft and the Earth. It is shown that the two methods complement each other. The dual frequency method is capable of measuring the structure of a plasma inhomogeneity, whereas the DRVID method is capable of locating this inhomogeneity within the ray path of the electromagnetic tracking signal.

I. Derivation of the Pertinent Expressions

Suppose, an electromagnetic signal (either a continuous or a modulated wave) is propagating along the x axis of a cartesian coordinate system toward a spacecraft. It will then interact with the interplanetary plasma. For the high frequency involved ($\omega \approxeq 10^{10}$ sec^{-1}) only the electrons of the plasma will contribute to the degradation of the signal. Assuming that the electron density N depends only on x and the time t, that is $N = N(x, t)$, it can be shown that the field equation for the amplitude of the electric field E of the wave is given by

$$-V^2E + \frac{1}{c^2}\ddot{E} = -\frac{\alpha}{c^2}N(x,t)\,E \tag{1}$$

the electric field is polarized in a direction perpendicular to x, the direction of propagation. $\alpha = 4\pi e^2/m$. A term of the order of $\omega^{-1}\dot{N}$ has been neglected in Eq. (1), since surely

$$\omega^{-1}\dot{N} << N \tag{2}$$

because time variations of N are measured in minutes for typical solar plasma inhomogeneities (plasma clouds).

Equation (1) may be solved by the ansatz:

$$E = e^{i(kx+F(x,t)-\omega t)} \tag{3}$$

Inserting Eq. (3) into Eq. (1), we obtain for F the following equation:

$$\frac{\partial F}{\partial x} + \frac{1}{c}\frac{\partial F}{\partial t} = -\frac{\alpha}{2kc^2}N(x,t) \tag{4}$$

neglecting $(dF/dx)^2$ and d^2F/dx^2, since it can be shown that these terms are small compared to k^2. The solution of Eq. (4) for $F = 0$ when $N \equiv 0$, is

$$F = -\frac{\alpha}{2kc^2}\int_0^x N\left(x', t + \frac{x'-x}{c}\right)dx' \tag{5}$$

with an as yet undetermined integration constant C.

A phase point (wave crest) moves with a velocity dx/dt obtained from

$$kx - \frac{\alpha}{2kc^2}\int_0^x dx' N\left(x', t + \frac{x' - x}{c}\right) - \omega t = 0 \qquad (6)$$

If at $t = 0$ the distance x traveled by the phase point is zero, or in other words the wave crest in question is emitted at $t = 0$, then $C = 0$ and the integration constant is determined. Neglecting N in Eq. (6) leads to

$$x = ct, \qquad \text{or} \qquad \frac{dx}{dt} = c, \qquad (7)$$

the vacuum value for the phase velocity. But since the derivative of the integral in Eq. (6) is small compared to k we may use Eq. (7) for the time argument of N in Eq. (6). Anything better would only lead to second-order effects which have been neglected here in the first place. Accordingly, the phase may be expressed by:

$$kx - \frac{\alpha}{2kc^2}\int_0^x N\left(x', \frac{x'}{c}\right) dx' - \omega t = 0 \qquad (8)$$

from which it follows that the instantaneous phase velocity at x and $t = t' = x/c$ given by

$$\dot{x} = v_P(x, t) = c\left(1 + \frac{\alpha}{2\omega^2} N(x, t')\right) \qquad (9)$$

as intuitively expected. For rapid fluctuations of N and low frequencies, however, the result (9) would be totally inadequate. The group velocity is also given by Eq. (9) if α is interchanged with $-\alpha$.

Let us now suppose that a particular wave crest is emitted from the antenna at position $x = 0$ at time t. Let us also suppose that the *true* distance to the spacecraft, the range, is R (in meters). Then the transit time T_U (U for uplink) for arrival at the spacecraft is

$$T_U = \int_0^R \frac{dx}{v_P\left(x, \frac{x}{c} + t\right)} = \frac{R}{c}\left(1 - \frac{\alpha}{2\omega^2}\frac{1}{R}\int_0^R N\left(x, \frac{x}{c} + t\right) dx\right) \qquad (10)$$

Likewise, for the downlink transit time T_D for arrival at the earthbound receiver we have

$$T_D = \frac{R}{c}\left(1 - \frac{\alpha}{2\omega_D^2}\frac{1}{R}\int_0^R N\left(x, T_D + T_U - \frac{x}{c} + t\right) dx\right) \qquad (11)$$

where ω_D is the transponder frequency of the spacecraft (usually $240/(221)\omega$). The total roundtrip time is $T_U + T_D$ and the apparent range is defined as:

$$R' = \frac{c}{2}(T_U + T_D) \qquad (12)$$

Eq. (10) and (11) apply to the phase velocity. For the group velocity of the modulated signal Eqs. (10) and (11) apply if α is replaced by $-\alpha$, as already stated. From Eqs. (10), (11), and (12) we find

$$R' = R - \frac{\alpha}{4\omega^2}\int_0^R \left[N\left(x, \frac{x}{c} + t\right) + \left(\frac{\omega}{\omega_D}\right)^2 N\left(x, T_D + T_U - \frac{x}{c} + t\right)\right] dx \qquad (13)$$

The apparent range for the modulation (group velocity) is

$$R'' = R + \frac{\alpha}{4\omega^2}(\text{integral of Eq. 13}) \qquad (14)$$

This is true, since the time T_U and T_D in the argument of the electron density may be expressed by $c^{-1}R$, $c^{-1}R'$ or $c^{-1}R''$, the difference between any of these choices being of second order. Forming the "differenced range minus integrated doppler" (Ref. 1) we have the equation[1]:

$$\text{DRVID}(t) = R''(t) - R'(t) = \frac{\alpha}{2\omega^2}\int_0^R \left[N\left(x, \frac{x}{c} + t\right) + \left(\frac{\omega}{\omega_D}\right)^2 N\left(x, \frac{2R - x}{c} + t\right)\right] dx \qquad (15)$$

The quantity needed to correct the doppler data (phase velocity) is then

$$-\frac{1}{2}\frac{d}{dt}\text{DRVID}(t) = -\frac{1}{2}\frac{d}{dt}(R''(t) - R'(t)) \qquad (16)$$

[1]Disregarding the doppler shift which is trivially incorporated, if needed.

We turn now to the dual-frequency method extensively used by the Stanford group (e.g., Ref. 2). The method consists in transmitting simultaneously two signals at two different frequencies along the ray path toward the spacecraft. The delay time difference is measured at the spacecraft and telemetered back to earth. From Eq. (1) we find for the time difference:

$$\Delta T = T_{U_1} - T_{U_2} = -\frac{\alpha}{2c}\left(\frac{1}{\omega_1^2} - \frac{1}{\omega_2^2}\right)\int_0^R N\left(x, \frac{x}{c} + t\right) dx \tag{17}$$

Where ω_1 and ω_2 are the two frequencies (usually 50 and 425 MHz). The apparent range change is then for the dual-frequency method (DFM)

$$\mathrm{DFM}(t) = c\Delta T \tag{18}$$

If the group velocity is employed, the sign of α changes in Eqs. (17) and (18). We see that the DFM measures only the uplink electron content. But from Eqs. (15) and (18) we obtain

$$\mathrm{DRVID}(t) + \frac{\omega_1^2\omega_2^2}{\omega^2(\omega_1^2 + \omega_2^2)}\,\mathrm{DFM}(t) = \frac{\alpha}{2}\left(\frac{\omega}{\omega_0}^2\right)\int_0^R N\left(x, \frac{2R - x}{c} + t\right) dx \tag{19}$$

which is a measure of the downlink electron content alone. There is, however, no new information in Eq. (19), since it is the one way information of Eq. (18) shifted by R/c in time. From Eq. (15) it is obvious that if the electron content changes significantly in times short compared to the transit time of the signal, the analysis of the interplanetary plasma is hampered by the occurrence of the two integrals in Eq. (15), one being shifted in time by the amount R/c, the transit time. Large and fairly quick electron content changes can happen when a plasma cloud emitted from an active area of the sun passes the raypath (Refs. 3 and 4).

II. Application

To see more clearly what is involved, let us take a plasma cloud of length L which is entering the ray path at $t = 0$. We also assume for simplicity that the width of the cloud is short compared to the range R and that therefore the transit time through the cloud is negligibly small compared to R/c. Further, we assume a parabolic electron density distribution within the cloud with maximum at the center. If this cloud enters the raypath at $x = x_0$, it may conveniently be described by the following expression:

$$N(x,t) = LN_0\,\delta(x - x_0)\left[1 - \frac{4}{L^2}\left(\frac{L}{2} - vt\right)^2\right] \times\left[S(t) - S\left(t - \frac{L}{v}\right)\right] \tag{20}$$

Here $\delta(x)$ is the delta function and $S(t)$ the step function

$$S(t) = \begin{cases} 0 \text{ for } t < 0 \\ 1 \text{ for } t > 0 \end{cases} \tag{21}$$

To simplify the analysis, let us investigate the integrals

$$I_2 = \int_0^R \left[N\left(x, \frac{x}{c} + t\right) + N\left(x, \frac{2R - x}{c} + t\right)\right] dx \tag{22}$$

representative for the DRVID data, Eq. (15) and

$$I_1 = \int_0^R N\left(x, \frac{x}{c} + t\right) dx \tag{23}$$

representative for the DFM data, Eq. (17).

With the plasma cloud given by Eq. (2) we have

$$I_1 = LN_0\left[1 - \frac{4}{L^2}\left(\frac{L}{2} - v\left(\frac{x_0}{c} + t\right)\right)^2\right] \times\left[S\left(\frac{x_0}{c} + t\right) - S\left(\frac{x_0}{c} + t - \frac{L}{v}\right)\right] \tag{24}$$

and

$$I_2 = I_1 + LN_0\left[1 - \frac{4}{L^2}\left(\frac{L}{2} - v\left(\frac{2R - x_0}{c} + t\right)\right)^2\right] \times\left[S\left(\frac{2R - x_0}{c} + t\right) - S\left(\frac{2R - x_0}{c} + t - \frac{L}{v}\right)\right] \tag{25}$$

Four examples of Eq. (24) and (25) are depicted in Fig. 1. By and large, characteristic values of the various parameters have been chosen for the computation of these curves. It is clear from these figures that the time rate of change of the electron density within the plasma cloud is measured differently between DRVID and DFM. Of course, we know from our previous analysis that the DFM data give a direct measure of electron concentration time variation, whereas DRVID degrades this information.

Let us look more carefully at the statement just made. We strip the analysis from all unessentials such as constant factors, etc. The conclusion is, simply, that DRVID measures the quantity:

$$\Phi(t) = N(t) + N(t + \delta) \tag{26}$$

where $N(t)$ is proportional to the electron density of the plasma inhomogeneity. The DFM however, measures

$$\Psi(t) = N(t) \tag{27}$$

and, therefore, gives a direct measurement of the structure of the plasma cloud. Now, it is important to notice that the delay time δ of Eq. (26) actually can be measured by DRVID. This delay time determines the location of the cloud within the ray path. The DFM is incapable of furnishing this information. The determination of the location of a plasma cloud in the ray path is done by an autocorrelation analysis of the tracking data, or what it amounts to in our simplified analysis, the quantity $\Phi(t)$ of Eq. (26). For details see Ref. 3. However, even with the knowledge of δ in Eq. (26), the determination of $N(t)$ meets with difficulties. For, if $\Phi(t)$ is known and δ is known, the solution of Eq. (26) is

$$N(t) = a \sum_{n=1}^{\infty} (-1)^{n+1} \Phi(t - n\delta) + (1 - a) \sum_{n=0}^{\infty} (-1)^n \Phi(t + n\delta) \tag{28}$$

where a is an integration constant to be determined by the initial conditions (no cloud prior to a certain time for instance). In any case, we see that the determination of $N(t)$ hinges on values of $\Phi(t)$ measured at many different times. If ϵ is the error of a measurement of $\Phi(t)$ and if n values of $\Phi(t)$ are needed in each of the sums of Eq. (28), the error in the determination of $N(t)$ would roughly be $\epsilon\sqrt{2n}$. Assuming that the DFM has the same accuracy as DRVID, the error in determining the solar plasma cloud structure would only be ϵ, which may be considerably less than the accuracy of the DRVID cloud structure determination. For $\delta = 4$ min and the passage of the cloud through the ray path lasting 40 min, we need about $2 \cdot 40/4 = 20$ terms in Eq. (28). The inaccuracy of Eq. (26) versus Eq. (27) would be 4.5 times worse in this case. We have not mentioned the inaccuracy in the value of δ. This brings in additional errors in the cloud structure determination by DRVID which are difficult to ascertain.

There is, however, another method for determining δ, assuming only one cloud is present, that avoids the correlation analysis mentioned earlier. It consists simply in the following: There is a point in time when DRVID ceases to pick up information from the cloud on the downlink. This happens when the round-trip time from the cloud to the spacecraft and back is equal to the time for the cloud to just have left the ray path. This time is given by

$$2\frac{R - x_0}{c} = \frac{L_1}{v} \tag{29}$$

where L_1 is that part of the cloud that affects only the uplink information. DRVID and DFM become identical (Eqs. 22 and 23). But the time L_1/v is equal to the time difference between the time DRVID and DFM become equal and the time the cloud ceases to affect the data. L_1/v can therefore be measured. Knowing the range it is now easy to compute x_0, i.e., the location of the tail end of the cloud. A similar analysis shows that the location of the front end of the cloud may be determined by Eq. (29) where now L_1/v is the time difference between the time the cloud starts to affect DRVID and the time it starts to be seen by DFM.

III. Summary

To summarize this analysis, we wish to make the following statements: Given that the inherent accuracy of the DFM and DRVID are the same, and there is no reason to believe otherwise, the two methods complement each other nicely. Whereas DRVID alone is capable of locating solar plasma inhomogeneities, the DFM alone is capable of determining the structure (that is, the spatial electron density variations) of a solar plasma inhomogeneity. It is felt therefore, that if both methods are available, a great deal more can be learned about the solar wind of which so pitifully little is known to this date.

The author is grateful for discussions with Jack Lorell and Harry Lass. Particularly appreciated is the computational assistance given by Brendan Mulhall.

References

1. MacDoran, P. F., "A First-Principles Derivation of the Differenced Range Versus Integrated Doppler (DRVID) Charged-Particle Calibration Method," in *The Deep Space Network*, Space Programs Summary 37-62, Vol. II, pp. 28–34. Jet Propulsion Laboratory, Pasadena, Calif., March 31, 1970.
2. Eshleman, V. R., Gallagher, P. B., and Barthle, R. C., *J. Geophys. Res.*, Vol. 65, p. 3079, 1960.
3. MacDoran, P. F., Callahan, P. S., and Zygielbaum, A. I., "Probing the Solar Plasma With *Mariner* Radio Metric Data, Preliminary Results," in TR 32-1526, Vol. I, pp. 14–21. Jet Propulsion Laboratory, Pasadena, Calif., Feb. 15, 1971.
4. Koehler, R. L., *J. Geophys. Res.*, Vol. 73, p. 4883, 1968.

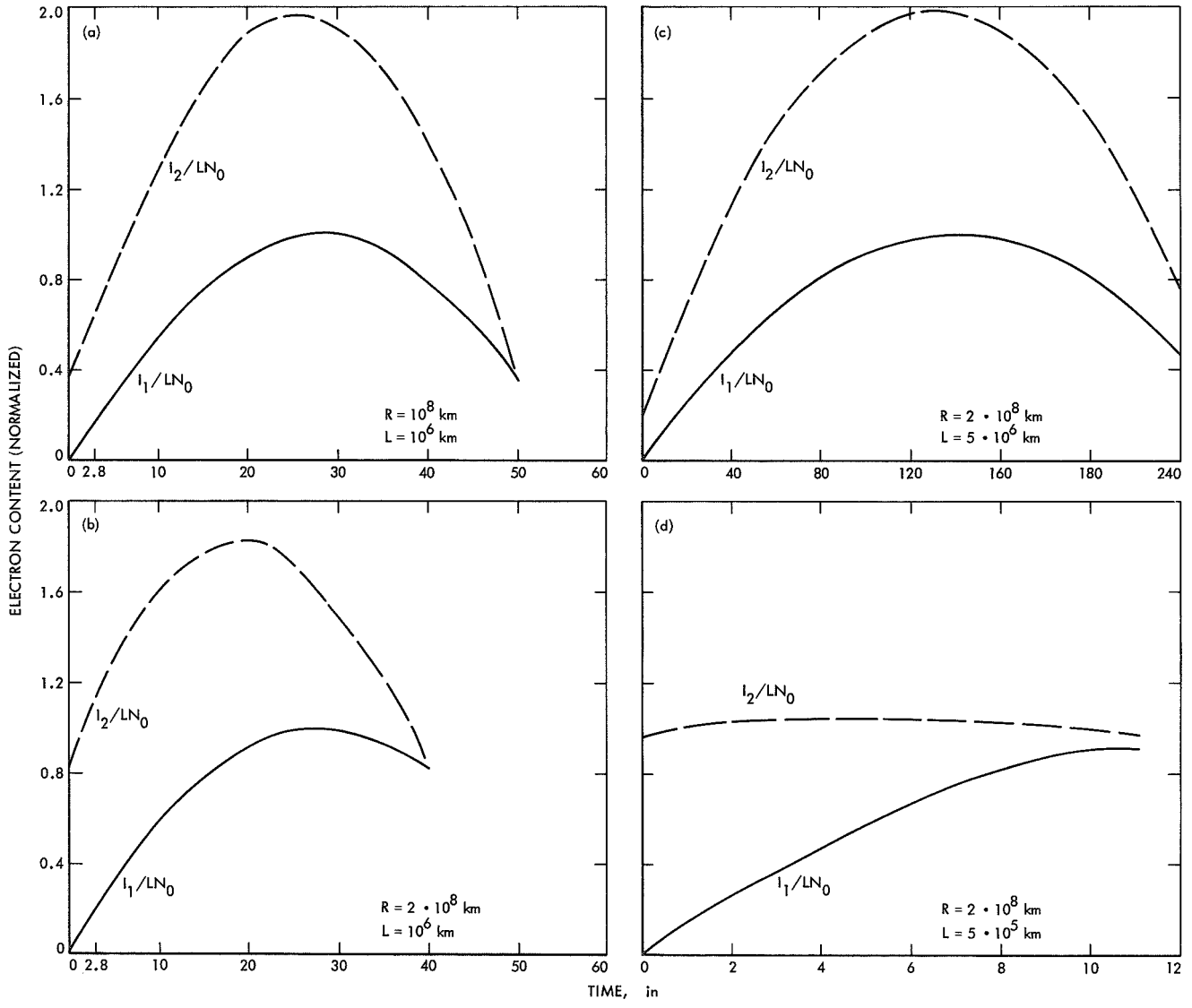

Fig. 1. Four selected solutions of Eqs. (24) and (25): (a) $R = 10^8$ km and $L = 10^6$ km, (b) $R = 2.10^8$ km and $L = 10^6$ km, (c) $R = 2 \times 10^8$ km and $L = 5 \times 10^6$ km, and (d) $R = 2.10^8$ km and $L = 5 \times 10^8$ km

A First-Order Theory for Use in Investigating the Information Content Contained in a Few Days of Radio Tracking Data

V. J. Ondrasik and D. W. Curkendall
Tracking and Orbit Determination Section

An approximation to the topocentric range rate of a spacecraft is developed which is first order in both the time past epoch and the ratio between the distance of an observing station from the geocenter and the geocentric range. This approximation is compared with a numerical integrated trajectory to obtain some idea of the duration over which it may be reliable. The development is extended to include an analytical determination of the errors in the spacecraft state produced by errors in the range rate data. It is also shown how range data may be incorporated into this cursory error analysis. The partial derivatives of the gravitational geocentric acceleration with respect to range, declination, and right ascension are obtained analytically and shown graphically.

I. Introduction

The determination of an orbit from range and range rate data and obtaining a measure of the accompanying errors is a complicated process. The physical understanding of this process is greatly enhanced if it is possible to develop a simple analytical theory, which although only an approximation, contains the pertinent features of the real problem. A major step in this direction was taken by Hamilton and Melbourne (Ref. 1) in their classical paper describing the information content of a single pass of doppler data when the geocentric range rate, declination, and right ascension may be assumed to be constant. Curkendall and McReynolds (Ref. 2) extended the theory to include first-order temporal variation in these quantities. The development which will be undertaken here is a refinement of the Curkendall and McReynolds approach and not conceptually a new method. Some new features which are presented are:

(1) Analytical derivation of the partial derivatives of the geocentric gravitational acceleration with respect to range, declination, and right ascension.

(2) Completely analytical description of errors in the full spacecraft state produced by station location errors.

An attempt is also made to obtain a better idea of how and when this first-order theory is no longer reliable.

II. Expansion of the Topocentric Range and Range Rate in terms of r_s/r and z_s/r

From the coordinate system shown in Fig. 1, it is easily seen that the magnitude of the topocentric range vector ρ may be written as

$$\rho = [(x - r_s \cos\varphi)^2 + (y - r_s \sin\varphi)^2 + (z - z_s)^2]^{1/2} \tag{1}$$

For a distant spacecraft the range equation may be put in a more convenient form by expanding the right-hand side of Eq. (1) in terms of the small quantities r_s/r and z_s/r as given below:

$$\begin{aligned}\rho = r\Bigg\{ & 1 - \frac{r_s}{r}\left(\frac{x}{r}\cos\varphi + \frac{y}{r}\sin\varphi\right) - \frac{z_s}{r}\frac{z}{r} \\ & + \frac{1}{2}\frac{r_s^2}{r^2}\left[1 - \frac{1}{2}\left(\frac{x^2}{r^2} + \frac{y^2}{r^2}\right)\right. \\ & \left. - \frac{1}{2}\left(\frac{x^2}{r^2} - \frac{y^2}{r^2}\cos 2\varphi\right) - \frac{xy}{r^2}\sin 2\varphi\right] \\ & - \frac{r_s}{r}\frac{z_s}{r}\frac{z}{r}\left(\frac{x}{r}\cos\varphi + \frac{y}{r}\sin\varphi\right) \\ & + \frac{1}{2}\frac{z_s^2}{r^2}\left(1 - \frac{z^2}{r^2}\right) + \cdots\Bigg\}\end{aligned} \tag{2}$$

Deleting terms higher than the first order in r_s/r and z_s/r from the above equation and expressing the spacecraft coordinates in terms of a spherical system result in a very simple approximation for ρ, which is shown below. Starting with this equation, techniques may be developed that are extremely useful in interpreting various physical situations.

$$\rho \approx r - [r_s \cos\delta \cos(\varphi - \alpha) + z_s \sin\delta] \tag{3}$$

where

r = geocentric range

δ = declination

α = right ascension

The range rate to the same accuracy may be obtained by differentiating Eq. (3) with respect to time and is given below:

$$\begin{aligned}\dot\rho \approx \dot r - z_s\,\dot\delta\cos\delta + r_s(\dot\varphi - \dot\alpha)\cos\delta\sin(\varphi - \alpha) \\ + r_s\,\dot\delta\sin\delta\cos(\varphi - \alpha)\end{aligned} \tag{4}$$

III. Expansion of the Range Rate to the First Order in Time

After deriving an expression similar to Eq. (4), Hamilton and Melbourne (Ref. 1) proceed under the assumption that $\dot r$, δ, and α are constant. Curkendall and McReynolds (Ref. 2) have shown that the analysis is improved if the spacecraft variables in Eq. (4) are expressed as first-order expansions in time, as given below:

$$\begin{aligned}\dot r &= \dot r_0 + \ddot r_0\, t \\ \delta &= \delta_0 + \dot\delta_0\, t \\ \dot\delta &= \dot\delta_0 + \ddot\delta_0\, t \\ \alpha &= \alpha_0 + \dot\alpha_0\, t \\ \dot\alpha &= \dot\alpha_0 + \ddot\alpha_0\, t\end{aligned}$$

where a_0 denotes that the quantity a is evaluated at $t = 0$. Substituting the above set of equations into Eq. (4), and assuming, for the present, that

$$\varphi = \varphi_0 + \dot\varphi_0\, t$$

yields the following first-order expansion of the topocentric range rate in both r_s/r, z_s/r and time:

$$\begin{aligned}\dot\rho(t) \approx\ & \dot r_0 - z_s\,\dot\delta_0\cos\delta_0 + r_s(\dot\varphi_0 - \dot\alpha_0)\cos\delta_0 \\ & \times \sin(\varphi_0 + \dot\varphi_0\, t - \alpha) \\ & + r_s\,\dot\delta_0\sin\delta_0\cos(\varphi_0 + \dot\varphi_0\, t - \alpha_0) \\ & + [\ddot r_0 + z_s\,\dot\delta_0^2\sin\delta_0 - z_s\,\ddot\delta_0\cos\delta_0]t \\ & + r_s[-(\dot\varphi_0 - 2\dot\alpha_0)\,\dot\delta_0\sin\delta_0 \\ & - \ddot\alpha_0\cos\delta_0]\, t\sin(\varphi_0 + \dot\varphi_0\, t - \alpha_0) \\ & + r_s[-(\dot\varphi_0 - \dot\alpha_0)\,\dot\alpha_0\cos\delta_0 \\ & + \dot\delta_0^2\cos\delta_0 + \ddot\delta_0\sin\delta_0]\, t\cos(\dot\varphi_0 + \varphi_0\, t - \alpha_0)\end{aligned} \tag{5}$$

This equation is not in a suitable form for analysis because $\ddot r_0$, $\ddot\delta_0$, and $\ddot\alpha_0$ are not independent of r_0, α_0, δ_0, $\dot r_0$, $\dot\delta_0$, and $\dot\alpha_0$.

IV. Calculation of $\ddot{r}$, $\ddot{\delta}$, and $\ddot{\alpha}$

Before initiating the derivation for $\ddot{r}$, $\ddot{\delta}$, and $\ddot{\alpha}$, it is convenient to obtain some relations between the unit vectors, $\mathbf{i}$, in the cartesian and spherical coordinate systems. These relations may be obtained by obtaining from Fig. 1 the following equations:

$$\left.\begin{aligned} \mathbf{i}_r &= \cos\delta\cos\alpha\,\mathbf{i}_x + \cos\delta\sin\alpha\,\mathbf{i}_y + \sin\delta\,\mathbf{i}_z \\ \mathbf{i}_\alpha &= -\sin\alpha\,\mathbf{i}_x + \cos\alpha\,\mathbf{i}_y \\ \mathbf{i}_\delta &= -\sin\delta\cos\alpha\,\mathbf{i}_x - \sin\delta\sin\alpha\,\mathbf{i}_y + \cos\delta\,\mathbf{i}_z \end{aligned}\right\} \quad (6)$$

Since the cartesian coordinate system is assumed to be an inertial frame of reference,

$$\dot{\mathbf{i}}_x = \dot{\mathbf{i}}_y = \dot{\mathbf{i}}_z = 0$$

and

$$\left.\begin{aligned} \dot{\mathbf{i}}_r &= \dot{\delta}\,\mathbf{i}_\delta + \cos\delta\,\dot{\alpha}\,\mathbf{i}_\alpha \\ \dot{\mathbf{i}}_\delta &= -\dot{\delta}\,\mathbf{i}_r - \sin\delta\,\dot{\alpha}\,\mathbf{i}_\alpha \\ \dot{\mathbf{i}}_\alpha &= -\cos\delta\,\dot{\alpha}\,\mathbf{i}_r + \sin\delta\,\dot{\alpha}\,\mathbf{i}_\delta \end{aligned}\right\} \quad (7)$$

The geocentric range vector $\mathbf{r}$ may be written as

$$\mathbf{r} = r\,\mathbf{i}_r$$

Taking the derivative with respect to time and using Eq. (7) yields

$$\dot{\mathbf{r}} = \dot{r}\mathbf{i}_r + r\,(\dot{\delta}\,\mathbf{i}_\delta + \cos\delta\,\dot{\alpha}\,\mathbf{i}_\alpha)$$

Similarly

$$\begin{aligned} \ddot{\mathbf{r}} = {} & [\ddot{r} - r\,(\dot{\delta}^2 + \dot{\alpha}^2\cos^2\delta)]\,\mathbf{i}_r \\ & + (2\dot{r}\dot{\delta} + r\dot{\alpha}^2\sin\delta\cos\delta + r\,\ddot{\delta})\mathbf{i}_\delta \\ & + (2\dot{r}\dot{\alpha}\cos\delta - 2r\dot{\delta}\,\dot{\alpha}\sin\delta + r\cos\delta\,\ddot{\alpha})\mathbf{i}_\alpha \end{aligned} \quad (8)$$

From Fig 2, $\mathbf{r}$ may also be written as

$$\mathbf{r} = \mathbf{r}_p - \mathbf{r}_e \quad (9)$$

If both the earth and spacecraft are assumed to move under the influence of the sun only, the second derivative of $\mathbf{r}$ may be written as

$$\ddot{\mathbf{r}} = -\mu\left(\frac{\mathbf{r}_p}{r_p^3} - \frac{\mathbf{r}_e}{r_e^3}\right)$$

where μ is the sun's gravitational constant. Substituting Eq. (9) into the above equation gives

$$\ddot{\mathbf{r}} = -\mu\left[\frac{\mathbf{r}}{r_p^3} - \mathbf{r}_s\left(\frac{1}{r_p^3} - \frac{1}{r_e^3}\right)\right] \quad (10)$$

where $\mathbf{r}_s$ is the earth to sun vector, which in component form may be written as

$$\begin{aligned} \mathbf{r}_s = {} & r_e\cos\delta_s\cos\alpha_s\mathbf{i}_x \\ & + r_e\cos\delta_s\sin\alpha_s\mathbf{i}_y + r_e\sin\delta_s\,\mathbf{i}_z \end{aligned} \quad (11)$$

where

r_e = earth–sun distance

δ_s = declination of the sun

α_s = right ascension of the sun

Using the inverses of Eq. (6) allows Eq. (11) to be written as

$$\begin{aligned} \mathbf{r}_s = {} & r_e\,[\cos\delta\cos\delta_s\cos(\alpha - \alpha_s) + \sin\delta\sin\delta_s]\mathbf{i}_r \\ & + r_e\,[-\sin\delta\cos\delta_s\cos(\alpha - \alpha_s) + \cos\delta\sin\delta_s]\,\mathbf{i}_\delta \\ & - r_e\cos\delta_s\sin(\alpha - \alpha_s)\mathbf{i}_\alpha \end{aligned}$$

Substituting this equation into Eq. (10) results in

$$\begin{aligned} \ddot{\mathbf{r}} = -\mu\Bigg\{ & \left[\frac{r}{r_p^3} - r_e\left(\frac{1}{r_p^3} - \frac{1}{r_e^3}\right) < \cos\delta\cos\delta_s \right. \\ & \left. \times\cos(\alpha - \alpha_s) + \sin\delta\sin\delta_s > \right]\mathbf{i}_r \\ & - \left[r_e\left(\frac{1}{r_p^3} - \frac{1}{r_e^3}\right) < -\sin\delta\cos\delta_s \right. \\ & \left. \times\cos(\alpha - \alpha_s) + \cos\delta\sin\delta_s > \right]\mathbf{i}_\delta \\ & + \left[r_e\left(\frac{1}{r_p^3} - \frac{1}{r_e^3}\right) < \cos\delta_s \right. \\ & \left. \times\sin(\alpha - \alpha_s) > \right]\mathbf{i}_\alpha \Bigg\} \end{aligned} \quad (12)$$

Comparing the right-hand side of this equation with the right-hand side of Eq. (8) gives the following expressions for $\ddot{r}$, $\ddot{\delta}$ and $\ddot{\alpha}$ in terms of r, δ, α, $\dot{r}$, $\dot{\delta}$, and $\dot{\alpha}$:

$$\left.\begin{aligned} \ddot{r} &= r\left(\dot{\delta}^2 + \dot{\alpha}^2 \cos^2\delta\right) + \ddot{r}_g \\ \ddot{\delta} &= -\dot{\alpha}^2 \sin\delta\cos\delta - 2\frac{\dot{r}}{r}\dot{\delta} + \ddot{\delta}_g \\ \cos\delta\,\ddot{\alpha} &= 2\dot{\delta}\,\dot{\alpha}\sin\delta - 2\frac{\dot{r}}{r}\dot{\alpha}\cos\delta + \ddot{\alpha}_g \end{aligned}\right\} \tag{13}$$

where

$$\ddot{r}_g = -\mu\left[\frac{r}{r_p^3} - r_e\left(\frac{1}{r_p^3} - \frac{1}{r_e^3}\right) < \cos\delta\cos\delta_s \times \cos(\alpha - \alpha_s + \sin\delta\sin\delta_s >\right]$$

$$\ddot{\delta}_g = -\mu\frac{r_e}{r}\left(\frac{1}{r_p^3} - \frac{1}{r_e^3}\right) < \sin\delta\cos\delta_s\cos(\alpha - \alpha_s) - \cos\delta\sin\delta_s$$

$$\ddot{\alpha}_g = -\mu\frac{r_e}{r}\left(\frac{1}{r_p^3} - \frac{1}{r_e^3}\right)\cos\delta_s\sin(\alpha - \alpha_s)$$

$$r_p = \{r^2 + r_e^2 - 2r\,r_e\,[\cos\delta\cos\delta_s\cos(\alpha - \alpha_s) + \sin\delta\sin\delta_s]\}^{1/2} \tag{14}$$

Finally substituting Eq. (13) into Eq. (5) gives the following approximation of the topocentric range rate:

$$\dot{\rho} \approx a' + b'\sin(\varphi_0 - \alpha_0 + \dot{\varphi}_0 t) + c'\cos(\varphi_0 - \alpha_0 + \dot{\varphi}_0 t) + d't + e'\,t\sin(\varphi_0 - \alpha_0 + \dot{\varphi}_0 t) + f'\,t\cos(\varphi_0 - \alpha_0 + \dot{\varphi}_0 t) \tag{15a}$$

where

$$a' = \dot{r}_0 - z_s\dot{\delta}_0\cos\delta_0$$

$$b' = r_s(\dot{\varphi}_0 - \dot{\alpha}_0)\cos\delta_0$$

$$c' = r_s\dot{\delta}_0\sin\delta_0$$

$$d' = r_0\left(\dot{\delta}_0^2 + \dot{\alpha}_0^2\cos^2\delta_0\right) + \ddot{r}_{g0} + z_s\left(\dot{\delta}_0^2\sin\delta_0 + \dot{\alpha}_0^2\cos^2\delta_0\sin\delta_0 + 2\frac{\dot{r}_0}{r_0}\dot{\delta}_0\cos\delta_0 - \ddot{\delta}_{g0}\cos\delta_0\right)$$

$$e' = r_s\left(-\dot{\varphi}_0\dot{\delta}_0\sin\delta_0 + 2\frac{\dot{r}_0}{r_0}\dot{\alpha}_0\cos\delta_0 - \ddot{\alpha}_{g0}\right)$$

$$f' = r_s\left(-\dot{\varphi}_0\dot{\alpha}_0\cos\delta_0 + \dot{\alpha}_0^2\cos^3\delta_0 + \dot{\delta}_0^2\cos\delta_0 - 2\frac{\dot{r}_0}{r_0}\dot{\delta}_0\sin\delta_0 + \sin\delta_0\ddot{\delta}_{g0}\right) \tag{15b}$$

V. Range Rate Partials and the Validity of the Approximations

From Eq. (15) it is very easy to obtain an approximation for the partial derivatives of the topocentric range rate with respect to the spacecraft coordinates at some epoch r_0, δ_0, α_0, $\dot{r}_0$, $\dot{\delta}_0$, and $\dot{\alpha}_0$, and also with respect to the station location coordinates r_s, z_s and the longitude λ, since as will be shown later $\partial/\partial\lambda = \partial/\partial\varphi$. Before any analysis is performed with partials obtained in this way, it would be desirable to have some idea of the validity of the approximation. To obtain a sample of such information, the procedure outlined in Table 1 was used.

The time behavior of some of the coefficients obtained by fitting $\Delta\dot{\rho}(t)$, generated by a station longitude error of 10^{-6} rad, is shown in Fig. 3 for a particular *Viking* type II trajectory. To easily see how well the coefficients generated in this way agree with the corresponding coefficients predicted from Eq. (15), Fig. 3 actually plots the ratio of these two sets of coefficients, or a quantity which is a function of this ratio.

If the expression given in Eq. (15) were an equality and not an approximation, the coefficients determined from the fit should be independent of the amount of data in the fit and should agree with the coefficients predicted from Eq. (15). An examination of Fig. 3 shows that the C and E coefficients determined by the fit are fairly constant over the 10-day interval and agree reasonably well with the coefficients predicted from Eq. (15). Unfortunately, the B and F coefficients determined by the fit, although initially agreeing fairly well with the coefficient predicted from Eq. (15), show a substantial time variation after a few days. The time variation of this parameter severely degrades any error

analysis which involves a station longitude error and the B and F terms of Eq. (15), when more than a few days of data are under consideration.

The abnormal behavior of the first point on three of the curves shown in Fig. 3 probably receives contributions from both the fact that there are only a small number of points after the first day, and that the time is not large enough to give strength to the last three terms.

Computations similar to those used in generating Fig. 3 were made for perturbations in the spacecraft initial coordinates and the remaining station coordinates. Table 2 contains the coefficients obtained from fitting three and ten day's worth of $\Delta\dot{\rho}(t)$ data generated in this way. For comparison purposes the corresponding coefficients predicted by Eq. (15) are also included in Table 2.

An examination of Table 2 shows that for its particular type of trajectory, an error analysis based upon Eq. (15) may be very unreliable in several parameters if more than a few days worth of data is under consideration.

The various sets of $\Delta\dot{\rho}(t)$ used in Table 2 and generated by changes in spacecraft and station coordinates were also fitted by the following polynomial:

$$
\begin{aligned}
&A + B\sin(\varphi - \alpha + \dot{\varphi}\,t) + C\cos(\varphi - \alpha + \dot{\varphi}\,t)\\
&\quad + D\,t + E\,t\sin(\varphi - \alpha + \dot{\varphi}\,t)\\
&\quad + Ft\cos(\varphi - \alpha + \dot{\varphi}\,t)\\
&\quad + G\,t^2 + H\,t^2\sin(\varphi - \alpha + \dot{\varphi}\,t)\\
&\quad + I\,t^2\cos(\varphi - \alpha + \dot{\varphi}\,t)\\
&\quad + J\sin[2(\varphi - \alpha + \dot{\varphi}\,t)]\\
&\quad + K\cos[2(\varphi - \alpha + \dot{\varphi}\,t)]\\
&\quad + Lt\sin[2(\varphi - \alpha + \dot{\varphi}t)]\\
&\quad + M\,t\cos[2(\varphi - \alpha + \dot{\varphi}\,t)]
\end{aligned}
$$

where the $2(\varphi - \alpha + \dot{\varphi}\,t)$ terms were suggested by Eq. (2). The first six coefficients obtained from this fit had substantially less time behavior than the coefficients in Table 2 and the larger coefficients in each case agreed to at least 4 figures with the value predicted by Eq. (15), and almost all of the remaining non-zero coefficients agree to a few percent.

VI. Selection of the Dominant Terms in the Range-Rate Approximation

The purpose of finding analytical approximations to the range, range rate, and their associated partial derivatives with respect to the spacecraft and station coordinates is to gain a better understanding of the physical situation. If the range-rate approximation given by Eq. (15) is used, the understanding is clouded by the fact that almost all of the coefficients in Eq. (15) are functions of almost all of the spacecraft and station coordinates. The ease of understanding would be considerably improved if it were possible to isolate which terms in Eq. (15) contribute a negligible amount to an error analysis and may be deleted. To facilitate such a procedure, it is convenient to generate a quantity which compares the change in a particular coefficient of Eq. (15) due to a change in a particular spacecraft or station coordinate with the maximum change in this same coefficient due to a change in any spacecraft or station coordinate. For example, for the trajectory and changes in the nominal spacecraft and station coordinates used in Table 2, the change in e due to a change in r is $\Delta e(\Delta r) = 8 \times 10^{-14}$, and the maximum change in e, $\Delta e_{\max}$, due to the change in any of the spacecraft and station coordinates comes from a change in α, so that the quantity of interest is $\Delta e(\Delta r)/\Delta e_{\max}(\Delta\alpha) = 0.4$. Table 3 gives this ratio for all coefficients and changes in spacecraft or station coordinates for the nominals and changes used in Table 2.

We will make the rather arbitrary decision that if a particular element in the above table is less than 5% as big as the largest element in either its corresponding row or column, the partial derivative associated with that element may be ignored in an error analysis. This of course may change for different trajectories but probably not substantially. For example, since the (3,2) element in Table 3 is much less than the largest element in the $\Delta b'/\Delta b'_{\max}$ column or $\Delta\alpha$ row, the $\partial b/\partial\alpha$ partial may be ignored. Using this criterion allows the range-rate approximation given by Eq. (15) to be considerably simplified to the form given below:

$$
\begin{aligned}
\dot{\rho} \approx\ & a'' + b''\sin(\varphi_0 - \alpha_0 + \dot{\varphi}_0\,t)\\
&+ c''\cos(\varphi_0 - \alpha_0 + \dot{\varphi}_0\,t) + d''\,t\\
&+ e''\,t\sin(\varphi_0 - \alpha_0 + \dot{\varphi}_0\,t)\\
&+ f''\,t\cos(\varphi_0 - \alpha_0 + \dot{\varphi}_0\,t) \qquad (16a)
\end{aligned}
$$

where

$$a'' = \dot{r}_0 - z_s\,\dot{\delta}_0 \cos\delta_0$$

$$b'' = r_s\,\dot{\varphi}_0 \cos\delta_0$$

$$c'' = 0$$

$$d'' = r_0\,(\dot{\delta}_0^2 + \dot{\alpha}_0^2 \cos^2\delta_0) + \ddot{r}_{g0}$$

$$e'' = -\,r_s\,\dot{\varphi}_0\,\dot{\delta}_0 \sin\delta_0$$

$$f'' = -\,r_s\,\dot{\varphi}_0\,\dot{\alpha}_0 \cos\delta_0$$

$$\ddot{r}_{g0} = -\,\mu\left[\frac{r_0}{r_{p0}^3} - r_e\left(\frac{1}{r_{p0}^3} - \frac{1}{r_{e0}^3}\right) < \cos\delta_0 \cos\delta_{s0} \times \cos(\alpha_0 - \alpha_{s0}) + \sin\delta_0 \sin\delta_{s0} >\right] \tag{16b}$$

and the second term in a'' is needed only in computing $\partial\dot{\rho}/\partial z_s$.

VII. Modification of the Trigonometric Arguments

The physical understanding which results from the use of Eq. (16) may be further increased by judiciously choosing the form of trigonometric arguments used in this equation. Recall from Eq. (3) that these quantities had their origin in the term $\varphi - \alpha$, where φ is the angle between the mean vernal equinox of date and the meridian of the tracking station as shown in Fig. 4.

The universal time t_u is related to the quantities in the above figure through the following equation:

$$\omega t_u = H + \omega \cdot 12 \text{ hrs} \tag{17}$$

where the rotation rate of the earth ω is

$$\omega = \frac{2\pi}{86400} = 0.72722 \times 10^{-4} \text{ rad/sec} \tag{18}$$

and when the mean sun crosses the Greenwich meridian it is 12:00 universal time. Clearly the right ascension of the Greenwich meridian as a function of universal time may be written as

$$\theta = \omega t_u + (\alpha_\odot - 180°) \tag{19}$$

The right ascension of the mean sun is given by (Ref. 3)

$$\alpha_\odot = 280°.0755426 + 0°.98564734\,d + 2°.9015 \times 10^{-13}\,d^2 \tag{20}$$

where

$$d = \text{days past Jan. 1, 1950, 0 hrs}$$

The second term in Eq. (20) accounts for the annual motion of the earth about the sun; the third term is extremely small and may be neglected. Substituting Eq. (20) into Eq. (19) yields

$$\theta = (100°.0755426 + 0°.98564734\,d) + \omega t_u$$

From this equation it is easily seen that if the time is measured in units of universal time, the right ascension of Greenwich may be written as

$$\theta = \theta_0 + \dot{\theta}_0\,t$$

where

$$\theta_0 = \text{right ascension of Greenwich at some epoch } t = 0$$

$$\dot{\theta}_0 = (0.72722 + 0.00198) \text{ rad/sec} = 0.7 \text{ rad/sec} \tag{21}$$

Clearly, since

$$\varphi = \theta + \lambda$$

the argument of the trigonometric function in Eq. (16) may be written as

$$\varphi_0 - \alpha_0 + \dot{\varphi}_0\,t = \theta_0 + \lambda - \alpha_0 + \dot{\theta}_0\,t \tag{22}$$

Hamilton and Melbourne (Ref. 1) have shown that at this point in the development it is convenient to specify *a priori* information about α and λ, and to make the following definitions:

$$\left.\begin{aligned} \epsilon_\lambda &= \lambda - \lambda^* = (\text{true—}a\ priori\text{) station longitude} \\ \epsilon_a &= \alpha_0 - \alpha_0{}^* = (\text{true—}a\ priori\text{) spacecraft right ascension} \\ \epsilon &= \epsilon_\lambda - \epsilon_a \end{aligned}\right\} \tag{23}$$

Substituting these equations into Eq. (22) yields

$$\varphi_0 - \alpha_0 + \dot{\varphi}_0\,t = \theta_0 + \lambda^* - \alpha_0{}^* + \epsilon_\lambda - \epsilon_a + \dot{\theta}_0\,t \tag{24}$$

This equation may be considerably simplified if the time t is specified to be measured from a point when the spacecraft crosses the staiton's nominal meridian. Using this particular epoch the first three terms of Eq. (24) cancel, allowing Eq. (16) to be written as

$$\dot{\rho} \approx a'' + b'' \sin(\dot{\theta}_0 t + \epsilon) + c'' \cos(\dot{\theta}_0 t + \epsilon) + d'' t + e'' t \sin(\dot{\theta}_0 t + \epsilon) + f'' t \cos(\dot{\theta}_0 t + \epsilon)$$

where for this, and all future equations, $t = 0$ is understood to occur at a nominal meridian crossing.

Since ϵ is small enough so that ϵ^2 is negligible, the above equation may be rewritten as

$$\dot{\rho} \approx a'' + (b'' - \epsilon c'') \sin \dot{\theta} t + (c'' + \epsilon b'') \cos \dot{\theta} t + d'' t + (e'' - \epsilon f'') t \sin \dot{\theta} t + (f'' + \epsilon e'') t \cos \dot{\theta} t$$

or using Eq. (15b)

$$\dot{\rho} \approx a + b \sin \dot{\theta} t + c \cos \dot{\theta} t + d \dot{\theta} t + e \dot{\theta} t \sin \dot{\theta} t + f \dot{\theta} t \cos \dot{\theta} t \qquad (25a)$$

where

$$a = \dot{r}_0 - z_s \dot{\delta}_0 \cos \delta_0$$

$$b = r_s \dot{\theta} \cos \delta_0$$

$$c = r_s \dot{\theta} \cos \delta_0 [(\lambda - \lambda^*) - (\alpha_0 - \alpha_0^*)]$$

$$d = [r_0 (\dot{\delta}_0^2 + \dot{\alpha}_0^2 \cos^2 \delta_0) + \ddot{r}_{g0}] \frac{1}{\dot{\theta}}$$

$$e = - r_s \{\dot{\delta}_0 \sin \delta_0 - [(\lambda - \lambda^*) - (\alpha_0 - \alpha_0^*)] \dot{\alpha}_0 \cos \delta_0\}$$

$$f = - r_s \{\dot{\alpha}_0 \cos \delta_0 + [(\lambda - \lambda^*) - (\alpha_0 - \alpha_0^*)] \dot{\delta}_0 \sin \delta_0\} \qquad (25b)$$

where the z_s term of the first coefficient is nonnegligible only for the calculation of $\partial \dot{\rho} / \rho z_s$.

VIII. Error Analysis Using the Range-Rate Approximation

As pointed out by Curkendall and McReynolds (Ref. 2), any error analysis based upon Eq. (25) proceeds by treating the coefficients a, b, c, d, e, and f as data points which describe the range-rate observable. However, these "data" points are not independent, and in fact may be highly correlated. The correlations and appropriate weights associated with the coefficients may be found by first taking the partial of $\dot{\rho}$ with respect to $a \rightarrow f$ and forming the information matrix J_a in the usual manner. If data is taken often enough so that summations may be represented by integrals, J_a may be written as

$$J_a = \frac{N}{\sigma_{\dot{\rho}}^2} \frac{1}{\varphi} \begin{bmatrix} \int_p d\varphi & \int_p \sin\varphi \, d\varphi & \int_p \cos\varphi \, d\varphi & \int_p \varphi \, d\varphi & \int_p \varphi \sin\varphi \, d\varphi & \int_p \varphi \cos\varphi \, d\varphi \\ & \int_p \sin^2\varphi \, d\varphi & \int_p \sin\varphi \cos\varphi \, d\varphi & \int_p \varphi \sin\varphi \, d\varphi & \int_p \varphi \sin^2\varphi \, d\varphi & \int_p \varphi \sin\varphi \cos\varphi \, d\varphi \\ & & \int_p \cos^2\varphi \, d\varphi & \int_p \varphi \cos\varphi \, d\varphi & \int_p \varphi \sin\varphi \cos\varphi \, d\varphi & \int_p \varphi \cos^2\varphi \, d\varphi \\ & \text{sym.} & & \int_p \varphi^2 \, d\varphi & \int_p \varphi^2 \sin\varphi \, d\varphi & \int_p \varphi^2 \cos\varphi \, d\varphi \\ & & & & \int_p \varphi^2 \sin^2\varphi \, d\varphi & \int_p \varphi^2 \sin\varphi \cos\varphi \, d\varphi \\ & & & & & \int_p \varphi^2 \cos^2\varphi \, d\varphi \end{bmatrix} \qquad (26)$$

where

$\varphi = \dot{\theta}_0 t$

$\sigma_{\dot{\rho}}$ = variance of the white noise associated with the range-rate measurements

N = number of range-rate data points

$\int_p$ indicates that the integral extends over the full tracking interval, but has a non-zero contribution only when data is being taken

In using the six coefficients $a \rightarrow f$ as data points, the orbit determination solution filter accepts changes in these coefficients which have been generated in some manner, and modifies six parameters from among the nine spacecraft and station coordinates so that the range-rate observable is changed as little as possible. For example, if the effect of the ionosphere on the range-rate observable could be represented by an error in the c parameter, a solution for the spacecraft state would make a compensating error in the right ascension of the space-

craft, so that the value of $\dot{\rho}(t)$ is best preserved. Using the classical least-squares technique this solution procedure may be represented by the following equation:

$$\Delta \mathbf{x} = [A^T WA]^{-1} A^T W \, \Delta \mathbf{a} \tag{27}$$

where

$\Delta \mathbf{x}$ = the solution vector for up to six parameters selected from among the spacecraft and station coordinates

$\Delta \mathbf{a}$ = a vector representing changes or residuals in the coefficients $a \rightarrow f$ which have been generated in some manner

$W = J_a$ = weighting matrix for the coefficients $a \rightarrow f$ which are being treated as data

$$A = \frac{\partial \mathbf{a}}{\partial \mathbf{x}}$$

The matrix of partials, A, is obtained by selecting columns from the matrix, A^*, whose elements are obtained by differentiating Eq. (25b) and which is given below:

$$A^* = \frac{\partial (a, b, c, d, e, f)}{\partial (r, \delta, \alpha, \dot{r}, \dot{\delta}, \dot{\alpha}, r_s, \lambda, z_s)}$$

$$= \begin{bmatrix} 0 & 0 & 0 & 1 & 0 & 0 & 0 & 0 & -\dot{\delta}_0 \sin \delta_0 \\ 0 & -r_s \dot{\theta} \sin \delta_0 & 0 & 0 & 0 & 0 & \dot{\theta} \cos \delta_0 & 0 & 0 \\ 0 & 0 & -r_s \dot{\theta} \cos \delta_0 & 0 & 0 & 0 & 0 & r_s \dot{\theta} \cos \delta_0 & 0 \\ \xi/\dot{\theta} & \eta/\dot{\theta} & \zeta/\dot{\theta} & 0 & 2r_0 \dot{\delta}_0/\dot{\theta} & 2r_0 \dot{\alpha}_0 \cos^2 \delta_0/\dot{\theta} & 0 & 0 & 0 \\ 0 & -r_s \dot{\delta}_0 \cos \delta_0 & -r_s \dot{\alpha}_0 \cos \delta_0 & 0 & -r_s \sin \delta_0 & 0 & -\dot{\delta}_0 \sin \delta_0 & r_s \dot{\alpha}_0 \cos \delta_0 & 0 \\ 0 & r_s \dot{\alpha}_0 \sin \delta_0 & r_s \dot{\delta}_0 \sin \delta_0 & 0 & 0 & -r_s \cos \delta_0 & -\dot{\alpha}_0 \cos \delta_0 & -r_s \dot{\delta}_0 \sin \delta_0 & 0 \end{bmatrix} \tag{28}$$

where

$$\xi = \partial \ddot{r}_{g0}/\partial r \,|_0 + (\dot{\delta}_0^2 + \dot{\alpha}_0^2 \cos^2 \delta_0)$$

$$\eta = \partial \ddot{r}_{g0}/\partial \delta \,|_0 - 2r_0 \dot{\alpha}_0^2 \cos \delta_0 \sin \delta_0$$

$$\zeta = \partial \ddot{r}_{g0}/\partial \alpha \,|_0$$

The partials of the gravitation acceleration with respect to the position of the spacecraft may be obtained by using the first and last of Eq. (14) and are

$$\frac{\partial \ddot{r}_g}{\partial r}\bigg|_0 = \frac{\mu}{r_{p0}^3}(2 - 3 \sin^2 \psi_0)$$

$$\frac{\partial \ddot{r}_g}{\partial \delta}\bigg|_0 = \mu r_e \cos \sigma \left[\left(\frac{1}{r_p^3} - \frac{1}{r_e^3}\right) - 3\frac{r_0}{r_{p0}^5}(r_0 - r_e \cos \chi_0)\right]$$

$$\frac{\partial \ddot{r}_g}{\partial \alpha}\bigg|_0 = \mu r_e \cos \delta_0 \cos \delta_s \sin (\alpha - \alpha_s) \left[-\left(\frac{1}{r_{p0}^3} - \frac{1}{r_{e0}^3}\right) + 3\frac{r_0}{r_{p0}^5}(r_0 - r_e \cos \chi_0)\right] \tag{29}$$

where

$$\cos \sigma = -\sin \delta \cos \delta_s \cos (\alpha - \alpha_s) + \cos \delta \sin \delta_s$$

$$\cos \chi = \cos \delta \cos \delta_s \cos (\alpha - \alpha_s) + \sin \delta \sin \delta_s$$

$$\sin \psi = r_e/r_p \sin \chi$$

χ = sun–earth–spacecraft angle

ψ = earth–spacecraft–sun angle

The curves of constant $\partial \ddot{r}_g/\partial r$ have been shown before by Curkendall and McReynolds (Ref. 2), but will be included here as Fig. 5 for completeness. The curves of constant $\partial \ddot{r}_g/\partial \delta$ and $\partial \ddot{r}_g/\partial \alpha$ are not as easily obtained because of their dependence on δ, δ_s α, and α_s. However, some idea of the behavior of the constant $\partial \ddot{r}_g/\partial \delta$ and $\partial \ddot{r}_g/\partial \alpha$ curves may be obtained from Figs. 6 and 7 where the spacecraft declination has been specified to be zero. To obtain some feeling of how the gravitational field may influence the orbit determination solution for various missions, trajectories representative of *Mariner* Venus–Mercury 1973 and *Viking* 1975 have been included in Figs. 5, 6, and 7.

IX. Error Analysis for the Spacecraft State

Almost all orbit determination error analysis has as its goal an investigation of errors in the spacecraft state. Using the approximation techniques developed here and the classical least-squares method, the error analysis of the full spacecraft state, resulting from range-rate-only information, would proceed from the following equation:

$$\begin{bmatrix} \Delta r \\ \Delta\delta \\ \Delta\alpha \\ \Delta\dot{r} \\ \Delta\dot{\delta} \\ \Delta\dot{\alpha} \end{bmatrix} = \{A_s^T J_a A_s\}^{-1} A_s^T J_a \begin{bmatrix} \Delta a \\ \Delta b \\ \Delta c \\ \Delta d \\ \Delta e \\ \Delta f \end{bmatrix} \tag{30}$$

where A_s is composed of the first six columns of the A^* matrix in Eq. (28). The state covariance is easily found by taking the inverse of the terms in braces in the above equation. As before $\Delta a \rightarrow \Delta f$ represented changes in the coefficients $a \rightarrow f$ produced by some physical phenomena, which degrades the range-rate observable. For example, if one wanted to investigate the errors in the spacecraft state which result from station location errors, the $\Delta a \rightarrow \Delta f$ which reflect this situation would be obtained by multiplying the partials of $a \rightarrow f$ with respect to r_s, λ, z_s (i.e., the last three columns of A^* in Eq. 28) by Δr_s, $\Delta\lambda$, and Δz_s, respectively.

Since A_s is a 6×6 matrix when the full spacecraft state is being included in the solution, the determination of $\Delta r \rightarrow \Delta\alpha$ is unique and Eq. (30) may be written as

$$\begin{bmatrix} \Delta r \\ \cdot \\ \cdot \\ \cdot \\ \Delta\dot{\alpha} \end{bmatrix} = A_s^{-1} \begin{bmatrix} \Delta a \\ \cdot \\ \cdot \\ \cdot \\ \Delta f \end{bmatrix}$$

Because of the many zero elements contained in A_s, it may be conveniently inverted. Hence, the changes in the full spacecraft state which result from changes in the six parameters describing the range-rate observable may easily be obtained from the following equation:

$$\begin{bmatrix} \Delta r \\ \Delta\delta \\ \Delta\alpha \\ \Delta\dot{r} \\ \Delta\dot{\delta} \\ \Delta\dot{\alpha} \end{bmatrix} = \frac{1}{\dot{\theta} r_s} \begin{bmatrix} 0 & \dfrac{2r\dot{\alpha}^2 \sin^2\delta\cos\delta + \dfrac{\partial d}{\partial\delta}\sin\delta - 2r\dot{\delta}^2\cos\delta}{\partial d/\partial r \sin^2\delta} & \dfrac{\dfrac{\partial d}{\partial\alpha}\sin\delta - 2r\dot{\alpha}\dot{\delta}\cos^3\delta}{\partial d/\partial r \cos\delta\sin\delta} & \dfrac{\dot{\theta}^2 r_s}{\partial d/\partial r} & \dfrac{2r\dot{\delta}\dot{\theta}}{\partial d/\partial r \sin\delta} & \dfrac{2r\dot{\theta}\cos\delta\dot{\alpha}}{\partial d/\partial r} \\ 0 & -1/\sin\delta & 0 & 0 & 0 & 0 \\ 0 & 0 & -1/\cos\delta & 0 & 0 & 0 \\ \dot{\theta} r_s & 0 & 0 & 0 & 0 & 0 \\ 0 & \dot{\delta}/\tan\delta\sin\delta & \dfrac{\dot{\alpha}}{\sin\delta} & 0 & -\dot{\theta}/\sin\delta & 0 \\ 0 & \dot{\alpha}/\cos\delta & -\dot{\delta}\tan\delta/\cos\delta & 0 & 0 & -\dot{\theta}/\cos\delta \end{bmatrix} \begin{bmatrix} \Delta a \\ \Delta b \\ \Delta c \\ \Delta d \\ \Delta e \\ \Delta f \end{bmatrix} \tag{31}$$

When a range point is available in addition to the range-rate data, a cursory error analysis for the δ, α, $\dot{r}$, $\dot{\delta}$, $\dot{\alpha}$ portion of the spacecraft state may be performed by assuming the geocentric range to be known and deleting it from the solution. This technique is expressed in the following equation:

$$\begin{bmatrix} \Delta\delta \\ \Delta\alpha \\ \Delta\dot{r} \\ \Delta\dot{\delta} \\ \Delta\dot{\alpha} \end{bmatrix} = \{A_r^T J_a A_r\}^{-1} A_r J_a \begin{bmatrix} \Delta a \\ \Delta b \\ \Delta c \\ \Delta d \\ \Delta e \\ \Delta f \end{bmatrix} \tag{32}$$

where A_r is a 6×5 matrix composed of the second through sixth columns of A^* contained in Eq. (28). This system is over-determined and the solution must be obtained by using least-squares techniques.

The classical A^TWA form of the least-squares problem has been used in the last two sections because it was felt that it was probably very familiar to most potential readers. However, the inversion of A^TWA, generated by using the approximation discussed here may have numerical difficulties which would require recasting the problem in its square-root form.

X. Summary and Discussion

The preceding sections have been concerned with arriving at a first-order expansion of the topocentric range rate in terms of r_s/r, z_s/r, and time, which may be put in a form which is convenient to use for error analysis. Although at times the development was somewhat laborious and involved, the resulting error analysis procedure is quite easy to use. For example, over the range of validity of the approximations, a great deal of the state only–range rate only error analysis can be performed analytically. Although this technique may be used to obtain quantitative estimates regarding the inherent accuracy of particular orbit determination problems, it should always be borne in mind that the primary reason for undertaking the development was to provide a vehicle which can promote a better physical understanding of the orbit determination process.

The limiting feature of this approximation technique is the relatively short time periods over which it is reliably applicable. For example, for the *Viking* trajectory used here as an example, the method is severely degraded in many of the parameters after only a few days. This feature is particularly irritating when one wants to determine the information content contained within long arcs of data. It may be possible to develop techniques similar to the one achieved here, but applicable to long arc solutions, by using the closed form f and g expansions of celestial mechanics.

References

1. Hamilton, T. W., and Melbourne, W. G., "Information Content of a Single Pass of Doppler Data from a Distant Spacecraft," in *The Deep Space Network,* Space Programs Summary 37-39, Vol. III, pp. 18–23. Jet Propulsion Laboratory, Pasadena, Calif., May 31, 1966.
2. Curkendall, D. W., and McReynolds, S. R., "A Simplified Approach for Determining the Information Content of Radio Tracking Data," *J. Spacecraft Rockets,* Vol. 6, No. 5, pp. 520–525, May 1969.
3. Holdridge, D. B., *Space Trajectories Program for the IBM 7090 Computer,* Technical Report 32-223, p. 56. Jet Propulsion Laboratory, Pasadena, Calif., Mar. 2, 1962.

Table 1. Procedure for verifying Eq. (15)

Step	Procedure
1	From a nominal trajectory, with only the mass of the sun $\neq 0$, obtain the topocentric range rate from one station every hour for 10 days.
2	Same as step 1, except perturb either the initial conditions of the spacecraft or the station location coordinates by some amount.
3	Difference the range rate values obtained in steps 1 and 2 to obtain $\Delta\dot{\rho}(t)$.
4	Starting with one day's data and then increasing the data arc a day at a time, make a least-squares fit of $\Delta\dot{\rho}(t)$ to the following polynomial: $A + B \sin(\varphi - \alpha + \dot{\varphi}t) + C \cos(\varphi - \alpha + \dot{\varphi}t) + D\,t + E\,t \sin(\varphi - \alpha + \dot{\varphi}t) + F\,t \cos(\varphi - \alpha + \dot{\varphi}t)$

Table 2. Changes in $a \rightarrow f$ resulting from changes in spacecraft and station coordinates

Coordinate change	$\Delta r = 100$ km			$\Delta \delta = 10^{-6}$ rad			$\Delta \alpha = 10^{-6}$ rad		
Coefficient source	Eq. (15)	3-day fit	10-day fit	Eq. (15)	3-day fit	10-day fit	Eq. (15)	3-day fit	10-day fit
$\Delta a'$ or A	—	-0.65×10^{-9}	-0.96×10^{-9}	0.352×10^{-10}	0.303×10^{-10}	0.238×10^{-10}	—	-0.20×10^{-8}	-0.24×10^{-7}
$\Delta b'$ or B	—	0.17×10^{-9}	0.91×10^{-9}	-0.1234×10^{-6}	-0.1235×10^{-6}	-0.1239×10^{-6}	0.417×10^{-10}	0.646×10^{-9}	0.244×10^{-8}
$\Delta c'$ or C	—	0.30×10^{-9}	0.47×10^{-9}	0.112×10^{-9}	0.381×10^{-11}	0.186×10^{-9}	-0.3320×10^{-6}	-0.3311×10^{-6}	-0.3314×10^{-6}
$\Delta d'$ or D	0.2042×10^{-11}	0.2058×10^{-11}	0.2108×10^{-11}	0.6512×10^{-12}	0.6464×10^{-12}	0.6338×10^{-12}	0.4892×10^{-11}	0.4942×10^{-11}	0.5068×10^{-11}
$\Delta e'$ or E	-0.244×10^{-15}	-0.724×10^{-15}	-0.126×10^{-14}	-0.821×10^{-14}	-0.739×10^{-14}	-0.5873×10^{-14}	-0.3176×10^{-13}	-0.3176×10^{-13}	-0.3279×10^{-13}
$\Delta f'$ or F	0.991×10^{-17}	-0.290×10^{-14}	-0.116×10^{-14}	0.109×10^{-13}	0.114×10^{-14}	0.9332×10^{-14}	0.270×10^{-14}	-0.417×10^{-14}	0.536×10^{-14}

Coordinate change	$\Delta \dot{r} = 10^{-6}$ km/s			$\Delta \dot{\delta} = 10^{-14}$ rad/s			$\Delta \dot{\alpha} = 10^{-14}$ rad/s		
Coefficient source	Eq. (15)	3-day fit	10-day fit	Eq. (15)	3-day fit	10-day fit	Eq. (15)	3-day fit	10-day fit
$\Delta a'$ or A	1.00000×10^{-6}	1.000049×10^{-6}	1.00075×10^{-6}	-0.3857×10^{-10}	-0.501×10^{-10}	-0.18×10^{-9}	—	-0.17×10^{-9}	-0.19×10^{-8}
$\Delta b'$ or B	—	-0.14×10^{-10}	-0.72×10^{-10}	—	0.24×10^{-11}	0.45×10^{-10}	-0.455×10^{-10}	0.75×10^{-11}	0.17×10^{-11}
$\Delta c'$ or C	—	-0.24×10^{-10}	-0.48×10^{-10}	0.169×10^{-10}	0.22×10^{-10}	0.213×10^{-10}	—	0.76×10^{-10}	0.11×10^{-12}
$\Delta d'$ or D	0.214×10^{-17}	0.119×10^{-14}	0.515×10^{-14}	0.43557×10^{-13}	0.4384×10^{-13}	0.4462×10^{-13}	0.13859×10^{-12}	0.142×10^{-12}	0.1532×10^{-12}
$\Delta e'$ or E	0.917×10^{-17}	0.58×10^{-16}	0.10×10^{-16}	-0.12354×10^{-15}	-0.1218×10^{-14}	-0.1148×10^{-15}	0.1578×10^{-16}	-0.213×10^{-15}	-0.405×10^{-15}
$\Delta f'$ or F	-0.941×10^{-18}	0.244×10^{-15}	0.18×10^{-16}	-0.3624×10^{-17}	-0.48×10^{-16}	0.529×10^{-17}	-0.3316×10^{-14}	-0.384×10^{-14}	-0.281×10^{-14}

Coordinate change	$\Delta r_s = 10$ m			$\Delta \lambda = 10^{-6}$ rad			$\Delta z_s = 10$ m		
Coefficient source	Eq. (15)	3-day fit	10-day fit	Eq. (15)	3-day fit	10-day fit	Eq. (15)	3-day fit	10-day fit
$\Delta a'$ or A	—	-0.16×10^{-11}	-0.88×10^{-11}	—	0.13×10^{-10}	-0.44×10^{-11}	-0.23048×10^{-9}	-0.23058×10^{-9}	-0.2308×10^{-9}
$\Delta b'$ or B	0.6827×10^{-6}	0.6827×10^{-6}	0.6829×10^{-6}	-0.4166×10^{-10}	-0.554×10^{-10}	-0.193×10^{-10}	—	0.13×10^{-10}	0.13×10^{-10}
$\Delta c'$ or C	0.856×10^{-10}	0.107×10^{-9}	0.359×10^{-10}	0.33196×10^{-7}	0.33200×10^{-7}	0.33210×10^{-7}	—	0.32×10^{-13}	0.23×10^{-13}
$\Delta d'$ or D	—	-0.49×10^{-16}	-0.90×10^{-17}	—	0.14×10^{-18}	0.16×10^{-16}	0.31731×10^{-16}	0.323×10^{-16}	0.339×10^{-16}
$\Delta e'$ or E	-0.558×10^{-14}	-0.683×10^{-14}	-0.847×10^{-14}	0.2957×10^{-13}	0.2989×10^{-13}	-0.3068×10^{-13}	—	-0.15×10^{-17}	-0.15×10^{-17}
$\Delta f'$ or F	-0.608×10^{-13}	-0.613×10^{-13}	-0.630×10^{-13}	-0.3078×10^{-14}	-0.3342×10^{-14}	-0.4121×10^{-14}	—	-0.12×10^{-17}	-0.10×10^{-17}

Table 3. The quantity used in selecting the dominate terms for error analysis

Coordinate	$\Delta a'/\Delta a'_{max}$	$\Delta b'/\Delta b'_{max}$	$\Delta c'/\Delta c'_{max}$	$\Delta d'/\Delta d'_{max}$	$\Delta e'/\Delta e'_{max}$	$\Delta f'/\Delta f'_{max}$
Δr	—	—	—	0.4	1×10^{-2}	2×10^{-3}
$\Delta \delta$	0.4×10^{-4}	0.4	0.3×10^{-1}	1	0.4	0.2
$\Delta \alpha$	—	0.6×10^{-4}	1	1	1	0.5×10^{-1}
$\Delta \dot{r}$	1	—	—	0.4×10^{-6}	0.3×10^{-3}	0.2×10^{-4}
$\Delta \dot{\delta}$	0.4×10^{-9}	—	0.7×10^{-4}	0.8×10^{-2}	0.3×10^{-1}	0.7×10^{-4}
$\Delta \dot{\alpha}$	—	0.6×10^{-4}	—	2×10^{-2}	0.3×10^{-3}	0.5×10^{-1}
Δr_s	—	1	0.3×10^{-3}	—	0.2×10^{-2}	1
$\Delta \lambda$	—	0.6×10^{-4}	1	—	1	0.5×10^{-1}
Δz_s	0.2×10^{-3}	—	—	0.6×10^{-5}	—	—

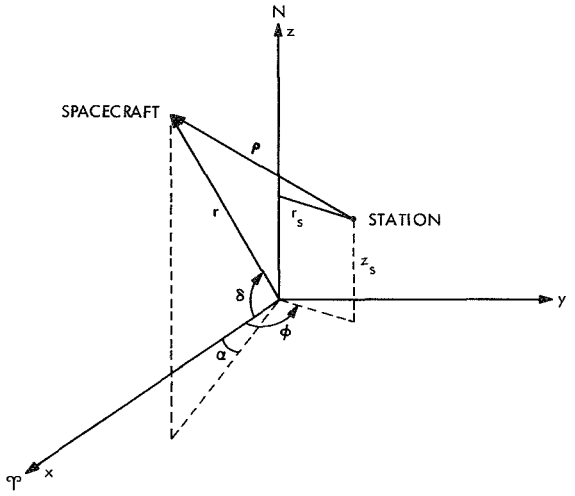

Fig. 1. Topocentric range in terms of spacecraft and station coordinates

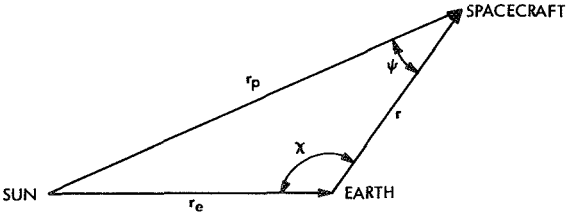

Fig. 2. Relative positions of the sun, earth, and spacecraft

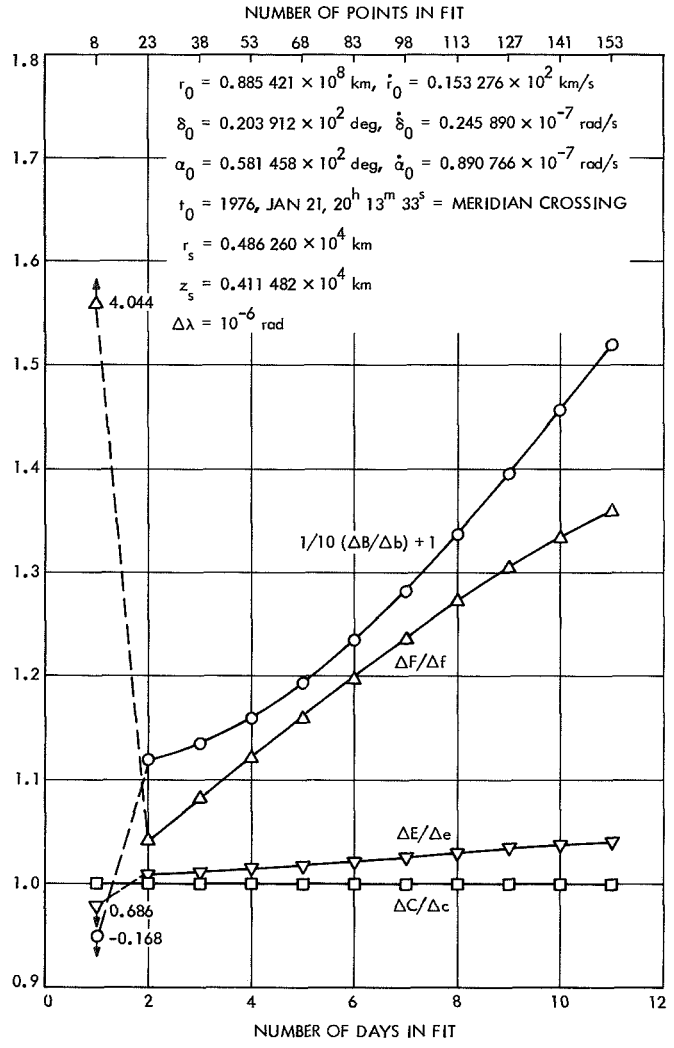

Fig. 3. Time behavior of six parameter fits for $\Delta\lambda = 10^{-6}$ rad

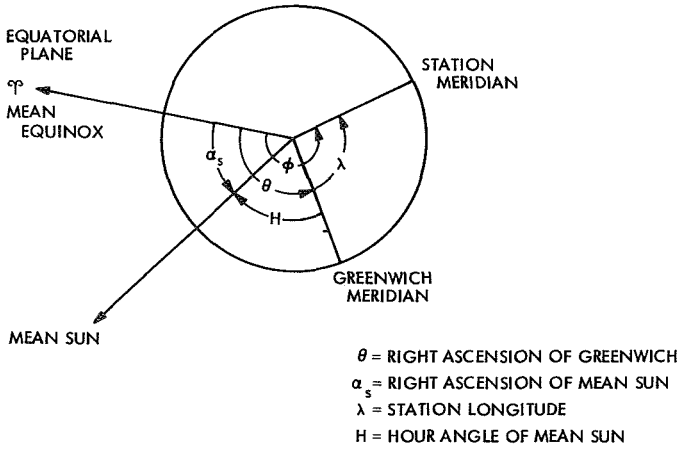

Fig. 4. Angles pertinent in determining behavior of ϕ

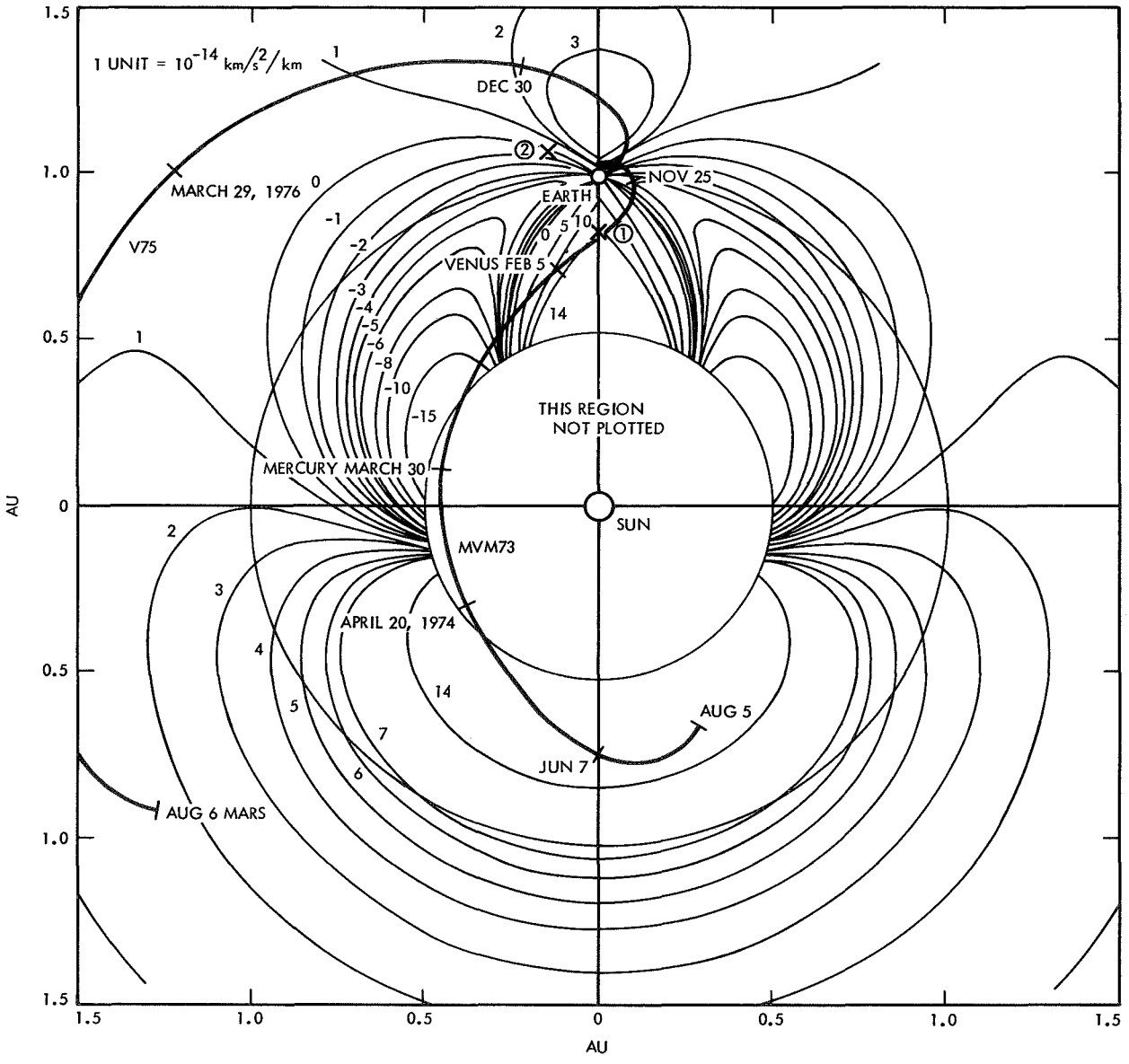

Fig. 5. Partial derivative of the gravitational acceleration of *r* with respect to *r*

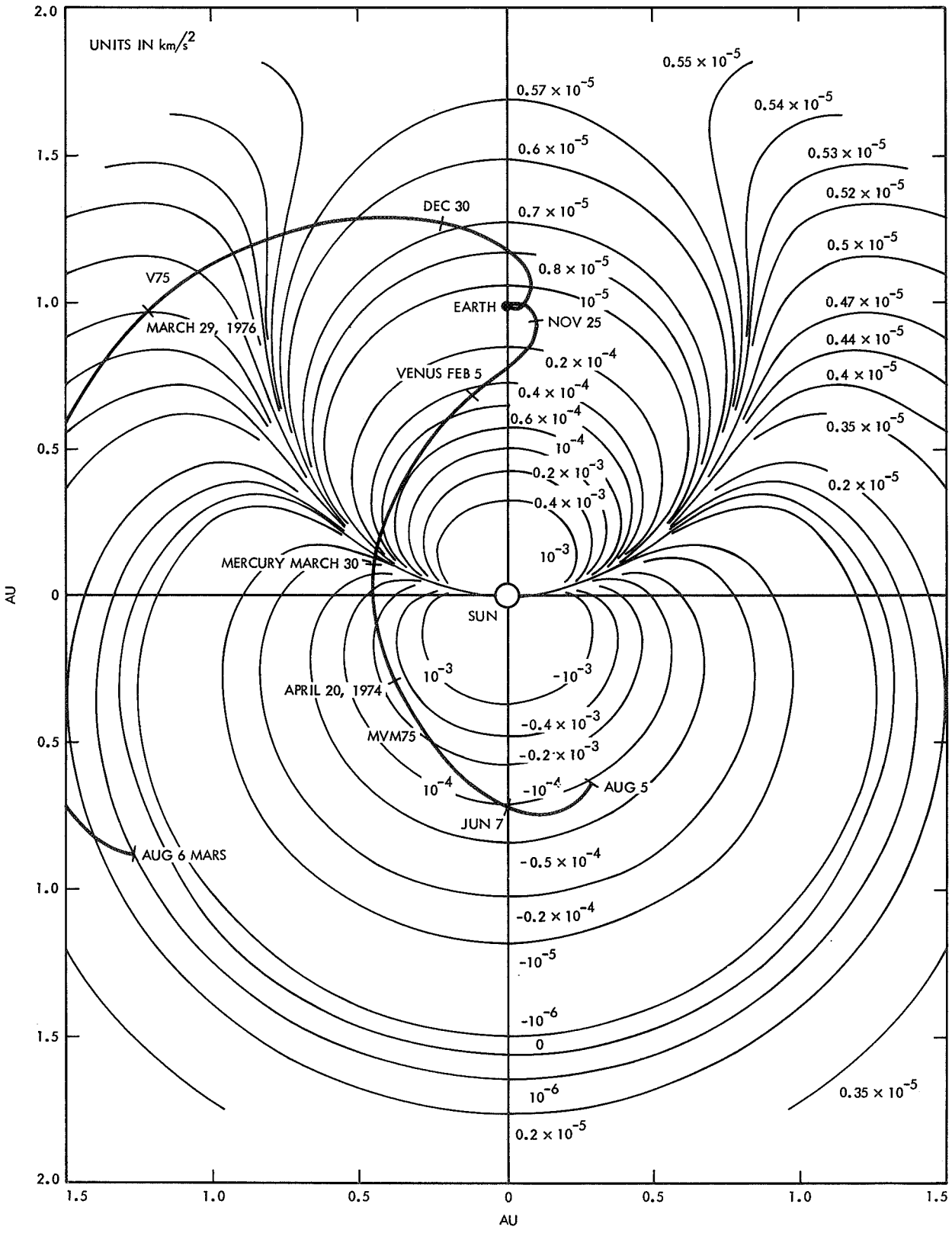

Fig. 6. Partial derivative of the gravitational acceleration of r with respect to δ divided by sin δ_s, when $\delta = 0$

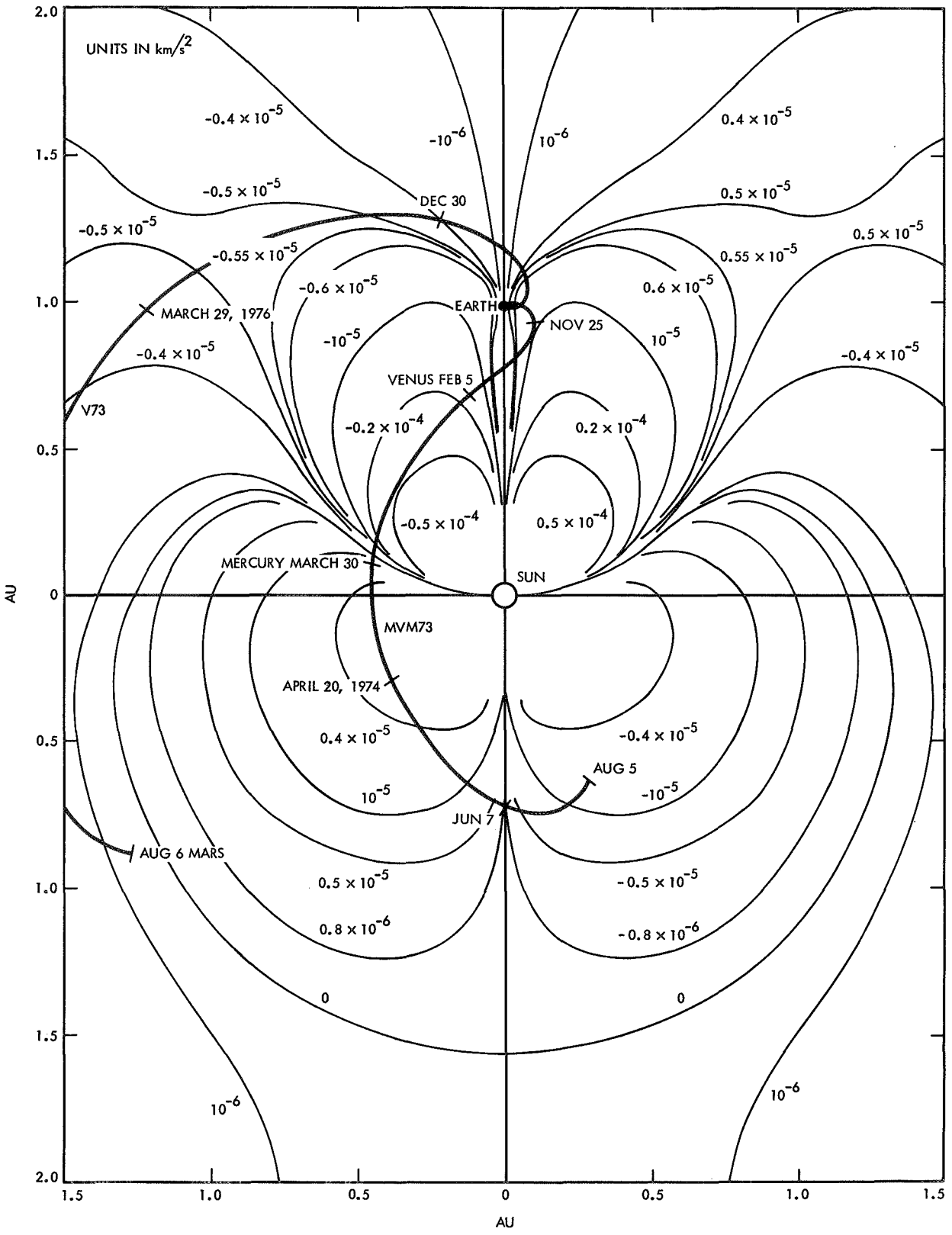

Fig. 7. Partial derivative of the gravitational acceleration of r with respect to α divided by cos δ_s, when $\delta = 0$

Estimating the Parameters of the Distribution of a Mixture of Two Poisson Populations

I. Eisenberger
Communications Systems Research Section

If a random variable is such that, with probability p, it comes from a Poisson distributed population with parameter γ_1 and, with probability $(1 - p)$, it comes from a Poisson-distributed population with parameter γ_2, its density function is given by

$$g(x) = \frac{p\gamma_1^x e^{-\gamma_1} + (1-p)\gamma_2^x e^{-\gamma_2}}{x!}, \qquad x = 0,1,2,\cdots$$

The problem of estimating p, γ_1, and γ_2 is considered with respect to a DSIF application involving certain types of equipment for which the density function of time to failure obeys the exponential law.

I. Introduction

The general purpose of this article is to consider the problem of estimating the parameters of the distribution of a mixture of two Poisson populations. In particular, the method used in estimating the parameters will be applied to a practical problem arising in DSIF subsystems reliability.

Suppose one has M pieces of equipment, or devices, and the following are known:

(1) The distribution of the failure time of m_1 of these devices obeys the exponential law, $\lambda_1 \exp(-\lambda_1 t)$.

(2) The distribution of the failure time for the remaining $m_2 = M - m_1$ devices obeys the exponential law $\lambda_2 \exp(-\lambda_2 t)$.

(3) Each device can be repaired after failure and put back into service with no change in its operating characteristics.

The parameters m_1, λ_1 and λ_2 are unknown and it is desired to estimate these values from the failure information gained by operating the devices simultaneously for a given length of time, T.

It will be seen that by a suitable choice of a statistical model the problem of estimating m_1, λ_1 and λ_2 is transformed into that of estimating the parameters of the distribution of a mixture of two Poisson populations.

II. Distribution of a Mixture of Two Poisson Populations

If a random variable is such that, with probability p, it comes from a population which is Poisson distributed with parameter γ_1, and with probability $1 - p$ it comes from a population which is also Poisson distributed but with parameter γ_2, then its probability density function is given by

$$g(x) = \frac{p\gamma_1^x e^{-\gamma_1} + (1-p)\gamma_2^x e^{-\gamma_2}}{x!}, \qquad x = 0,1,2,3,\cdots$$

Here is a simple statistical model which makes use of the well-known fact that the number of failures in time T for a device with an exponential failure law is Poisson distributed with parameter λT. Let us assume that each device was chosen randomly and independently from a large reservoir of devices such that $100p\%$ of them have a failure rate λ_1 and the remainder have a failure rate λ_2. Under this assumption, the number of failures in time T for each device can be considered as a set of M independent observations taken from a population which is distributed as a mixture of two Poissons with parameters p, $\gamma_1 = \lambda_1 T$ and $\gamma_2 = \lambda_2 T$.

It should be observed, first, that $p \neq m_1/M$. In fact, m_1 is itself a random variable with a binomial distribution and, if it were known, m_1/M would be the maximum-likelihood estimate of p in the event that our statistical model described the actual physical situation and we were interested in the value of p for its own sake. As it is, m_1 can be estimated as the nearest integer to $\hat{p}M$.

It should also be noted that the cases of interest in this analysis are those for which, for a given T, the difference between λ_1 and λ_2 is not too great. For example, suppose $\lambda_1 = 0.01$, $\lambda_2 = 0.05$, $T = 500$, $M = 20$ and $m_1 = 14$. Then, after time T, we would have a group of 14 observations clustered about a mean value of 5 with a standard deviation of $\sqrt{5}$, and a group of 6 observations clustered about a mean value of 25 with a standard deviation of 5, and it would be highly unlikely, under the given statistical circumstances, that we would assign a given observation to the wrong group. Thus by knowing m_1 with virtual certainty, we would take m_1/M as an estimate of p (if that is what is desired) $N_1/14T$ as an estimate of λ_1 and $N_2/6T$ as an estimate of λ_2, where N_1 is the total number of failures in time T for the first group of 14 devices and N_2 is the total number of failures in time T for the devices in the second group.

It is only when it is impossible to classify the observations into two such groups with reasonable certainty that our statistical model comes into play. On the other hand, if λ_1 and λ_2 do not differ sufficiently for given T, then what is likely to happen, as we shall see, is that the solutions to the likelihood equations will converge to $\hat{p} = 1$ or 0, $\hat{\lambda}_1 = \hat{\lambda}_2 = N/MT$, where N is the total number of failures for all devices in time T. However, since the difference between the means of the component populations of the mixture is proportional to T, while the standard deviations are proportional to $\sqrt{T}$, then, for T sufficiently large more meaningful estimates can be obtained.

III. Maximum-Likelihood Estimators of p, λ_1 and λ_2

The method of maximum-likelihood (M.L.) will be used to estimate p, γ_1 and γ_2. Then M.L. estimates of λ_1 and λ_2 are given by $\hat{\lambda}_1 = \hat{\gamma}_1/T$, $\hat{\lambda}_2 = \hat{\gamma}_2/T$.

Due to the assumed independence of the observations, the likelihood function can be written as

$$L = \prod_{i=1}^{M} \frac{p\gamma_1^{k_i} e^{-\gamma_1} + (1-p)\gamma_2^{k_i} e^{-\gamma_2}}{k_i!}$$

where k_i is the number of failures in time T for the ith device. Then one has

$$\ell n\, L = \sum_{i=1}^{M} \left\{ -\ell n\, k_i + \ell n \left[p\gamma_1^{k_i} e^{-\gamma_1} + (1-p)\gamma_2^{k_i} e^{-\gamma_2} \right] \right\}$$

$$\frac{\partial \ell n L}{\partial p} = \sum_{i=1}^{M} \frac{A_1(k_i)}{D(k_i)}$$

$$\frac{\partial \ell n L}{\partial \gamma_1} = \sum_{i=1}^{M} \frac{A_2(k_i)}{D(k_i)}$$

$$\frac{\partial \ell n L}{\partial \gamma_2} = \sum_{i=1}^{M} \frac{A_3(k_i)}{D(k_i)}$$

where

$$A_1(k_i) = {\gamma_1}^{k_i} e^{-\gamma_1} - {\gamma_2}^{k_i} e^{-\gamma_2}$$

$$A_2(k_i) = pe^{-\gamma_1}\left(k_i{\gamma_1}^{k_i-1} - {\gamma_1}^{k_i}\right)$$

$$A_3(k_i) = (1-p)e^{-\gamma_2}\left(k_i{\gamma_2}^{k_i-1} - {\gamma_2}^{k_i}\right)$$

$$D(k_i) = k_i!\, g(k_i)$$

Setting the three partial derivatives equal to zero and solving for p, γ_1 and γ_2 provides the M.L. estimates of the parameters.

IV. Estimating p, λ_1 and λ_2 using Real Data

By using random numbers, 17 sets of sample values were generated such that each set can be considered as being taken from a population with density function $g(x)$, for various conditions and parameters. The method used for solving the likelihood equations was as follows.

Let

$$F_1 = \frac{\partial \ell n L}{\partial p}, F_2 = \frac{\partial \ell n L}{\partial \gamma_1}, F_3 = \frac{\partial \ell n L}{\partial \gamma_2}$$

Then, using the initial values $p^{(1)} = p$, $\gamma_1{}^{(1)} = \gamma_1$ and $\gamma_2{}^{(1)} = \gamma_2$, the following system of linear equations were solved in order to obtain the increments Δp, $\Delta\gamma_1$ and $\Delta\gamma_2$.

$$\frac{\partial F_i}{\partial p}\Delta p + \frac{\Delta F_i}{\partial \gamma_1}\Delta\gamma_1 + \frac{\partial F_i}{\partial \gamma_2}\Delta\gamma_2 = -F_i, \qquad i = 1,2,3$$

The above procedure was then repeated with $p^{(2)} = p^{(1)} + k\Delta p\gamma_1{}^{(2)} = \gamma_1{}^{(1)} + k\Delta\gamma_1$ and $\gamma_2{}^{(2)} = \gamma_2{}^{(1)} + k\Delta\gamma_2$, where k is a proportionality factor usually, but not always, taken as one. This iterative procedure was continued until the F_i were all zero or near zero. The final values of p, λ_1 and λ_2 were taken as the estimates. The results are shown in Table 1. It can be seen that for cases 1, 2, 6 and 12, $\hat{p}$ converged to one or zero and $\hat{\lambda}_1 = \hat{\lambda}_2$. However, for each case more satisfactory results were obtained when T was increased.

The large sample variances of the estimators were also computed and given in the last three columns of Table 1.

The author is grateful to Dr. Gary Lorden of Caltech for suggesting the statistical model used in the above analysis.

Table 1. Maximum-likelihood estimates of the parameters of the distribution of a mixture of two Poisson populations and the large sample variances of the estimators

Case	p	λ_1	λ_2	M	T	Maximum likelihood			Large sample		
						$\hat{p}$	$\hat{\lambda}_1$	$\hat{\lambda}_2$	M var. $(\hat{\lambda}_1)$	M var. $(\hat{\lambda}_2)$	M var. $(\hat{p})$
1	0.7	.01	.0125	20	1000	1	.0106	.0106	3.048×10^{-5}	1.527×10^{-4}	8.7234
2	0.7	.01	.0125	40	1000	1	.0109	.0109			
3	0.7	.01	.0125	40	1500	.8366	.0103	.0144	5.285×10^{-6}	2.573×10^{-5}	1.4534
4	0.7	.01	.0125	20	2000	.8811	.0100	.0169	4.552×10^{-6}	2.163×10^{-5}	.6787
5	0.7	.01	.0125	40	2000	.7380	.00953	.0140			
6	0.7	.01	.016	20	500	1	.0110	.0110	1.540×10^{-5}	8.209×10^{-5}	.7323
7	0.7	.01	.016	20	1000	.8089	.00982	.0184	3.114×10^{-6}	1.590×10^{-5}	.1327
8	0.7	.01	.016	20	1500	.7699	.0116	.0182	1.338×10^{-6}	6.569×10^{-6}	.0544
9	0.7	.01	.025	20	500	.7109	.0107	.0249	2.738×10^{-6}	1.858×10^{-5}	.0233
10	0.7	.01	.025	40	500	.7616	.0109	.0258			
11	0.7	.01	.03	20	500	.6156	.0114	.0302	2.027×10^{-6}	1.557×10^{-5}	.0142
12	0.3	.01	.0125	40	1500	0	.0117	.0117	2.603×10^{-5}	6.385×10^{-6}	1.6169
13	0.3	.01	.0125	40	2000	.6131	.0129	.0138	2.116×10^{-5}	5.491×10^{-6}	.7431
14	0.3	.01	.016	20	1500	.2344	.00944	.0157	4.846×10^{-6}	2.040×10^{-6}	.0589
15	0.3	.01	.016	40	1500	.1878	.00950	.0155			
16	0.3	.01	.025	20	500	.3400	.0110	.0225	9.192×10^{-6}	6.396×10^{-6}	.0254
17	0.3	.01	.025	40	500	.3767	.0108	.0227			

Stability Comparison of Three Frequency Synthesizers

R. Meyer
Communications Systems Research Section

The HP 5100A/5110A, Dana 7030, and Fluke 644A synthesizers were evaluated to determine the typical drift and stability that can be expected in a control room environment. All synthesizers were judged equal in short-term drift, and the Dana synthesizer was found to be superior in long-term drift. The HP and the Dana synthesizers were the most stable, while the Fluke synthesizers did not perform reliably.

I. Introduction

The HP 5100A/5110A (0–50 MHz), Dana 7030 (0–11 MHz), and Fluke 644A (0–40 MHz) synthesizers were tested at 5 MHz to determine the typical drift and stability that can be expected in a control room environment. Measurements were taken at normal laboratory room temperatures of 20 to 25°C. The synthesizers were standard units used in the laboratory. A total of eight test runs, numbered in chronological order, were made using the same synthesizers throughout the testing (except the Fluke which eventually failed and required a replacement). By testing two synthesizers simultaneously during each run it was possible to: (1) accurately compare the performance under identical conditions of temperature and electrical disturbance, (2) differentiate between intrinsic and systematic errors in the data and, (3) measure the repeatability of the data, since one unit of the pair would always appear in a subsequent run. Over 245 h of data were taken; the long-term runs averaged about 50 h and the short-term runs required less than an hour to determine the phase shift in a 100-sec interval.

II. System Description

Noise and drift are minimized in the phase detection scheme of Fig. 1 by using Schottky barrier diode double balanced mixers with about a 600 mV p-p S-curve. The 1-kHz filter preceding the chart recorder determines the noise bandwidth. The required 90-deg phase shift between the mixer ports is obtained by using the synthesizer's search control to vary the frequency until a dc null appears at the mixer output, whereupon the search oscillator is switched out, locking in the 90-deg phase shift. The distribution amplifier that supplies the cesium reference has low noise and is AGC'd to minimize AM to PM conversion.

III. Results

Test results are shown in Tables 1 and 2. A section taken from run 8 (Fig. 2) is representative of the long-term runs and shows the diurnal variations of phase with temperature, including two spontaneous perturbations generated by the Fluke synthesizer 2. The first Fluke failed after the fourth run by shifting 5 to 6 Hz off frequency at 5 MHz, therefore making the previous data suspect. The second Fluke, the replacement unit, performed satisfactorily until the last run when two perturbations were observed and were assumed to be internally generated, since corresponding fluctuations did not appear in the adjacent phase plot of the Dana. The Dana's poorest stability occurred at 6:00 pm on Feb. 14, 1971 due to a thermal transient that affected both synthesizers. The Fluke was affected to a lesser extent because of its large thermal mass. Interestingly, during run 5, no phase deviations were detected from the HP or the Dana synthesizers during the severe California earthquake of February 9.

Run 6 (Fig. 3) shows the short-term drift and high-frequency noise of the Dana and HP synthesizers. The initial runs had been somewhat inconsistent; so, beginning with run 5, ground loops were carefully controlled and a Wanlass PD-1410 power line conditioner was added that provided 60 dB isolation of the measurement system from line transients. This improved the data and eliminated large unexplainable data fluctuations in the long-term runs. Even with these precautions the data was slightly more stable during the weekends when there was less activity.

Run 6 also shows that the HP synthesizer exhibited greater high-frequency noise (around 1 Hz) than the Dana. In Ref. 1, p. 58 the phase noise for the Fluke in the 4-100 Hz spectrum was found to be about 6 dB less than the Dana and the HP. Since the Dana uses a digital counting technique in the phase-locked loop of the synthesizer, it was suspected that certain frequency settings on the front panel could cause unusual digital patterns rippling in the phase register and result in a substantial increase of the phase noise. Upon investigation the maximum change in phase noise in a 5 to 100 Hz bandwidth was less than ½ dB when switching from 5,000,000 to 5,000,001 Hz.

IV. Conclusions

Short-term drift. All synthesizers exhibited about the same short-term drift.

Total drift. The Dana exhibited about 2.5 times less drift than the HP and 6.5 times less drift than the Fluke.

Stability. The Dana and the HP exhibited about the same stability but were 5 times more stable than the Fluke.

High-frequency noise. (Centered around 1 Hz) The Dana and the Fluke were about the same but exhibited 5 times less high frequency noise than the HP.

Power line conditioning. It was not determined that power line transients were actually affecting synthesizer phase stability and it is suspected that line conditioning improved the data by merely isolating the voltage sensitive elements of the measuring system.

Reliability. The first Fluke synthesizer failed after the fourth run and its replacement, Fluke 2, produced a spontaneous phase perturbation in the eighth run that reduced the overall stability to 65 times less than the Dana synthesizer.

It was noted during the testing that the Dana selector switches can apparently become dirty and increase the phase noise two to three times. A similar problem has been noted with the HP's wherein the selector switches will not make contact when depressed and repeated actuation is required to successfully operate the switch. Conclusions are summarized in Table 3.

Reference

1. Meyer, R., and Sward, A., "Frequency Generation and Control: The Measurement of Phase Jitter," in *The Deep Space Network*, Space Programs Summary 37-64, Vol. II, pp. 55–58. Jet Propulsion Laboratory, Pasadena, Calif., Aug. 31, 1970.

Table 1. Synthesizer short-term drift measurements (5 MHz)

Run	Synthesizer	Maximum p-p phase shift in 100-sec interval, deg
3	Dana HP	0.17 0.19
4	Dana Fluke 1	0.16 0.45 (data suspect)
6	Dana HP	0.18 0.25
7	Dana Fluke 2	0.22 0.23

Table 2. Synthesizer long-term drift measurements (5 MHz)

Run	Period, h	Synthesizer	Maximum p-p drift, deg	Maximum drift rate millideg/sec	Stability (parts in 10^{13})
1	45	Dana Fluke 1	3.3 30.6	0.15 1.5	0.82 8.2
2	65	Dana HP	8.0 6.5	0.94 1.8	5.2 1.0
5	40	Dana HP	1.8 8.0	0.23 0.45	1.4 2.5
8	92	Dana Fluke 2	2.9 19.0	0.34 1.8 23.0 (Fluke perturbation)	1.9 10.0 130.0 (Fluke perturbation)

Table 3. Typical synthesizer performance

Synthesizer	Max p-p drift, deg	Max drift rate, millideg/sec	Stability	Max p-p phase shift in 100-sec intervals, deg
Dana 7030	3	0.4	2×10^{13}	0.2
HP 5100A/ 5110A	8	0.4	2	0.2
Fluke 644A	20	2.0	10	0.2
Fluke 644A		23.0	130 (due to spontaneous perturbation)	

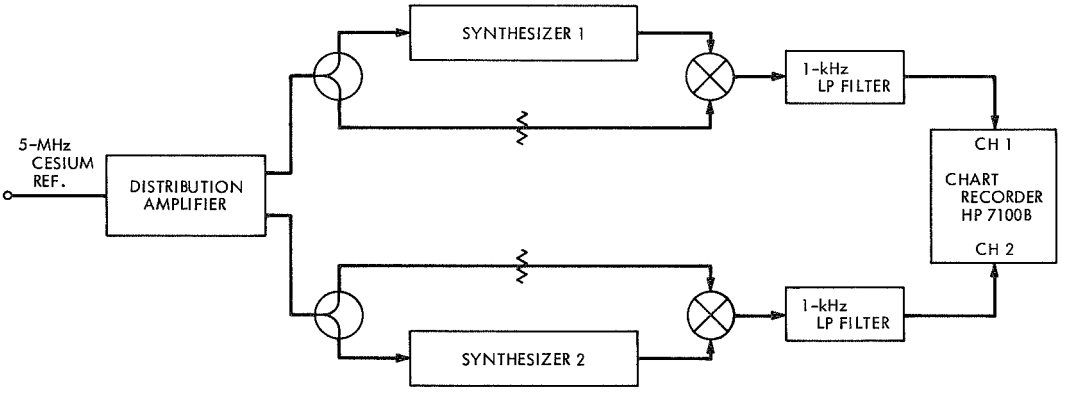

Fig. 1. Synthesizer stability measurement system

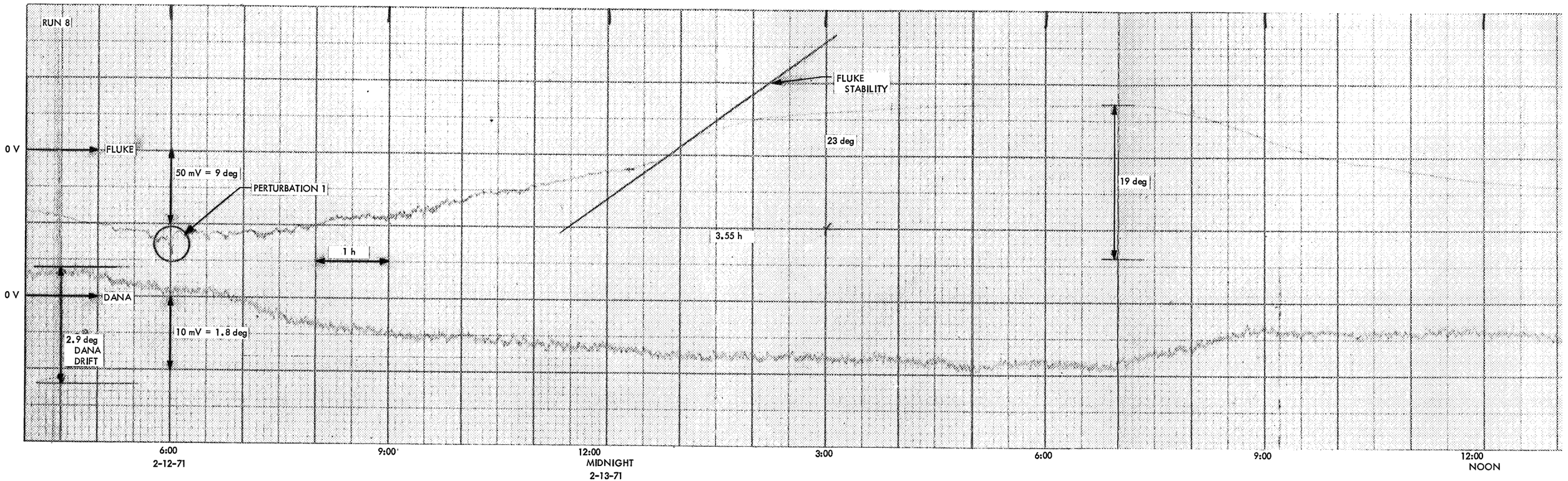
RUN 8
0 V
FLUKE
50 mV = 9 deg
PERTURBATION 1
1 h
FLUKE
STABILITY
23 deg
3.55 h
19 deg
0 V
DANA
10 mV = 1.8 deg
2.9 deg
DANA
DRIFT
6:00
2-12-71
9:00
12:00
MIDNIGHT
2-13-71
3:00
6:00
9:00
12:00
NOON

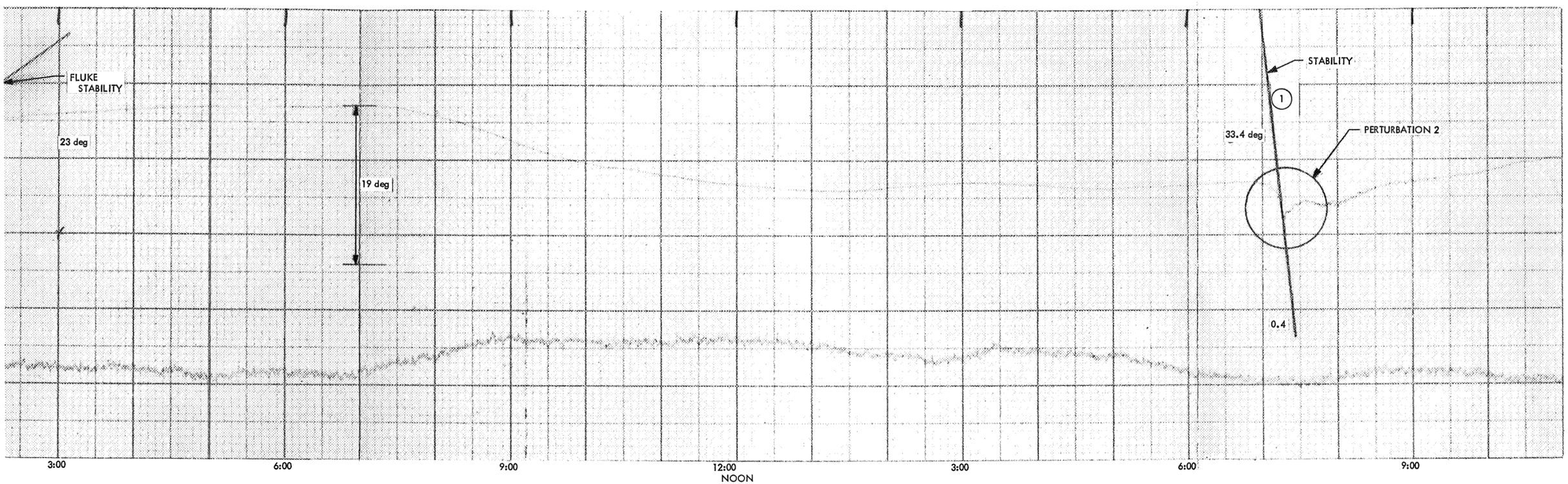

Fig. 2. Synthesizer stability test run 8 (long-term)

2

3

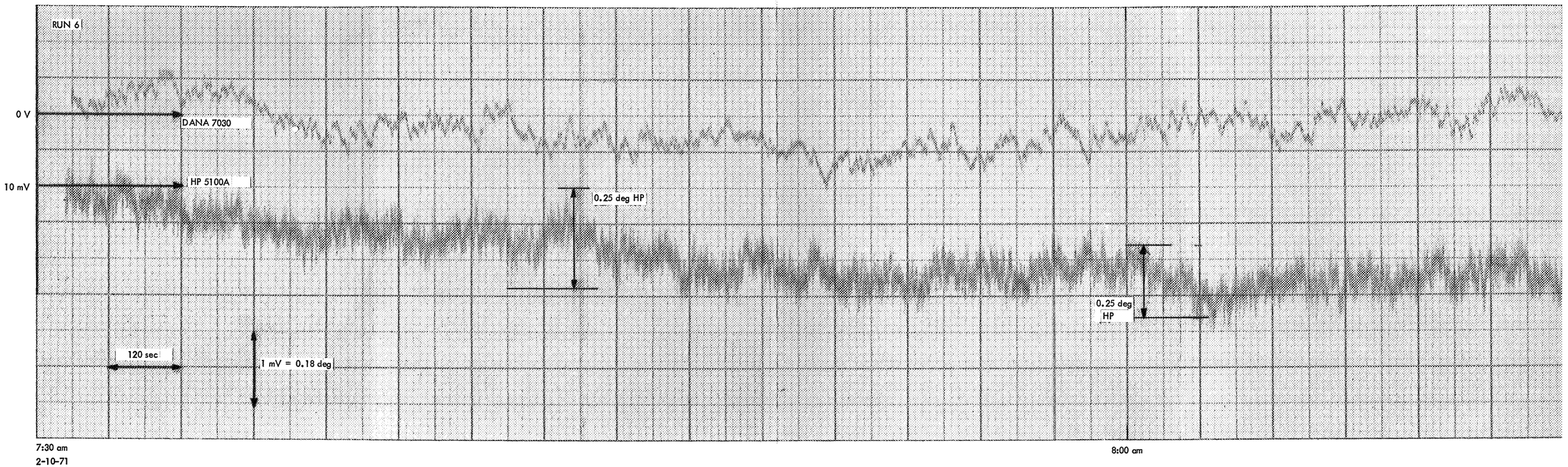

Fig. 3. Synthesizer stability test run 6 (short-term)

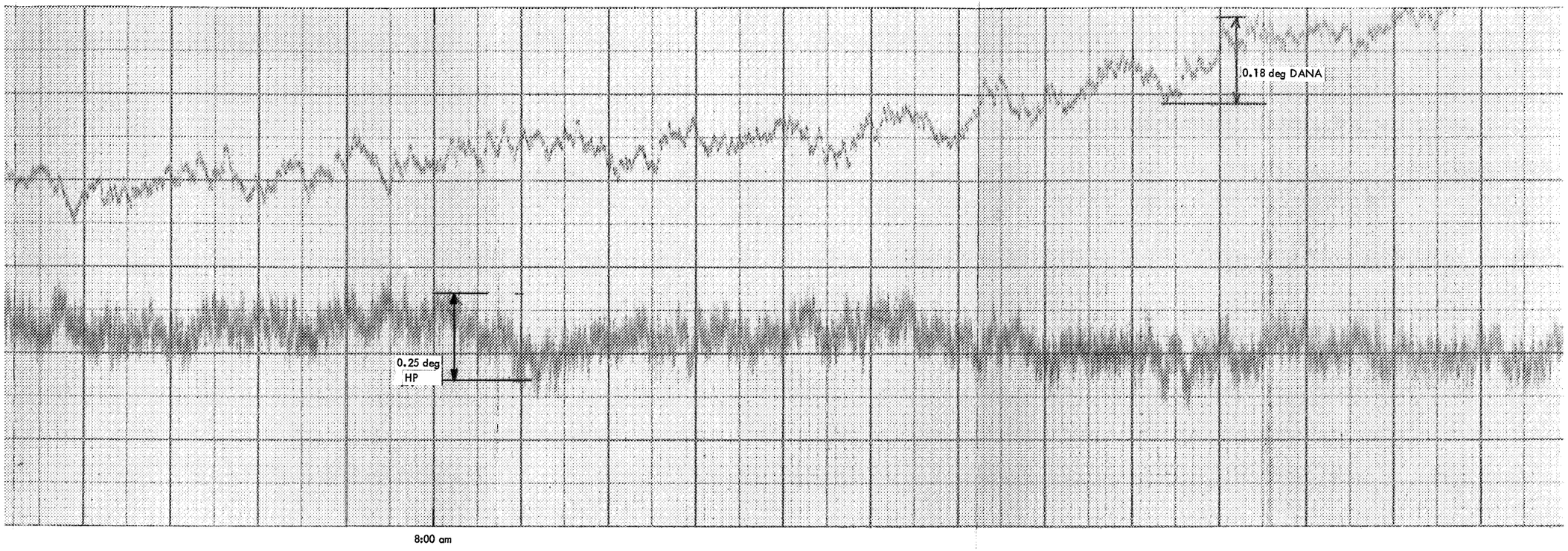

2

3

The Problem of Synchronization of Noisy Video

R. J. McEliece
Communications Systems Research Section

The problem of acquiring and maintaining TV line synchronization with the use of a PN prefix on each scan line, in the presence of random noise is discussed, and the recommendation is made that on the Mariner Mercury-Venus flight, a PN of length 63 be used.

I. Introduction

The currently proposed method of detecting a loss of TV line synchronization on the *Mariner* Mercury-Venus flight is to prefix each line with a 31-bit PN sequence, and to assume that a loss of synchronization has occurred if the PN appears to have suffered 9 or more bit errors. The underlying assumption is, of course, that a loss of sync will result in a misframing of the PN sequence, so that what is supposed to be the PN has no close relationship to it at all. At high signal-to-noise ratios this method behaves satisfactorily, but at the low signal-to-noise ratios which could occur at Mercury, the PN sequence can actually suffer 9 or more random bit errors with a significant probability. To be precise: if the TV data is uncoded and if the signal-to-noise ratio drops to a value which gives a bit error probability of 0.1, then the probability that a correctly synched PN prefix will suffer 9 or more errors is 0.003. Since each TV picture contains 700 scan lines, each picture will suffer, on the average, 2.1 cases of this "spurious line drop." The 0.01 bit error probability case will also be discussed, since even 0.01 is higher than previous design points (5×10^{-3}) for synching.

It is the object of this note to point out that this problem of spurious line drop can be overcome in a simple fashion without sacrificing protection against a true loss of synchronization. In addition we shall propose a method of reacquiring line synchronization once it has been irretrievably lost, which is practical for real-time operation at 117 kbps, the highest bit rate which has been suggested for use on the mission.

II. Analysis

Let us first of all remark that, as stated, the problem admits of several very easy solutions. Two of these are:

(1) Relax the running threshold somewhat; e.g. allow up to 10 bit errors before becoming alarmed. At a bit error probability of 0.1, this would reduce the probability of spurious line drop to 0.0001.

(2) Wait until two lines in a row fail the PN test. At a bit error probability of 0.1, this would reduce the probability of spurious line drop to about 10^{-5}.

However, let us remember that once line sync has been irretrievably lost, we must face the prospect of reacquiring it. And at the extremely high bit rates which will be in use, the only practical method is to search all 31-bit segments of the incoming data until one of the segments looks "enough" like the PN sequence that we can be reasonably sure that we have located the start of a new

TV line. It is here that serious problems occur. For if our criterion for recognizing the PN sequence is too stringent, we may miss seeing it because of the noise in the channel. Conversely, if the criterion is not stringent enough, among the 7056 possible frameup of a TV line a 31-bit sequence which is not the PN sequence might pass the test. We call these two alternatives *failure to detect* and *false detection*, and have computed Table 1 for prefixes of lengths 31, 47, and 63.

In order to compute Table 1 we made the assumption that a TV line was a sequence of 7056 0's and 1's chosen independently and with probability ½. The parameter T represents the largest acceptable number of errors in a PN sequence. It is easy to see that with these assumptions the probability of false detection is not dependent on the bit error probability. On the other hand, we see that the probability of failure to detect the PN is highly sensitive to the BEP.

We draw several conclusions from Table 1.

(1) For $N = 31$, at $P = 0.1$ the best algorithm for reacquiring sync once it has been lost is to look for a 31-bit sequence which looks like the PN with up to 4 errors allowed. This procedure will relocate sync about 75% of the time within one line of the sync loss. However, 12% of the time the algorithm will lock onto the wrong synchronization, and 20% of the time it will make no decision at all during the first line. This is unacceptable.

(2) For $N = 31$ and $P = 0.01$ we should choose T to be 2, and then sync will be reacquired within one line of its loss more than 99% of the time. Notice, however, that if we keep $T = 4$, we get a 12% rate of false detection. Incidently, $N = 31$ is used on the high-rate telemetry system with a bit error probability of 5×10^{-3}, and the length 31 need not increase for 0.01 operation.

(3) Thus, to get the best performance at $N = 31$, we would change T as the signal-to-noise ratio changes, and in the worst case ($p = 0.1$) we will fail, 25% of the time, to correctly re-establish sync.

(4) If the prefix is longer than 31, however, performance can be much improved: at $N = 47$ we get a worst-case failure rate of about 5%; at $P = 0.01$ we get a failure rate of 10^{-4} or less; at $N = 63$, a worst-case rate of less than 0.01; and at $P = 0.01$ a failure rate of $< 10^{-5}$. Notice that at $N = 63$, if we take $T = 12$, we get a failure rate of less than 1% at any BEP which is 0.1 or less.

III. Conclusion

We conclude that the problem of spurious line drop-out is not serious and can easily be eliminated with almost no change in existing procedures. However, we also conclude that the problem of reacquiring line sync once it has been lost presents much greater difficulties, especially at high bit rates (which prohibit sophisticated search schemes) and low signal-to-noise ratios (which cause the PN prefix to be maimed somewhat). In particular we have shown that the best algorithm for finding line sync in the first line will fail 20% of the time, and 12% of the time it will produce false synchronization. This is not adequate performance. However, a PN prefix of length 63 can be used to reduce these probabilities to 0.008 and 0.002 at a BEP of 0.1, and this is acceptable. Thus we recommend this prefix.

Table 1. Probabilities of false detection and failure to detect for algorithm which looks for a prefix of length N and allows $\leq T$ errors (uncoded TV line of 7056 bits)

N	T	Probability of false detect	Probability of failure to detect PN BER = 0.1	Probability of failure to detect PN BER = 0.01
31	1	0.0001	0.830	0.03
	2	0.002	0.611	0.003
	3	0.017	0.376	0.0003
	4	0.12	0.193	10^{-5}
	5	0.70	0.083	10^{-6}
	6	1.0	0.03	10^{-7}
	7	1	0.009	10^{-7}
	8	1	0.003	10^{-7}
47	5	0.0001	0.328	10^{-5}
	6	0.0006	0.186	10^{-6}
	7	0.004	0.093	10^{-8}
	8	0.02	0.041	10^{-9}
	9	0.09	0.016	$<10^{-10}$
	10	0.35	0.005	$<10^{-10}$
	11	1.0	0.001	$<10^{-10}$
63	8	$<10^{-5}$	0.175	$<10^{-8}$
	9	2×10^{-5}	0.094	$<10^{-9}$
	10	0.0001	0.046	$<10^{-9}$
	11	0.0006	0.021	$<10^{-9}$
	12	0.002	0.008	$<10^{-10}$
	13	0.01	0.003	$<10^{-10}$
	14	0.04	0.001	$<10^{-10}$
	15	0.13	0.0004	$<10^{-10}$

N = PN length.

T = number of errors permitted.

Probably of false detection is independent of bit error rate, but probability of failure to detect PN is not.

These probabilities are also independent of which N-bit prefix is selected. A PN sequence is recommended because it provides maximum protection against sync "slips" of just a few bits.

Level Sets of Real Functions on the Unit Square

D. Johnson and E. Rodemich
Communications Systems Research Section

Suppose f is a real-valued continuous function on the unit square. The problem of finding a level curve of f which joins opposite sides of the square is investigated. It is shown that while f need not have such a level curve, it at least always has a level connected set with the desired property. This problem is connected with the problem of minimizing the bandwidth of a certain matrix.

I. Introduction

Suppose we are given a real-valued function f on the unit square I^2, $f: I^2 \to I$ Viewed as a topographic map on the square, we seek to find a level path from one side of the square to the opposite side. We don't specify which pair of opposite sides are to be used, but only require that it must be somehow crossed at a single level. The original problem asks if this is always possible for, say, continuous functions f, or if not, whether suitable restriction of f (e.g., C^∞, analytic, PL = piecewise linear, etc.) will do the trick. This problem was suggested by Professor J. Franklin in connection with the problem of minimizing the "bandwidth" of the incidence matrix of the graph of an $n \times n$ square grid (Ref. 1).

We first give a C^∞ function having no solution, and then a proof of the appropriate restatement of the theorem.

II. A C^∞ Counterexample

(1) We let the square I^2 be represented by the set of (x, y) with $|x \pm y| \leqq 2$ (Fig. 1). The vertical strip between the dotted lines is given by $|x| \leqq 1$.

We define f as follows:

$$f = \begin{cases} 0 \text{ if } |x| \geqq 1 \text{ (the shaded triangles)} \\ e^{-w}(y - \sin w), \text{ where } w = \dfrac{1}{1 - x^2} \end{cases} \text{ if } |x| \leqq 1$$

f is C^∞ in the whole x, y plane: e^{-w} approaches 0 very fast as $|x| \to 1$, as well as all the derivatives, and $(y - \sin w)$ is bounded (for any y); this is the usual "smooth joining" technique.

(2) f is zero on the two shaded triangles (closed) as well as on the infinitely oscillating curve $y = \sin w\,(|x| \leqq 1)$. Above the sine curve f is > 0, below the sine curve f is < 0; thus there is no hope of traversing the square at any other level except $f = 0$. But to traverse at level zero, we clearly must start at one of the shaded triangles and cross to the other, *via* the sine curve. This cannot be done since the sine curve is not *pathwise* connected to either triangle.

(3) We note that the 0-level set, although not pathwise connected, is however connected; we have just the standard example of a connected non-path-connected space.

Thus we might expect the proper generalization of the theorem to be: if $f:I^2 \to I$ is continuous there exists a connected level set containing points of two opposite sides.

III. Proof of the General Theorem

We shall show that if $f:I^2 \to I$ is continuous then there exists a level set connecting a pair of opposite sides.

(1) We assume that m is the minimum value such that $A_m = f^{-1}[0, m]$ connects two opposite sides, assumed top and bottom (E_1 & E_0 resp., with $E = E_0 \cup E_1$). There must be such an m; in fact $A_1 = I^2$ certainly connects opposite sides, and it is easy to see that the infimum of numbers having this property also has it.

(2) Let μ be any arc, disjoint from E, connecting the left and right vertical sides. Then μ must intersect A_m, for otherwise μ would separate A_m into two disjoint open sets containing E_0 & E_1, respectively (i.e., the part below μ and the part above μ) contrary to the definition of A_m connecting E. Now since μ is an interval, its image $f(\mu)$ is an interval, and $f(\mu) \cap [0, m]$ is not empty. But f cannot be always less than m on μ, for then μ would connect two sides at a lower value than m, contrary to choice of m. Thus we must have some points of μ with *exactly* the value m, i.e., if $L = f^{-1}(m)$ then $\mu \cap L$ is not empty.

(3) Now suppose that L does not connect E. Then we may choose two disjoint open sets V_0, V_1, containing E_0 and E_1, respectively, and such that $L \subset V_0 \cup V_1$. If we divide I^2 into a small enough mesh of squares, we may replace V_i by the set W_i of all those squares which intersect $L_i = V_i \cap L$, and in this way get polyhedral neighborhoods W_i separating $L \cup E$.

(4) Next look at the component K of W_0 which contains E_0. Being PL and connected, its boundary is a PL circle (part of which is E_0 itself). As we follow its boundary around, starting at, e.g., the left side, it may leave the left side and return again, but eventually it must leave the left side and travel directly to the right. This is depicted in Fig. 2.

Thus the traversal gives us an arc μ which is outside the interior of W_0 and hence does not intersect L, a contradiction which proves that L does in fact connect E, and proves the theorem.

Reference

1. Franklin, J., *Matrix Theory*, Prentice-Hall Inc., Englewood Cliffs, N. J., 1968.

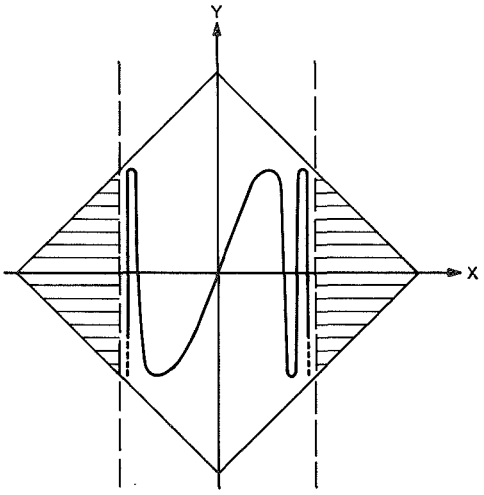

Fig. 1. The function f

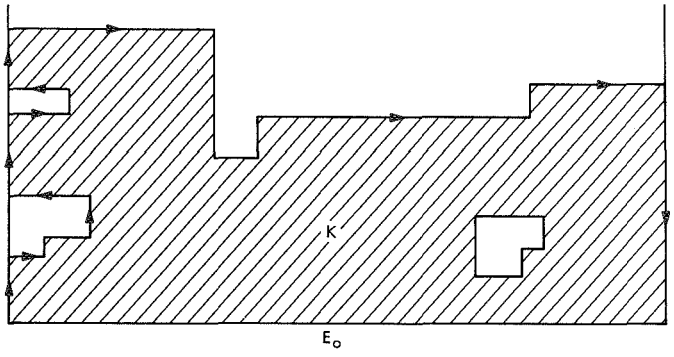

Fig. 2. E_0 component

A Wideband Digital Pseudo-Gaussian Noise Generator

W. J. Hurd
Communications Systems Research Section

A digital system has been constructed for the generation of wideband gaussian noise with a spectrum which is flat to within ±0.5 dB from 0 to 10 MHz. These characteristics are substantially better than those of commercially available analog noise generators, and are required in testing and simulation of wideband communications systems. The noise is generated by the analog summation of thirty essentially independent binary waveforms, clocked at 35 MHz, and low-pass filtered to 10 MHz.

I. Introduction

A digital system has been constructed for the generation of wideband gaussian noise with a spectrum which is flat to within ±0.5 dB from 0 to 10 MHz. This is substantially better than other noise sources now available. Noise of this bandwidth and spectral flatness is required in the testing and simulation of communications systems whose performance in the presence of noise must be accurately known. For example, by doing this accurate testing, margins of uncertainty are reduced, so that data rates can increase. The first application of this noise generator was in the evaluation of a prototype model of a code-regenerative spacecraft ranging transponder, the ranging clean-up loop for outer planet use.

II. General Description

Wideband video gaussian noise is required to test communications systems and in the simulation of many other types of systems. The required noise bandwidths may range from zero or close to zero Hertz to several Megahertz. Commercially available analog noise generators, using noise tube or diode sources, are often not satisfactory for several possible reasons: the bandwidth may not be wide enough; the spectral density may not be flat enough in the passband; the probability distribution may not be close enough to gaussian; and the stability of the noise parameters may not be good enough. The amplitude distribution is often so skewed that the sample waveform is visibly asymmetric when viewed on an oscilloscope, and the spectral density is typically specified as flat to within only ±1 or ±3 dB. Noise with these characteristics is clearly not acceptable in testing a communication system whose performance must be known to within one or two tenths of a decibel.

Recently, noise generators have become available which use digital logic to generate pseudo-random binary waveforms. The binary waveforms are then low-pass filtered to obtain quasi-gaussian noise. The principle is that according to the Central Limit Theorem, the distribution of the sum of a number of independent random variables tends toward gaussian as the number of terms in the sum is increased. The low-pass filtering performs the required summing. The problem with this type of system is that the

distribution of the pseudonoise becomes more gaussian only as the filter bandwidth is made progressively smaller with respect to the clock rate of the binary sequence. For some applications, the noise may be close enough to gaussian only if the clock rate is hundreds of times higher than the filter bandwidth, which means that the noise bandwidth will be much less than the digital clock rate—perhaps 100 kHz if the clock rate is 35 to 50 MHz.

Since the closeness of the distribution to gaussian depends on the number of independent terms in a summation, we observe that these terms can be generated either sequentially, as above, or in parallel. For example, the outputs of a large number of different binary pseudo-noise generators could be summed, and then low-pass filtered only enough to reduce the transient effects of the clocking and to shape the spectrum. It is this general principle which is used in the noise generator described here. One major improvement is made, however, which considerably reduces the hardware: a large number of different shifts of the same sequence are generated simultaneously, with each additional shift requiring only one simple integrated circuit, not an entire new shift register. The different shifts are essentially uncorrelated, and are far enough apart in time so that no shift contributes more than once to any experiment. The actual system constructed is clocked at 35 MHz, and the quasi-gaussian noise has a spectrum which is flat to ± 0.5 dB from 0 to 10 MHz.

III. Algebraic Theory

Suppose we have two maximal length linear shift register ($pn-$) sequences generated in shift registers X and Y of relatively prime lengths N and M, respectively. The sequences at the various shift register stages are labeled $X_i(k)$ and $Y_j(k)$ where the subscripts $i = 0, 1, \cdots, N-1$ and $j = 0, 1, \cdots, M-1$ denote the register stages, the argument k denotes time, and the binary values are taken to be $+1$ and -1. The shifting is from higher to lower numbered stages, so

$$X_i(k+1) = X_{i+1}(k), \qquad k = 0, 1, \cdots, N-2$$
$$Y_j(k+1) = Y_{j+1}(k), \qquad k = 0, 1, \cdots, M-2$$

and $X_{N-1}(k+1)$ and $Y_{M-1}(k+1)$ are linear functions of the values in the respective registers at time k.

We can now form the sequences $Z_{ij}(k) = X_i(k)\,Y_j(k)$. The periods of the X, Y, and Z sequences are $p_x = 2^N - 1$, $p_y = 2^M - 1$, and $p_z = p_x p_y = 2^{N+M} - 2^N - 2^M + 1$. Note that for reasonably large N and M, p_z is almost equal to the maximum length of a linear sequence generated by a shift register of $N + M$ stages.

The correlation properties of Z are similar to those of X and Y, so that Z is approximately a white noise sequence. The normalized in phase correlations of X and Y are 1, and the out of phase correlations are $-1/p_x$ and $-1/p_y$, respectively. For Z, the in phase correlation is 1, and the out-of-phase correlation is $+1/p_z$, except for phase shifts np_x and $np_y \pmod{p_z}$, at which points it is $-1/p_y$ and $-1/p_x$, respectively. For reasonably large p_x and p_y, all of the out of phase correlations are small, as desired for "white" noise. The cycle and add property of pn-sequences also extends to the product sequences, with similar exceptions as for the correlation properties.

One property of pn-sequences which does not extend to the product sequence is that of having all of the p_x (or p_y) possible non-trivial N (or M)-tuples occur exactly once in the cycle of length p_x (or p_y). Almost all possible $(N + M)$-tuples occur in Z, however. There are $2^{N+M} - 1$ possible nontrivial $(N + M)$-tuples in a maximum length linear sequence from a shift register of N stages, but the period of Z is $2^N + 2^M - 2$ less than this. Hence all but $2^N + 2^M - 2$ of the nontrivial $(N + M)$-tuples occur. The number not occurring is relatively small if N and M are moderately large, so that the effect on the randomness properties of the sequence is negligible.

The phase relationships between the $Z_{ij}(k)$ can be determined by the phase of each with respect to a reference sequence, which we choose to be $Z_{oo}(k)$. Denoting the delay from Z_{ij} to Z_{oo} by t_{ij}, we have $Z_{ij}(k) = Z_{oo}(k + t_{ij})$ for all k. This requires that $X_i(k) = X_o(k + t_{ij})$ and $Y_j(k) = Y_o(k + t_{ij})$, both for all k. Since

$$X_i(k) = X_0(k + i + np_x)$$

for all n and k, and

$$Y_j(k) = Y_o(k + j + mp_y)$$

for all m and k, we have

$$t_{ij} \equiv i \pmod{p_x}$$
$$\equiv j \pmod{p_y}$$

Now, since p_x and p_y are relatively prime, we can use the Euclidean algorithm to find a_x and a_y such that

$$a_x p_x + a_y p_y = 1$$

Finally,

$$t_{ij} \equiv i\,a_x p_x + j a_y p_y \,(\mathrm{mod}\, p_x p_y)$$

For the noise generator constructed, N and M were chosen to be 41 and 23, respectively. For this case,

$$a_x = 2^{21} + 2^{18} + 2^{16} + 2^{13} + 2^{11} + 2^8 + 2^6 + 2^3 + 2^0$$

and

$$a_x p_x = 1 - a_y p_y = a_x (2^{41} - 1)$$

Expressed as binary fractions,

$$a_x p_x / p_z \approx 0.0100101001 \cdots$$

which is approximately a repeating fraction equal to 9/31. Thus

$$t_{ij} \approx \frac{9}{31}(i - j)\, p_z$$

with the approximation being valid for small enough i and j that the repeating fraction approximation is good. We see from this that by carefully selecting pairs i and j, we can obtain 31 shifts of Z_{ij} which are approximately equally spaced modulo p_z.

In the actual implementation, 30 such shifts were used. These shifts could have been chosen by fixing j and choosing 30 consecutive taps of X. This has the disadvantage, however, that although the Z_{ij} thus obtained would be uncorrelated, adjacent sums of the thirty Z_{ij} are highly dependent, since 29 of the 30 terms in adjacent sums would be the same, except possibly for the sign. This is seen by expanding the sums and comparing, for example,

$$\sum_{i=0}^{29} X_o(k)\, Y_i(k) = X_o(k)\,[Y_o(k) + \sum_{i=1}^{29} Y_i(k)]$$

and

$$\sum_{i=0}^{29} X_o(k+1)\, Y_i(k+1) = X_o(k+1) \sum_{i=0}^{29} Y_{i+1}(k)$$

$$= X_o(k+1)\,[Y_{31}(k) + \sum_{i=1}^{29} Y_i(k)]$$

These two sums differ only by $Y_0(k) - Y_{31}(k)$ when $X_o(k) = X_o(k+1)$, and are similarly related but of opposite sign when $X_o(k) = -X_o(k+1)$. For this reason, care was taken to use different X_i for each Z, and to use no Y_j more than twice. Some duplication of Y_j's was necessary, because only 21 were available. The actual Z_{ij} selected correspond to $(i, j) = (n, 21 - n)$, $n = 0, 1, \cdots, 21$, and $(i, j) = (30, 7)$, $(31, 6)$, $(28, 1)$, $(23, 4)$, $(36, 5)$, $(35,2)$, $(38, 3)$, and $(37, 0)$.

With a system clock rate of 35 MHz, Z repeats approximately every 17000 years, and each pair of Z_{ij}'s is separated by over 500 years.

The shift register sequences are defined by the polynomials

$$x^{41} + x^3 + x^2 + x + 1 = 0$$

and

$$y^{23} + y^{17} + y^{11} + y^5 + 1 = 0$$

The polynomial for X was selected because the nonzero terms are consecutive, which means that implementation can be accomplished by toggling three of the stages according to the inputs to these stages, instead of implementing the multiplication. The polynomial for Y was chosen for a more important reason. This is that this polynomial divides no trinomials of degree less than 500. This algebraic property tends to lessen any possible skewedness of the distribution of sums of consecutive terms in the sequence (Ref. 1). To eliminate any residual skewedness, half of the thirty Z_{ij}'s generated are inverted in the final summation. Since their distributions are identical, this symmetrizes the distribution of the sum.

IV. Implementation

A block diagram of the noise generator is shown in Fig. 1. The digital portion is implemented entirely out of dual-in-line integrated circuit flip-flops, primarily because higher speed circuitry is available in flip-flops than in shift registers, and because access to both outputs of most stages was required. Since logical "1" and "0" in the digital circuitry correspond to -1 and $+1$, respectively, of the previous section, the EXCLUSIVE-OR operation corresponds to multiplication. The multiplications of the X_i and Y_j are thus implemented using AND-OR input flip-flops connected to perform EXCLUSIVE-OR's. This technique is also used to generate the feedback function for the Y register. For the X register, it was only necessary

to connect three stages so as to toggle when the previous stage is logically "1," instead of shifting, because ot the previously mentioned property of the polynomial.

The outputs of the Z_{ij} are summed using a resistor network at the input to a wideband operational amplifier. At the amplifier output, the signal is filtered by a parallel tank circuit to eliminate the clock frequency, and passed through a 50-Ω resistor to provide a standard 50-Ω source impedance. When loaded with 50 Ω, the spectrum of the system output is flat to within about ±0.5 dB from zero to 10 MHz.

It is planned to increase the clock rate of the system to about 50 MHz by replacing the current integrated circuits with faster but PIN-compatible circuits. When this is accomplished, the output spectrum will be further shaped by filtering to obtain the flattest spectrum possible, and statistical tests of the noise properties will be undertaken.

Reference

1. Lindholm, J. H., "An Analysis of the Pseudo-Randomness Properties of Subsequences of Long m-Sequences," *IEEE Trans. Info. Theory*, Vol. IT-14, pp. 569–576, July 1968.

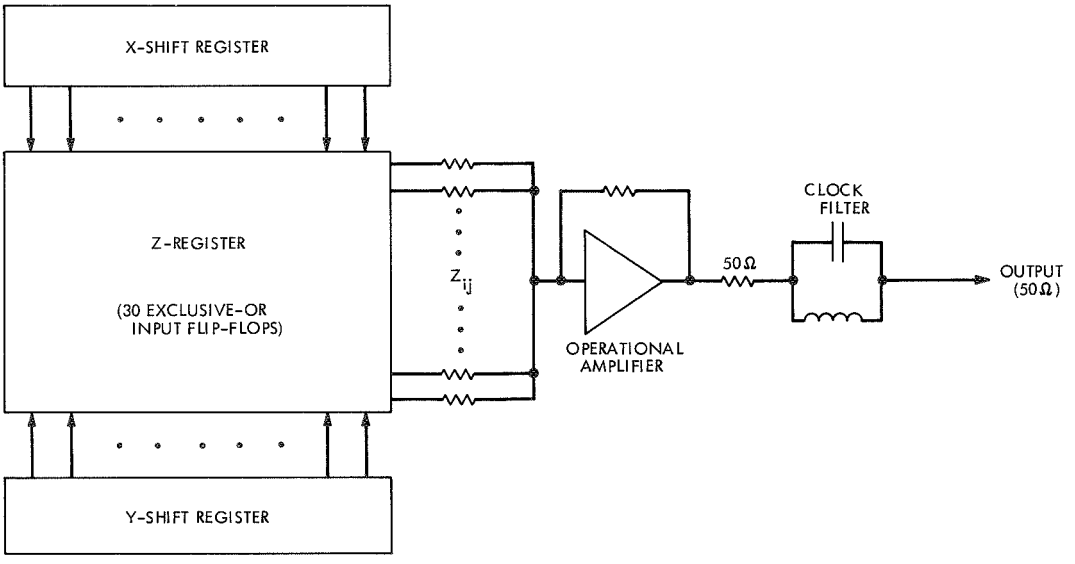

Fig. 1. Noise generator block diagram

Matched Filters for Binary Signals: A Correction and Elaboration

S. Zohar
Communications Systems Research Section

This article is a correction and elaboration of "Matched Filters for Binary Signals," appearing in The Deep Space Network, Technical Report 32-1526, Vol. I, Jet Propulsion Laboratory, Pasadena, Calif., Feb. 15, 1971.

A preceding article (Ref. 1) contains two element value tables (Tables 2, 3) which were meant to cover network orders 1 to 7. Due to a regrettable error, the tables actually incorporated in Ref. 1 are valid only up to order 5 (as evidenced by the negative element values for orders 6, 7). A version of these tables valid up to order 7 is presented here.

Strictly speaking, the networks described here differ from those of Ref. 1. With the adopted number of digits, these differences are too small to be evident in the case of orders 1 and 2. However, they do increase with the order. Thus, we find in the networks of order 5 a maximal discrepancy of 28% (in C_2). In spite of that, the difference in performance as measured by ν_N/ν_∞ of the actual networks (see Table 1 and footnote on p. 58 of Ref. 1) is so small that Table 1 and Fig. 4 of Ref. 1 are applicable, without modification, to the networks of Ref. 1 up to order 5 as well as to all orders of the networks presented here.

Another modification relates to the transmission-zero frequencies $FR(I)$. In the tables presented here, $FR(I)$ is the zero realized by section I and is thus the parallel resonance frequency of $L(I)$, $CR(I)$. (In the original tables, $FR(I)$ of the Nth order network referred to section $N + 2 - I$.)

We conclude with a brief discussion of the relationship of the two sets of networks. It was pointed out on p. 58 of Ref. 1 that, given the set of transmission zeros, the desired matched filter could be synthesized through a ladder development of any of the following immittances: $Z_{11}(s)$, $Z_{22}(s)$, $Y_{11}(s)$, $Y_{22}(s)$. (However, see footnote 2 on p. 58 of Ref. 1.)

With infinite precision, all four expansions would have yielded the same network. With finite precision in a real computer, differences were bound to show up yielding four different networks (for each order). Which of the

four should one adopt? In considering this question we initially reasoned that since the ladder elements are computed in sequence, one would expect the errors in the element values to increase as the synthesis progressed. This suggested adopting the elements of the input half of the filter from $Z_{11}(s)$ or $Y_{11}(s)$ and the ouput half from $Y_{22}(s)$ or $Z_{22}(s)$.

Actual synthesis of all four families has revealed the presence of additional error mechanisms, leading to significant differences among the four families. The most striking difference is shown in the breakdown of the synthesis process. As networks of increasing order are synthesized, a point is eventually reached where the accumulated errors finally lead to negative elements and a breakdown of the process. This aspect of the four expansions is summarized in Table 4 of this article. Note the marked advantage of the $Z_{11}(s)$ expansion. Examination of Eq. (64) of Ref. 1 provides a clue to this behavior. $Z_{11}(s)$ is the only immittance whose construction from the polynomials $g(s), h(s)$ involves no "cancellation" errors, as it calls for the addition of positive numbers only. (The coefficients of $g_e(s)$, $g_o(s)$, $h_e(s)$ are all positive. Those of $h_o(s)$ are all negative.)

Obviously, the $Z_{11}(s)$ synthesis is the one to be preferred. Though it is valid up to order 8, we have decided to aim at higher precision and have restricted it to order 7. Tables 2 and 3 of this article (and originally meant for Ref. 1) are based on the $Z_{11}(s)$ expansion. On the other hand, the tables mistakenly incorporated in Ref. 1 are those based on the $Y_{22}(s)$ synthesis.

It should be stressed that the above arguments provide only a crude estimate of the reliability of the element values. As indicated in Section V of Ref. 1, a precise reliability indication was obtained through a direct and almost error-free analysis of the performance of the networks with the computed elements. In the present case, this approach turned out to be much simpler than the alternative of special synthesis techniques based on frequency transformations.

Reference

1. Zohar, S., "Matched Filters for Binary Signals," in *The Deep Space Network*, Technical Report 32-1526, Vol. I, pp. 52–62. Jet Propulsion Laboratory, Pasadena, Calif., Feb. 15, 1971.

Table 2. Network elements for $T = \pi$ sec, $R_1 = 1\ \Omega$

UNITS SECOND,HERTZ,OHM,HENRY,FARAD
T= 3.1415927+00
RGEN= 1.000+00

NET, ORDER	1	2	3	4	5	6	7
RLOAD	1.500+00	1.000+00	1.000+00	1.000+00	1.000+00	1.000+00	1.000+00
SAMPLE GAIN	6.170-01	5.076-01	5.051-01	5.039-01	5.031-01	5.026-01	5.016-01
L (1)	1.410+00	5.006-01	2.997-01	2.158-01	1.689-01	1.389-01	1.176-01
CR(1)	0.000	0.000	0.000	0.000	0.000	0.000	0.000
C (1)	1.182+00	8.890-02	2.270-02	1.030-02	5.878-03	3.813-03	2.373-03
L (2)		4.908-01	7.718-02	2.866-02	1.436-02	8.429-03	5.425-03
CR(2)		4.075-01	6.920-01	8.575-01	9.837-01	1.088+00	1.187+00
FR(2)		3.559-01	6.886-01	1.015+00	1.339+00	1.662+00	1.983+00
C (2)		1.749+00	6.944-02	1.312-02	4.669-03	2.114-03	2.074-03
L (3)			4.672-01	8.516-02	3.323-02	1.708-02	1.047-02
CR(3)			4.642-01	6.575-01	7.636-01	8.469-01	8.929-01
FR(3)			3.418-01	6.726-01	9.991-01	1.323+00	1.646+00
C (3)			1.995+00	7.014-02	1.318-02	4.689-03	2.431-03
L (4)				4.597-01	8.804-02	3.521-02	1.872-02
CR(4)				4.897-01	6.517-01	7.335-01	7.831-01
FR(4)				3.354-01	6.645-01	9.903-01	1.314+00
C (4)				2.100+00	7.061-02	1.326-02	4.324-03
L (5)					4.557-01	8.939-02	3.641-02
CR(5)					5.048-01	6.517-01	7.177-01
FR(5)					3.318-01	6.594-01	9.846-01
C (5)					2.160+00	7.095-02	1.309-02
L (6)						4.531-01	9.006-02
CR(6)						5.150-01	6.537-01
FR(6)						3.295-01	6.559-01
C (6)						2.198+00	7.110-02
L (7)							4.518-01
CR(7)							5.217-01
FR(7)							3.278-01
C (7)							2.233+00

Table 3. Network elements for $T = 10\ \mu s$, $R_1 = 50\ \Omega$

UNITS MICROSECOND,MEGAHERTZ,OHM,MICROHENRY,MICROFARAD
T= 1.0000000+01
RGEN= 5.000+01

NET, ORDER	1	2	3	4	5	6	7
RLOAD	7.500+01	5.000+01	5.000+01	5.000+01	5.000+01	5.000+01	5.000+01
SAMPLE GAIN	6.170-01	5.076-01	5.051-01	5.039-01	5.031-01	5.026-01	5.016-01
L (1)	2.244+02	7.967+01	4.769+01	3.435+01	2.689+01	2.211+01	1.871+01
CR(1)	0.000	0.000	0.000	0.000	0.000	0.000	0.000
C (1)	7.526-02	5.660-03	1.445-03	6.557-04	3.742-04	2.427-04	1.510-04
L (2)		7.812+01	1.228+01	4.561+00	2.285+00	1.341+00	8.633-01
CR(2)		2.594-02	4.406-02	5.459-02	6.262-02	6.928-02	7.557-02
FR(2)		1.118-01	2.163-01	3.190-01	4.208-01	5.221-01	6.231-01
C (2)		1.114-01	4.421-03	8.350-04	2.973-04	1.346-04	1.320-04
L (3)			7.435+01	1.355+01	5.289+00	2.718+00	1.666+00
CR(3)			2.955-02	4.186-02	4.861-02	5.391-02	5.684-02
FR(3)			1.074-01	2.113-01	3.139-01	4.158-01	5.172-01
C (3)			1.270-01	4.465-03	8.391-04	2.985-04	1.548-04
L (4)				7.316+01	1.401+01	5.604+00	2.980+00
CR(4)				3.117-02	4.149-02	4.670-02	4.985-02
FR(4)				1.054-01	2.087-01	3.111-01	4.129-01
C (4)				1.337-01	4.495-03	8.441-04	2.753-04
L (5)					7.252+01	1.423+01	5.795+00
CR(5)					3.214-02	4.149-02	4.569-02
FR(5)					1.042-01	2.072-01	3.093-01
C (5)					1.375-01	4.517-03	8.334-04
L (6)						7.211+01	1.433+01
CR(6)						3.279-02	4.162-02
FR(6)						1.035-01	2.061-01
C (6)						1.400-01	4.526-03
L (7)							7.190+01
CR(7)							3.321-02
FR(7)							1.030-01
C (7)							1.421-01

Table 4. Breakdown behavior

Immittance used for ladder expansion	Network order in which negative elements first appear
$Z_{11}(s)$	9
$Z_{22}(s)$	5
$Y_{11}(s)$	7
$Y_{22}(s)$	6

Noise Diode Evaluation

K. B. Wallace
Communications Elements Research Section

Noise diodes are installed in all R&D microwave receiver systems to check broadband receiver performance required for radiometric applications, such as radio astronomy and atmospheric studies. An application to which noise sources are particularly suited is the noise-adding radiometer; another application being studied is automated system performance evaluation. In this article, noise diodes similar to those in use at Deep Space Stations 13 and 14 are evaluated for variations in noise output due to temperature.

I. Introduction

Noise diodes are installed in all R&D microwave receiver systems at DSSs 13 and 14. They are used to check broadband receiver performance required for radiometric applications, such as radio astronomy and atmospheric studies. A well-calibrated noise source may be used to measure system temperature, the magnitude of astronomical radio sources, and other parameters for which discrete frequency measurements are not applicable.

An application to which noise sources are particularly suited is the noise-adding radiometer (NAR) (Ref. 1). Another application being studied is automated system performance evaluation.

In all of these, noise diode stability is an important parameter. The purpose of this evaluation is to determine temperature characteristics of a few samples. Further evaluations at S-band and other frequency ranges are in progress.

II. Discussion

Four solid-state noise sources have been tested to determine output variations with respect to temperature. Of these, two are similar to those presently in use at Goldstone. They are manufactured by Microwave Semiconductor Corporation (MSC), designated MC 7025, serial numbers 701 and 703. Except for noise output, the two are alike in other respects.

The third sample was supplied by International Microwave Corporation (IMC), designated NCM-2030-3S, serial number 187. The fourth sample was manufactured by Texas Instruments, Model MIC 93S, serial number 15. This device is a microwave integrated circuit, complete with constant-current bias supply.

The test setup is shown in Fig. 1. An S-band receiver of equivalent input noise temperature of approximately 1000 K is terminated at the input with a liquid-nitrogen-cooled coaxial load of equivalent noise temperature of

85 K at 2295 GHz. The purpose of this load is to eliminate receiver variations due to ambient temperature changes.

The receiver is followed by a noise-adding radiometer developed by the Radio Frequency Techniques (RFT) Group, Section 333. This NAR is similar to those in use at Goldstone (Ref. 1), except that it employs a Hewlett-Packard Calculator, HP 9100A and accessories, for computation and control. The NAR is insensitive to gain changes and other receiver fluctuations.

The test device, enclosed in a thermally isolated chamber, is connected to the receiver input through a 20-dB directional coupler.

Samples 1, 2, and 3 are powered by an external constant-current power supply, range 0 to 10 mA. The sample chamber was operated over a temperature range of 0 to 50°C. The system has the capability to measure variation of noise power of a test device to an accuracy of approximately 0.1%. Absolute accuracy is approximately 1%. No effort was made to improve absolute accuracy, since the purpose of the test was the determination of noise power variations of the samples with temperature. The results of the tests are shown in Figs. 2 and 3, and summarized in Table 1.

The conversion of noise output (excess noise) expressed in kelvin to noise output expressed in dB is given by the expression

$$T_{N\,(\mathrm{dB})} = 10 \log \left(\frac{T_{N\,(\mathrm{deg})}}{290} + 1 \right) \tag{1}$$

This conversion is frequently used since manufacturer's specifications of excess noise are in dB and DSN system parameters are expressed in kelvin. Sample 4 could not be operated over a range of bias current. It was run at constant bias over a temperature range of 0 to 50°C.

III. Conclusion

It may be inferred from the test results that higher-power devices show greater percentage variation. Further testing of other noise sources will be required to verify this. Since the higher-power devices are required in R&D systems, the temperature variation must be reduced by using better noise sources or by temperature control.

Reference

1. Batelaan, P. D., Goldstein, R. M., and Stelzried, C. T., "A Noise-Adding Radiometer for Use in the DSN," in *The Deep Space Network*, Space Programs Summary 37-65, Vol. II, pp. 66–69. Jet Propulsion Laboratory, Pasadena, Calif., Sept. 30, 1970.

Table 1. Summary of results

Sample	Noise at receiver at ambient temperature, K	Noise from test device at ambient temperature		Maximum variation at peak		Manufacturer's specification
		K	dB	%/°C	dB/°C	dB/°C
Sample 1 (MSC MC 7025, SN 701)	1760	176,000	27.8	0.06	0.01	0.01
Sample 2 (MSC MC 7025, SN 703)	3280	328,000	30.5	0.30	0.12	0.01
Sample 3 (IMC, NCM-2030-3S)	3160	888,000	34.9	0.50	0.10	—
Sample 4 (MIC 93S)	310	31,000	20.1	0.07	0.003	—

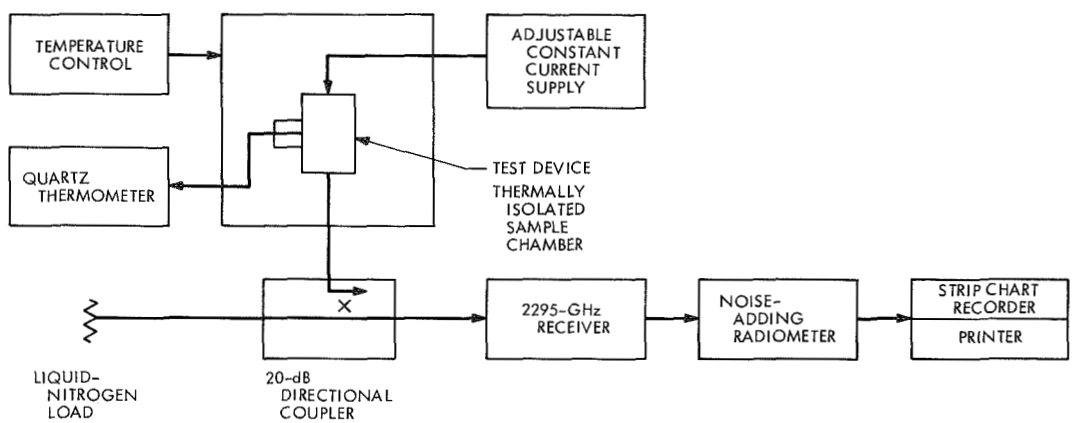

Fig. 1. Test setup

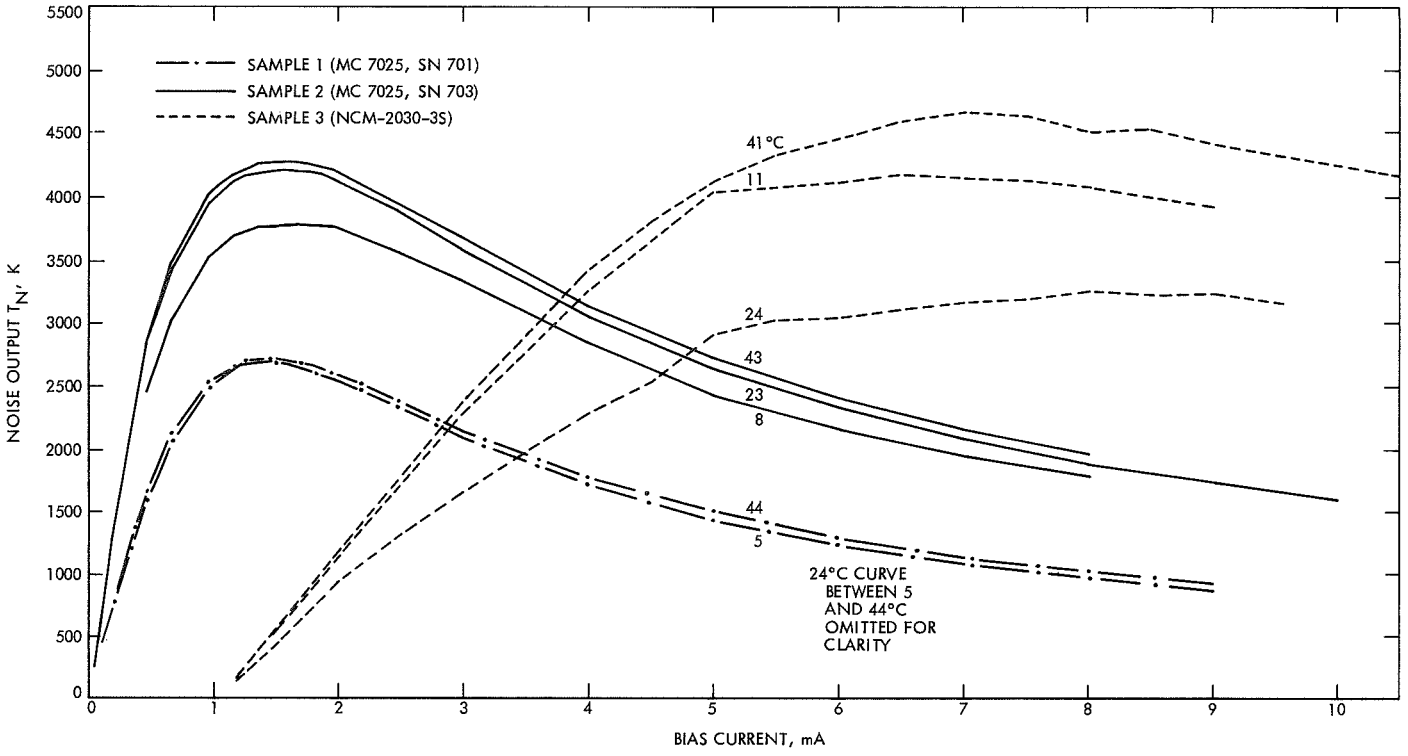

Fig. 2. Noise source output vs bias current and temperature

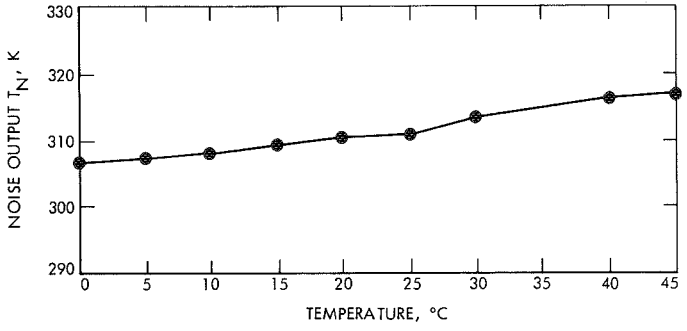

Fig. 3. Test results of sample 4

Analysis of the Boresight Error Calibration Procedure for Compact Rotary Vane Attenuators

T. Y. Otoshi
Communications Elements Research Section

In previous studies of the compact rotary vane attenuator, the possible error due to stator vane misalignment was not considered. It is shown in this article that even though the stator vanes are misaligned with respect to each other, the boresight error calibration procedure will tend to cause the residual attenuation error to reduce to a type B error which is generally negligible. This analysis applies to conventional as well as to compact rotary vane attenuators.

I. Introduction

At the Jet Propulsion Laboratory it has been recognized for several years that, for purposes of antenna gain and noise temperature calibrations, it is desirable to incorporate a precision rotary vane attenuator (RVA) in the receiving system. The RVA would enable power ratio measurements to be made by RF substitution methods and therefore reduce the present requirements for amplifiers with a high degree of linearity over a large dynamic range. The "front end" of the deep space communication antenna systems operating at 2.3 GHz utilizes WR 430 waveguide components that are assembled inside a Cassegrainian cone housing. Due to the need to keep the waveguide losses to a minimum, the installation of a conventional WR 430 RVA [1.2 to 1.5 m (4 to 5 ft) in length] was not considered practical. The requirements for a shorter low residual loss unit promoted the development of the compact RVA.

In Ref. 1, the results of tests on a test model compact RVA were presented. The test model that was developed in WR 112 waveguide size may be seen in Fig. 1. Excellent agreement was obtained between experimental and theoretical attenuations of the compact RVA which had a total dynamic range of about 30 dB. The theoretical attenuations were computed from a modified law that was derived for compact RVAs. It was shown in Ref. 2 that the same modified law could be used to extend the accurate dynamic attenuation range of a conventional RVA.

In previous studies of the compact RVA, the possible error due to mutual misalignment of stator vanes was not considered. In this article it is shown that it is permissible to neglect the effect of misaligned stator vanes if the described boresight error calibration procedure is used.

II. Modified Law

As derived in Ref. 3, the modified attenuation law for rotary vane attenuators is

$$A_{dB} = -10 \log_{10} [\cos^4 \theta + 10^{-L_{dB}/20} (2 \cos \phi \cos^2 \theta \sin^2 \theta) + 10^{-L_{dB}/10} \sin^4 \theta] \quad (1)$$

where

L_{dB} = attenuation (in decibels) at $\theta = 90$ deg relative to the attenuation at $\theta = 0$ deg

ϕ = phase shift at the rotor output at $\theta = 90$ deg relative to the phase shift at $\theta = 0$ deg

and

$$\theta = \theta_I + \alpha_1 + \alpha_2(\theta_I) \tag{2}$$

where

θ_I = indicated vane angle

α_1 = boresight error (difference between indicated and actual zero-degree vane angle positions)

$\alpha_2(\theta_I)$ = rotary vane angle runout error calibrated relative to $\theta_I = 0$ deg setting. (This error is a function of θ_I, and is due to gearing errors, bearing runout, eccentricities, etc.)

It should be pointed out that the parameters L_{dB} and ϕ are frequency sensitive. However, their values over a broad band of frequencies can be calibrated rapidly and economically by an automatic network analyzer.

The vane angle errors α_1 and $\alpha_2(\theta_I)$ must also be calibrated to ensure that the attenuator follows the law given by Eq. (1). A procedure for calibrating runout error $\alpha_2(\theta_I)$ was previously described in Ref. 3. The method for calibrating the boresight error α_1 will be described in this article.

It is of interest to examine some special cases of the modified law which are important to consider in boresight error calibrations. Analysis of Eq. (1) will reveal that, when $\cos\phi < 10^{-L_{dB}/20}$, the incremental attenuation will become a maximum at a vane angle setting less than 90 deg and have a maximum value greater than L_{dB}. The following relationships apply for $\cos\phi < 10^{-L_{dB}/20}$:

$$(A_{dB})_{max} = A_{dB}\big|_{\theta=\theta_M} = L_{dB} + 10\log_{10}\left(\frac{L - 2\sqrt{L}\cos\phi + 1}{L\sin^2\phi}\right) \tag{3}$$

where

$$L = 10^{L_{dB}/10} \tag{4}$$

$$\theta_M = \cos^{-1}\sqrt{\frac{1 - \sqrt{L}\cos\phi}{L - 2\sqrt{L}\cos\phi + 1}} \tag{5}$$

If $\cos\phi \geqq 10^{-L_{dB}/20}$,

$$(A_{dB})_{max} = L_{dB} \tag{6}$$

$$\theta_M = \pi/2 \tag{7}$$

Figure 2 illustrates the maximum attenuation characteristics of a compact RVA having a value of L_{dB} equal to 30. These curves were generated by the Univac 1108 computer[1] using the modified attenuation law equation. It is of interest to note in the family of curves that when ϕ is in the region $88.2° \leqq |\phi| \leqq 180°$, the maximum attenuation is greater than L_{dB} and will occur at a vane angle setting which is less than 90 deg.

III. Boresight Error Calibration Equations

Substitution of $\sin^2\theta = 1 - \cos^2\theta$ and algebraic manipulations of Eqs. (1) and (2) will lead to the explicit relationship for α_1 given as

$$\alpha_1 = \pm\arccos\sqrt{x} - \theta_I - \alpha_2(\theta_I) \tag{8}$$

where

$$x = \frac{-B \pm \sqrt{B^2 - 4AC}}{2A} \tag{8a}$$

$$A = 1 - \frac{2\cos\phi}{\sqrt{L}} + \frac{1}{L} \tag{8b}$$

$$B = 2\left(\frac{\cos\phi}{\sqrt{L}} - \frac{1}{L}\right) \tag{8c}$$

$$C = \frac{1}{L} - 10^{-A_{dB}/10} \tag{8d}$$

and L was previously defined by Eq. (4).

The plus sign shown in Eq. (8) is chosen if θ_I has a positive value and the minus sign is chosen if θ_I has a negative value. For most cases, the plus sign shown in Eq. (8a) is applicable. The minus sign in Eq. (8a) is used only for special cases where $\cos\phi < 10^{-L_{dB}/20}$ and the vane angle setting falls in the region $\theta_M < |\theta| < \pi/2$, where θ_M is given by Eq. (5).

[1]Computer program written by T. Cullen of the Communications Elements Research Section.

IV. Boresight Error Calibration Procedure

The procedure used to calibrate α_1 of the compact RVA is identical to the one described by Larson (Ref. 4) for conventional RVAs except that measured attenuation values are substituted into the above general α_1 expression derived from the modified law rather than from the $\cos^2\theta$ law. It is necessary that an initial approximate calibration of L_{dB} and ϕ for the compact RVA be obtained. Then, the α_1 calibration procedure is to measure the incremental attenuation at a θ_I setting and substitute the measured value for A_{dB} in Eq. (8d) and compute α_1 from Eq. (8). After computing α_1 values based on measured attenuations at several θ_I settings, an average value of α_1 is computed. For best accuracy, use of data obtained at vane angle settings close to minimum and maximum attenuation regions should be avoided.

Due to the fact that attenuations of a compact RVA deviate significantly from the $\cos^2\theta$ law even at vane angle settings as low as 20 deg, the use of the more general α_1 expression (given by Eq. 8) is recommended for accurate calibration of α_1. As will be shown later, a beneficial outcome of the use of the described calibration procedure is that, if the stator vanes were misaligned with respect to each other, the effect of this misalignment would tend to reduce to a type B (Ref. 5) error which is generally negligible.

Since α_1 is a mechanical misalignment angle, its value can be determined from RF calibrations at a single frequency if internal reflection errors are small. Using 8448-MHz calibrated values of L_{dB} and ϕ and measured attenuation values in the general α_1 expression, average values equal to $(0.0064 \pm 0.0018\, s_{\bar{x}})$ degree and $(-0.178 \pm 0.004\, s_{\bar{x}})$ degree were calibrated for the test model compact RVA (Fig. 1) in the tapered and stepped transition configurations, respectively. The symbol $s_{\bar{x}}$ denotes the calculated standard error based on the number of measurements. The average α_1 value for each configuration was based on measured attenuations at 27 different vane angle settings (between 19 and 80 deg). The differences of the α_1 values for the two transition configurations were attributed mainly to differences in the mechanical alignments of the stator vanes.

V. Effect of Stator Vane Misalignment

The purpose of this analysis is to show that if the stator vanes were misaligned with respect to each other, the α_1 calibration procedure will cause the actual rotor index plane to be established at a plane located approximately midway between the two stator vanes. By establishing the rotor index at this plane, a good fit will result between measured attenuations and the modified law.

Figure 3 depicts the geometry of a general stator vane misalignment case. An arrow at the end of an arc indicates the plane to which the angle is measured with respect to the reference plane located at the beginning of the arc. When the arrow points in a counter-clockwise direction, the angle has a positive value in the equations presented in this analysis. For the general stator vane misalignment geometry of Fig. 3, the equation for theoretical attenuations (relative to minimum attenuation) can be derived as

$$A'_{dB} = -20\log_{10}\left|\cos\theta_v\cos(\theta_v+\theta') + \frac{e^{j\phi}}{\sqrt{L}}\sin\theta_v\sin(\theta_v+\theta')\right| \tag{9}$$

where

$$\theta_v = \theta_I + \alpha_2(\theta_I) + \delta = \theta - \alpha_1 + \delta \tag{10}$$

and

δ = angle between the output stator card and the indicated rotor index plane, rad

θ' = angle of misalignment between stator vanes, rad

Other angles used in this analysis were previously defined by Eq. (2) or can be defined from Fig. 3.

In the absence of internal reflections, the measured attenuation values will closely follow those given by Eq. (9). Substitution of Eq. (9) for A_{dB} in Eq. (8d) and computations of α_1 using Eq. (8) at many vane angle settings will result in an average α_1 value of

$$\bar{\alpha}_1 \simeq \delta + \frac{\theta'}{2} + \bar{\epsilon} \tag{11}$$

where the angles are expressed in radians and

$$\bar{\epsilon} = \frac{1}{N}\sum_{i=1}^{N}\left\{\frac{\left(\frac{\theta'}{2}\right)^2}{\sin 2\theta_i}\left[1 + \frac{2\left(\frac{\cos\phi}{\sqrt{L}}\cos^2\theta_i + \frac{\sin^2\theta_i}{L}\right)}{\cos^2\theta_i - \frac{\cos\phi}{\sqrt{L}}\cos 2\theta_i - \frac{1}{L}\sin^2\theta_i}\right]\right\} \tag{12}$$

and

$$\theta_i = \theta_I + \delta + \frac{\theta'}{2} \tag{13}$$

The derivation of Eq. (12) is involved and therefore presented separately in the Appendix of this article. The approximate formula given by Eq. (11) is useful for showing the relationship between θ' and the calibrated α_1 value. For most compact RVA cases likely to be encountered in practice, the accuracy of the approximate formula for $\bar{\alpha}_1$ will typically be better than 0.001%. The approximate formula becomes inaccurate when vane angle settings approach $\theta = 0$, $\pi/2$, and θ_M, which was defined by Eq. (5).

From the geometry of Fig. 3 and substitution of Eq. (11), one can obtain

$$\alpha_0 = \theta' + \delta - \alpha_1 \approx \frac{\theta'}{2} - \bar{\epsilon} \tag{14}$$

The last expression shows that the new rotor index plane, established by the boresight error calibration procedure, will be located approximately midway between the two stator vanes. If the rotor index were located exactly midway between the stator vanes, the associated attenuation error would be called a type B error (Ref. 5) whose magnitude is very small when θ' is small.

Figure 4 is a sample computer program printout that illustrates the small residual difference between measured and corrected attenuations that results from the boresight calibration procedure even when stator vanes are significantly misaligned. Numerical values as computed from the approximate and exact formulas for α_1 are also compared.

VI. Conclusions

It has been shown that even when the stator vanes of a rotary vane attenuator are misaligned with respect to each other, the boresight error calibration procedure will tend to cause the residual attenuation error to become negligibly small.

A restriction on the analysis is that the effects of internal reflections must be small. If transitions used on the RVA have VSWRs of 1.02 or less, the effects of internal reflections can be neglected.

References

1. Otoshi, T. Y., "RF Calibration Techniques: A Precision Compact Rotary Vane Attenuator," in *The Deep Space Network*, Space Programs Summary 37-62, Vol. II, pp. 81–87. Jet Propulsion Laboratory, Pasadena, Calif., Mar. 31, 1970.
2. Otoshi, T. Y., "Improved RF Calibration Techniques: Rotary Vane Attenuator Calibrations," in *The Deep Space Network*, Space Programs Summary 37-60, Vol. II, pp. 41–43. Jet Propulsion Laboratory, Pasadena, Calif., Nov. 30, 1969.
3. Otoshi, T. Y., and Stelzried, C. T., "Improved RF Calibration Techniques: WR 430 Waveguide Precision Rotary Vane Attenuator Calibration," in *The Deep Space Network*, Space Programs Summary 37-46, Vol. III, pp. 73–82. Jet Propulsion Laboratory, Pasadena, Calif., July 31, 1967.
4. Larson, W., "Analysis of Rotation Errors of a Waveguide Rotary Vane Attenuator," *IEEE Trans. Instrumentation and Measurements*, Vol. IM-12, pp. 50–52, Sept. 1963.
5. Larson, W., "Analysis of Rotationally Misaligned Stators in the Rotary Vane Attenuator," *IEEE Trans. Instrumentation and Measurements*, Vol. IM-16, pp. 225–231, Sept. 1967.

Appendix

Derivation of Approximate α_1 Formula for Misaligned Stator Vane Case

Derivation of the approximate formula given by Eq. (12) is laborious and the details are involved. However, due to the importance of the approximate formula and the insight it provides for stator vane misalignment analysis, details of the derivation are presented here. The same analysis applies to conventional as well as to compact RVAs.

It was found from studying numerical results from a computer that substitutions of Eq. (9) into Eqs. (8a) and (8) generally produced the result

$$\alpha_1 = \delta + \frac{\theta'}{2} + \epsilon \tag{15}$$

where ϵ is very small compared to θ'. It is difficult to prove this result analytically from direct analysis of Eq. (8). However, an approximate formula for ϵ was derived by use of the following indirect but equivalent method. Let the expression for α_1 as given by Eq. (15) be substituted into Eq. (10). Then, further substitution of Eq. (10) into Eq. (9) results in

$$A'_{dB} = -10\log_{10}\left|\cos\left(\theta - \frac{\theta'}{2} - \epsilon\right)\cos\left(\theta + \frac{\theta'}{2} - \epsilon\right) + \frac{e^{j\phi}}{\sqrt{L}}\sin\left(\theta - \frac{\theta'}{2} - \epsilon\right)\sin\left(\theta + \frac{\theta'}{2} - \epsilon\right)\right|^2 \tag{16}$$

From use of trigonometric identities and the assumptions that θ' and ϵ are small radian angles, the following approximate formula can be derived:

$$A'_{dB} \simeq -10\log_{10}\left|\left(\cos^2\theta + \frac{e^{j\phi}}{\sqrt{L}}\sin^2\theta\right) + \left(z - \frac{e^{j\phi}}{\sqrt{L}}[z + 2k]\right)\right|^2 \tag{17}$$

where

$$z = \epsilon\sin 2\theta - k \tag{18}$$

$$k = \left(\frac{\theta'}{2}\right)^2 \tag{19}$$

As was previously described, the exact procedure for determining α_1 is to substitute Eq. (16) into Eq. (8d) and compute α_1 from Eq. (8). The approximate equivalent procedure is to equate Eq. (17) to the modified law; then solve for ϵ and then substitute the derived expression for ϵ back into Eq. (15).

As a result of equating Eq. (17) to the modified attenuation law which can also be expressed as

$$A_{dB} = -10\log_{10}\left|\cos^2\theta + \frac{e^{j\phi}}{\sqrt{L}}\sin^2\theta\right|^2 \tag{20}$$

a quadratic equation[2] of the form

$$az^2 + bz + c = 0 \tag{21}$$

is obtained. For compact and conventional RVAs the condition $b^2 >> 4ac$ nearly always applies and, therefore, the approximate solution of the quadratic equation $z \simeq -c/b$ can be used. Using this approximation and omitting higher order terms and then solving for ϵ yields the expression

$$\epsilon \simeq \frac{\left(\frac{\theta'}{2}\right)^2}{\sin 2\theta}\left[1 + \frac{2\left(\frac{\cos\phi}{\sqrt{L}}\cos^2\theta + \frac{\sin^2\theta}{L}\right)}{\cos^2\theta - \frac{\cos\phi}{\sqrt{L}}\cos 2\theta - \frac{1}{L}\sin^2\theta}\right] \tag{22}$$

where ϵ, θ' are expressed in radians. For convenience of computations, one can substitute $\theta = \theta_I + \delta + \theta'/2$ in Eq. (22) and sacrifice only a small loss of accuracy.

[2]If u and v are general complex expressions and $|u + v|^2 = |u|^2$, then the condition $|v|^2 + 2\,\mathrm{Re}\,[uv^*] = 0$ must hold. The symbol (*) denotes complex conjugate.

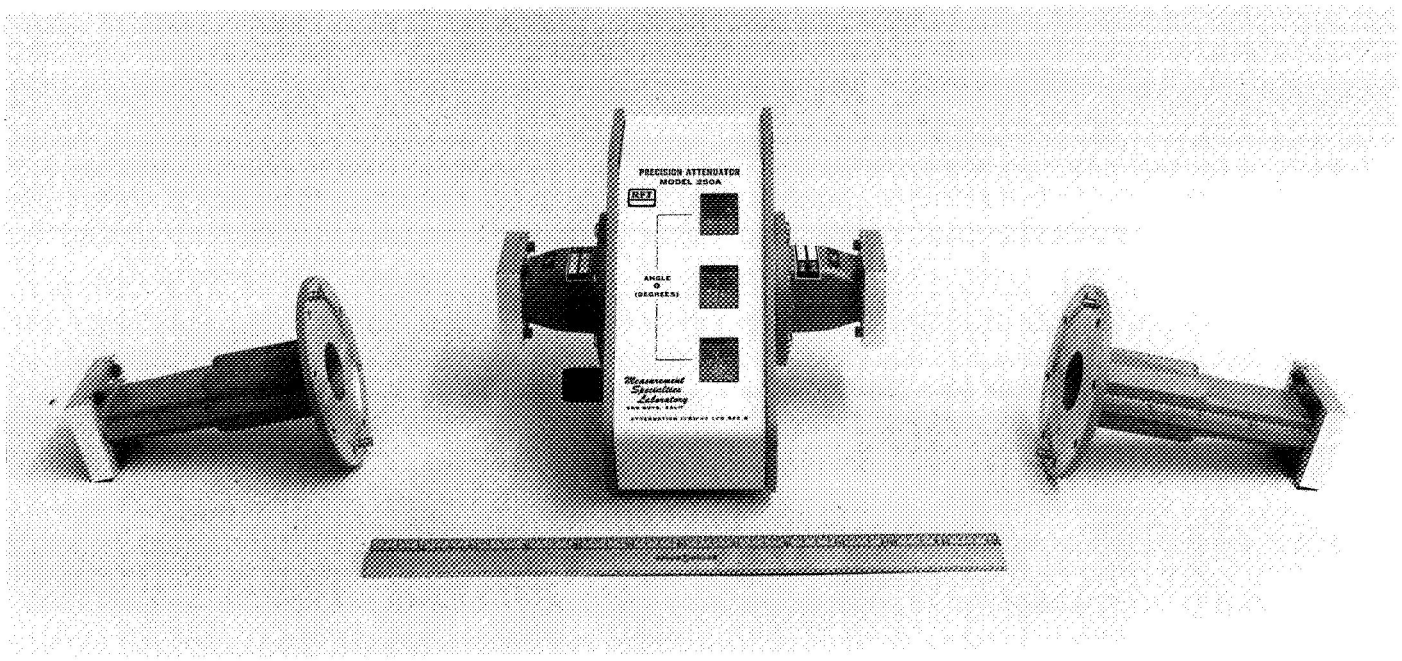

Fig. 1. Test model compact RVA shown with interchangeable transitions

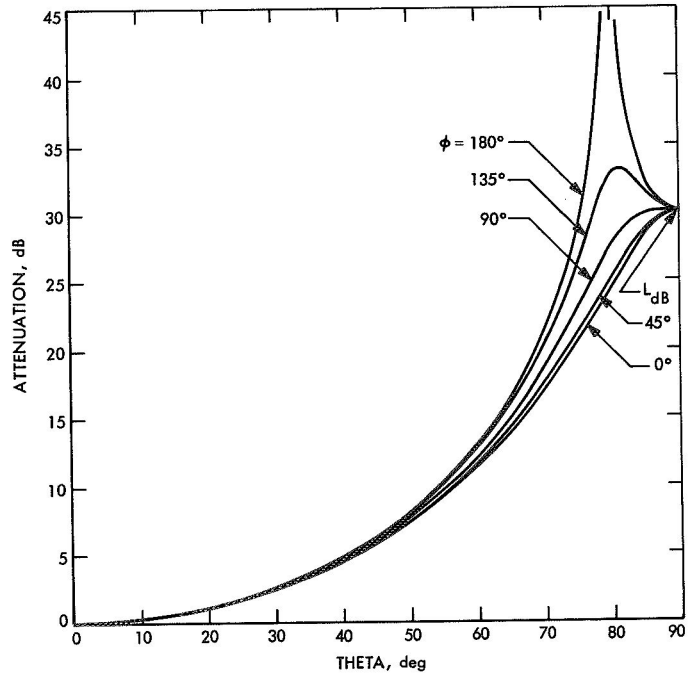

Fig. 2. Compact RVA attenuator curves for $L_{dB} = 30$

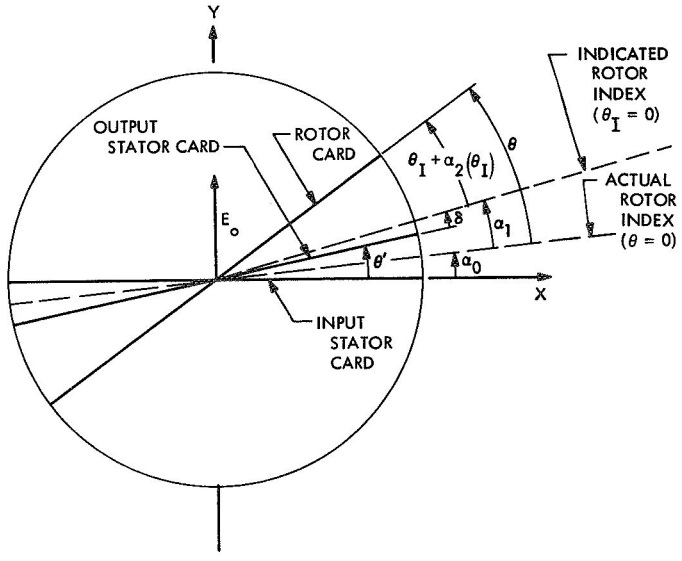

Fig. 3. Geometry for a general rotor and stator vane misalignment case

PROGRAM IN CULTYO-8M0D

GENERALIZED RVA BORESIGHT ERROR ANALYSIS

CASE DESCRIPTION...TEST CASE 38 NO MISMATCHES TP=2.0 DEG PHI = 135 DEG

LDB= 30.000 DB PHI= 135.00 DEG LDBM= 30.000 DB PHIM= 135.00 DEG

DELTA = .0000 DEG THETAP= 2.0000 DEG

THETA1 (DEG)	ALPHA-2 (DEG)	THETAV (DEG)	ADBP (DB)	MISMATCH (DB)	ADBPP (DB)	ADB-C (DB)	ALPHA1 (DEG)	APP ALPHA1 (DEG)	DIFF (DEG)
5.0000	.0000	5.0000	.1002	.0000	.1002	.0976	1.07975	1.08027	-.524-03
10.0000	.0000	10.0000	.3322	.0000	.3322	.3294	1.04447	1.04455	-.867-04
15.0000	.0000	15.0000	.7051	.0000	.7051	.7023	1.03147	1.03150	-.294-04
20.0000	.0000	20.0000	1.2255	.0000	1.2255	1.2225	1.02493	1.02495	-.149-04
25.0000	.0000	25.0000	1.9030	.0000	1.9030	1.8997	1.02118	1.02118	-.662-05
30.0000	.0000	30.0000	2.7510	.0000	2.7510	2.7474	1.01890	1.01891	-.432-05
35.0000	.0000	35.0000	3.7882	.0000	3.7882	3.7841	1.01755	1.01756	-.337-05
40.0000	.0000	40.0000	5.0402	.0000	5.0402	5.0354	1.01686	1.01687	-.192-05
45.0000	.0000	45.0000	6.5428	.0000	6.5428	6.5372	1.01672	1.01672	-.204-05
50.0000	.0000	50.0000	8.3478	.0000	8.3478	8.3409	1.01709	1.01709	-.224-06
55.0000	.0000	55.0000	10.5324	.0000	10.5324	10.5234	1.01804	1.01804	.432-06
60.0000	.0000	60.0000	13.2186	.0000	13.2186	13.2065	1.01975	1.01975	.112-05
65.0000	.0000	65.0000	16.6148	.0000	16.6148	16.5970	1.02259	1.02259	.550-05
70.0000	.0000	70.0000	21.1098	.0000	21.1098	21.0806	1.02741	1.02739	.134-04
80.0000	.0000	80.0000	33.1776	.0000	33.1776	33.1614	1.08362	1.07818	.544-02
-5.0000	.0000	-5.0000	.0459	.0000	.0459	.0433	.88182	.88008	.174-02
-10.0000	.0000	-10.0000	.2227	.0000	.2227	.2201	.94615	.94599	.160-03
-15.0000	.0000	-15.0000	.5387	.0000	.5387	.5359	.96449	.96445	.445-04
-20.0000	.0000	-20.0000	.9991	.0000	.9991	.9963	.97291	.97289	.189-04
-25.0000	.0000	-25.0000	1.6124	.0000	1.6124	1.6094	.97755	.97754	.826-05
-30.0000	.0000	-30.0000	2.3903	.0000	2.3903	2.3870	.98032	.98031	.547-05
-35.0000	.0000	-35.0000	3.3492	.0000	3.3492	3.3455	.98199	.98199	.304-05
-40.0000	.0000	-40.0000	4.5116	.0000	4.5116	4.5074	.98293	.98293	.186-05
-45.0000	.0000	-45.0000	5.9088	.0000	5.9088	5.9039	.98328	.98328	.603-06
-50.0000	.0000	-50.0000	7.5853	.0000	7.5853	7.5793	.98312	.98312	.103-05
-55.0000	.0000	-55.0000	9.6065	.0000	9.6065	9.5990	.98242	.98242	-.127-06
-60.0000	.0000	-60.0000	12.0733	.0000	12.0733	12.0632	.98104	.98104	-.200-05
-65.0000	.0000	-65.0000	15.1520	.0000	15.1520	15.1376	.97872	.97872	-.348-05
-70.0000	.0000	-70.0000	19.1427	.0000	19.1427	19.1200	.97485	.97486	-.974-05
-80.0000	.0000	-80.0000	31.7001	.0000	31.7001	31.6430	.95230	.95246	-.159-03

AVERAGE ALPHA-1= .9994700 DEG

STD DEV = .72589722-02 DEG

N= 30

AVERAGE EXACT ALPHA-1 = .9994700 DEG

AVERAGE APPROX ALPHA-1 = .99925411 DEG

ADBMAX = .33204480+02 DB AT THETA = 81.400170 DEG

Fig. 4. Sample printout of computer program showing relationship of θ' to α_1

Switched Carrier Experiments

R. B. Kolbly
R.F. Systems Development Section

This article describes experiments to produce a practical system for time-sharing a klystron amplifier between two up-link frequencies. Attempts to produce intermodulation products in the Deep Space Instrumentation Facility (DSIF) receiver passband and observations on intermodulation products at a DSIF station (Pioneer Deep Space Station) are described.

I. Introduction

The DSIF has a requirement in support of the *Viking* Mission for simultaneous transmission of two carriers from one 64-m antenna. These carriers would be separated by approximately 5 MHz and carry ranging modulation. The power level required is a minimum of 40 kW in each carrier and its associated sidebands. The 400-kW transmitter can supply this easily if excitation is supplied at the two frequencies, but past experience has shown that intermodulation (IM) products in the receiver passband well above receiver threshold are generated by this approach. These products are generated whenever two carriers are present in a nonlinear system. There is evidence that they are generated in the waveguide equipment or antenna structure.

If the excitation could be switched so that the klystron and antenna see only one carrier at a time, these intermodulation products would not be generated.[1] The Goldstone Development Support Group of the RF Systems Development Section has been performing experiments to determine the feasibility of this method.

[1]Proposed by M. Easterling.

This experiment to investigate the feasibility of time-sharing a klystron amplifier was conducted in several parts:

(1) Development of 66-MHz switch.

(2) Investigation of DSIF multiplier chain under switched-carrier conditions.

(3) Development of 2115-MHz switching techniques

(4) Investigation of klystron performance under switched-carrier conditions.

(5) Investigation of klystron and antenna performance under simultaneous carrier conditions.

A. Development and Performance of a 66-MHz Switch

The diode switch described in Ref. 1, p. 82 and Ref. 2 was unsatisfactory because of internally generated IM products created by the diodes in the switch. These IM products were −22 dB relative to the two input carriers. Also the switch described with its associated driver did not have independent control of each frequency on and off times.

A pair of commercial diode switches (Relcom S2) were procured and suitable driver units were fabricated (Fig. 1). Although the switch is a SPDT switch, two switches and associated driver units were used to allow independent control of each frequency "on" and "off" times. Each Relcom switch and its associated driver was driven with a pulse generator. Figure 2 is a block diagram of the equipment used to investigate the performance of the switches and the DSIF Block III multiplier chain.

The Relcom switches performed satisfactorily in this configuration. A typical 66 MHz spectrum is shown in Fig. 3. Time domain is shown in Figs. 4 and 5. However, the DSIF Block III multiplier chain distorted the output spectrum and generated excessive noise in the S-band spectrum. The strongest spectral line at the output of the multiplier chain was, in general, *not* the carrier frequency but the first switching sideband (Fig. 6). Although it has not been fully investigated, this phenomenon is thought to be due to the self-bias circuits in the multiplier.

B. S-Band Switching

Because of the unpredictable performance of the DSIF Block III Multiplier under switched-carrier conditions, it was decided to accomplish the switching at the output of the multiplier. This was accomplished by the equipment shown in Fig. 7. Hewlett-Packard Model 8732A PIN-diode modulators were used as switches. A fixed bias of −4 Vdc applied to the switches resulted in best performance. As with the 66-MHz switches, each S-band switch was independently controlled by a pulse generator. The use of isolators and a hybrid isolated the two switches so that no interaction was detected. Figures 8 and 9 show the spectrum and envelopes obtained by S-band switching. By adjustment of the switching voltages, independent control of the duty cycle of each carrier is possible.

The switched-carrier signal generated in this manner was used to drive a Model 5K70SG klystron amplifier. The 5K70SG klystron is a 20-kW CW output klystron used in both MSFN and DSIF 20-kW transmitters. Also, this klystron utilizes the same electron beam optics as the Eimac X3075 klystron, which is presently used in the DSIF 400-kW transmitters. It is expected that the 5K70SG klystron performance under these conditions will be representative of the X3075 klystron performance.

When driving the klystron amplifier with one carrier keyed at a 500-kHz rate (analogous to 100% square wave amplitude modulation), the even-order sideband suppression is degraded when amplified by the klystron. When both carriers are present, the even-order sideband suppression is improved somewhat. Figures 10 and 11 show input and output spectrums under single-switched carrier and dual-switched carrier, respectively. Operating the klystron saturated produced the most severe degradation of the even-order sideband suppression. The spectra in Fig. 11 were measured with the klystron operating under saturated conditions.

In order to determine if there would be any degradation in DSIF system performance when operating under switched carrier conditions, a DSIF S-band Cassegrain monopulse/traveling-wave maser (SCM/TWM) microwave subsystem was diplexed using switched-carrier drive. The particular SCM used in these tests was a unit returned from service because of excessive noise bursts. Using wideband noise instrumentation (Fig. 12), no degradation of system temperature was noted when operating in the switched-carrier mode.

C. Attempts to Generate a Receive Band IM Product

Attempts were made to produce a detectable intermodulation product in the receiver passband. Transmitter frequencies were selected so that the 240/221 turnaround ratio of one frequency (2113.3125) would be within range of the Microwave Test Facility phase-lock receiver. The second transmitter frequency (2116.3919) was selected so that a predicted intermodulation distortion product would also be within the receiver's tuning range.

By operating this klystron well into saturation, maximum intermodulation distortion was observed. However, we were unable to detect any intermodulation products stronger than the receiver threshold (−170 dBmW). Measurement of IM product amplitudes in the vicinity of the two carriers showed each successive IM product was, on the average, 3.8 dB below the previous one. By extrapolating these data to the DSIF receiver band, the IM product would be 220 dB down from the carriers, or approximately −150 dBmW. The isolation between the transmitter and maser is typically 130 to 160 dB, so IM products generated *in the klystron* would be expected to be well below receiver threshold.

Attempts were made to generate IM products by placing various nonlinear devices in the near-field of the Cassegrain feed horn. The following types of nonlinear devices were tried:

1. PN-type junctions (such as are found in semiconductors). An example of this would be a microwave mixer diode, such as a type 1N21B. In this attempt, a PN silicon rectifier junction (1N4005 diode with the leads forming

both half-wave dipoles and full-wave resonant loops) were placed approximately 0.3 m in front of the feed horn. Although increases in system temperature were noted (~50 to 100°K) as the diodes started conducting, no IM products were detected. The next experiment used a WR-430 to coax transition, a 1N21 crystal holder pointed down the feed at an approximate 0.3-m distance. Again, temperature increases were noted, but no IM products detected.

2. Corroded metal joints and dissimilar metal joints. In this experiment, metal strips of aluminum and OFHC copper ($25 \times 3 \times 0.32$ cm approximate dimensions) were joined together with approximately 10 cm of overlap with stainless steel screws and placed 0.3 m in front of the feed horn. One of these test pieces was fresh, and the other test piece was dipped into a nitric-sulphuric acid solution (this solution is normally used for cleaning fabricated copper and copper-based alloy parts) to induce joint corrosion. Both of these test pieces, when placed in the beam of the feed horn produced 50 to 100°K noise bursts, but no detectable IM products.

3. Ionization. To simulate the nonlinear phenomenon that would be present in corona discharge, neon lamps and fluorescent lighting tubes were suspended in the beam of the feed horn. With power output of approximately 1 kW, the 50 to 100°K noise bursts were observed. Increasing the power resulted in an erratic system temperature increase as the gas tube ionized. Again, no IM products were detected.

4. Arcs. To produce an RF arc in the feedhorn beam, a spark gap was made of two 6.35 mm (0.25 in.) stainless steel rods placed $\lambda g/4$ from a short in WR-430 waveguide. The gap was centered in the waveguide at the point of maximum electric field. The gap was set to approximately 1 mm spacing and suspended approximately 0.3 m above the feedhorn with the open end of the waveguide. Due to the weight of the gap assembly, it was necessary to use a 4×9 cm ("two-by-four") Douglas fir beam to suspend the arc gap. This arc gap fired at approximately 5 kW transmitter power. The transmitter was operated at 15 kW total power output during the search for an IM product. Although no IM product was detected, the fir beam scorched and started to burn. The power density encountered was sufficient to burn the wood in the center of the beam.

All of the above nonlinear devices produced broadband noise, but no detectable intermodulation products were produced. At the present time we have no explanation for the negative results. All of the above devices should have produced IM products but none were detected.

D. IM Product Experiments at DSS 11

Earlier work (Ref. 3) measured IM products on the DSS 11 26-m antenna when operating under dual carrier conditions. Time was made available at DSS 11 to verify these results and to attempt to learn more about the nature of IM product generation. Because the station was only available in the MSFN configuration, MSFN frequencies were used for these experiments. The frequencies used for transmission were 2101.8021 and 2106.5517 MHz. A stable (in frequency) IM product was received on 2282.2869 MHz, which agrees with a predicted IM product frequency. The amplitude of this product varied rapidly ($T < 1$ sec) between -130 and -150 dBmW, with a signal strength normally around -140 dBmW. To conduct the tests at DSS 11, the incoherent AGC was on one channel of a chart recorder and the coherent AGC with a 4.5-Hz bandwidth recorded on another channel of the same chart recorder. One of the event markers was used to indicate receiver lock conditions. The incoherent AGC channel corresponds to system temperature. Figure 13 shows a portion of this chart recorder graph and shows the calibrations of the coherent AGC channel. Figure 14 shows the noise bursts and amplitude of the IM products. It can be seen that the IM product amplitude has a definite positive correlation with the system temperature bursts. Individual footsteps of a man climbing the antenna were detectable in both the incoherent and coherent AGC channel.

To find if the bursts in the incoherent AGC channel were due to IM products or wideband noise, another receiver with a 1 MHz bandwidth was tuned to a frequency between two IM products. The maser noise instrumentation subsystem was used to set the bandwidth and detect the noise bursts. Interfacing the noise instrumentation subsystem with the receiver recorder posed difficulties, but the data indicate that the noise bursts are broadband in nature, and correlate with the IM product amplitude (Fig. 14). Pointing the antenna at the collimation tower resulted in a drastic increase in both system temperature and IM product amplitude (Fig. 12). Offsetting the 2106.5517 transmitter frequency driver frequency 1 Hz (96 Hz change in transmitter frequency) resulted in the IM product receiver VCO frequency changing 38 Hz (IM product moved 3648 Hz). In a similar manner changing the VCO frequency of the 2106.5517 MHz moved

the VCO frequency of the IM product driver *down* in frequency 37 Hz.

E. Future Experiments

Efforts will continue to produce IM products under laboratory conditions. From the experiments at DSS 11, it seems that the same mechanism that produces noise bursts also produces IM distortion products. More controlled arcs and coronas will be used, as well as injection of various contaminants into the waveguide. Dual-carrier experiments at other DSIF stations will be made to determine the IM product problem's relation to the age and construction of the antennas.

References

1. Chernoff, R. C., and Hartop, R. W., "Noise and Intermodulation Interference in MSFN Back-Up Tracking Systems During Transmission of Dual Up-Link Carrier," in *The Deep Space Network*, Space Programs Summary 37-57, Vol. II, pp. 138–145, Jet Propulsion Laboratory, Pasadena, Calif., May 31, 1969.
2. Kolbly, R. B., "Switched-Carrier Experiments," in *The Deep Space Network*, Space Programs Summary 37-65, Vol. II, pp. 81–84, Jet Propulsion Laboratory, Pasadena, Calif., Sept. 30, 1970.
3. Kolbly, R. B., "Switched Carrier Experiments," in *The Deep Space Network*, Space Programs Summary 37-66, Vol. II, pp. 84–88, Jet Propulsion Laboratory, Pasadena, Calif., Nov. 30, 1970.

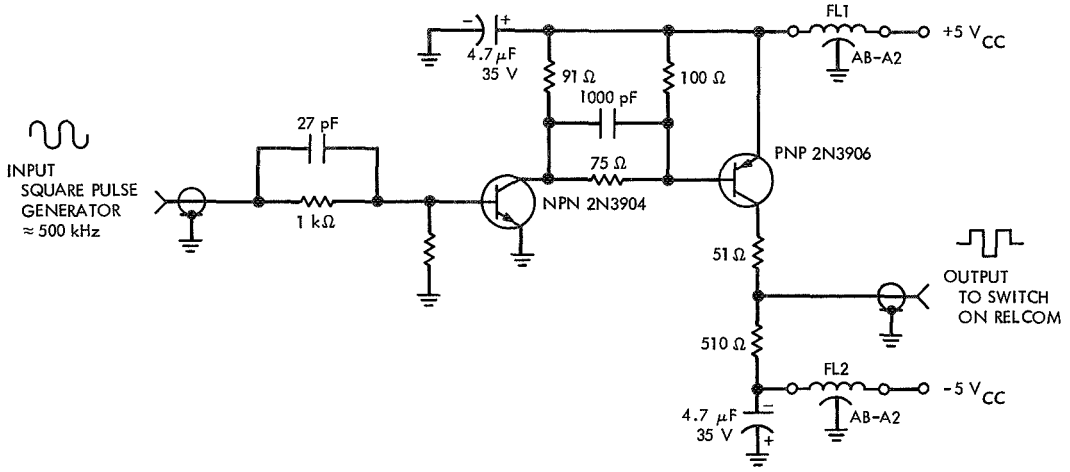

Fig. 1. Schematic diagram of driver unit for RELCOM S2 switch

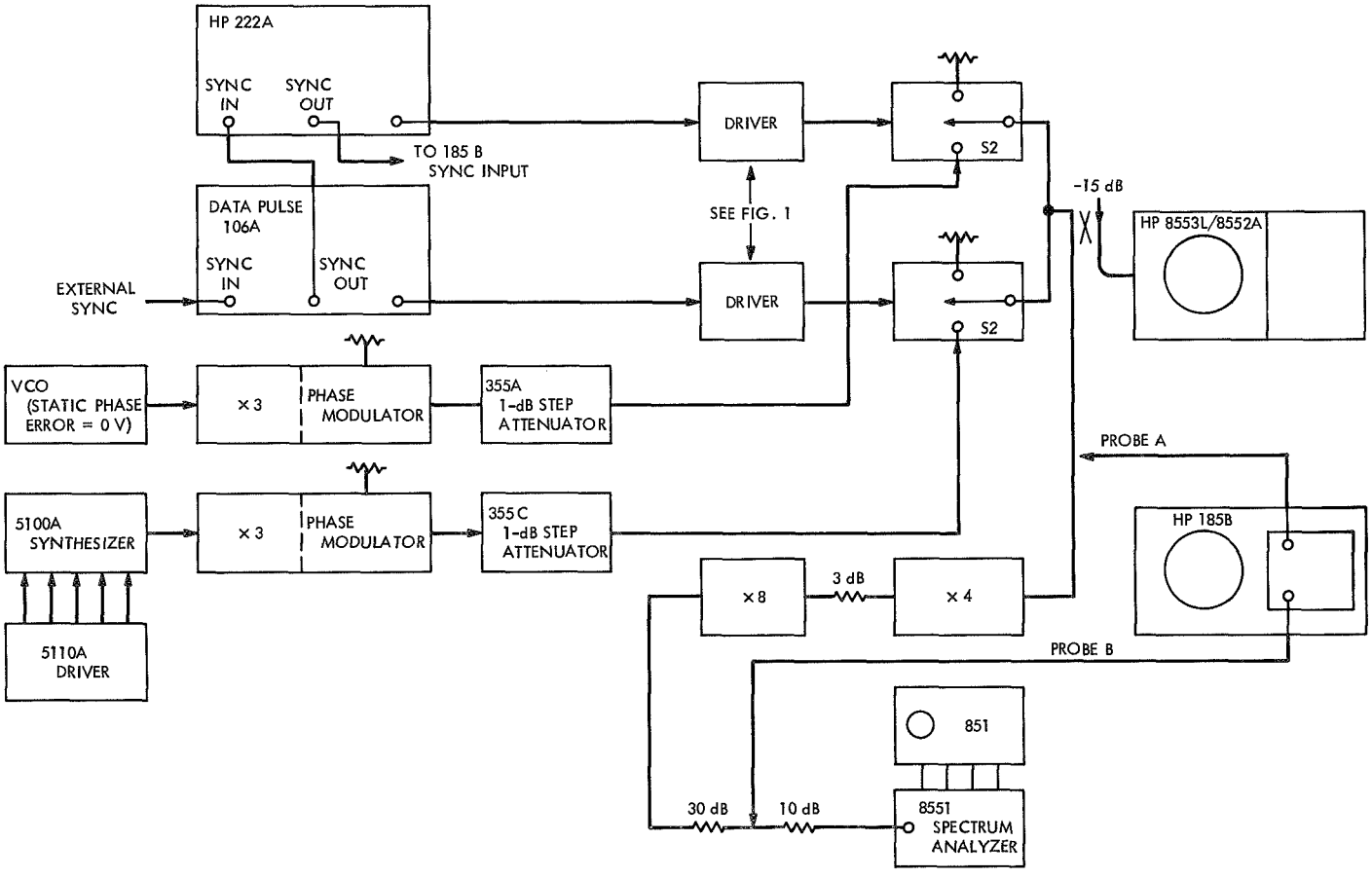

Fig. 2. Switched-carrier spectrum/time domain tests

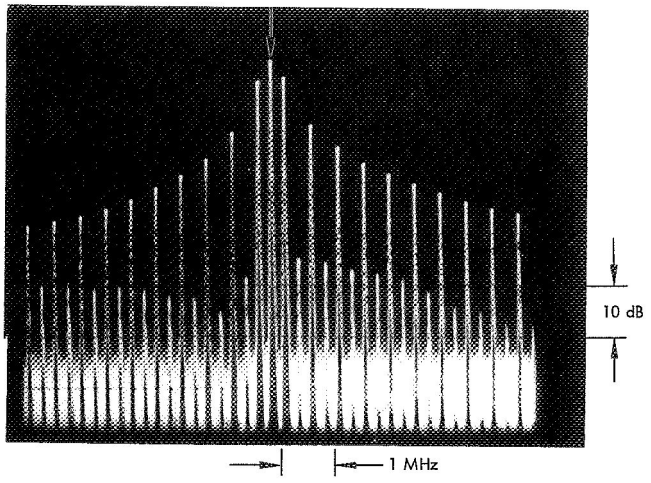

Fig. 3. Typical 66-MHz switched-carrier spectrum

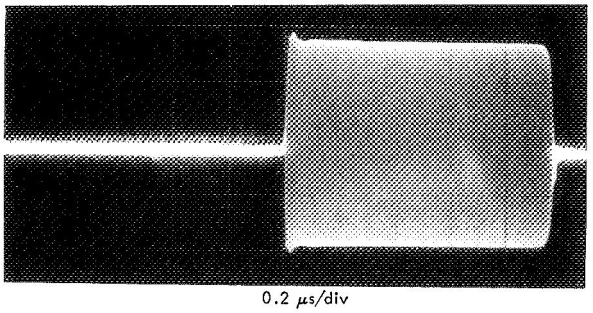

Fig. 4. 66-MHz single carrier

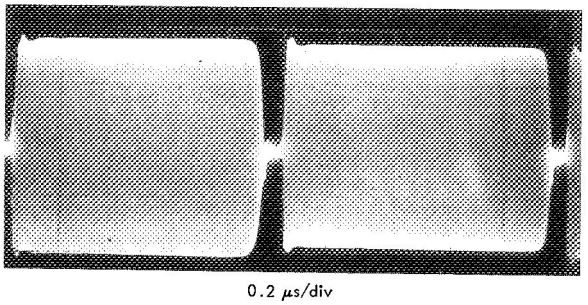

Fig. 5. 66-MHz switching (two carriers)

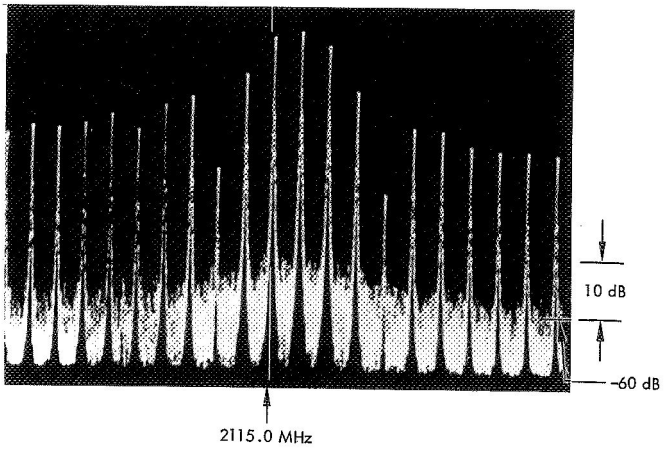

Fig. 6. Output spectrum of DSIF Block III multiplier chain

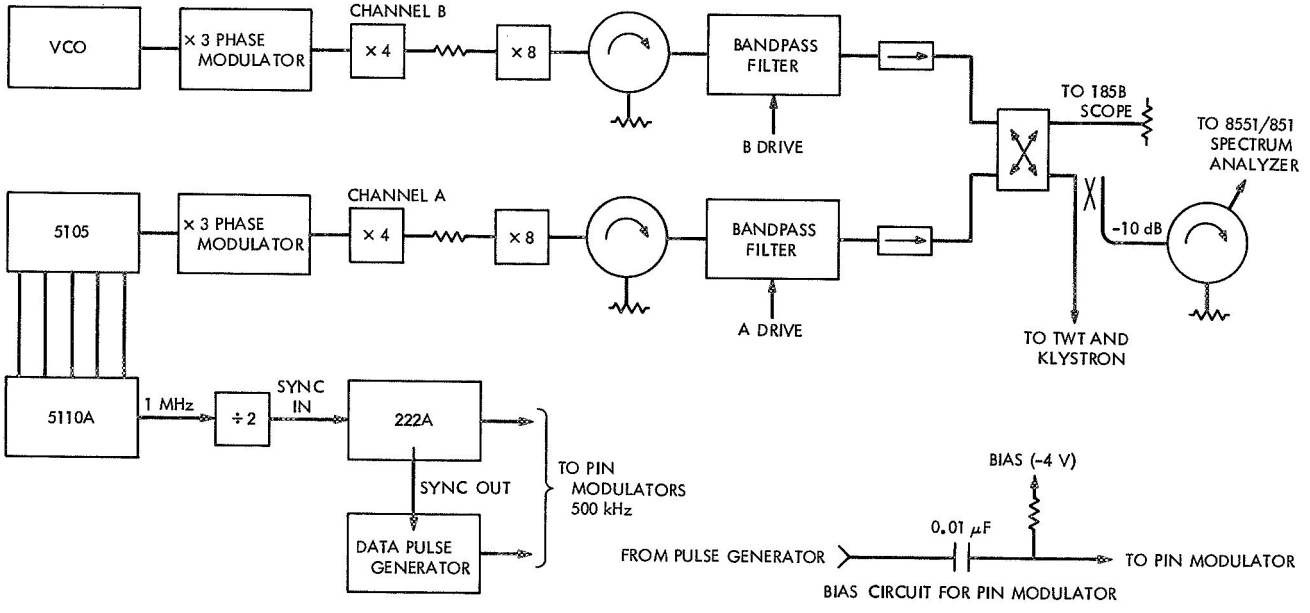

Fig. 7. Equipment configuration for switching at S-band

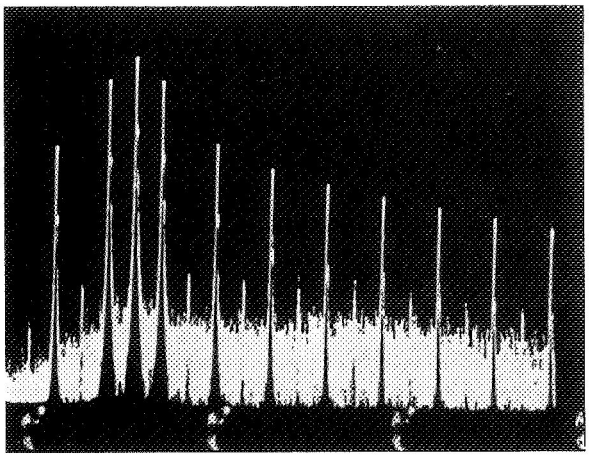

2110.0 MHz ONLY

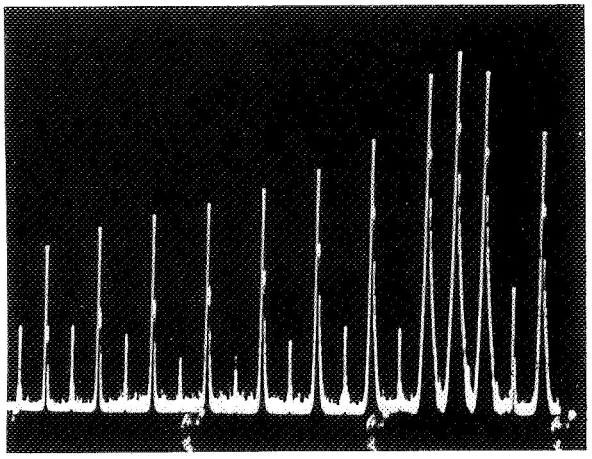

2115.7 MHz ONLY

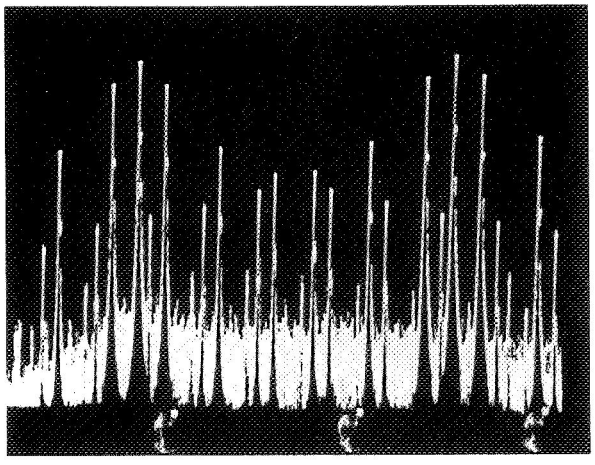

2110.0 AND 2115.7 MHz

Fig. 8. Spectra of drive signal with S-band switching

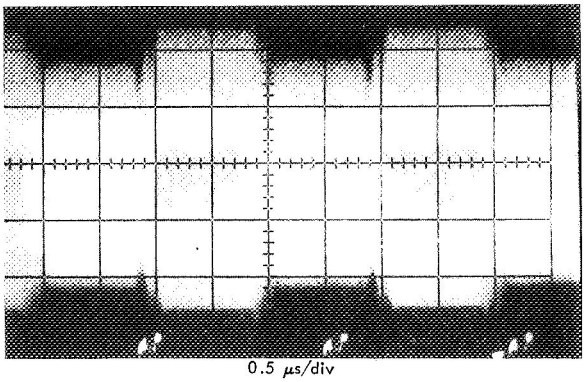

0.5 μs/div

Fig. 9. Time domain display of spectrum in Fig. 8(c)

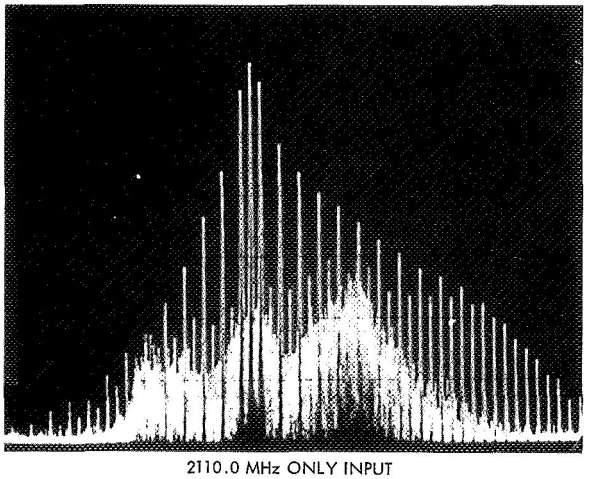

2110.0 MHz ONLY INPUT

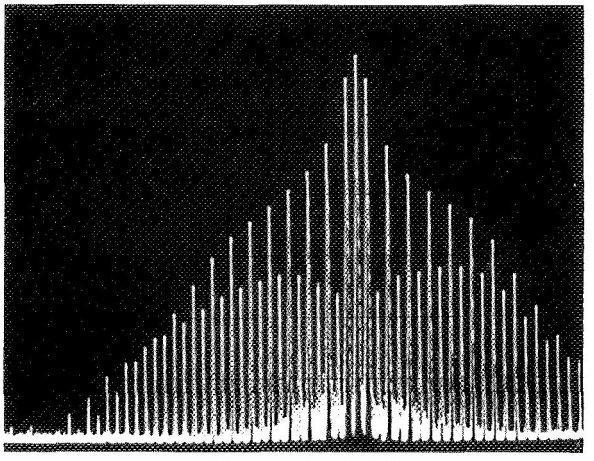

2115.7 MHz ONLY INPUT

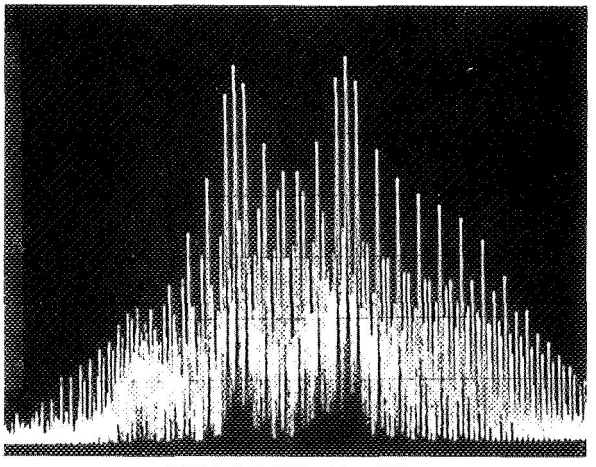

2110.0 AND 2115.7 MHz INPUT

VERTICAL: 10 dB/div
HORIZONTAL: 3 MHz/div

Fig. 10. Input spectra to 5K70SG klystron

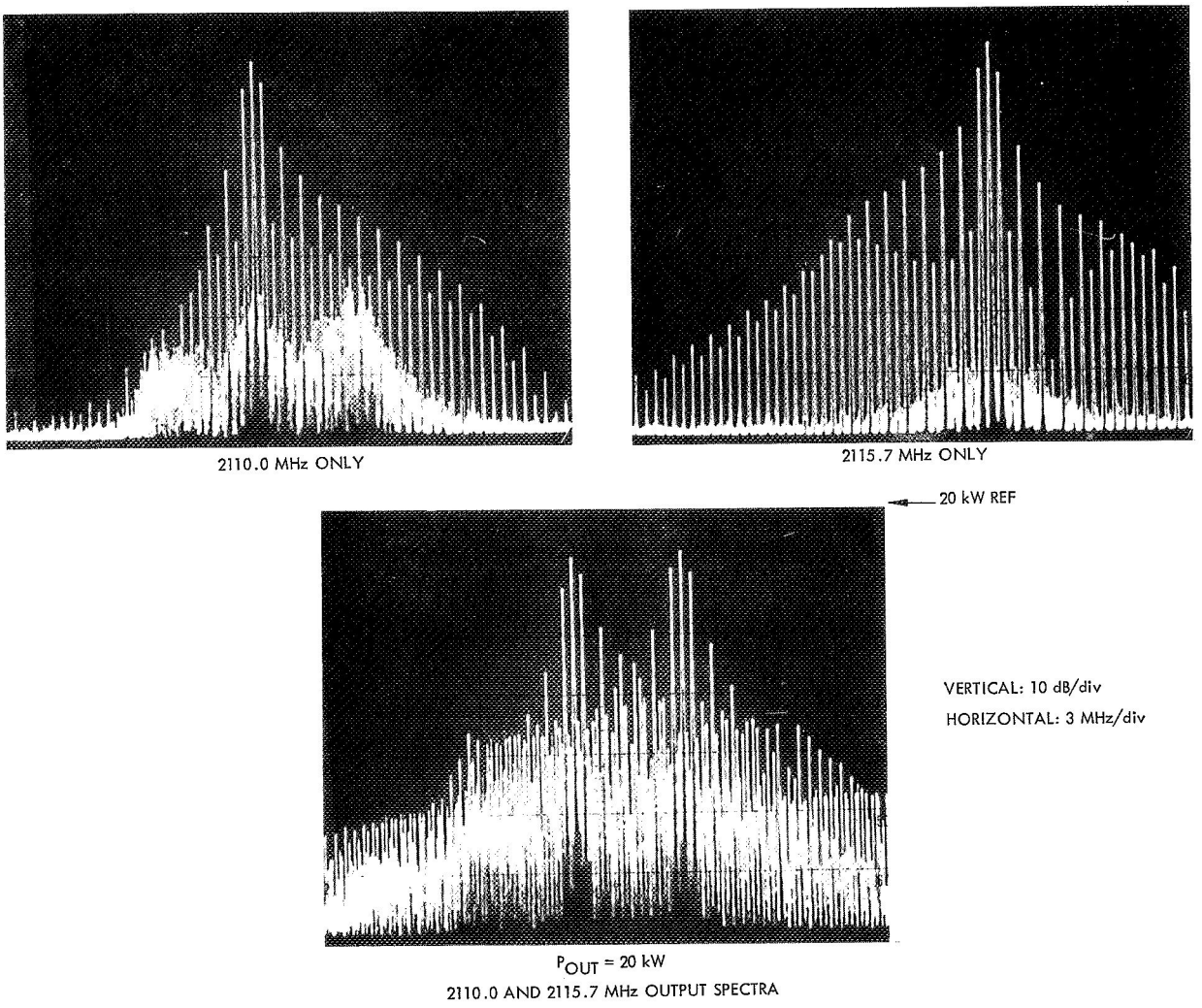

Fig. 11. Output spectra of 5K70SG klystron; S-band switching, 500-kHz switch rate klystron broadband-tuned

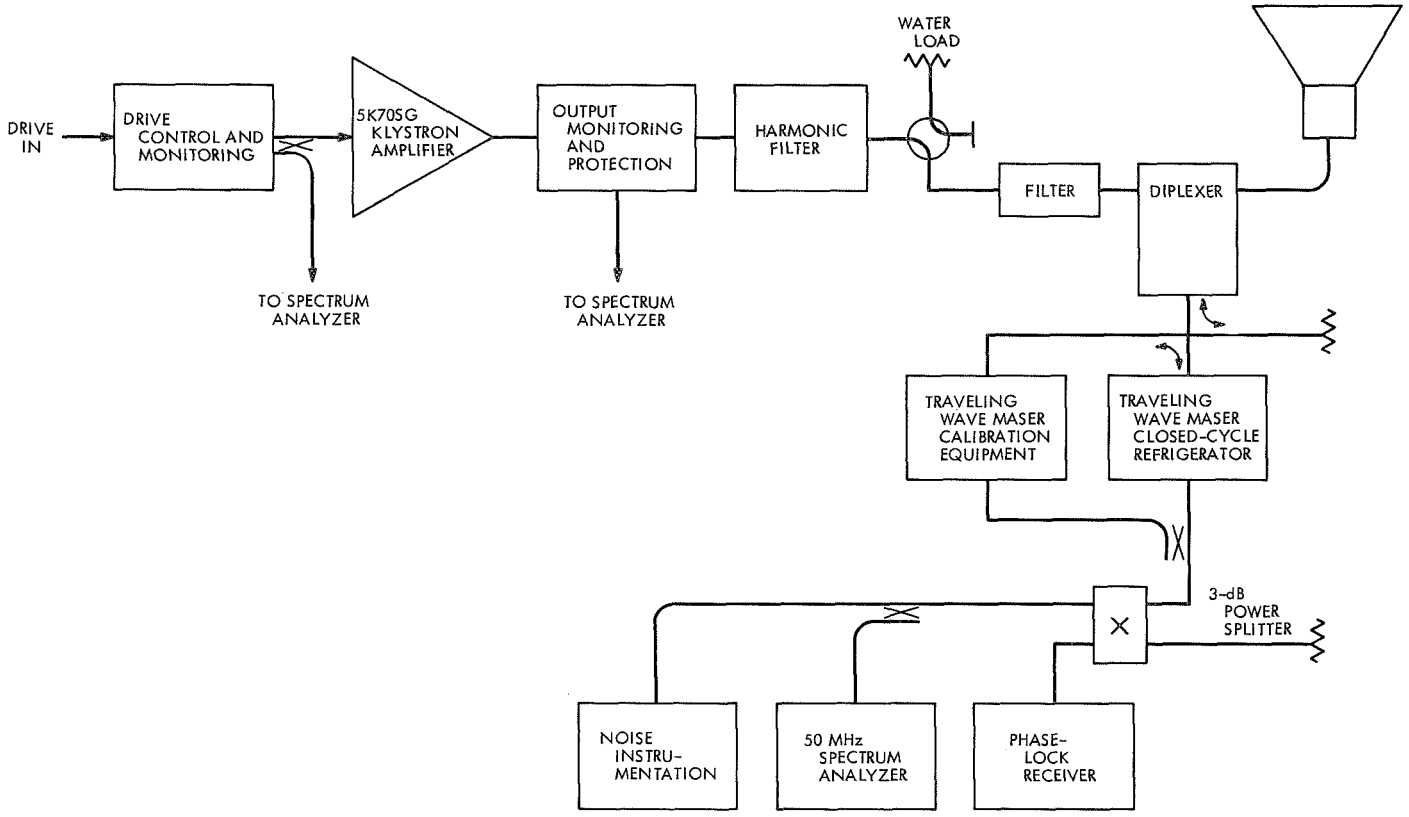

Fig. 12. SCM/TWM test configuration

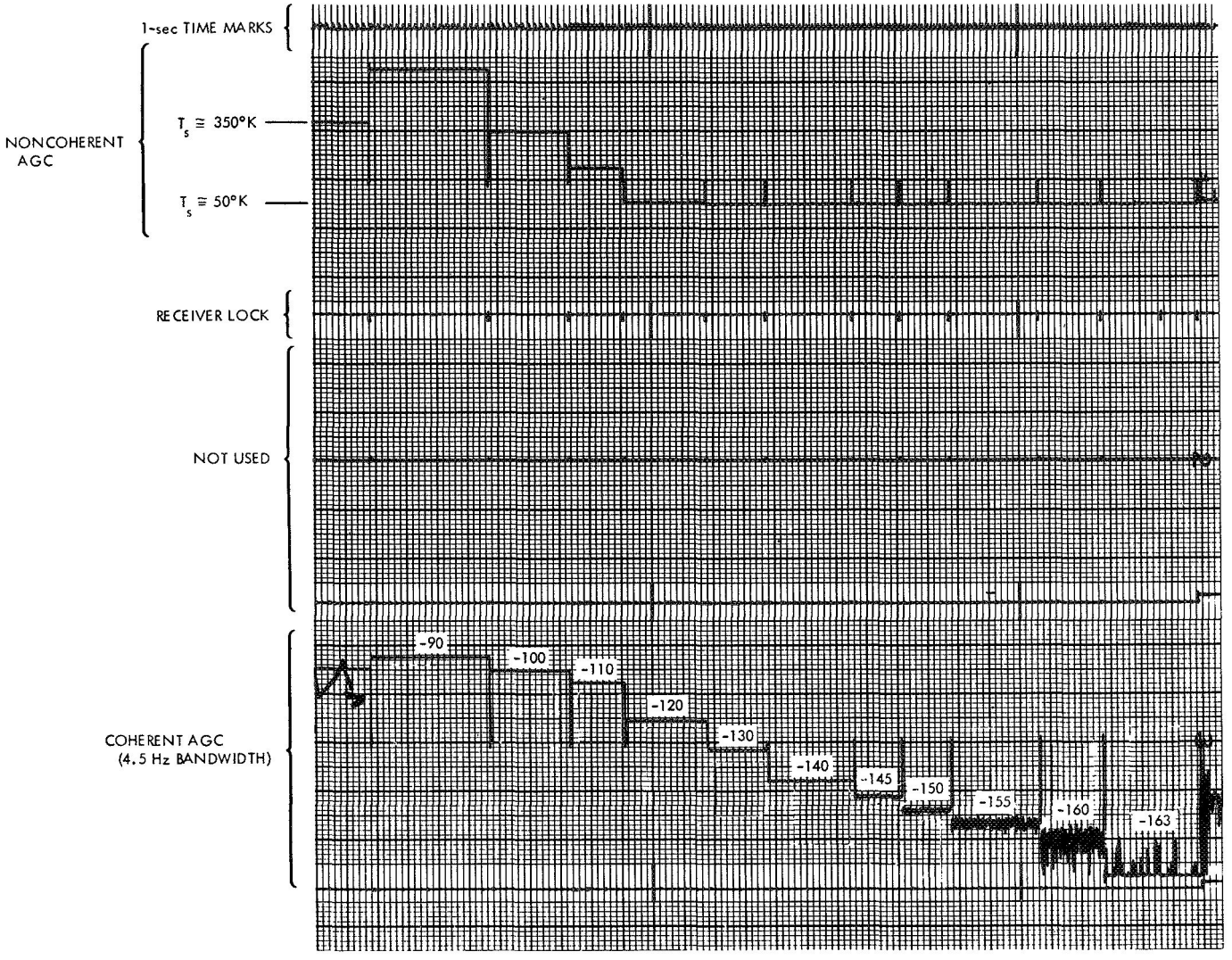

Fig. 13. Chart recorder output at DSS 11

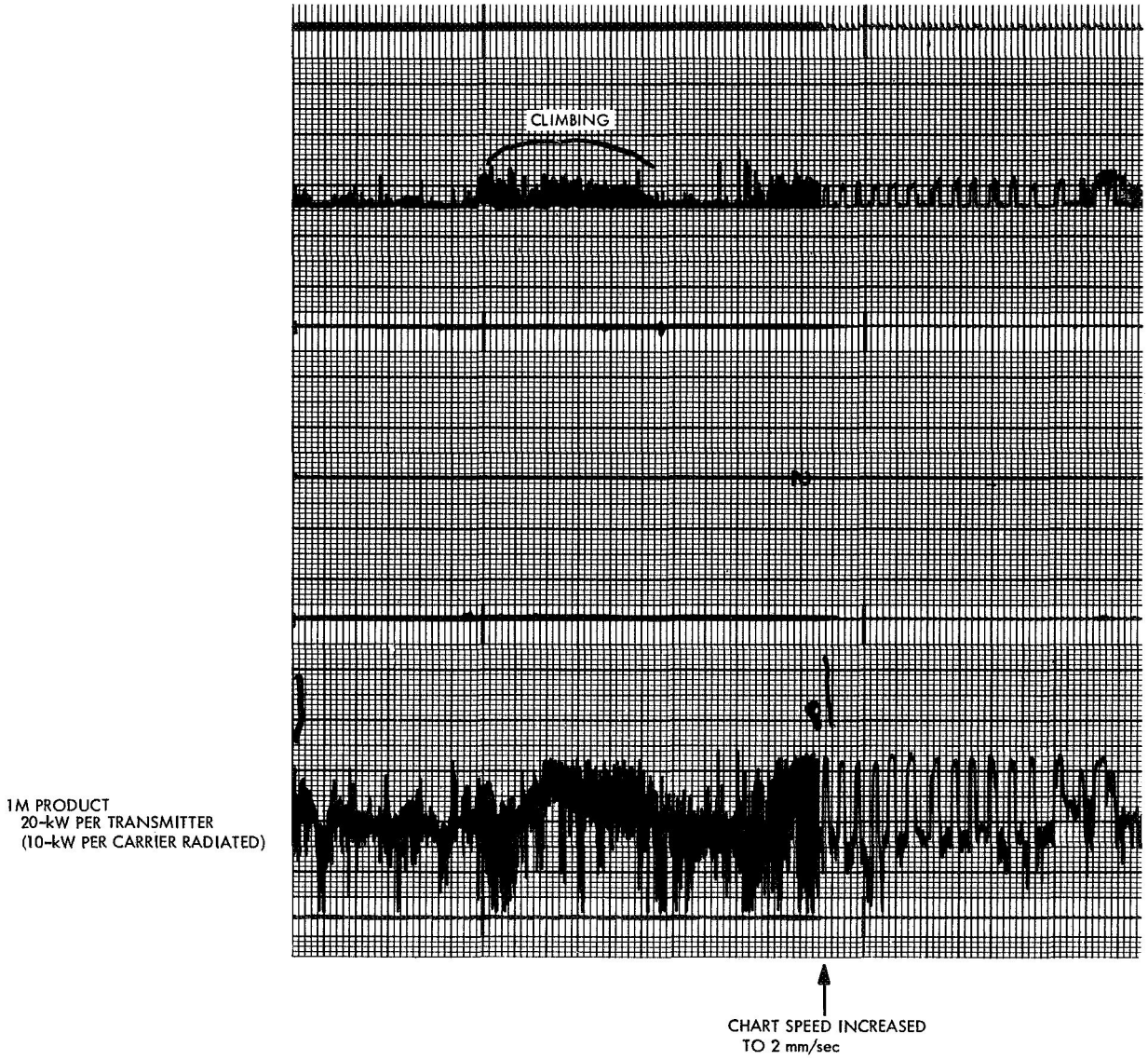

Fig. 14. Noise bursts and IM product amplitude at DSS 11

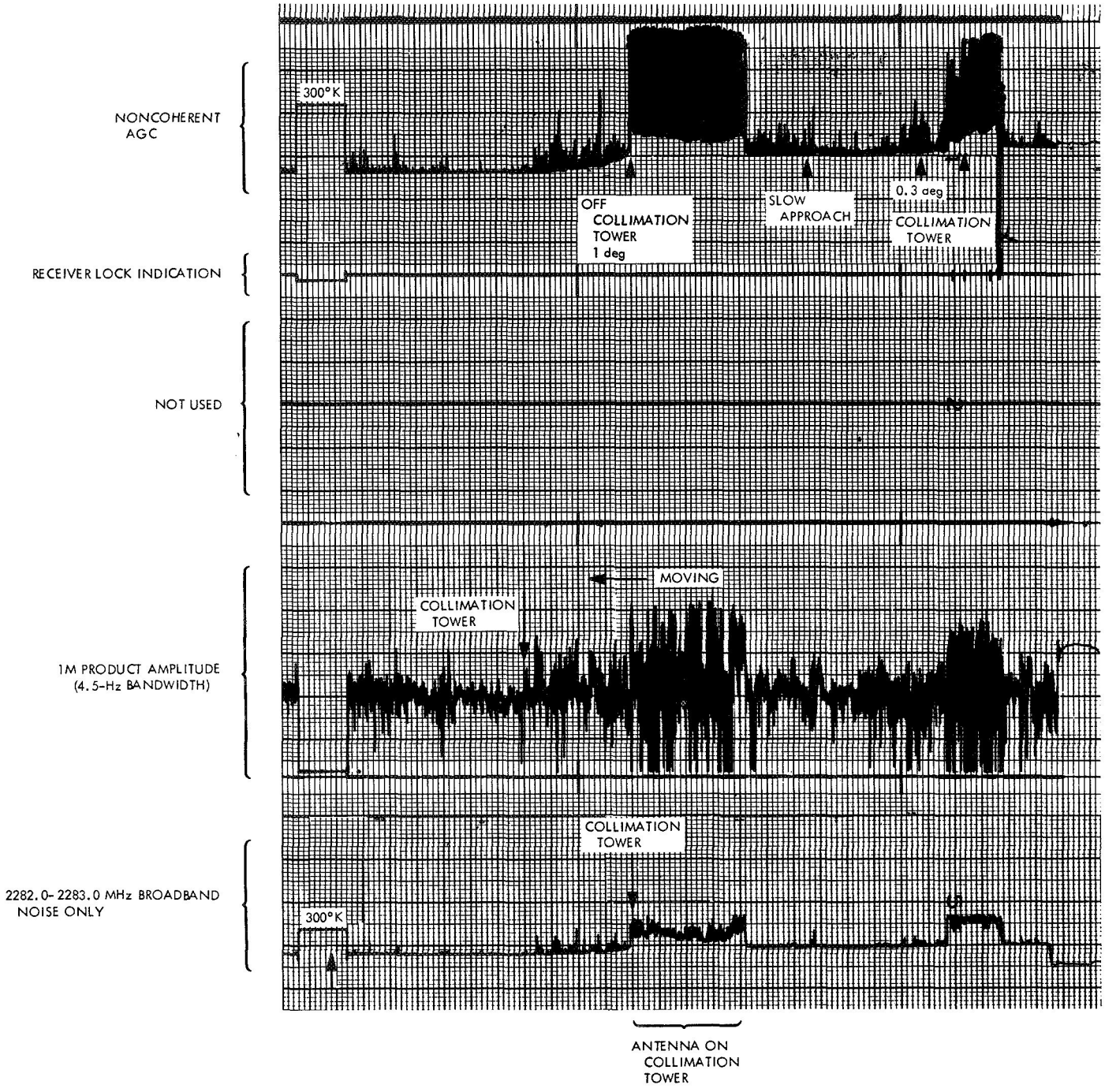

Fig. 15. IM product amplitude and broadband noise with antenna pointed to vicinity of collimation tower

A New High-Voltage Crowbar

E. J. Finnegan
R. F. Systems Development Section

A crowbar is described which is capable of holding off very high voltage, 80 kV or greater, using two or more mercury-pool ignitrons connected in series. This system will replace a single high-voltage ignitron which has required lengthy processing prior to use and which failed to stand off voltages above 70 kV. It was necessary to perfect a higher voltage device in order to improve the reliability of the crowbar used to protect the high-powered (high voltage) klystron from self-destructive arcs. An experimental version of the crowbar was built and operated. Also an experimental photon generator, using a light-emitting diode and fiber optics and a silicon-controlled rectifier with which to pulse the ignitron, was built and tested. Test results are presented, and the performance has been essentially as predicted. The device will be used on the 400-kW transmitting subsystem.

I. Introduction

The 400-kW transmitter located at GDSCC utilizes a klystron to generate and transmit the necessary RF signals to track and recover telemetry from space vehicles. Due to the high voltage (70 kV) used on the klystron tubes, they may experience internal arcing. This arcing can very easily destroy the klystron. Therefore, it is advisable to protect the tube from these high-voltage arcs by the use of a crowbar. A crowbar is a protective instrument that detects high-voltage arcs in the klystron and short circuits the destructive high currents from the klystron through the crowbar until the high voltage can be removed. A number of different types of crowbars were considered: triggered spark gaps, spark gaps, thyratrons, and mercury pool ignitrons. Most devices could not handle the high current, high voltage, or were too slow, but the chief problem was the high voltage. An earlier version of an ignitron protective device (crowbar) was designed and developed in 1967 using a multigridded ignitron (NL1028). See Ref. 1. These ignitrons were designed to operate at high voltage; however it was found that only a very small percentage of tubes manufactured may be used for high voltage. Their initial cost is very high and the yield is poor; a new tube requires 72 h of processing prior to use. These are the events that led to the development of the new series ignitrons. Therefore, it was decided to place two smaller 50-kV

mercury-pool ignitrons in series so as to use their excellent high-current characteristics and their fast response time. The 50-kV unit has been in volume production and has a good record for reliability. This paper will present data to this date and outline future plans.

II. High-Voltage Crowbar System

Figure 1 shows the two mercury-pool ignitrons as they are mounted in their plastic tubing and corona shield, and Fig. 2 shows the electrical schematic as the ignitrons are connected.

In this configuration, the tubes must be triggered on simultaneously; they can be gated on with a balanced pulse transformer or as shown in Fig. 2. The latter technique was chosen because the pulse transformer would have to be insulated for 35 kV and balanced. This would make the transformer very large and cumbersome.

Figure 2 shows the experimental configuration. Each tube (GL37248) has a maximum hold-off voltage of 50 kV. Theoretically, the crowbar system described herein is capable of 100 kV and would be more than adequate for reliable operation in the 400-kW transmitter at 70 kV. The circuit operates in the following manner. If the klystron arcs, the arc is sensed and develops a pulse through a light-emitting diode (diode laser), which will be explained later. This infrared pulse is transmitted through fiber optics to the high-voltage deck and triggers an infrared detector which, in turn, gates a large silicon-controlled rectifier (SCR). The SCR must be capable of being pulsed for 10 μs and must carry 1000 A. This pulse is then applied to the ignitor through a step-up transformer which, in turn, ionizes the mercury in V1. V1 then conducts discharging C1 through R4. The voltage drop across R4 ignites V2 which goes into conduction also. The ignitrons are almost a perfect switch when conducting, the internal resistance being only 1 mΩ. The small power supply in Fig. 2 is connected to the holding anode. This is needed if the current decreases too fast and turns the tube off (squelches the mercury arc). Test results indicate that this does occur at lower voltages, 50 kV or less.

One of the problems existing in the crowbar is that the cathode is floating at -70 kV. This means that isolation must be maintained between the photon generator operating at ground potential and the ignitor firing circuit operating at klystron cathode potential. Figure 3 shows a block diagram of the entire protective system. Isolation is accomplished by generating infrared pulses using a gallium arsenide (GA) laser, transmitting these photons through the light pipe (isolator) and triggering the infrared detector on the high-voltage deck which develops the high-powered pulse to the ignitor and causes the ignitrons to conduct. All of the components are solid state. In many of the components separate tests had to be made in order to decide if they were usable. For instance, published data on the large SCR gave a delay time of 1.5 μs, but it was established that if the gate were pulsed hard, the delay was 200 ns, with no apparent degradation. A very sensitive gate circuit had to be developed in order to use the GA laser as there is a large loss factor (75%) through the fiber optics (light pipe). This uses a sensitive, light-activated SCR which triggered another sensitive SCR. The SCR generated an electrical pulse suitable to fire the laser which propagated a light pulse through the fiber optics, and the light detector responded every time.

This crowbar system has been pulsed many hundreds of times and is performing as expected. The measured response time of 3 μs, using the two tubes in series along with the fiber optics, is more than adequate to protect the klystron. The device has been tested at 80 kV, triggers reliably, and passes the 20,000-A surge current without incident.

Further testing will be done in the future with the holding anode power supply in order to evaluate its effects and at voltages above 80 kV.

Reference

1. Finnegan, E. J., "Klystron Protective Device," in *The Deep Space Network,* Space Programs Summary 37-41, Vol. III, Jet Propulsion Laboratory, Pasadena, Calif., Sept. 30, 1966.

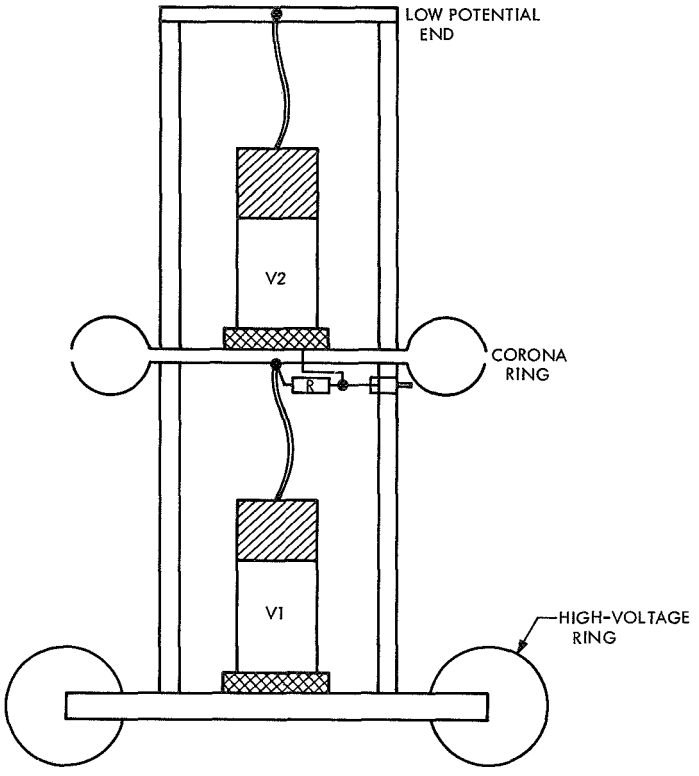

Fig. 1. Series Mercury-pool ignitrons

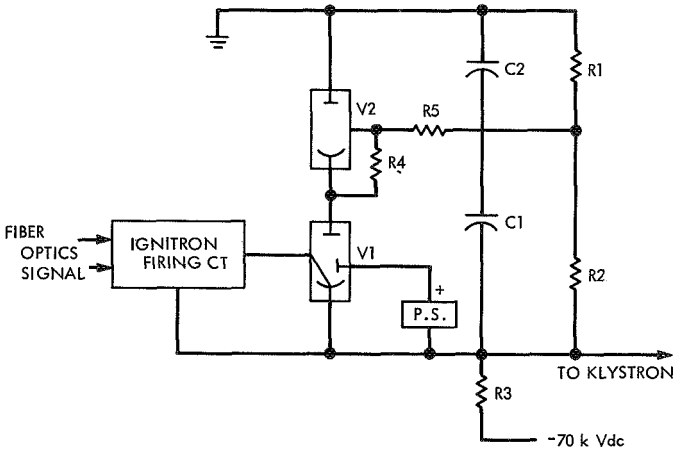

Fig. 2. Experimental configuration, series ignitrons

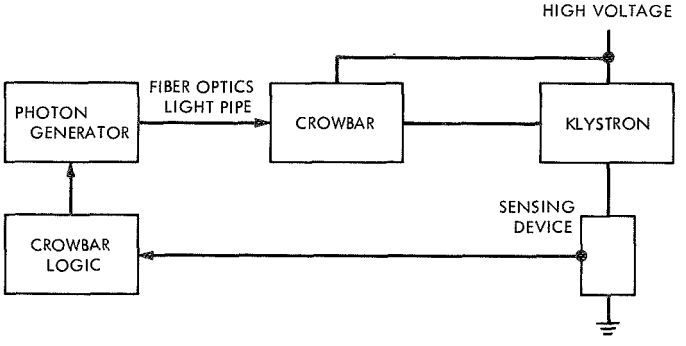

Fig. 3. Crowbar protective system block diagram

S-Band Demodulator

C. F. Foster
R. F. Systems Development Section

This report describes a portable S-band demodulator. The demodulator is a first-order phase-locked loop designed to work directly with the nominal levels out of the Deep Space Instrumentation Facility exciter and or transmitter. This demodulator provides an independent means for verification of the exciter/transmitter performance. Its primary utilization is the measurement of exciter/transmitter, amplitude stability, short-term phase stability, modulation index, bandpass, and modulation fidelity.

I. Introduction

A requirement for a means of evaluating broadband modulation spectrum was defined by the multimission command. Modulation could not be evaluated because no existing instrumentation previously available allowed broadband observation of the total exciter/transmitter chain. To meet these requirements a wide-band demodulator was developed. This device is a first-order phase-locked loop whose predetection bandwidth is two orders of magnitude greater than the exciter/transmitter bandwidth.

II. Implementation

The decision to mount the demodulator in a standard attaché case dictated the use of miniature microwave components. The feasibility model was constructed on an aluminum chassis (Fig. 1). All intermodule cabling is semirigid coax to ensure phase stability versus temperature and vibration. The S-band demodulator is self-contained, requiring only standard 60-Hz line power and a coherent 66-MHz reference signal.

The phase detectors (Fig. 2), and all S-band modules have a bandwidth two decades greater than the exciter/transmitter spectrum bandwidth.

The S-band demodulator has a built-in self-calibration provision which takes a sample of the reference signal and injects it into the demodulator. This self-test provides a measurement of the demodulator amplitude stability and short-term phase jitter.

There are three internal meters that monitor the following functions:

(1) The reference level meter provides assurance that the 66-MHz input is connected, and that the X 32 frequency multiplier, the limiting amplifier, and the voltage-controlled phase shifter are all operating.

(2) The AGC voltage meter provides a measurement of the input S-band signal strength and can be used to set modulation index using the suppressed carrier method. The resolution of this meter is coarse, and is only used when modulation index setting is not critical (i.e., when measuring modulator bandwidth).

(3) The phase shifter input control voltage meter is calibrated in degrees of phase and has a 2-deg resolution. It is used to assure that the voltage-controlled phase shifter is in the center of its linear range and can be used to measure phase shift as well as setting low-frequency squarewave modulation index.

The outputs of the S-band demodulator are two phase detectors, one in quadrature with respect to the other. The 90-deg detector output is used to monitor carrier amplitude. It is calibrated to provide a reading of input level in dBmW into 50 Ω. This output is also used in either the MGC or AGC modes to provide short- and long-term exciter/transmitter amplitude stability. It can also provide an indication of modulation index by measuring carrier suppression.

The 0-deg detector output is used to measure exciter/transmitter short-term phase stability, exciter/transmitter bandpass, and the fidelity and power loss of the command modulation chain, by comparing the input modulation to the demodulated output waveform.

Table 1 lists design goals and achieved performance.

III. Summary

Testing of the demodulator for compatibility with DSIF has been successfully completed at CTA 21.

The S-band demodulator has been used to evaluate fidelity of planetary ranging modulation through the DSIF exciter chain, and has proved useful as a means of trouble-shooting individual exciter chain modules.

The S-band demodulator feasibility model will continue to be used for DSIF exciter-transmitter system performance confirmation and new system development.

Table 1. Design goals and achievement

Parameter	Design goal	Achievement
Relative amplitude of carrier	30-dB range	60-dB range
Modulation sideband spectra	± 2 MHz	13 MHz
Dynamic range	40 dB	45 dB
Noise figure at maximum gain	No specification	9 dB
Amplitude stability	No specification	$\geq .05$ dB
Loop bandwidth	No specification	1 and 0.5 Hz
AGC loop bandwidth	No specification	0.1 Hz
Internal phase meter	No specification	2 deg resolution
Modulation index measurement using square wave modulation	10 to 90 deg	0 to 90 deg

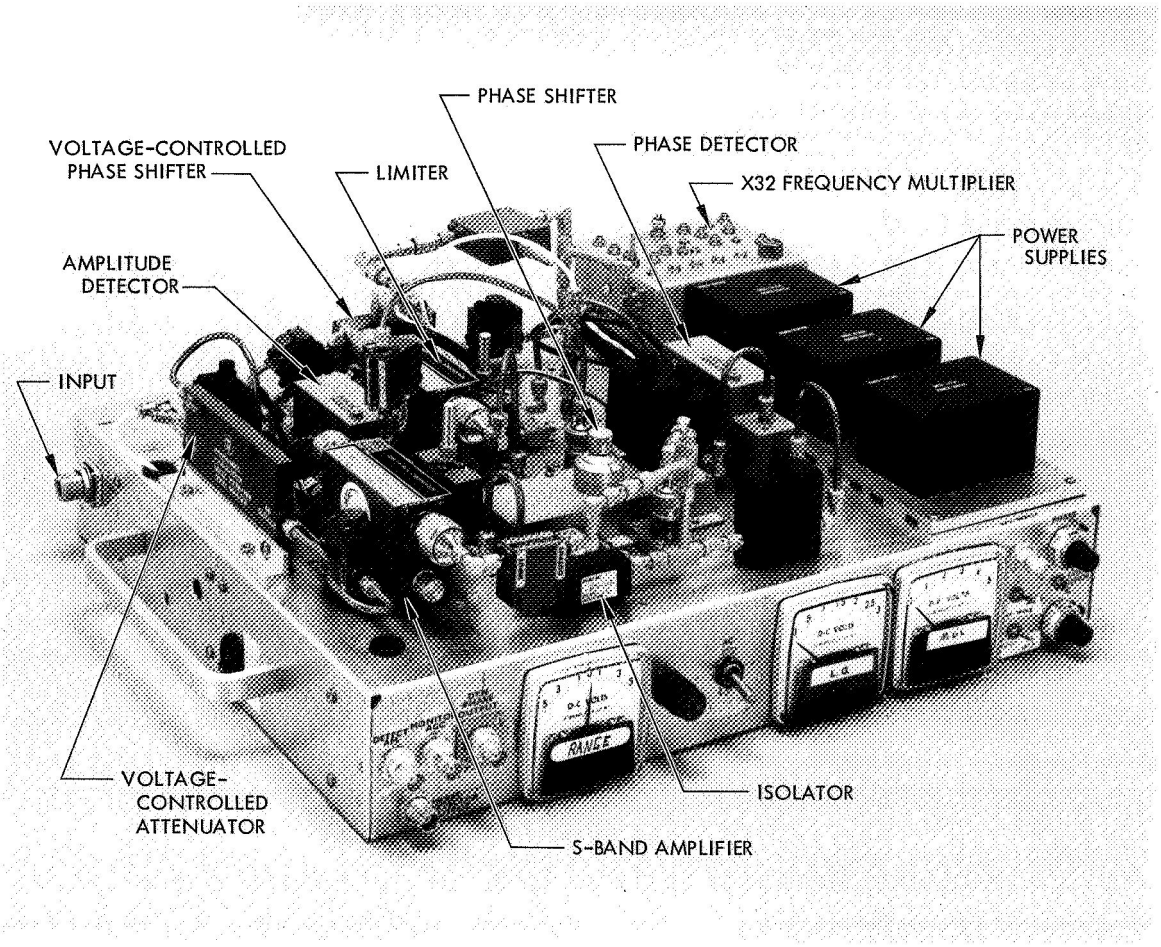

Fig. 1. S-band demodulator

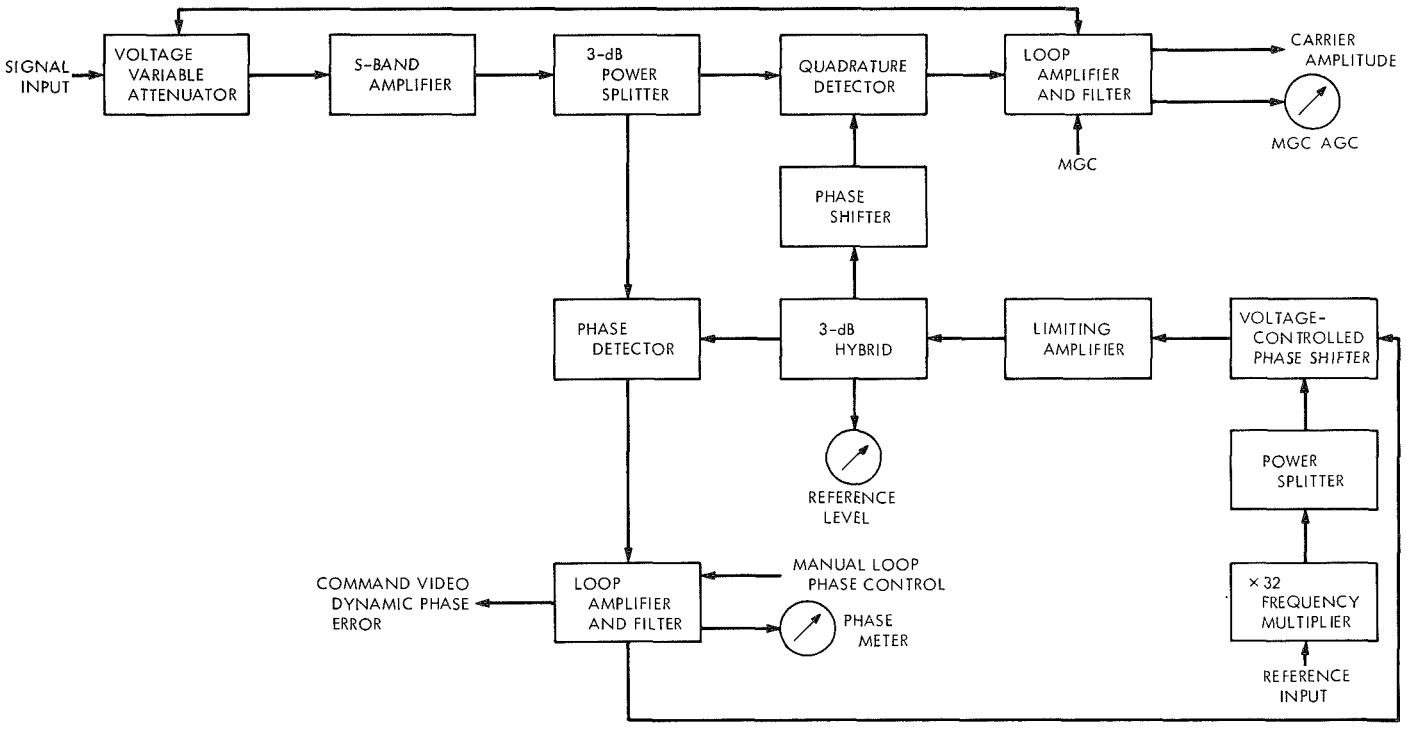

Fig. 2. S-band demodulator simplified block diagram

DSN Research and Technology Support

E. B. Jackson
R. F. Systems Development Section

Major activities in support of the Deep Space Network (DSN) research and technology program are presented for the last 6 mo. Work was performed at both the Venus Deep Space Station and the Microwave Test Facility. Progress and performance summaries are given in the following areas: radiometric observations (20–25 GHz); pulsars and planetary radar; 26-m antenna upgrade; precision antenna gain measurements; weak source observations; and radio star observations (Cygnus A); the Mars Deep Space Station transmitter rework and testing; transmitter development; 100-kW clock synchronization (X-band); switched carrier experiment; 400-kW harmonic filter; dual 20-kW transmitters; horizontal mill installation; clock synchronization transmissions; and acceptance testing of DSIF klystrons.

The Development Support Group, was recently or is currently engaged in the following activities at DSS 13 and the Microwave Test Facility at GDSCC:

I. DSS 13 Activities

A. In Support of JPL Section 325

Section 325 personnel have equipped the 9-m antenna with a multichannel radiometer operating between 20 and 25 GHz. On a noninterference basis, they have been making radiometric observations, principally of Venus, but also of various radió sources and interstellar and intergalactic spaces, for several years. They time share the antenna, antenna drive computer, and servo system with the Development Support Group of Section 335 on a noninterference basis.

B. In Support of Section 331

1. Pulsars. In a continuing program, ongoing now for more than two years, twenty of the approximately fifty known pulsars are observed at DSS 13 at 2388 MHz. The averaged pulse power density spectrum of each pulsar, the pulse spacing (to eight significant figures) and pulse arrival time at the DSS 13 26-m antenna comprise the data extracted from these observations. With timing controlled by a cesium frequency standard, the receiver output is sampled at a rate of 5,000 samples per pulse

period (except for pulsar 0833, which is sampled at a rate of 5,000 samples per three pulse periods) and data from successive pulses are integrated to improve the signal-to-noise ratio. (Table 1 tabulates the pulsars which are regularly observed.)

2. Planetary radar. In another continuing program, from the inception of DSS 13, various planets are illuminated with a CW or PM signal and the reflected signal is received. The planet Venus is the target most observed. Mars and Mercury have also been successfully observed, using both total spectrum and ranging techniques. (High-precision ranging of Mars was performed prior to *Mariner* 1969 encounter to provide the project with an improved ephemeris for use during the encounter sequence. Range to the surface of Mars was measured to a resolution of better than 1500 m.)

Using bistatic techniques (transmitting from DSS 13 and receiving at DSS 14), the range to Venus and Mercury is currently being measured on a weekly basis. The range resolution to Venus is better than 1500 m, while the resolution to Mercury is somewhat worse. Various transmitter powers have been used over the years in which this project has been continuing, but currently we use 400 kW at DSS 13 and will have 400 kW at DSS 14 later this year. (The DSS 14 transmitter has been removed and is undergoing renovation at DSS 13.)

C. In Support of Section 332

1. 26-Meter antenna upgrade. During a three-month period commencing in January 1971, extensive structural work was done on the 26-m antenna. It had been discovered during previous studies that the moment arms of the two elevation ball screws were not identical, and this differential movement caused localized distortion of the attaching girder, resulting in a raised area in the dish surface. By mounting the elevation bearing of one of the ball screws on an eccentric (a 6.35-mm [¼ in.] eccentric was used after a 3.2-mm [⅛ in.] one was discovered to not have enough range) and adjusting it, the localized dish surface distortion was minimized.

Three-inch angles were welded into a truss structure to increase the stiffness in the outer ring of the antenna backup structure and were installed behind the outer row of surface panels. Measurements of surface deformation due to gravity were taken before and after installation of the stiffeners, but data reduction had not yet been accomplished. After the changes to the elevation bearing and the installation of the stiffeners, the surface deviation from the desired parabola was measured and panel adjustment accomplished for a best-fit parabola. Unfortunately, weather conditions prevented complete measurements from being made within the scheduled time and the data set is incomplete.

D. In Support of Section 333

1. Precision antenna gain measurement. Using the ALSEP left on the Moon by *Apollo 12* as a collimation signal source, observations are being made with the 26-m antenna and a gain standard horn (gain measurement traceable to NBS) in order to measure the ratio of power received by the two antennas. Observations made to date indicate that overall stability is worse than anticipated, and digital processing techniques will be necessary to data collection, rather than the simpler analog chart recordings which had been planned. A program has been written[1] for this effort which samples the receiver AGC voltage once per second, and records the output level, along with a time tag and a start-run stop-run signal, onto magnetic tape. The program also provides simultaneous printout of sample values while recording. Run-to-run averaging, plotting of results on an X-Y plotter and punching averaged runs onto paper tape while recording on magnetic tape is also provided. Operational utilization of this data collection approach will commence on April 15, 1971.

2. Weak source observation. To improve the minimum observable change in total system temperature while observing weak radio sources, the effects of gain changes in the receiving system are removed by time sharing the system between a signal from the radio source and a signal from the radio source plus a calibrated noise source (noise diode). Knowing the noise power output to be expected from the calibrated noise source, the effects of gain changes subsequent to the injection point can be computed and corrected. The antenna pointing, keying of the noise diode, sampling of the receiver output and computation are done by the SDS-930 computer. Work is under way to provide an addition to the program which will "scan" the antenna back and forth across the source in a "raster" scan similar to the manner in which the electron beam in a television set scans the face of the CRT. Current schedules provide for weak source observation for 24 h each month.

3. Radio star observations (Cygnus A). To provide data on a radio source which can be used by all the

[1]By Robert Gosline.

DSIF stations, observations of Cygnus A are made and the increase in system temperature resulting from this source is measured. These data, along with the gain ratio data from the ALSEP observations, can then be used by other DSIF stations to make antenna gain measurements by measuring the increase in their antenna system temperature when observing Cygnus A. For the Venus station 26-m antenna, the measured increase in system temperature from Cygnus A clusters around 100°K, but further measurements will narrow the error bars on this data.

E. In Support of Section 335

1. DSS 14 transmitter rework and testing. On March 15, 1971, the two 400-kW transmitters were removed from DSS 14 and brought to DSS 13 for rework and acceptance testing in preparation for official transfer to an operational status. Reinstallation of the DSN 400-kW transmitter is scheduled to take place not later than July 1, 1971.

2. Transmitter development. As part of the continuing program of development carried out by Section 335, generation of dual uplink carriers is being experimented with at DSS 13 by use of two separate exciters whose outputs are combined and used as input power to the 400-kW klystron. To reduce intermodulation distortion, the power levels are reduced to a nominal 40 kW per carrier. Measurements are made of the resulting sideband amplitudes, stability, frequency pulling, etc.

Transmitter automation approaches are being tested at DSS 13. The first step is installation of a programmable high-voltage control and monitoring circuit in which the desired voltage level is loaded into registers and the device then brings up high voltage and maintains it at the desired point. Installation of a computer for monitoring of several hundred test points, as well as control of the system, is planned for the near future.

3. 100-kW Clock synchronization (X-band). By installation of a larger capacity heat exchanger and cooling water circulation system, modification of the high-voltage power supply for higher voltage, and procurement of a new transmitter klystron and feed system, the power output of the clock synchronization transmitter will be increased to 100 kW at 7149.9 MHz as compared to 25 kW at 8450.1 MHz now existing.

Strengthening of the antenna-mounted electronics house has been completed, the installation of a stronger floor is one half completed, a platform and associated hoist has been installed for raising and installing the transmitter klystron, and additional power capacity for operation of pumps and fans has been installed on the antenna.

An auxiliary power supply has been installed with which to maintain operation while connection and initial testing of the final high-voltage supply is underway. The solid-state rectifier, high-voltage transformer, and filter capacitor and choke for the final high-voltage power supply have been installed in the power supply building (G-61). Work continues on a noninterference basis with operation of the clock synchronization transmissions.

F. In Support of Section 337

1. Clock synchronization transmissions. Using the 9-m antenna, equipped with a 25-kW transmitter operating at 8450.1 MHz, pseudonoise-coded, phase-modulated signals are broadcast to DSSs 14, 41, 42, 51, and 62 using the moon as a reflector. These transmissions, whose frequency and timing are controlled by a rubidium and cesium frequency standard, allow the receiving station to compare time within plus/minus 10 μs with the master clock at DSS 13. The DSS 13 clock is adjusted as necessary to maintain a time within ± 3 μs of NBS clock 8. (Generally the adjustments are made just prior to each transmission, and resolution of 0.1 μs with reference to the timing pulse from the Standard Laboratories at DSS 12 is achieved.) Operation on this system, which has been out of service for 15 days for modification, will resume on April 15, 1971 with an increase in transmitter power to 100 kW planned for October 1, 1971, at which time a frequency change to 7149.9 MHz will take place.

II. Microwave Test Facility (MTF) Activities

A. In Support of Section 335

1. Switched carrier. In general support of the requirement for generation of two simultaneous uplink carriers, an investigation[2] into timesharing a single transmitter klystron between two exciters, has been under way for approximately nine months. Technical feasibility has been demonstrated, but no spacecraft experiments were conducted. A more detailed look at this investigation is given in "Switched Carrier Experiments" by Richard Kolbly, which appears on p. 133

2. 400-kW Harmonic filter. The installation of the DSN 400-kW transmitter at DSS 14, operating at the

[2]Suggested by Mahlon Easterling.

spacecraft uplink frequency (2115 MHz) rather than the research frequency (2388 MHz) used at DSS 13, necessitated suppression of harmonic radiation lest it interfere with the spacecraft downlink reception. Procurement of a harmonic filter, in WR-430 waveguide, to operate at this power level, proved somewhat difficult and problems were experienced with noise bursts.

Examination of a partially disassembled filter indicated that it contained dirt, copper shavings (machining residue), general debris and some unknown chemical deposits or growth. After consultation with the manufacturer to determine what adhesives were employed in construction of the device, cleaning was undertaken. While disassembled for cleaning, modifications to the water cooling circuits were made to improve cooling and decrease leak problems. Due to the segmented construction of the harmonic absorbers, cleaning was difficult, but by use of special solvents and careful manual scrubbing, the filter was completely cleaned, the water circuits modified, and the filter repainted white.

3. ***Dual 20-kW transmitter.*** To improve test capability, and also to have the capability for conventional generation of dual carriers, a 20-kW transmitter (surplus from the STADAN project) was obtained and installed. This second transmitter is now operational and the Microwave Test Facility can simultaneously generate two 20-kW carriers at appropriate uplink frequencies.

4. ***Horizontal mill.*** For increased efficiency in fabricating waveguide sections and milling of waveguide flanges, a horizontal mill (surplus from Edwards Air Force Base) was obtained and installed. The machine has been connected to power, thoroughly cleaned, motor operation verified, and is ready for operation as soon as cutting heads are installed.

B. In Support of Section 337

1. ***Acceptance testing of DSIF klystrons.*** To avoid a testing operation in an operational DSIF station, incoming transmitter klystrons are brought to the MTF for formal acceptance testing. The klystron is tuned, bandwidth and drive requirements ascertained, compliance with power output specifications verified, and nominal values of all parameters, especially magnet current, obtained. These data are recorded onto an acceptance test data sheet which is then packed with the klystron when it leaves the facility for its station destination. Additionally, klystrons removed from DSIF stations are tested at MTF to ensure that the klystron is, in fact, defective, prior to shipment to the vendor for rebuild or repair. During the year ending April 1, 1971, twenty-four DSIF klystrons have been tested at MTF, either for incoming acceptance tests or verification of reported failure.

Table 1. Pulsars currently being observed at DSS 13 at 2388 MHz

Pulsar	Sidereal hour angle	Declination
0031	351.834	352.497
0329	307.314	54.482
0525	278.253	21.986
0628	262.577	331.438
0823	233.728	26.722
0833	231.415	314.929
0950	212.098	8.070
1133	186.368	16.011
1237	170.423	25.045
1642	109.164	356.750
1749	92.221	331.891
1818	85.169	355.591
1911	71.915	355.250
1929	67.291	10.926
1933	66.384	16.210
2016	55.788	28.571
2021	54.606	51.765
2045	48.267	343.618
2111	41.882	46.684
2218	25.209	47.769

Description of a Telemetry Procedural Language

R. I. Ścibor-Marchocki
Flight Operations and DSN Programming Section

A procedural language and a compiler for it are being developed as an aid in the writing of programs which will process telemetry data received from spacecraft. This article describes the language. Also, the philosophy that leads to the choice of the language is briefly presented.

I. Introduction

A study has been undertaken to demonstrate the effectiveness of a high-level programming language in the design of a mission-independent telemetry processor. While an assembly language provides greater freedom to the programmer, the greater ease, hence speed, with which a program can be written in a high-level language can be decisive in a real-time environment.

As a first step in this study a Telemetry Procedural Language (TPL) has been defined. TPL is oriented toward the specific programming procedures involved in a subset of a telemetry processor. This subset has been chosen because (1) it constitutes a relevant part of the whole telemetry software subsystem, and (2) it requires extensive changes from one mission to another. In the design of TPL, a large choice of sophistication nuances was available. A descriptive approach requires from the programmer only the description of the processor. A more functional approach provides the programmer with very powerful tools, but the concern with the program logic is left to him. Each approach has its own advantages as well as disadvantages. A descriptive language depends heavily upon the actual configuration of the telemetry processor, and the corresponding compiler generates progressively worse code as the configuration changes from the original one. A functional language, however, is much more versatile and more suitable in a mission-independent environment. Hence, TPL has been defined as a functional language.

II. Formal Specification of TPL

A given language, e.g., TPL, has to be described in some language. A language which is used to describe another is called a meta-language. English can serve as such a meta-language. However, ordinary English is not concise enough and lacks the necessary precision. The Backus–Naur Form (BNF) is somewhat better, but still inadequate.

The transmogrification language (TMGL) is similar to the BNF and may be used to specify a given language. TMGL is both human-readable (i.e., a publication language) and computer-readable [i.e., by the transmogrification (TMG) system]. A specification of a given language, consisting of the grammar and a translation into another language (usually an assembly language) written in TMGL, can be compiled by the TMG system to yield a compiler for the given language. Therefore, such a speci-

fication of a given language is definitive: There can be no discrepancy between the human-readable specification and the compiler's performance.

This article provides an informal specification of TPL. A formal precise specification of TPL is being written in TMGL.

III. The Features of TPL

TPL is a FORTRAN-like language. Most of the usual features of FORTRAN IV H are provided in TPL. The four features of FORTRAN IV which intentionally are not part of TPL are:

(1) There are *no* DOUBLE PRECISION variables or constants.

(2) There are *no* COMPLEX variables.

(3) Variables may *not* be declared as either REAL or INTEGER. Instead, they are identified exclusively by their initial letter.

(4) The EQUIVALENCE statement is *not* allowed.

TPL is intended to be a living, growing language; thus, new features will be introduced as the need for them arises. The following material describes those features, beyond FORTRAN, which already have been introduced into TPL.

A. Commas Are Optional

Commas are optional as syntactical delimiters between like entities. If a syntactical confusion would result, a delimiter is necessary but may be either a space or a comma. For example, one may declare

```
DIMENSION A(11 12 13)B(14 15)
```

The easy safe procedure that may be adopted by the programmer is to employ a space wherever FORTRAN would desire a comma or a space. However, the specific rules are as follows:

0 Excess spaces are permissible, except inside of a word.

1 A space has to be used as a delimiter between the logical operators X or V and any preceding or following name of a variable.

2 A space has to be used as a delimiter between the logical operators X or V and any following constant.

3 A space has to be used as a delimiter, on one side only, when the logical operator . is preceded by an integer constant and followed by a constant.

4 A space or a comma has to be used as a delimiter between a constant and a following constant.

5 A space or a comma has to be used as a delimiter between a variable and a following variable or constant.

6 A space has to be used as a delimiter between a keyword and a following variable or constant.

Violation of any of these rules may lead to an unpredictable misinterpretation, consisting of one or more of the following results, listed in order of decreasing probability:

1 Erroneous target code, which will yield incorrect computed results during execution.

2 The error message "incomprehensible."

3 Correct recovery.

4 Other error message(s).

5 If a subroutine or function call is involved, a failure during execution.

6 Partial recovery, which will yield correct computed results but be wasteful of computer time.

B. Active Field Is Columns 1–5, 7–72

A non-blank column 6 indicates that a given physical card is a continuation of the preceding physical card. Column 6 may *not* be used for any other purpose. The active field on any physical card consists of columns 1 through 5 inclusive and 7 through 72 inclusive. A logical card consists of the active field of any physical card with a blank in the continuation column and the active fields of as many continuation cards as contiguously follow the given physical card. Both the statement number, if present, and the statement may be placed anywhere on a logical card, subject to the constraint that the statement number, if present, must precede the statement on a given logical card.

C. Asterisk * for Comment

The asterisk * is used as a designator of a comment card. This asterisk must be the first non-blank character in the given logical card. It need not be in column one.

D. Mixed (IBM vs UNIVAC) Style Punching

TPL utilizes a 54-character set. Since the IBM 407 has only 48 positions on its print wheels, it cannot list cards of the TPL source language unambiguously. Forty-four characters are identical on the IBM 360 and UNIVAC 1108/9300 computers:

26 Alphabetic characters	ABCDEFGHIJKLMNOPQRSTUVWXYZ
10 Numeric characters	0123456789
1 Space | blank	␣
7 Special characters	,$.-*/;

These characters may be keypunched or listed on any modern equipment without any difficulty. An additional 10 special characters differ among the various modern equipments:

plus	+
hyphen	−
right parenthesis	)
logical OR	|
ampersand	&
logical NOT	¬
apostrophe	'
double quote	"
equal sign	=
left parenthesis	(

For these characters TPL will accept either the IBM system 360 punching or the UNIVAC 1108/9300 punching, mixed in any manner intra | inter card. Hence, cards may be punched originally or corrected in either style, at the immediate convenience of the programmer, but with a view toward which equipment he intends to employ for the listing of the deck.

E. IF|OTHERWISE|ANYHOW

The blocking set of keywords

IF|OTHERWISE|ANYHOW

is available and preferable to the use of numbered statements for the execution of exclusive alternative blocks of coding. A complete description of this feature is contained in the articles referenced in the Bibliography and will not be repeated here.

F. DO|DO_END

The blocking set of keywords DO|DO_END is available and preferable to the use of numbered statements for the execution of a DO-loop. See the references for a complete description of this feature.

G. SECTION

The keyword SECTION can be employed for semantically delimiting local blocks of coding with regards to real names and statement numbers. Thus, the source coding within each numbered SECTION must use statement numbers in the closed integer interval [1, 999] and the same numbers may be reused in other sections. Similarly, the same source names may be reused in other sections. THE SECTIONs must be numbered in strictly increasing order with the numbers taken from the closed integer interval [1, 25].

H. UP|DOWN

The keywords UP|DOWN may be employed to nest blocks of local variables (but *not* statement numbers) to any depth. A new SECTION will force as many UP steps as necessary to return to the standard level. An automatic drop down to the previous level will *not* follow.

I. An Arithmetical Sub-atom Includes a Logical Sum in Parentheses

In addition to the two standard FORTRAN recursions resulting from the definition of a logical atom to include a logical sum in parentheses and an arithmetical sub-atom to include an optionally signed arithmetical sum in parentheses, the third recursion resulting from the definition of an arithmetical sub-atom to include a logical sum in parentheses is permitted. The BNF definitions are

$$\langle \text{LA} \rangle = (\langle \text{LS} \rangle) \mid \left\{ \begin{matrix} \& \\ \neg \end{matrix} \right\} \langle \text{LA} \rangle \mid \langle \text{AS} \rangle \langle \text{relational operator} \rangle \langle \text{AS} \rangle \mid \langle \text{primitives} \rangle$$

$$\langle \text{AAI} \rangle = (\langle \text{SAS} \rangle) \mid (\langle \text{LS} \rangle) \mid \langle \text{primitives} \rangle$$

J. NEW_DECK

For multiple compilation, the compiler program is reinitialized by the use of the keyword NEW_DECK. A new HEADER card optionally may follow immediately.

K. ASSIGN

The built-in in-line integer replacement function ASSIGN uses the syntax

$$\text{ASSIGN } \langle \text{scalar integer variable} \rangle = \left\{ \begin{matrix} \langle \text{integer constant} \rangle \\ \langle \text{arithmetic sum} \rangle \end{matrix} \right\}$$

Thus, the syntax is the same as that of an arithmetical equation, but preceded by the keyword ASSIGN. For example,

ASSIGN I = 3

L. Logical Operations Performed on 32 Bits in Parallel

The logical variables are 32 bit integers with

0 = .FALSE.

−1 = .TRUE.

The choice of −1, rather than +1, for TRUE yields an all-one-bits word as TRUE. Such a word easily may be masked to yield one-bits at any desired position in the word without the necessity of shifting or propagating operations. Each of the logical operations, as well as the statement

IF (⟨LS⟩) ⟨integer variable which reduces to a scalar⟩ = ⟨LS⟩

is executed as 32 bits in parallel subject to the same indicated operators. In all other logical IF statements; i.e.,

IF (⟨LS⟩) . . .

the argument of the IF is tested for non-zero; namely,

IF (⟨LS⟩ .NE. 0) . . .

In summary, .FALSE. is always zero. .TRUE. is generated as minus one, is computed upon as 32 bits in parallel, and is used as non-zero; i.e., at least one bit being a one.

M. Extracting Triplet

An extracting ordered triplet has been introduced as an additional logical atom. This triplet permits the unpacking of integer|logical variables and right justifying them in one operation. (This is similar to the UNIVAC FORTRAN V FLD function.) In BNF notation, this triplet is defined as:

⟨logical atom⟩ = . . . | (⟨logical sum⟩ , ⟨integral arithmetical sum⟩ , ⟨integral arithmetical sum⟩) | (⟨logical sum⟩ , ⟨integral arithmetical sum⟩) | . . . .

The elements of the triplet are:

a logical sum from which the extraction is to be performed

b integral arithmetical sum indicating the starting bit position

c integral arithmetical sum indicating the quantity of contiguous bits to be extracted

The third element defaults to a one. For example,

J = (I, 22, 3)

extracts the bits 22 23 and 24 from I and right justifies them. The equivalent FORTRAN coding is

```
DATA M3/Z7/
J = LAND(SHFTR(I,7),M3)
```

N. Exclusive OR Operator

The exclusive OR operator X has been introduced at the top of the hierarchy of logical operators; i.e., over the inclusive OR operator V and the AND operator.. For example, the parentheses in the expression

(A.LE.B).(C.GT.D)X((E=F).(G$=H)V I)X(J.K.L)

are redundant; thus, the foregoing expression is equivalent to the expression

A.LE.B . C.GT.D X E=F.G$=H V I X J.K.L

O. Logical-Shift Operators

The logical-shift operators Q and R have been introduced over the top of the hierarchy of strictly logical operators. They are the logical-left-shift and logical-right-shift operators, respectively. Since these logical-shift operators are placed between dissimilar elements, they cannot be used more than once in a given logical sum. The OR operators X and V may be used left-recursively. In BNF notation, their comparative syntax is

⟨LS⟩ = ⟨LSX⟩ ⟨QR⟩ ⟨integer arithmetic sum⟩ | ⟨LSX⟩

⟨LSX⟩ = ⟨LSV⟩ X ⟨LSX⟩ | ⟨LSV⟩

⟨LSV⟩ = ⟨LP⟩ V ⟨LSV⟩ | ⟨LP⟩

.

.

.

⟨QR⟩ = Q | R

In the example

```
DATA M/Z380/
J = I . M R 7
```

we extract bits 22 23 and 24 from I and right justify them into J. The same result could be achieved by the triplet

```
J = (I 22 3)
```

The equivalent FORTRAN coding would be

```
DATA M/Z380/
J = SHFTR(LAND(I, M), 7)
```

and

```
DATA M3/Z7/
J = LAND(SHFTR(I, 7), M3)
```

respectively.

P. Generalized Limits for the DO-Index

In addition to permitting the usual integer or scalar integer variable as the two or three limits for the index in a DO-statement, a scalar arithmetical sum also is acceptable as any one or more of the DO-limits. For example, the one statement

```
DO I = I1+I2*I3 7*I4-I5 I6+1
```

is equivalent to the four statements

```
J1 = I1+I2*I3
J2 = 7*I4-I5
J3 = I6+1
DO I = J1 J2 J3
```

where the Js are dummy variables. Alternatively, a single integer array, with all of the subscripts except the first being specified integers or scalar integer variables which are constant within the DO-loop, may be specified as the set of values to be taken on by the DO-index. For example, if the array II has been declared

```
DIMENSION II(31 52 13)
```

then the one statement

```
DO I = II(I2-3*I12 2*I3)
```

is equivalent to the four statements

```
J2 = I2-3*I12
J3 = 2*I3
DO J1 = 1 31
I = II(J1 J2 J3)
```

The DO-array may *not* be employed in an implicit DO-statement, e.g., in an IO-statement.

Q. RETRIEVE

The built-in in-line integer replacement function of two variables RETRIEVE has been defined. This function uses a syntactical structure patterned after that of the ASSIGN function; namely,

RETRIEVE ⟨integer variable which reduces to a scalar⟩ = ⟨integer array⟩ (⟨integer variable which reduces to a scalar⟩)

For example, the declaration

```
DIMENSION K(100)
```

followed by the statement

```
RETRIEVE I = K(L)
```

is equivalent to the FORTRAN coding consisting of the same declaration

```
DIMENSION K(100)
```

followed by the five statements

```
    DO 1 I = 1,100
    IF(K(I).EQ.L) GO TO 2
1   CONTINUE
    I = 0
2   CONTINUE
```

The result is that I becomes the subscript whose corresponding element in the array K has the value of the argument L. If no element has the value L, then I is set to zero to indicate the failure to find a match.

If the array has more than one dimension, the additional subscripts may be specified immediately to the right of the second argument. These additional subscripts

are not involved in the retrieval process. In the foregoing example, let us assume that the array K had been declared

```
DIMENSION K(100 2 3)
```

and that the subscripts for the second and third dimensions are M2 and M3, respectively. Then the statement

```
RETRIEVE I = K(L M2 M3)
```

is equivalent to the same FORTRAN coding as in the original example, except that the IF-statement is replaced by

```
IF(K(I,M2,M3).EQ.L) GO TO 2
```

Thus, contrary to appearances, L is an argument but M2 and M3 are subscripts.

R. GOTO|SKIP

A syntactically new version of the GOTO has been introduced to facilitate the execution of a selected one out of several blocks of coding. The BNF definition of this version of the computed GOTO is

⟨GOTO⟩ = . . . |GO TO ⟨integer variable⟩, ⟨integer constant⟩| . . . .

The integer constant specifies how many alternative blocks of coding are expected to follow contiguously. The integer variable selects the individual block of coding to be executed immediately after the execution of the given GOTO.

The semantical requirement upon the alternatives is that the blocks of coding must follow the GOTO contiguously in sequence and that each block of coding be terminated by a SKIP statement. The amount of SKIPs (and hence of alternative blocks of coding) must equal that specified by the integer constant in the governing GOTO statement.

For example, the four-way branch coded in the TPL

```
GO TO I, 4

s1 *
SKIP

s2 *
SKIP

s3 *
SKIP

s4 *
SKIP

s5
```

is equivalent to the FORTRAN computed GOTO

```
GO TO (1, 2, 3, 4), I
```

immediately followed by the coding

```
1  s1 *
   GO TO 5
2  s2 *
   GO TO 5
3  s3 *
   GO TO 5
4  s4 *
5  s5
```

In each of the foregoing two cases, the statements s with subscripts are any executable statements. The asterisk * following an s indicates that one or more statements may be inserted at the indicated location in the coding.

These GOTO with their SKIPs may be semantically nested to any depth.

S. Four Lexical Structures for REAL Constants

Only four alternative lexical structures for a REAL constant are permitted; i.e.,

⟨sign⟩ ⟨one-or-more digits⟩ . ⟨one-or-more digits⟩

⟨sign⟩ ⟨one-or-two digits⟩|

⟨sign⟩ ⟨one-or-more digits⟩ . ⟨one-or-more digits⟩|

⟨one-or-more digits⟩ . ⟨one-or-more digits⟩

⟨sign⟩ ⟨one-or-two digits⟩|

⟨one-or-more digits⟩ . ⟨one-or-more digits⟩

T. Integer Constant | Variable Employed as Logical

Since any integer constant|variable may be employed as a logical constant|variable, there is no provision for the declaration of LOGICAL variables.

U. Single Character Symbols for Logical Operators

Single character symbols are used for certain of the logical operators:

TPL		FORTRAN	
.	=	.AND.	
V	=	.OR.	(inclusive)
|	=	.OR.	(inclusive)
X	=	.XOR.	(exclusive)
$	=	.NOT.	
¬	=	.NOT.	
=	=	.EQ.	
$=	=	.NE.	
¬=	=	.NE.	

These indicated FORTRAN style multiple-character symbols are *not* part of the TPL.

V. Abbreviations of Certain Keywords

The keywords

```
ANYHOW
DIMENSION
FUNCTION
OTHERWISE
RETRIEVE
RETURN
SUBROUTINE
```

optionally may be abbreviated in TPL to

```
ANY
DIM
FUN
OTH
RET
RET
SUB
```

respectively. For example, it is permissible to write

```
SUB A(B N C)
DIM B(N) C(N)
DO I = 1 N
C(I) = F(B(I))
DO END
RET
FUN F(X)
F = X*X
RET
```

W. A Subroutine Call Accomplished Without the Keyword CALL

A subroutine call is accomplished without the keyword CALL. Thus, for example,

```
SUBA(B C D E)
```

is equivalent to the FORTRAN

```
CALL SUBA(B,C,D,E)
```

The keyword CALL is *not* part of the TPL.

X. A Define-Before-Use Diagnostic

A semantical diagnostic system which reports any use of a variable before that variable has been defined and also reports any definitions of a given variable after it already has been defined once has been introduced. Therefore, the source coding has to be written in the order of execution; i.e., any unconditional, computed, or assigned GO TO has to point downwards, except if it is employed to close a DO-loop that has been coded explicitly.

The only syntactical effect is that the input and output variables of a subroutine (or function) call must be designated. The convention that all of the input variables are stated first while all of the output variables are stated last is adopted. A semicolon ; is required as a delimiter between these two sets of variables. For example, the coding in a routine

```
SUBA(B C ; D E)
```

calls the subroutine

```
SUBROUTINE SUBA(B C ; D E)
```

Here, we designated that the variables B and C are evaluated, prior to the call, in the higher level routine then used by the subroutine SUBA as input variables from which to compute the output variables D and E. These latter variables are passed up to the higher level routine for further use. If no semicolon is present, it is assumed that all the variables are input variables. It is a syntactical error to place the semicolon at the end of the calling sequence.

The semicolon syntactically is considered as another element in the calling sequence. Thus, if one insists in

inserting the optional delimiting commas, the foregoing two lines of coding would be

```
SUBA(B,C,;,D,E)
SUBROUTINE SUBA(B,C,;,D,E)
```

IV. An Example of the Usefulness of TPL in Telemetry

The following example shows how one might unpack successive values of the array IT, report the state of several two-bit logical variables, and print the values of several other integral variables. It is assumed that suitable declarations of the arrays would have DIMENSIONed them and set their values by means of, e.g., DATA statements.

The seven arrays contain the indicated information:

- IA list of the code numbers of the logical variables
- IB list of the code numbers of the integral variables
- ID list of the code numbers of all of the variables
- IO list of the subscripts of the array IT designating the element in which the given variable is located
- IP list of the applicable starting positions
- M list of the applicable masks
- IR list of the applicable required right shifts

The coding follows:

```
    DO ITT = 1, ITTMAX
    READ(5, 8) IT
8   FORMAT(7Z8)
    IF(IT(...).mask)
    DO I=IA
    RET J = ID(I)
    K = IIT(IO(J) IP 2) + 1
    GO TO K, 4
    WRITE(6, 1) I
1   FORMAT(1X, T16, I6, T28, 4HZERO)
    SKIP
    WRITE(6, 2) I
2   FORMAT(1X, T16, I6, T28, 3HONE)
    SKIP
    WRITE(6, 3) I
3   FORMAT(1X, T16, I6, T28, 3HTWO)
    SKIP
    WRITE(6, 4) I
4   FORMAT(1X, T16, I6, T28, 5HTHREE)
    SKIP
    WRITE(6, 5)
5   FORMAT(13H+THE VALUE OF, 10X,
          3HWAS)
    DO END
    DO I=IB
    RET J = IB(I)
    K = IT(10(J)).M(J) R IR(J)
    WRITE(6, 6) I, K
6   FORMAT(15H THE VALUE OF , I6,
          7H WAS    , I12)
    DO END
    DO END OTHERWISE
    WRITE(6, 9) ITT
9   FORMAT(33H1REQUESTED TERMINATION
          ON ITT = , I6)
    ANYHOW
    IF($ITT) WRITE(6, 10)
10  FORMAT(22H1EXHAUSTED TERMINATION)
```

V. Remarks

Some of the features of the TPL were already present in the spacecraft-simulation procedural language. These features are described in greater detail in the original articles (Refs. 1 and 2).

References

1. Ścibor-Marchocki, R. I., "A Spacecraft-Simulation Problem-Oriented Language," in *The Deep Space Network*, Space Programs Summary 37-58, Vol. II, pp. 87–96. Jet Propulsion Laboratory, Pasadena, Calif., July 31, 1969.
2. Ścibor-Marchocki, R. I., "Additional Features of the Spacecraft-Simulation Problem-Oriented Language," in *The Deep Space Network*, Space Programs Summary 37-62, Vol. II, pp. 99–107. Jet Propulsion Laboratory, Pasadena, Calif., Mar. 31, 1970.

Diagnostics for the SFOF Mark IIIA Central Processing System: Real-Time Background Routines

C. Zandell
SFOF/GCF Development Section

The on-line diagnostics for the Space Flight Operations Facility (SFOF) Central Processing System (CPS) have been modified to provide real-time diagnosis of equipment performance. Real-time diagnostics can be run while mission flight support continues. This is possible since any diagnostic can now run as an independent task under the mission real-time job step. The real-time capability allows certification of CPS hardware elements immediately preceding their commitment to mission flight support.

I. Introduction

This article describes an extension of the Diagnostic Monitor (DIAMON) for use on IBM 360/75-related hardware. In its improved form, DIAMON provides additional assurance that the Central Processing System (CPS) is completely operational by testing selected hardware interfaces and on-line devices concurrent with flight support (i.e., in real time). Previous articles (Refs. 1, 2, and 3) have described the independent or "standalone" diagnostics, their implementation for pre-mission checking of the CPS, and the on-line diagnostics.

II. Required Capabilities

The use of multiprogramming in Mark IIIA limits the value of a diagnostic that requires an operating system different from the flight support system, or exclusive use of key facilities. The proven worth of hardware diagnostics led to the evolution of DIAMON from one which operated under the JPL Operating System (JPLOS) with exclusive use of the real-time job step (RTJS) to one which would run as one of several independent tasks under the mission RTJS.

Sharing the RTJS requires additional features: attaching DIAMON to the Mission RTJS, routing data from the tested device exclusively to DIAMON, and returning the tested devices to the original user.

III. Implementation

Figure 1 shows the current Mark IIIA 360/75 Operating System and the relations between the RTJS, DIAMON, and the Mission Support System.

The real-time diagnostics run under JPLOS with first-level control by DIAMON. Control messages have been provided which attach and delete DIAMON as an independent task under the mission RTJS. Other control messages start and stop input/output to peripheral devices. The control messages are entered on CRT display stations.

IV. Operation

After DIAMON has been attached to the mission RTJS, selected CRT display stations may be used to enter diagnostic requests. Diagnostics can be run on any device that is allocated to the mission RTJS. The diagnostic request for a device also results in reserving the device for DIAMON. The same program logic used to control input/output to devices also isolates the device exclusively for DIAMON use.

Diagnostics can be run concurrently on different device types. Some diagnostics are re-entrant, allowing several devices of the same type to be checked at the same time.

V. Further Extension

The real-time diagnostic capability also provides a base for detecting system faults as soon as they occur. Under a combination of operator and program control, diagnostics would be used to exercise selected system functions during periods of low activity. DIAMON would be expanded to also test the instruction set, arithmetic functions, and some control functions. Core reliability would be checked by making normal core requests, testing the assigned area, and then relinquishing it. This type of continuous verification would significantly enhance system performance by detecting system faults in time to be corrected for mission support.

VI. Conclusion

The modification of DIAMON now provides a real-time diagnostic capability that can be used without significant impact on mission support. When not required, it is disk-resident and only the essential modules are loaded when a diagnostic request is entered. Sharing the RTJS allows other mission programs to continue with the remaining facilities.

With the real-time diagnostics, it is now practical to verify proper device operation prior to every usage rather than to wait until problems degrade the system below mission requirements.

References

1. Wells, R. A., "Diagnostics for the SFOF Mark IIIA Central Processing System: Standalone Acceptance and Maintenance Routines," in *The Deep Space Network*, Space Programs Summary 37-65, Vol. II, pp. 97–99. Jet Propulsion Laboratory, Pasadena, Calif., Sept. 30, 1970.
2. Wells, R. A., "Diagnostics for the Mark IIIA Central Processing System: IBM 360/75 Computer On-Line Test Routines," in *The Deep Space Network Progress Report*, Technical Report 32-1526, Vol. I, pp. 103–106. Jet Propulsion Laboratory, Pasadena, Calif., Feb. 15, 1971.
3. Wells, R. A., "Diagnostics for the SFOF Mark IIIA Central Processing System: Pre-Mission CPS/Facility Checkout Procedures," in *The Deep Space Network Progress Report*, Technical Report 32-1526, Vol. II, pp. 125–128. Jet Propulsion Laboratory, Pasadena, Calif., Apr. 15, 1971.

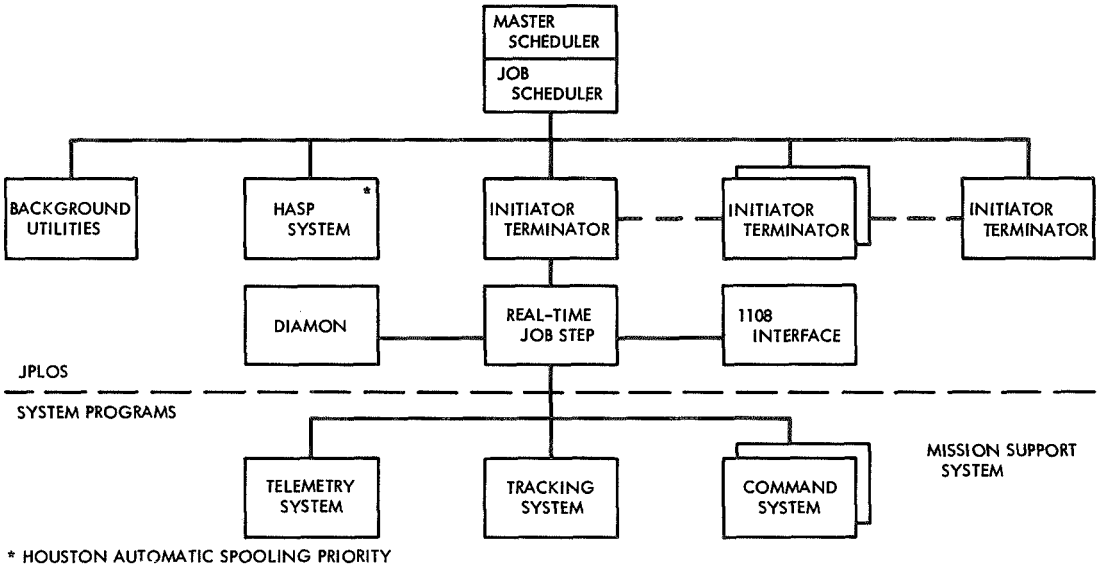

Fig. 1. Mark IIIA 360/75 Operating System

SFOF Mark IIIA User Terminal and Display Subsystem Design

K. Kawano
SFOF/GCF Development Section

The user terminal and display subsystem (UTD) provides various users with the means to communicate with the Central Processing System in the SFOF. Prints, plots, alphanumeric, and graphic displays are presented on various peripheral devices and on digital television. This article discusses the requirements, design considerations, and implementation of the UTD.

I. Introduction

The user terminal and display subsystem (UTD) is one of eleven subsystems comprising the Space Flight Operations Facility (SFOF) Mark IIIA. Functions of all the SFOF subsystems were briefly described in Ref. 1. This article will describe in more detail the user terminal and display subsystem.

UTD provides the DSN and the flight projects with the tools to use the Central Processing System (CPS). See Ref. 2. The UTD is comprised of a variety of input/output (I/O) devices which, individually and collectively, provide the users with large amounts of data in easily digested form and at rates which are compatible with real-time decision making. The devices which provide these capabilities are partitioned into assemblies and subassemblies. This partitioning resulted from a design process based on many considerations. The prime consideration was user requirements.

II. Functional Requirements

For the support of spaceflight operations, each succeeding project requires more data from the spacecraft. The DSN in providing real-time support, also needs more data from its various facilities. This support ranges from sending commands in real-time, to the immediate viewing of spacecraft responses, to the recording of data for scientific analysis.

Functionally, the requirements for displaying information to the users have not really changed. However, the

amount of information which must be displayed has increased greatly. Also, the speed with which operations personnel must react has gone up in proportion to increasing spacecraft capabilities. In order to speed up reaction time, simpler means of communicating with various elements of the DSN and the spacecraft had to be devised. In achieving the increased capabilities to handle larger volumes of information, at faster rates, and in simpler formats, new user devices were required. Likewise, interfaces with other elements of the upgraded DSN had to be designed. Concomitant with the above considerations were reliability, maintainability, and cost of the new subsystem.

III. Technical Considerations

Throughout several years of spaceflight operations, JPL has gained experience which facilitates the design of a user terminal and display subsystem that optimizes the man-machine interface. This design has taken place in an evolutionary manner because of the necessity for continuing flight operations during upgrades of the SFOF. Teletype printers and mechanical plotters have been gradually replaced by more modern devices. However, this replacement, while welcomed by most users, has required changes in the operational philosophy of those users. People who have successfully used certain sets of devices for past missions tend to favor those devices for future operations. Yet, when consideration is given to greatly increased volumes of data, higher transmission and processing rates, and to the increased efficiency of modern computer peripherals, then the operators welcome the improved UTD capabilities.

In arriving at a final subsystem design, consideration was given to the creation of a universal user complex that could support all activities in the SFOF under a multimission environment. However, due to constraints of time and money, some compromises had to be made. With these constraints and with the decision to use the IBM 360/75 computer in the Central Processing System (Ref. 2) it became apparent that subsystem development had to proceed largely with off-the-shelf hardware. Furthermore, peripherals had to be selected such that they would be compatible with the JPL Real-Time Operating System (JPLOS) which constitutes the basic software used by all the SFOF systems and the flight projects. The selected devices were the IBM 2260 display station, the IBM 1443 line printer, and the IBM 2501 card reader. A user terminal switch assembly was designed for switching these peripheral devices between the CPS computers (Ref. 3).

Considerably less constraint was encountered in designing a means for data presentation. Large data volume, real-time decision making, and the multiplicity of users dictated a design which affords a visual display that simultaneously or separately presents many data formats in minimum time and in the most usable form. Although mechanical plotters have been removed, both strip plots and X-Y coordinate plots are required. It was determined that the foregoing considerations dictated the design of a multichannel digital television assembly (DTV) as part of the UTD subsystem. The DTV interfaces with the television assembly provided by the Ground Communications Facility which permits distribution of alphanumeric and graphic data for real-time usage throughout the SFOF. Reference 4 contains a description of the DTV.

IV. SFOF Mark IIIA UT&D Design

The above considerations resulted in a UTD design. The overall concept of the UTD and its assemblies are shown in Fig. 1. As mentioned earlier, the universal user complex could not be fully implemented, so the traditional user station concept was employed. Under this concept, the complement of equipment in each operating area was negotiated with the assigned users within the constraint of available resources.

Each area has been configured with some combination of user devices. The usage rationale for the devices is as follows:

DTV Display. Real-time data for mission operations will be displayed here. Immediate access to the data in an easily-used format will be provided. Both alphanumeric and graphics data can be displayed. Data needing immediate attention could be displayed with the background reversed. Wide distribution of data is possible through the TV assembly. For user versatility, a single monitor can access multiple channels.

IBM 1443 Line Printer. Data required in near-real time can be printed in a format convenient for usage in an operational area in a quick and efficient way. Administrative messages, such as processing status, alarms, and summaries, can be printed in multiple copies.

IBM 2501 Card Reader. Operational step initialization, parameter changes, special prearranged controls, prearranged device assignment changes and many other multiple input tasks that need near-real-time loading into the mission support computer.

IBM 2260 Display Station. The CRT display is used to display central processing unit and program status. The display is also used with the keyboard entry as an interactive terminal. The entry messages are composed. The computer reply will be displayed.

IBM 2260 Keyboard Entry Device. Operational control, command entry, program request, device assignment and format selection are available via this keyboard.

DTV Format Request Box. In cases where a user has cognizance over a number of DTV formats to be displayed on a few monitors and needs rapid changes, this box would be used.

DTV Hard Copy Printer. Although the DTV display is for real-time usage and therefore volatile, there will be occasions when a record would be needed for use in a time frame not suitable for off-line output. A hard copy of a display can be made for this purpose.

Teletype Printers. Some low-rate data, such as alarms and suppressed data, are provided on this type of printer. Until experience is gained on the other devices, these units will remain in service.

V. Conclusion

The SFOF Mark IIIA UTD Subsystem has been designed, and implementation is progressing. The *Mariner* Mars '71 flights and the *Pioneer F* launch will be supported from user areas located in the SFOF and the System Development Laboratory (SDL) respectively. Although located remotely from the SFOF, user areas in the SDL will be configured similarly to those in the SFOF.

References

1. Simon, H. S., "Functional Design of the Space Flight Operations Facility for the 1970–1972 Era," in *The Deep Space Network,* Space Programs Summary 37-66, Vol. II, pp. 90–94. Jet Propulsion Laboratory, Pasadena, Calif., Nov. 30, 1970.
2. Stiver, R. A., "SFOF IBM 360/75 Computer Configuration," in *The Deep Space Network,* Space Programs Summary 37-66, Vol. II, pp. 71–75. Jet Propulsion Laboratory, Pasadena, Calif., Nov. 30, 1970.
3. Habbal, N., "SFOF IBM 360/75 User Device Switching Assemblies," in *The Deep Space Network,* Space Programs Summary 37-66, Vol. II, pp. 75–77. Jet Propulsion Laboratory, Pasadena, Calif., Nov. 30, 1970.
4. Singleton, F. L., "SFOF Digital Television Assembly," in *The Deep Space Network,* Space Programs Summary 37-65, Vol. II, pp. 86–91. Jet Propulsion Laboratory, Pasadena, Calif., Sept. 30, 1970.

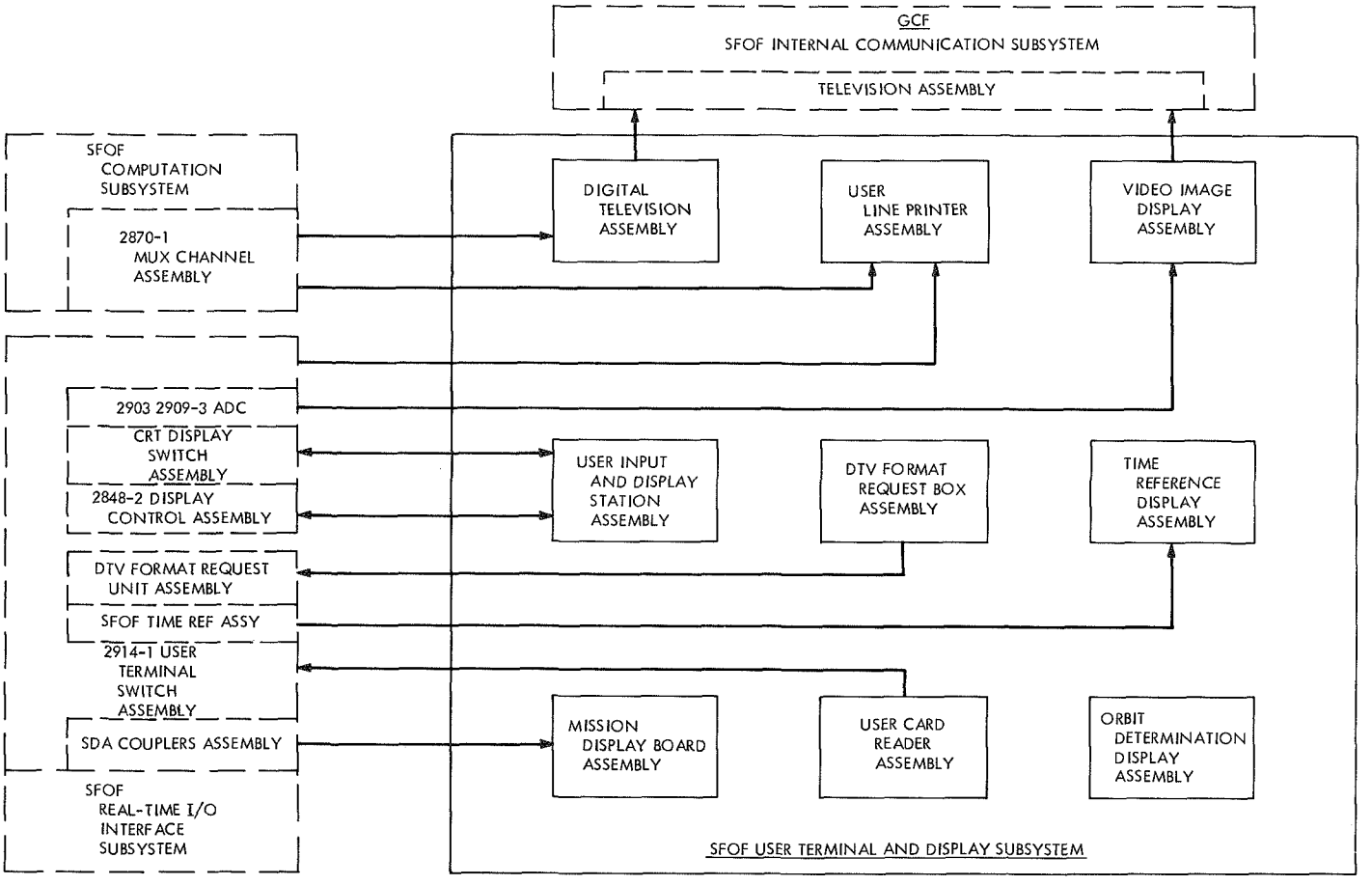

Fig. 1. User terminal and display subsystem assemblies and interfaces

SFOF Digital Television Computer Subassembly

G. E. Leach
SFOF/GCF Development Section

The SFOF digital television computer subassembly is part of the digital television assembly. It provides control functions and interfacing of two IBM 360/75's to 80 channels of television for real-time display of alphanumeric and graphic information.

The subassembly consists of a dual computer configuration which is utilized in a primary/alternate mode. This provides the capability for rapid detection and correction of failures in the mission operations environment.

I. Introduction

The Digital Television Assembly (DTV) is a part of the user terminal and display subsystem in the SFOF. The purpose of the DTV is to provide flight projects and DSN users with volatile real-time displays of spacecraft data and DSN equipment status.

This article supplements the SFOF digital television assembly description in Ref. 1. It provides details on the selection, configuration, application and interface characteristics of the computer subassembly. Future articles will also describe the display subassembly in greater detail.

II. Requirements for a Computer Subassembly

The selected proposal for a digital television assembly called for a display subassembly and a computer subassembly as shown in Fig. 1. Several factors influenced the selection of the Computer Subassembly:

(1) The computer subassembly was required to provide control functions for the modularized display subassembly. This control capability included accepting data input from dual SFOF processing computers and servicing of hard copy requests from the display subassembly.

(2) DSN requirements for rapid detection and correction of failures made it necessary to consider an

alternate path or backup capability for this critical display control function.

(3) Time constraints, in development of software for the *Mariner* Mars 1971 mission, made it necessary to design and check out the related SFOF data processing system (IBM 360/75's) software concurrent with development of the digital television assembly.

III. Design Approach

Two principal alternatives were considered in selecting a computer subassembly to meet the above requirements:

(1) Purchase the control computer proposed for the display subassembly.

(2) Utilize an existing JPL-owned dual computer (CDC 3100's) subassembly.

The second alternative was chosen because it offered the following advantages:

(1) The procurement cost was lowered.

(2) The existing computers were being totally decommitted from their current display control function.

(3) Major software design and checkout could be done before delivery of the display subassembly.

(4) The existing 3100 computer configurations would support future offline development activity concurrent with mission operations support.

The major problem incurred by this decision involved the definition of computer subassembly interfaces.

The display subassembly vendor was required to interface to a channel of each 3100. This interface became part of a special-purpose control unit which was necessary to communicate between the modular units of the display subassembly. It was designed to receive data from both 3100's on a sequential basis but would normally operate with a single 3100.

If the first alternative had been chosen, the display subassembly vendor would have interfaced to a specified channel of each 360/75. Since existing computers were to be used, an interface to the 360/75's was required from another source. The decision was to design and build this interface at JPL rather than buy from a vendor. Determining factors were time, cost, and unavailability of an existing design. Time was most important, since an operating 3100 and its input interface were required for early 360/75 software checkout.

IV. Computer Subassembly Configuration

As shown in Fig. 2, the major components of the DTV computer subassembly are two CDC 3100 computers which are designated A and B. Both 3100's are configured identically with the same complement of peripheral devices and processing capabilities. During normal operations, one 3100 will accept data from both 360/75's and output to the display subassembly. The alternate 3100 will either serve as a backup processor or support DTV development activity. Both 3100's can access the display subassembly sequentially under program control. However, each 360/75 input is routed via a configuration switch to one 3100 or the other.

The only new equipment in the computer subassembly is the two computer interface control (CIC) units. The design of these units and the selection of 3100 channel assignments were aimed at maximizing the data throughput capability. Channel 0, the highest priority channel, was assigned to service the display subassembly. This channel has the highest activity since it must output data received via channels 1 and 3, plus servicing hard copy requests from the display subassembly.

Each CIC provides its 360/75 with an independent path to either 3100 via a configuration switch. This allows the 3100 to utilize a separate channel for each 360/75 input. Channel 1 is configured to the corresponding 360/75 and the alternate 360/75 is configured to channel 3 which has the lowest priority. This assignment allows concurrent operation with both 360/75's. It also provides two independent CIC units which can be interchanged rapidly by swapping two cables from each 360/75. The CIC input comes from a selector subchannel on the multiplexer channel of each 360/75. This subchannel was chosen for most efficient transfer of large blocks of data, best choice of control features and the possibility of adding two-way data transfer in the future.

The shared disk is assigned to channel 2. Other peripherals share channel 3 with the alternate 360/75 input. These peripherals are only intended for use in development activities and for initializing or troubleshooting the

system. Therefore, they should not conflict with 360/75 activity during mission operations.

V. Conclusion

The choice of an existing computer subassembly, with in-house design of its input interfaces, allowed software development to begin before display subassembly delivery. Significant delays in delivery of the display subassembly made this a very valuable development capability. The resultant hardware and software design has provided the DSN with a DTV computer subassembly which has a dual configuration that can be easily interchanged, for detection and correction of failures, without significant interruption to mission operations displays.

Reference

1. Singleton, F. L., "SFOF Digital Television Assembly," in *The Deep Space Network,* Space Programs Summary 37-65, Vol. II, pp. 86–91. Jet Propulsion Laboratory, Pasadena, Calif., Sept. 30, 1970.

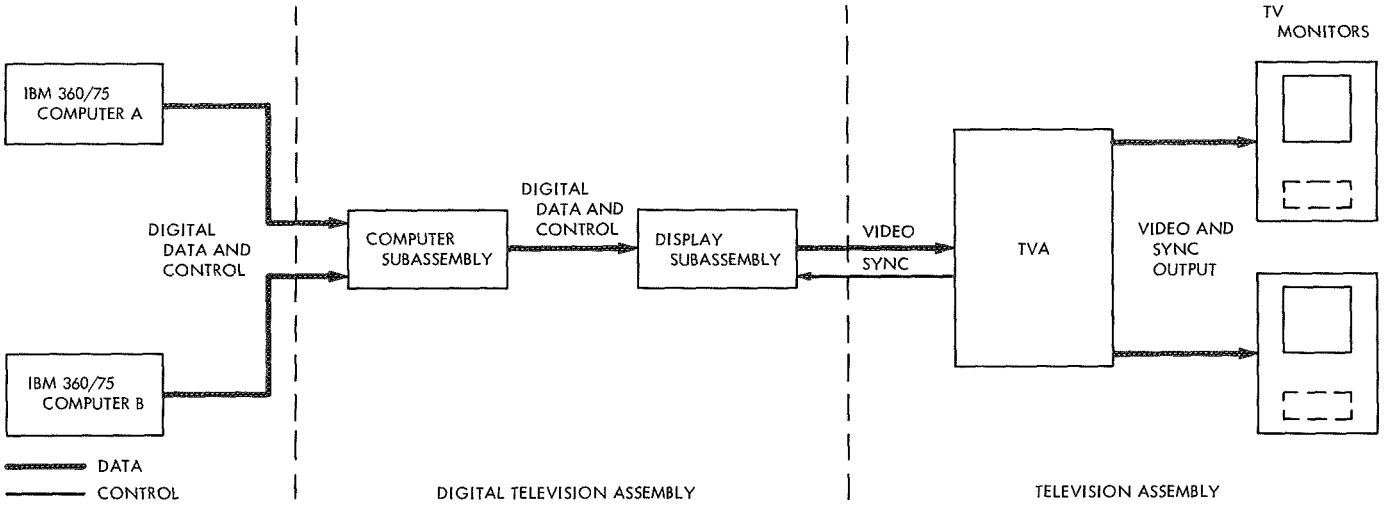

Fig. 1. DTV block diagram

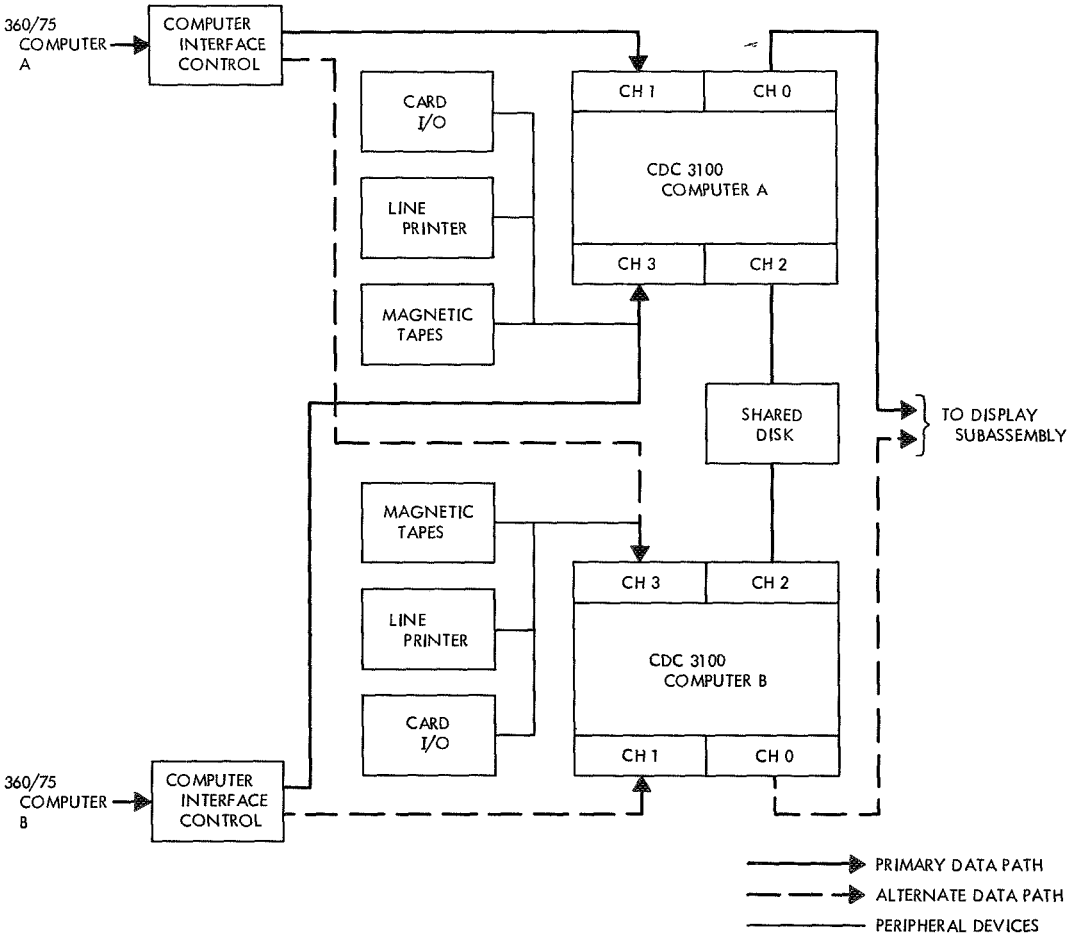

Fig. 2. DTV computer subassembly configuration

Mariner Mars 1971 Launch Phase Study Using the SFOF Mark IIIA Central Processing System Model

H. S. Simon
SFOF/GCF Development Section

Simulation models are currently being used for Space Flight Operations Facility (SFOF) development at the Jet Propulsion Laboratory. This report describes the results of three modeling runs made during April 1971 to evaluate the performance of the SFOF Mark IIIA Central Processing System, configured to support the launch phase of the Mariner Mars 1971 mission.

I. Introduction

Simulation models are currently being developed in the SFOF/GCF Development Section to support the design and implementation of the SFOF Mark IIIA Central Processing System (CPS).

SFOF Mark IIIA modeling studies began in May 1969 when it was learned that NASA would be providing JPL with IBM 360 Model 75 digital computers to form the nucleus of the SFOF Mark IIIA CPS.

The IBM computer system simulator (CSS) program was selected for model development activities since it runs on the 360/75 and the program itself applies specifically to computer systems.

The results of two modeling studies that were performed during the early stages of SFOF Mark IIIA development are described in Ref. 1.

This report describes the results of three modeling runs made during April 1971 to evaluate the performance of the SFOF Mark IIIA CPS, configured to support the launch phase of the *Mariner* Mars 1971 mission.

II. *Mariner* Mars 1971 Launch Phase Modeling Runs

A series of 10 runs was made using a model of the SFOF Mark IIIA CPS with *Mariner* Mars 1971 launch phase capabilities.

The primary objective of these system-level runs was to identify any apparent problem areas in the design of the hardware and software subsystems. Another objective was to determine the level of usage of available resources such as the central processing unit (CPU), core storage, and I/O devices.

The following events were simulated during the 10 runs:

(1) Processing and display of real-time tracking, telemetry and monitor data streams (one run).

(2) Real-time processing and the generation of tracking predicts (two runs).

(3) Real-time processing and the generation of sequence of events files (two runs).

(4) Real-time processing and the execution of the Command Generation program (COMGEN) (three runs).

(5) Real-time processing and the generation of tracking predicts and execution of COMGEN (two runs).

This report discusses the results of the three runs involving real-time processing and the execution of COMGEN.

III. Model Description

The model defined the hardware and software capabilities of the SFOF Mark IIIA CPS that will be required to support the launch phase of the *Mariner* Mars 1971 mission.

The IBM 360 Model 75J digital computer with one megabyte of main memory forms the nucleus of the hardware system. The following items are defined in the model:

(1) 2075J Processor with:

  (a) One megabyte of main memory.

  (b) Two megabytes of large capacity storage.

(2) 2870-1 Multiplexer channel with

  (a) 2821-5 control unit with on-line devices.

  (b) 2848-2 display controls with 2260 cathode ray tube devices.

  (c) 2803 tape control with two 7- and two 9-track drives.

  (d) 2403 tape control with two 7- and three 9-track drives.

  (e) Interface with digital TV assembly.

(3) 2860-2 Selector Channel with

  (a) 2314[1] disk file on channel 1.

  (b) 2314[1] disk file on channel 2.

  (c) Storage channel adaptor.

(4) 2909-3 Asynchronous data channel with

  (a) High-speed data input subchannels (6).

  (b) High-speed data output subchannels (4).

  (c) Comm processor input and output subchannels.

  (d) DTV format request unit input subchannel.

  (e) 1443/2501 selector subchannels (3) with seventeen 1443 printers and seven 2501 card readers.

The model defined the functional capabilities of the five SFOF software subsystems as given in Table 1. The statistics gathering system (SGS) that functions under the control of the 360/75 operating system provided timing information from the "live" system that was used to calibrate the model. In addition, data obtained from listings, flow charts and other design information provided a percentage of manual calibration, as given in Table 1.

IV. Environment and Sequence of Events

The runs were made to reflect processing that is expected to occur during the launch phase of the second *Mariner* Mars 1971 spacecraft. The same real-time input was assumed for all runs to provide a common basic activity for purposes of comparison. The first *Mariner* Mars 1971 spacecraft was assumed to have been launched successfully and was in cruise. The mission support system was assumed to have been running prior to the time period simulated.

In addition, *Pioneers* 6 through 9 were assumed to be operational. Tracking data from two of these spacecraft were received, processed and displayed by the 360/75.

[1]Model assumes 2314's are 1's.

Table 2 lists the real-time input data streams received at the 360/75 in the SFOF. All data were processed except duplicate engineering streams for the *Mariner* Mars spacecraft.

In addition to the processing of the real-time data shown in Table 2, the command subsystem was exercised to transmit standards and limits and station configuration data. The command subsystem was also used to transmit and enable a command card file using the input messages (MEDs) listed in Table 3.

During the five minutes simulated, telemetry data for the second *Mariner* Mars 1971 spacecraft were being recalled from the system data record (SDR), processed, and displayed on digital TV at a rate of one subframe every 10 sec.

After 2 min of simulated time, the monitor subsystem executed two raw data dumps of six blocks each on the 1443 printer.

Manual input message requests, using the DTV format request boxes, were simulated at the rate of one request per minute.

Table 4 lists the displays that were initialized during each run.

The 2314 disk packs were configured in the model according to the physical assignments made for the *Mariner* Mars 1971 Mission Operations test of March 17, 1971. The contents of the data sets on the disk packs in the model (Table 5) were similar to those in the JPL mission support software system, Model 2, Version 26.3.

V. Modeling Runs

Four minutes of real-time operation were simulated during Run 1 and 5 min during Runs 2 and 3. Statistics were printed after each 1-min SNAP interval.

Run 1 has normal processing of real-time data and the execution of COMGEN in the environment described in Section IV.

Run 2 has same script as for Run 1. The model itself was modified by moving the telemetry subsystem data tables (including the master data record) from the MSA3A2 and MSD3A2 mission disk packs to an empty pack. This pack was assigned in the model to disk drive 231. The objective of this change was to evaluate a possible method of alleviating the disk I/O problem noted in Run 1 and reduce the backlog of in-core, telemetry data blocks.

Run 3 has same script as for Run 1. The model was modified, relative to the Run 1 configuration, by moving all data tables of the near-real-time processors, including COMGEN from the MSA3A2, MSC3A2 and MSD3A2 disk packs to an empty disk pack. This pack was assigned in the model to disk drive 131. The objective of this run was to evaluate a second method of alleviating the disk I/O problem noted in Run 1 and also reduce the backlog of in-core telemetry data blocks.

VI. Results

The results of the three runs are summarized in Tables 6, 7, and 8. Each of the snap intervals represents one minute of simulated real-time.

A. Significant Items

Run 1 results are shown in Table 6. CPU utilization averaged slightly above 40%, leaving 60% of the time available for additional processing. The total amount of main memory available, with purging, varied between 134,000 and 174,000 bytes, while between 251,000 and 268,000 bytes of large capacity storage (LCS) were available. Disk drive 137 (MSD3A2) was heavily used. Excessively long delays for I/O caused ever increasing backlogs of telemetry input data because the telemetry processor required many data table accesses. Core lockout would soon occur.

Run 2 results are shown in Table 7. More was accomplished by COMGEN during this run than during Run 1. In Run 1, execution of the editor function was not completed. In Run 2, execution of the editor function was completed and the simulator function began execution. Had the newly created disk pack been placed on channel 1 of the 2860-2, rather than channel 2, a slightly better performance might have been realized.

CPU utilization increased due to the greater execution of COMGEN. However, during the last four minutes of the run, approximately 54% of the time the CPU was available for additional processing.

The total amount of main memory available, with purging, varied between 160,000 and 198,000 bytes, while between 131,000 and 268,000 bytes of LCS were available.

Task response times for the telemetry subsystem improved by a factor of better than 2:1. In addition, there was no backlog of in-core, telemetry data blocks.

Run 3 results are shown in Table 8. Slightly better performance by COMGEN, based on the increased number of data table accesses, was noted in comparison to the results achieved in Run 2.

CPU utilization increased slightly over the entire run. During the last four minutes of the run, approximately 50% of the time the CPU was available for additional processing.

The total amount of main memory available, with purging, varied between 148,000 and 194,000 bytes, while the amount of LCS available was the same as for Run 2.

Task response times for the telemetry subsystem improved slightly over Run 2. There was no backlog of in-core telemetry data blocks during Run 3.

VII. Conclusions

As shown in the results from Run 1, problems can arise when attempting to operate under a normal situation. Runs 2 and 3 were made to evaluate possible means of alleviating the problem. Either of these alternate data table allocations were shown to improve system performance and prevent data backlog because of heavy disk I/O:

(1) Move all telemetry data tables to an unused disk pack.

(2) Move all data tables used by near-real-time processors to an unused disk pack.

With the addition of more processing and the running of Mission Operation System (MOS), near-real-time programs during the orbital phase of the *Mariner* Mars 1971 mission, additional system problems may be encountered. Heavy usage of main core, LCS and disk I/O activity occurred during the launch phase simulation runs. Increased usage of these resources can be expected during the heavy activity, orbital phase.

VIII. Future Modeling Activities

The present version of the SFOF Mark IIIA model is being expanded to include those capabilities that will be implemented to support the orbital phase of the *Mariner* Mars 1971 dual spacecraft mission.

A series of runs will be made with the model subjected to loading conditions that will occur during the orbital phase.

Based upon the results of these runs, recommendations that could improve system performance and overall operating efficiency will be made.

Reference

1. Simon, H. S., "SFOF Mark IIIA Central Processing System Model Development," in *The Deep Space Network*, Technical Report 32-1526, Vol. I, pp. 95–102. Jet Propulsion Laboratory, Pasadena, Calif., Feb. 15, 1971.

Erratum

Referring to "SFOF Mark IIIA Central Processing System Model Development" by H. S. Simon in Technical Report 32-1526, Vol. I, Feb. 15, 1971, on p. 97; Table 1, col. 1, entry 5 should read "Supervisor/MVT service, %" instead of "Supervisor/mission and test video service, %."

Table 1. Software subsystem capabilities modeled with calibration data

Subsystem	Calibration data, % of capability	
	SGS	Manual
1. Master control (MC)		
Main storage management	100	100
Large capacity storage (LCS) management	10	100
Routing	100	100
Task management	100	100
Contents control (with purge)	100	100
Data table access method	100	100
I/O control	40	100
Real-time access methods (RTAM)	90	100
Logging	100	100
JPL Mods to Houston's real-time operating system (RTOS)		
Data accountability system (DAS)	10	100
Master data record access method (MDRAM)	100	100
Real-time access of tape (RTTAPE)	80	100
Card subroutine (RTCARD)	0	100
Fortran RTAM	100	100
Fortran I/O (real-time)	100	100
2. User interface (UI)		
Formatted output	35	100
Unformatted output	90	100
2260 User station input	90	100
Comm processor and high-speed data output	30	100
3. Tracking data subsystem		
Input processor (TYDIP)	70	75
Output processor (TYDOP)	100	75
Pseudo residuals	0	75
Master file program (MFP)	80	75
4. Telemetry data subsystem		
Mariner Mars 1971 engineering telemetry processor	100	50
5. Command data subsystem		
Command transmission and verification	75	100
6. Monitor and operations control data subsystem		
Accumulation and display of DSIF, GCF, and SFOF data	70	90
Transmission of tracking predicts	10	25
Transmission of DSN sequence of events	10	25
7. Near-real-time processors[a]		
Tracking predicts generator	50	75
COMGEN	10	25
Sequence of events generator	0	0

[a]Operate under the real-time job step.

Table 2. Input data streams

Input data	Via	Rate	Spacecraft	Station
Engineering telemetry	HSDL	33⅓ bps	*Mariner* '71A	1
Engineering telemetry	HSDL	33⅓ bps	*Mariner* '71B	2
Engineering telemetry	HSDL	33⅓ bps	*Mariner* '71B	4
Tracking	CP	1 sample/10 sec	*Mariner* '71A	1
Tracking	CP	1 sample/10 sec	*Mariner* '71B	2
Tracking	CP	1 sample/min	*Mariner* '71B	4
Tracking	CP	1 sample/min	*Pioneer*	5
Tracking	CP	1 sample/min	*Pioneer*	6
DSN performance/status	HSDL	1 block /5 sec		1
DSN performance/status	HSDL	1 block /5 sec		2
DSN performance/status	HSDL	1 block /5 sec		4
DSN summary	HSDL	1 block/30 sec		1
DSN summary	HSDL	1 block/30 sec		2
DSN summary	HSDL	1 block/30 sec		4
GCF monitor block	CP	1 block/20 sec		

HSDL = High-speed data line.

CP = Communications processor.

Table 3. Input messages (MEDs) used to transmit command card file

MED	Function
C02	Connect to command
C03	Set up HSD block header
C10	Connect to card file
C11	Start sending out file
C17	Enable block just sent out
C12	Send next block

Table 4. Initialized displays

Subsystem	Display device	Number of displays active
Command	DTV	6 Channels
Tracking	DTV	2 Channels
	1443	4 Devices
	TTY	1 For each station (404)
	TTY	1 For alarms (490)
Telemetry	DTV	32 Channels
	TTY	22 Devices
	1443	8 Devices
Monitor and operations control	DTV	20 Channels

DTV = digital TV.
TTY = printer driven by the comm processor using data received from the 360/75.

Table 5. Contents of data sets on disk packs

Disk pack	Contents	2314 Disk drive
RTOS A	System functions	130
MSB3A2	Mission data sets	133
MSD3A2	Mission data sets	137
MSA3A2	Mission data sets	230
MSC3A2	Mission data sets	236

Table 6. Statistics from Run 1. Real-time processing and COMGEN execution

	SNAP1	SNAP2	SNAP3	SNAP4
CPU utilization	40%	38%	42%	41%
Applications	19%	18%	19%	18%
Operating system overhead	21%	20%	23%	22%
I/O Utilization				
Channel 1	18%	17%	17%	18%
Disk drive 137	84%	86%	85%	87%
Disk drive 230	28%	19%	22%	20%
Seek time				
Disk drive 137	70 ms	79 ms	76 ms	76 ms
Disk drive 230	23 ms	19 ms	21 ms	19 ms
Main core usage				
Available without purge	16K	4K	2K	0K
Available with purge	174K	170K	146K	134K
Number of purges	9	14	14	24
Large capacity storage (LCS) used	1780K	1780K	1795K	1797K
Task queues				
Master data record write				
Number	11	10	13	11
Average time	379 ms	501 ms	398 ms	427 ms
Data table I/O				
Number	911	826	841	853
Average time	126 ms	139 ms	134 ms	138 ms
Data table availability				
Number	31	34	31	30
Average time	296 ms	266 ms	295 ms	217 ms
Real-time I/O				
Number	52	50	55	58
Average time	34 ms	18 ms	139 ms	52 ms
Core				
Number	0	0	0	4
Average time	—	—	—	107 ms
Digital TV (DTV)				
DTV operating system core buffers used (of 30 available)	23	21	22	22
Task response times				
Tracking subsystem	332 ms	311 ms	280 ms	329 ms
Telemetry subsystem	1686 ms	1811 ms	1906 ms	1882 ms
M&OC subsystem	196 ms	159 ms	195 ms	204 ms
Command transmission response time	—	—	337 ms	930 ms
Backlogged telemetry Input data block	9	17	23	29

K = 1000 8-bit bytes.

Table 7. Statistics from Run 2. Real-time processing and COMGEN execution

	SNAP1	SNAP2	SNAP3	SNAP4	SNAP5
CPU utilization	57%	45%	47%	45%	46%
Applications	27%	20%	20%	19%	19%
Operating system overhead	29%	24%	27%	26%	26%
I/O Utilization					
Channel 1	39%	11%	2%	2%	1%
Disk drive 137	45%	14%	2%	3%	2%
Channel 2	30%	42%	42%	43%	43%
Disk drive 230	17%	54%	70%	69%	68%
Disk drive 231	48%	46%	48%	48%	48%
Seek time					
Disk drive 137	2 ms	4 ms	15 ms	16 ms	21 ms
Disk drive 230	18 ms	19 ms	24 ms	22 ms	22 ms
Disk drive 231	43 ms	45 ms	45 ms	46 ms	45 ms
Main core usage					
Available without purge	20K	12K	30K	6K	6K
Available with purge	198K	190K	164K	160K	170K
Number of purges	11	10	15	16	20
Large capacity storage (LCS) used	1780K	1898K	1913K	1915K	1917K
Task queues					
Master data record write					
Number	11	10	9	7	10
Average time	251 ms	182 ms	98 ms	110 ms	96 ms
Data table I/O					
Number	2183	1629	1496	1553	1552
Average time	34 ms	62 ms	79 ms	75 ms	73 ms
Data table availability					
Number	19	26	22	16	17
Average time	95 ms	219 ms	150 ms	183 ms	171 ms
Real-time I/O					
Number	41	52	51	56	53
Average time	17 ms	50 ms	206 ms	66 ms	46 ms
Core					
Number	0	0	0	0	0
Average time	—	—	—	—	—
Digital TV (DTV)					
DTV operating system core buffers used (30 available)	23	23	23	21	22
Task response times					
Tracking subsystem	262 ms	506 ms	617 ms	579 ms	603 ms
Telemetry subsystem	613 ms	814 ms	898 ms	793 ms	875 ms
M&OC subsystem	189 ms	242 ms	279 ms	264 ms	236 ms
Command transmission response time	—	—	250 ms	1154 ms	815 ms

Table 8. Statistics from Run 3. Real-time processing and COMGEN execution

	SNAP1	SNAP2	SNAP3	SNAP4	SNAP5
CPU Utilization	57%	49%	51%	50%	50%
Applications	26%	21%	21%	20%	21%
Operating system overhead	30%	28%	30%	29%	29%
I/O Utilization					
Channel 1	48%	56%	60%	62%	60%
Disk drive 131	36%	44%	48%	49%	47%
Disk drive 137	31%	30%	32%	30%	31%
Channel 2	18%	18%	11%	11%	10%
Disk drive 230	33%	25%	27%	21%	21%
Seek time					
Disk drive 131	0 ms	0 ms	0 ms	0 ms	0 ms
Disk drive 137	29 ms	29 ms	32 ms	29 ms	31 ms
Disk drive 230	26 ms	14 ms	27 ms	18 ms	20 ms
Main core usage					
Available without purge	12K	16K	12K	6K	20K
Available with purge	176K	194K	182K	148K	168K
Number of purges	10	6	14	19	16
Large capacity storage (LCS) used	1780K	1898K	1913K	1915K	1917K
Task queues					
Master data record write					
Number	9	10	9	10	10
Average time	213 ms	224 ms	208 ms	225 ms	182 ms
Data table I/O					
Number	2090	2467	2649	2714	2624
Average time	36 ms	32 ms	30 ms	27 ms	28 ms
Data table availability					
Number	18	23	25	27	24
Average time	97 ms	136 ms	72 ms	116 ms	108 ms
Real-time I/O					
Number	42	51	55	46	47
Average time	18 ms	49 ms	345 ms	112 ms	81 ms
Core					
Number	0	0	0	0	0
Average time	—	—	—	—	—
Digital TV (DTV)					
DTV operating system core buffers used (30 available)	24	25	23	26	26
Task response times					
Tracking subsystem	345 ms	261 ms	334 ms	217 ms	218 ms
Telemetry subsystem	562 ms	558 ms	609 ms	595 ms	605 ms
M&OC subsystem	198 ms	176 ms	196 ms	250 ms	194 ms
Command transmission response time	—	—	278 ms	608 ms	449 ms

See Table 9 for a definition of terms.

Table 9. Definition of terms used in summary results of Tables 6, 7, and 8

CPU Utilization	Percentage of the snap time the 360/75 CPU was in use, i.e., not idle or waiting.
Applications	Percentage of the snap time the CPU was in use by a user program.
Operating system overhead	Percentage of the snap time the processor was in use by the operating system servicing user requests, or interrupts.
I/O Utilization	
Channel utilization	Percentage of the snap time the channel was busy. For the disk channels, the channel is not made busy by seek operations.
Device utilization	Percentage of the snap time the device was busy.
Main core	
Available without purge	The minimum amount of core not allocated during the snap interval. This value may be increased by a successful purge.
Available with purge	The minimum amount of core not allocated plus the amount of core allocated to load modules not in use. This represents the amount of core actually available.
Purges	The number of times during the snap, purge attempts were made to free unused load modules to satisfy a GETMAIN request.
Large capacity storage (LCS) used	The maximum amount of LCS used during the snap.
Task queues	
Number	The total number of times all tasks were placed in a wait state for the reason indicated.
Average time	The average time in milliseconds that tasks were in a wait state for the reason indicated.
Digital TV (DTV)	
DTV operating system core buffers used	Maximum number of core buffers required to be used by the DTV operating system.
Task response times	The average time all tasks in the indicated category require to process a real-time queue element, i.e., from the time the RTQEL is activated to the final EXIT under the task.
Backlog	The number of unprocessed RTQEL's at the end of the snap.
Command transmission response time	Average time from the initiation of the input message request to the transmission of the data block over the outbound high-speed data line.

GCF Television Assembly Design for the Systems Development Laboratory

E. F. Bird
SFOF/GCF Development Section

The newly constructed Systems Development Laboratory (SDL) at the Jet Propulsion Laboratory will serve as an extension of the Space Flight Operations Facility (SFOF). The Pioneer Project will utilize the SDL for conducting the operations of the Pioneer F and G missions. The Ground Communications Facility (GCF) provides intercommunication between the SDL and the SFOF. One of the communication media is television. This article defines the requirements and the resulting design of the GCF Television Assembly in the SDL.

I. Introduction

A new building is being constructed at the Jet Propulsion Laboratory which will serve as an extension of the Space Flight Operations Facility (SFOF). It is known as the Systems Development Laboratory (SDL) and it will be utilized by the *Pioneer* Project for missions *F* and *G*. As the SDL is a part of the Deep Space Network (DSN), it is the responsibility of the Ground Communications Facility (GCF) to provide for intercommunication capabilities between the SFOF and SDL. The Television Assembly (TVSA) to be installed in the SDL is a part of the Wideband System and is considered a constituent of the SFOF Internal Communications Subsystem (SICS). (See Ref. 1.) This article defines the requirements and the resulting design of the GCF TVSA in the SDL.

II. Requirements

The TVSA in the SDL makes available, to specified users in the SDL, television presentations that originate in the SFOF. Some TV monitors will display predetermined (hardwire-interconnected) channels while others will be programmed (keyboard-switched) by the individual users.

III. Design

Figure 1 is a functional block diagram of the SDL TVSA. A number of factors were considered in the design and the following technical decisions were made.

A. Interface

The SDL TVSA will interface the SFOF TVSA (and become a part of SICS) via balanced shielded video pairs. This type of transmission is selected in order to minimize noise and hum pickup along the path over which the cable must run and reduce the effect of ground potential differences between buildings.

B. Synchronization

The SDL TVSA will receive its master sync signal from the SFOF TVSA. The composite sync signal will be

added to the video signal after it has emerged from the switcher and is enroute to a monitor. This will be done in a distribution amplifier.

C. Number of Video Inputs

The SDL TVSA will have an input capacity of 40 video channels. All of these channels will originate in the SFOF.

D. Number of Fixed and Switchable TV Monitors

All of the monitors with fixed presentations will have 58.4-cm (23-inch) screens. There will be 18 of this type. The monitors with switchable presentations will have either 22.9- or 35.6-cm (9- or 14-inch) screens. They will number 44 and 11, respectively.

E. Switcher Matrix Capacity

The switcher is that part of the TVSA which responds to the user push-buttons by routing selected video signals to the appropriate monitors. This one will be equipped to switch a matrix size of 5 × 20, meaning that switchable monitors will be grouped in fives to select from the same set of 20 possible video channels.

F. Cost Factor

The cost factor is an inseparable part of all the above considerations. The more important decisions relating to cost reduction are those of (1) allowing video to be transmitted in one direction (SFOF to SDL) only, and (2) restricting the selection capacity of the switchable monitors to 20 channels. These decisions relate directly to synchronization (Item B) and matrix capacity (Item E), respectively. The equipment to be used in implementing the SDL TVSA will match (as closely as is practicable) the constituent equipment of the SFOF TVSA. This reduces spares requirements, personnel training, documentation, etc.

IV. Conclusion

The capability for meeting *Pioneer* television display requirements will be provided in the SDL. The SDL TVSA is capable of being expanded to meet more demanding requirements of future DSN missions (e.g., processing of SDL-originated video signals, increased matrix size, and bidirectional video transmission between the SFOF and SDL). Fabrication of the SDL TVSA, as described herein, is now underway.

Reference

1. Hanselman, R., "Wideband Digital Data System Terminal Configuration," in *The Deep Space Network*, Space Programs Summary 37-66, Vol. II, pp. 107–110. Jet Propulsion Laboratory, Pasadena, Calif., Nov. 30, 1970.

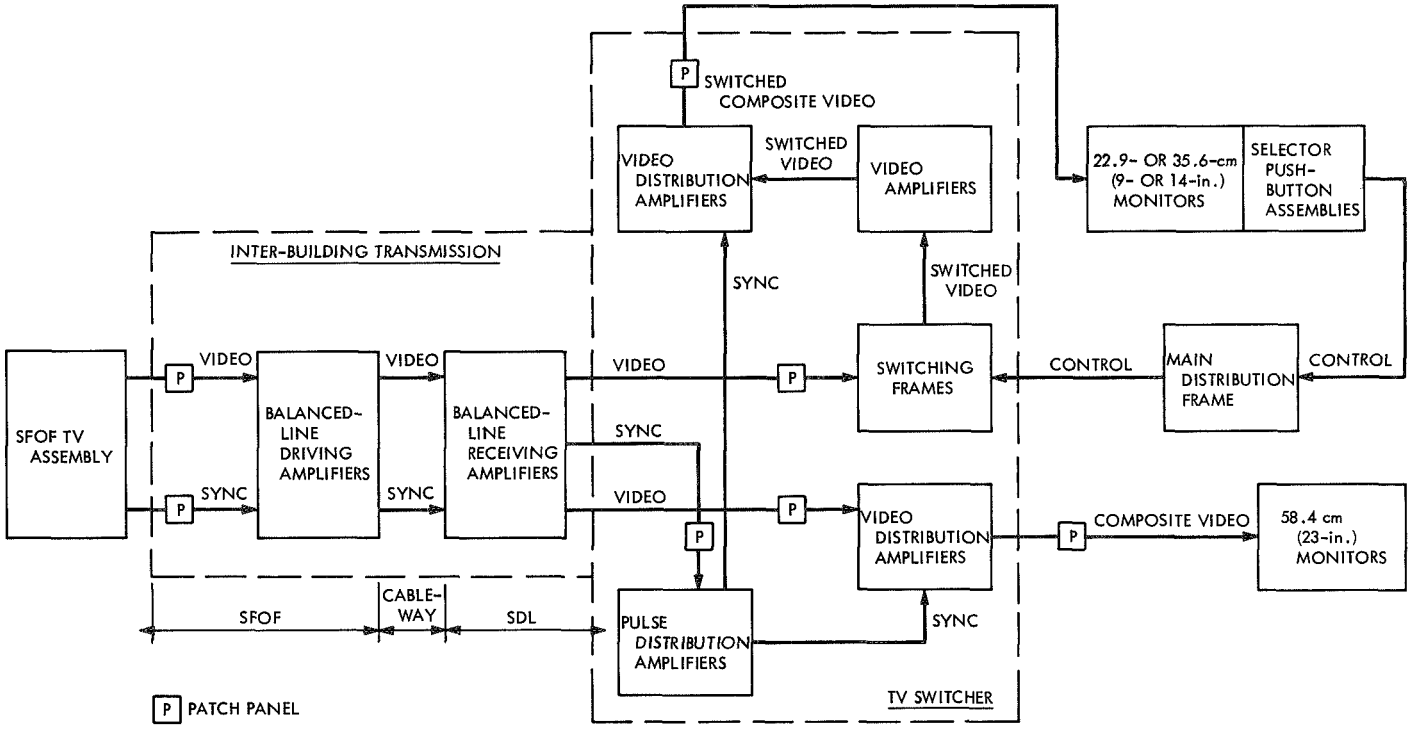

Fig. 1. SDL TVSA functional block diagram

Ground Communications Facility System Tests

D. Nightingale and J. P. McClure
SFOF/GCF Development Section

The Ground Communications Facility substantially upgraded the High-Speed System and implemented a new Wideband System for more comprehensive operational data transfers. Extensive tests were conducted prior to turning these systems over to operations personnel for integration into the Deep Space Network (DSN). This article summarizes the purpose and results of these tests, with the final objective of full committed support of Mariner Mars 1971 flight operations.

I. Introduction

The functional design requirements established by the Deep Space Network (DSN) for the necessary capabilities to support the *Mariner* Mars 1971 flight operations included specific items pertaining to the communications services from the tracking stations and the operations and data processing areas at JPL. Much of the required capability existed, yet much had yet to be engineered, installed, and operationally verified. (See Refs. 1, 2, 3, and 4.)

During 1970, the Ground Communications Facility (GCF) concentrated on two major changes to the Facility: (1) the conversion of the High-Speed Data System from 2400- to 4800-bps operation, and (2) the implementation of a Wideband System 50-kbps digital transmission capability. These developments have been completed and tested on a system basis.

The system tests were conducted to verify that the system operated properly and that it met the functional requirements which it was designed to satisfy. These tests also validated the design and exercised the proposed operational procedures. Though the system tests measured the overall bit error rates, detailed error statistics tests are being conducted and will be reported in future articles.

II. High-Speed Data

The upgraded high-speed data capability provides a single-channel full-duplex 4800-bps terminal at each Deep Space Station (DSS) and the Compatibility Test Area (CTA 21), as well as 3 channels in the Simulation Center (SIMCEN) and 6 channels in the SFOF Communications Terminal. Each DSS is connected to the Space Flight Operations Facility (SFOF) via transmission paths consisting of discrete links between major NASCOM switching centers and the end link to the DSS. At each NASCOM center, full-duplex regeneration capability is provided.

In every case, tests were conducted between each DSS and the SFOF, the test series being extended when anomalies were encountered. The stations were tested in the following chronological order, beginning in October

1970: DSSs 12, 41, 51, 62, 71, CTA 21, SIMCEN, and DSSs 14 and 11. DSSs 42 and 61 will be tested in April 1971.

It was originally intended to use a special test program which would exercise the interfaces between the GCF and Deep Space Instrumentation Facility (DSIF) and between the GCF and SFOF in addition to providing performance data on all installed equipment and operational circuits. However, unforeseen delays in the test program development and debug, as well as the availability of necessary machine time, required an alternative test sequence to be developed and used. This enabled all GCF equipment, procedures, and circuits to be checked out up to the DSIF interface. A separate test series validated the interface at the SFOF.

A number of discrepancies were discovered and rectified before acceptable all-around performance was obtained. Among the most notable of the discrepancies were:

(1) A severe impulse noise cross talk into Australian circuits between DSS 41 and Canberra Switching Center causing high error rates. This was subsequently cleared by the common carrier, after being found to be in Woomera Village. High-level dialing pulses were the prime cause of the problem.

(2) Early high error rate from DSS 51 due to lack of regeneration equipment at Ascension was improved into acceptable limits after regeneration became operational.

(3) Line level problems at Madrid Switching Center and DSS 62 delayed final acceptable test.

(4) In-house equipment installation delays at DSS 71 caused schedule slippage.

Other minor hardware discrepancies were also revealed at various locations and certain items of test equipment were found to be inadequate for the required tests. All such items were restored to a full operational condition.

The operational activation and use procedures were adjusted as a result of this test series and all personnel training was determined to have been sufficient.

Generally speaking, better than 99% of all transmitted data blocks (each block is 1200 bits) were received without error.

III. Wideband Data

The new wideband data capability provides 50-kbps terminal equipment at four locations: the SFOF, the Simulation Center, CTA 21, and DSS 14. Transmission paths connect each of the outlying locations to the SFOF.

Five tests were conducted, one for each of the functional paths:

(1) CTA 21 to SFOF.

(2) Simulation Center to SFOF.

(3) Simulation Center to CTA 21.

(4) DSS 14 to SFOF.

(5) Simulation Center to DSS 14.

These tests were conducted in November and December 1970 in accordance with a sequence-of-events. The tests exercised the end-to-end system between the GCF interface points. The tests did not exercise the DSIF nor the SFOF's interfacing equipment, since the other sides of these interfaces were not yet complete or were not yet cabled to the interface point. All GCF-furnished cables were tested to the distant connector.

The test results were satisfactory, though some minor discrepancies were revealed. Some jack panels were not labeled and one reversed connector shell was found. An ancillary test function would not operate properly, and an output converter was found to be inoperable. Some other minor hardware difficulties were revealed. The tests disclosed that several of the operating procedures were not appropriate. Training was also found to be inadequate in some cases.

The error rate tests showed a bit error rate of 7×10^{-7} for five tests totaling 14.4 hours. During three of the tests between CTA 21, the Simulation Center, and the SFOF, no errors were detected during 6.8 hours of activity. In a separate 6.5-hour test from DSS 14 to the SFOF, 99.97% of the 1200-bit blocks were received error-free.

All equipment discrepancies were cleared subsequent to the tests, and additional training was given. In order to provide familiarity with the equipment and the procedures, the DSS 14–SFOF circuit activation procedure was repeated weekly.

IV. Conclusion

The High-Speed and Wideband System tests detected some equipment problems, revealed inadequacies in the

proposed operating procedures, and produced accurate data on gross error rates. These tests were of direct and substantial benefit to the GCF. Similar tests will be conducted on future GCF system developments; however, such future tests will be designed to more fully exercise the interfaces in order to detect this type of problem at an earlier stage.

The 4800-bps and 50-kbps capabilities are now in the DSN's operational inventory.

References

1. McClure, J. P., "Ground Communications Facility Functional Design for 1971–1972," in *The Deep Space Network*, Space Programs Summary 37-66, Vol. II, pp. 99–102. Jet Propulsion Laboratory, Pasadena, Calif., Nov. 30, 1970.
2. Nightingale, D., "High-Speed System Design Mark IIIA," in *The Deep Space Network*, Space Programs Summary 37-66, Vol. II, pp. 103–105. Jet Propulsion Laboratory, Pasadena, Calif., Nov. 30, 1970.
3. Evans, R. H., "High-Speed Data Block Demultiplexer," in *The Deep Space Network*, Space Programs Summary 37-66, Vol. II, pp. 105–106. Jet Propulsion Laboratory, Pasadena, Calif., Nov. 30, 1970.
4. Hanselman, R., "Wideband Digital Data System Terminal Configuration," in *The Deep Space Network*, Space Programs Summary 37-66, Vol. II, pp. 107–110. Jet Propulsion Laboratory, Pasadena, Calif., Nov. 30, 1970.

Development of the Heat Exchanger for the 64-m Antenna Hydrostatic Bearing

H. Phillips
DSIF Engineering Section

Maintenance of oil temperature, as a means of viscosity control, is an essential requirement for the 64-m antenna hydrostatic bearing. Operational experience with the heat exchanger used for cooling the oil showed that it was not functioning adequately or in accordance with the design, and a resultant study showed a probable internal structural failure. A new heat exchanger was designed, with JPL assistance on the structural problem, and is now operating satisfactorily.

I. Introduction

The entire rotating weight of the 64-m antenna [approximately 2.5×10^6 kg (5.5×10^6 lb)] is carried on a pressurized hydrostatic bearing. In this bearing a fixed flow of pressurized oil is forced through the sills between three pads, which support the rotating weight, and the bearing runner, mounted on the concrete pedestal. The pressure required to force the fluid through the sill also acts upward to support the load on the pads. The height of the oil film between the pads and the runner is a function of the oil viscosity, and hence of the oil temperature. In operation this film height is critical, and a close control of the oil temperature is required. The oil is supplied by a system of precharge and high-pressure pumps (Fig. 1), and since no external work is accomplished by the pressurized oil, the entire motor output must be dissipated as heat. The heat loss rate, based on actual operating pressures, is approximately 105 kW (361,200 Btu/h) with one precharge pump operating and 117 kW (401,400 Btu/h) with both precharge pumps operating. Loss through the reservoir walls is negligible. Loss through the runner into the pedestal concrete varies with the season, with a minimum of 39 kW (132,600 Btu/h) total, assuming a diurnal average temperature of 27°C (80°F) and an oil temperature of 31°C (88°F). Hence, the heat exchanger must dissipate from 66 to 78 kW (228,600 to 268,800 Btu/h).

II. Heat Exchanger Parameters

The basic relationship giving the capacity of a heat exchanger is

$$q = F \cdot A \cdot U \cdot T_{lm} \tag{1}$$

where q is the heat dissipation in watts; F is a factor depending on the heat exchanger configuration and the operating temperatures; A is the heat exchanger area; and U is an overall heat transfer coefficient dependent on the heat exchanger design, the flow rates of the oil and cool-

ant, and on the viscosity of the oil and coolant. T_{lm} is the log mean temperature difference given by the equation

$$T_{lm} = \frac{\theta_a - \theta_b}{\ln \theta_a/\theta_b}$$

where θ_a is the temperature difference between the inlet oil and its surrounding coolant, and θ_b between the outlet oil and its surrounding coolant.

For the hydrostatic bearing system the oil flow and specific heat are constant. Equation (1) can then be rewritten

$$\Delta t = \frac{F \cdot A \cdot U \cdot T_{lm}}{Q \cdot S} \quad (2)$$

Δt is the oil temperature change, Q is the oil flow, and S is the specific heat of the oil.

The quantity $Q \cdot S/(F \cdot A \cdot U)$ is then an operational parameter by which the heat exchanger performance can be evaluated, based on measurements of oil and coolant temperatures. The water flow rate must be assumed constant, or measured, and the oil temperature, and hence its viscosity, must be within a reasonable range for meaningful results.

III. Original Heat Exchanger

The original heat exchanger at DSS 14 was designed for oil with a viscosity of 116 m^2/s (525 SSU) and to dissipate 75 kW (267,000 Btu/h) with oil inlet and outlet temperatures of 41.5 and 38.5°C (107 and 101°F) and coolant temperatures 34.9°C (95°F) in and 36.5°C (97.8°F) out. This gives an operating parameter as outlined above of 0.50. Trouble was experienced maintaining the oil temperature during the summer, and investigation found that: (1) a modulating valve for the water flow, controlled by oil temperature, always operated in the full open position; (2) the pressure drop across the heat exchanger on the oil side had dropped from a calculated 34.4 N/cm^2 to 17.2 N/cm^2 (50 psi to 25 psi); and (3) the operating parameter was about 0.90 rather than the 0.50 designed, implying loss of heat transfer ability. Since the unit could not be readily disassembled for inspection, the manufacturer's drawings were obtained and a stress analysis made on the structural elements.

The heat exchanger is a 2–4 type, as shown in Fig. 2, with 2 shell passes for the oil and 4 tube passes for coolant. The oil inlets and outlets are on opposite sides of the same end of the heat exchanger so that at that end the full pressure drop across the oil side of the unit was carried by the baffle. The baffle was 3.2-mm (0.125-in.) carbon steel with a yield strength of approximately 344 N/mm^2 (50,000 psi) while the bending stresses due to the pressure difference, carried over the 46-cm (18-in.) span, was 5350 N/mm^2 (776,000 psi). It was clear that some sort of failure had occurred permitting the oil to pass around or through the baffle, reducing both the pressure drop between oil inlet and outlet, and the effective area of heat transfer.

IV. Replacement Heat Exchanger

A review was made of the actual antenna operating conditions and a new heat exchanger was purchased to meet the following requirements:

(1) Cooling 11.4 dm^3/s (180 gpm) of oil having a viscosity of 176×10^{-6} m^2/s (800 SSU) from 42 to 37.7°C (108 to 100°F), using a coolant flowing up to 18.9 dm^3/s (300 gpm) and 34.9°C (95°F) at the inlet.

(2) Cooling 22.7 dm^3/s (360 gpm) of oil having a viscosity of 176×10^{-6} m^2/s (800 SSU) from 41 to 39°C (106 to 102°F) with the same coolant flow.

(3) Pass 22.7 dm^3/s (360 gpm) of oil having a viscosity of 198×10^{-6} m^2/s (900 SSU) with a pressure loss not to exceed 55.2 N/cm^2 (80 psi).

(4) Have identical piping connections to those on the original heat exchanger.

These specifications reflected the actual operating conditions, using a higher viscosity oil than originally specified, providing for operation with two precharge pumps (critical mission configuration) without excessive pressure drop, and permitting a quick change over from the original unit.

The heat transfer design of the new heat exchanger was carried out by the manufacturer and checked by JPL. It was a straightforward design using finned tubes and a slightly longer shell to meet the heat transfer and flow requirements. The manufacturer encountered a problem in the structural design, however, because of the pressure drop across the baffle which had been the problem in the initial design. The solution to this problem was suggested by JPL and consisted of using a 22-mm (0.875-in.)-thick plate of a material having a yield stress of 414 N/mm^2

(60,000 psi) and an allowable working stress under the Unfired Pressure Vessel Code of 104 N/mm² (15,000 psi). In order to minimize bending moments carried into the pressure shell, the baffle was simply supported at the pressure shell walls in a channel section welded into the wall as shown on Fig. 3. The groove along the edge of the baffle plate assures that the load will be carried into the wall at the minimum distance from the shell plate neutral axis, minimizing bending moment. This arrangement also permits removal of the baffle and tube bundle for inspection.

The new heat exchanger has been installed and is operating satisfactorily. Pressure and temperature taps were added to the oil and coolant piping, and platinum wire thermometers have been installed. These provide the measurement accuracy necessary to maintain proper monitoring of the unit.

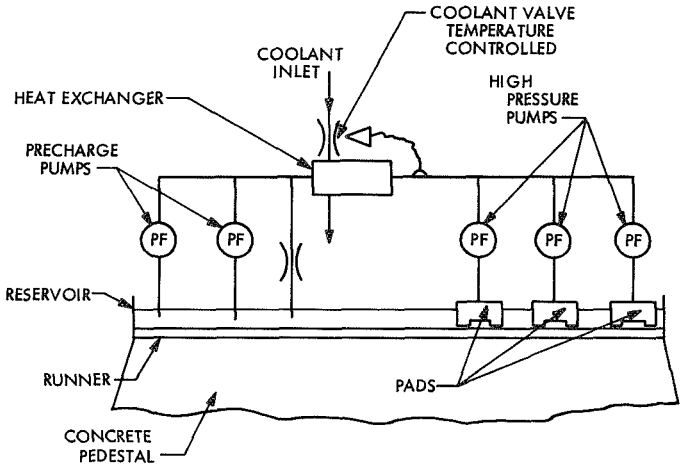

Fig. 1. Hydrostatic bearing oil cooling schematic

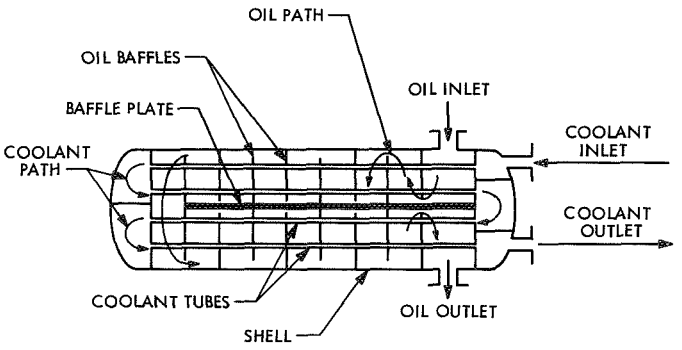

Fig. 2. Schematic of 2-4 heat exchanger

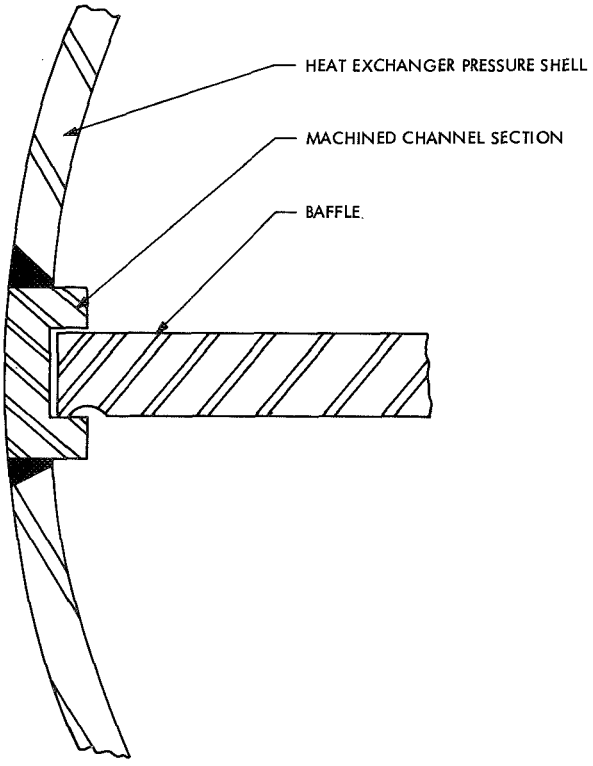

Fig. 3. Heat exchanger baffle support

MSFN/DSN Integration Program for the DSS 11 26-m Antenna Prototype Station

R. Weber
DSIF Engineering Section

A plan was proposed in mid-1971 wherein unique Deep Space Network (DSN) equipment would be installed in the 26-m antenna Manned Space Flight Network (MSFN) operations control room and integrated to function with pre-existing MSFN equipment. This effort was initiated at the Pioneer Deep Space Station (DSS 11) site in November 1970 and shortly thereafter at the two overseas sites. This plan allows the 26-m antenna DSN tracking capability to exist at these sites while the 64-m antenna is in the process of being built and integrated into the original 26-m antenna DSN control room.

The details of the integration efforts at the DSS 11 prototype station are outlined, and significant accomplishments and milestones are indicated. The equipment layout in the operations control room is illustrated and the unique operational and electrical interfaces between the DSN equipment and the MSFN equipment are described.

During the period from 1966 through mid-1971 the *Apollo* mission to the moon has been supported by a three-site dual-station S-band 26-m tracking network. Each site consisted of a 26-m X-Y antenna operated by the Goddard Space Flight Center and a 26-m HA-dec antenna shared with the Jet Propulsion Laboratory but utilizing a completely separate control room for *Apollo* manned missions.

With the approval of the construction of the two overseas 64-m DSN antennas to be built by the Jet Propulsion Laboratory and dedicated to the DSN, it was realized that the need for additional control room facilities and equipment would add a considerable financial burden to the stringent budget. This is a consequence of the requirement for simultaneous operation of the 26-m system and the 64-m system at the 64-m antenna sites. As a consequence, a plan was proposed in mid-1970 wherein the unique DSN equipment would be installed in the 26-m MSFN operations control room and integrated to function with the preexisting MSFN equipment where this equipment is similar to the DSN equipment. This effort was initiated at the DSS 11 site in November 1970 and shortly thereafter at the two overseas sites, DSS 42 and DSS 61. This plan has the added dividends of allowing the DSN to have 26-m antenna tracking capability at these sites while the 64-m overseas antennas are being constructed

and are being interfaced with new equipment in the original 26-m antenna DSN control room and furnishing the original 26-m DSN receiver to the 64-m antenna stations.

The *Apollo* wing 26-m joint MSFN/DSN sites, which include DSS 11, DSS 42, and DSS 61, operate with three categories of equipment as follows: (a) DSN and MSFN common equipment, (b) MSFN equipment equivalent to DSN equipment and (c) unique MSFN equipment.

The shared-equipment includes the 26-m cassegrain antenna and feed, the servo hydraulics and antenna drive system, the dual S-band masers, preamplifiers and control racks, the dual 20 kW S-band transmitter power amplifiers, control racks and power supplies (one of which is used in the DSN configuration), the site primary power and the 30-m collimation tower. Refer to Fig. 1 for a typical *Apollo* wing operations room layout.

The DSN equipment that has been replaced with equivalent MSFN equipment includes the servo electronics, the antenna pointing subsystem (APS) replaced with the antenna position programmer (APP), the tracking data handling subsystem (TDH) replaced with the tracking data processor (TDP), the frequency and timing subsystem (FTS) supplemented by the timing system (TMG), and the analog instrumentation system (AIS) recording replaced with the MSFN recording system and the S-band receiver-exciter subsystem (RCV) replaced by a dual S-band receiver-exciter system. In addition, the MSFN communications room teletype interfaces and control have been replaced by the DSN communications room equipment. However, the MSFN high speed data (HSD), the wing-to-prime site microwave link facilities, and the 112A MSFN station intercommunications system will be maintained in a separate MSFN communications room.

The unique MSFN equipments, located in the *Apollo* wing, include the verification receiver, the subcarrier oscillators (SCOs) housed in the collimation control rack, the incoming and outgoing data patching and multiplexing racks to interface with the wing-to-prime site microwave link. The MSFN collimation tower transponders and related equipment in the control room rack, the 1218 Univac computer for processing predicts which will be replaced by the DSN antenna pointing subsystem (APS), a Loran receiver for timing purposes and the wing-to-prime site microwave link and high-speed data (HSD) equipment referenced above.

The concept applied to the MSFN-DSN integration program is that of using the existing equivalent MSFN equipment wherever possible, with particular emphasis on the MSFN receiver-exciter, and establishing DSN functions and interfaces in the simplest manner possible. The resulting effort shall not degrade either the *Apollo* station performance or the DSN station performance; however, certain operational procedures and functions may be simplified or deleted where they do not directly affect the quality of the data to be acquired.

The integrated stations will perform all the *Apollo* requirements with the original MSFN equipment, with the exception of the DSN antenna pointing subsystem (APS) and the DSN simulation conversion assembly (SCA) units which will process antenna-pointing predict information in place of the 1218 Univac computer. A minor concession to the integrated configuration is the elimination of the seldom used on-line processing of the 29-point predict message and electrically driving the APP and the antenna directly from the computer. The processing of a drive tape and reloading it in the APP unit electrically or mechanically in the torn-tape mode is required in the integrated station (Fig. 2).

The DSN operation of the integrated stations will function very similarly to that of a normal MM'71 backup station. The first wing receiver will be interfaced with the subcarrier demodulator assembly (SDA) and command modulator assembly (CMA) units via new distribution amplifiers and a new exciter modulation mode-select unit in the exciter modulator system, respectively. The DSN loop bandwidth will be electrically selected when the DSN VCOs are installed. The *Apollo*-peculiar wide-band modifications will be installed in the second wing receiver in May 1971 and will not affect the DSN receiver configuration or performance. Two channels of telemetry will be provided by the SDAs, the symbol synchronizer assemblies (SSAs) and the dual telemetry and command processor (TCP). Two channels of command will be provided by two CMAs. A single 20-kW S-band transmitter will be available for DSN transmissions. The frequency and timing signals will be provided by the DSN frequency and timing subsystem (FTS). The exception will be the 5-MHz signals required by the SDAs which must be coherent with the receiver and will be provided by the MSFN timing subsystem.

The DSN FTS clock and the MSFN TMG clock will be compared and the DSN clock will be updated to provide the required 50 μs tracking tolerance. The DIS function at the integrated station will be provided by the 7-rack DIS-I which will provide monitor data to SFOF via HSD lines; however, station observation of monitor data will

require a backfeed mode from the SFOF wherein data is processed at the SFOF and fed to the station via the HSD line. The tracking data sent to SFOF in the DSN mode will originate in the MSFN TDP unit.

The HSD line output of the TDP will be sent to the SCA HSD receive-register for processing and changing into the DSN format by the SCA and APS computer. This processed data will then be transmitted from a HSD coupler in the APS to the SFOF via DSN HSD lines. The only teletype backup available will be the output of the TDP in MSFN format which is acceptable to DSN. The APS antenna pointing options will be reduced due to the computing load placed upon the 8-K word memory and software of the XDS-910; however, no compromise in data acquisition quality is expected. The 29-point DSN acquisition message may be received at the APS on either the HSD line or via teletype and the related "torn-tape" mode. The APS will be capable of producing an off-line drive tape from the 29-point acquisition message. This tape may then be used to drive the antenna by loading it into the APP unit and driving with one point per ten seconds.

The alternative mode is also available wherein the 29-point acquisition message may be processed by the APS and the result stored for subsequent electrical readout to the APP at a one-point-per-second rate. This "direct electrical drive" mode will, however, have to be interrupted in the event of being compelled to receive and process a new acquisition message from either the HSD input or the teletype torn-tape input. The previously cut drive tape must then be relied upon for antenna pointing, or autotrack or aided-track substituted, when this situation is presented during antenna pointing operations. The planetary mode and the injection-conditions mode will not be available due to the lack of APS/XDS-910 computer capacity.

In addition to the above integrated station features, the teletype functions of the DSN and MSFN communications rooms have been combined in the DSN communications room. Administrative traffic on GSFC collectives will be routed at the source through JPL NASCOM circuits. The special predict-message circuit and the prime-to-wing teletype circuit will be available on the station communications control group (SCCG) in the DSN communications room.

The program implementation began at the prototype DSS 11 station in November 1970. The period of time, prior to *Apollo 14* operations in mid-January 1971, was confined to moving the MSFN equipment to a more space-efficient location and moving the DSN microwave and transmitter racks into the new control room. In addition, the DSN recording racks, analog racks, the telemetry and command data handling subsystem (TCD), the patch-rack, a single SDA, SSA, and CMA rack, and the Alpha portion of the TCP telemetry processor, complete with a half patch-rack and a half communications buffer rack, were moved into the new integrated control room. Following the conclusion of the *Apollo 14* operations, the FTS-I and DIS-I (digital instrumentation system used for recording and displaying station parameters) systems were moved in place and were subsequently upgraded and tested in the new station configuration. The DSN modules and modifications to the first MSFN receiver were installed with JPL and GSFC participating at the site. The original MSFN communications room was enlarged and the two data multiplexing racks, used to interface the sending and receiving of inter-site microwave information with the receiver and exciter, were removed from the control room to the MSFN communications room. In addition, a new DSN rack was installed to house the additional television equipment required when the surveillance TV and antenna fence alarm system was integrated into the MSFN servo system. The DSN system monitor console (SMC) was reduced to three half-height racks and installed in the control room. It is presently being repackaged to house the DIS TV alarm display, the CMA status panel, the new tactical intercommunications station and other necessary station monitor indicators. Later, the three APS racks and the two racks of SCA equipment were installed and tested. The layout of the completed DSS 11 integrated station control room is shown in Fig. 3.

All presently installed DSN subsystems have been tested and are operating nominally. The system interface tests have begun and are expected to be completed after the arrival of the TCP Beta racks, the second SDA, SSA and CMA racks, and the receiver test rack which will replace the present RCV/1929 test rack. This event will be followed by DSN antenna-pointing software, tracking data software and monitor software testing with Ground Communication Facility (GCF) and Space Flight Operations Facility (SFOF) participation. The new APP-APS and the new APS-SCA-TDP hardware interfaces will be implemented at DSS 11 starting in May 1971. The APP-APS hardware interface for antenna pointing will be completed by the end of June 1971, in time for demonstration purposes during the *Apollo 15* mission. However, the hardware and software implementation of the DSN APS-SCA-TDP tracking data system will not be completed until the end of August 1971.

Concurrent with the implementation program, an *Apollo* operator training program is being conducted at DSS 11 during the month of April and half of May. This effort will provide *Apollo* mission operator certification in antenna servo, receiver-exciter, ranging, timing, tracking data processor (TDP), antenna position programmer (APP), 1218 Univac computer (used for *Apollo 15* only), 112A intercommunications system, teletype, 205 and 203 high-speed data modems, and documentation procedures. In addition to the 4 to 6 wk of classroom instruction in the above subjects, several weeks will be scheduled for hands-on training and simulations. Finally, an aircraft simulation fly-by will be scheduled for the first week of June as a final exercise before mission readiness testing.

The two overseas stations, DSSs 42 and 61, are presently undergoing integration installation and testing patterned after the prototype effort at DSS 11. These stations will be available to support the *Apollo 15* mission in July in the original MSFN configuration using the 1218 Univac computer. All three stations will be available to support *Pioneer F* and other DSN missions after September 15, 1971.

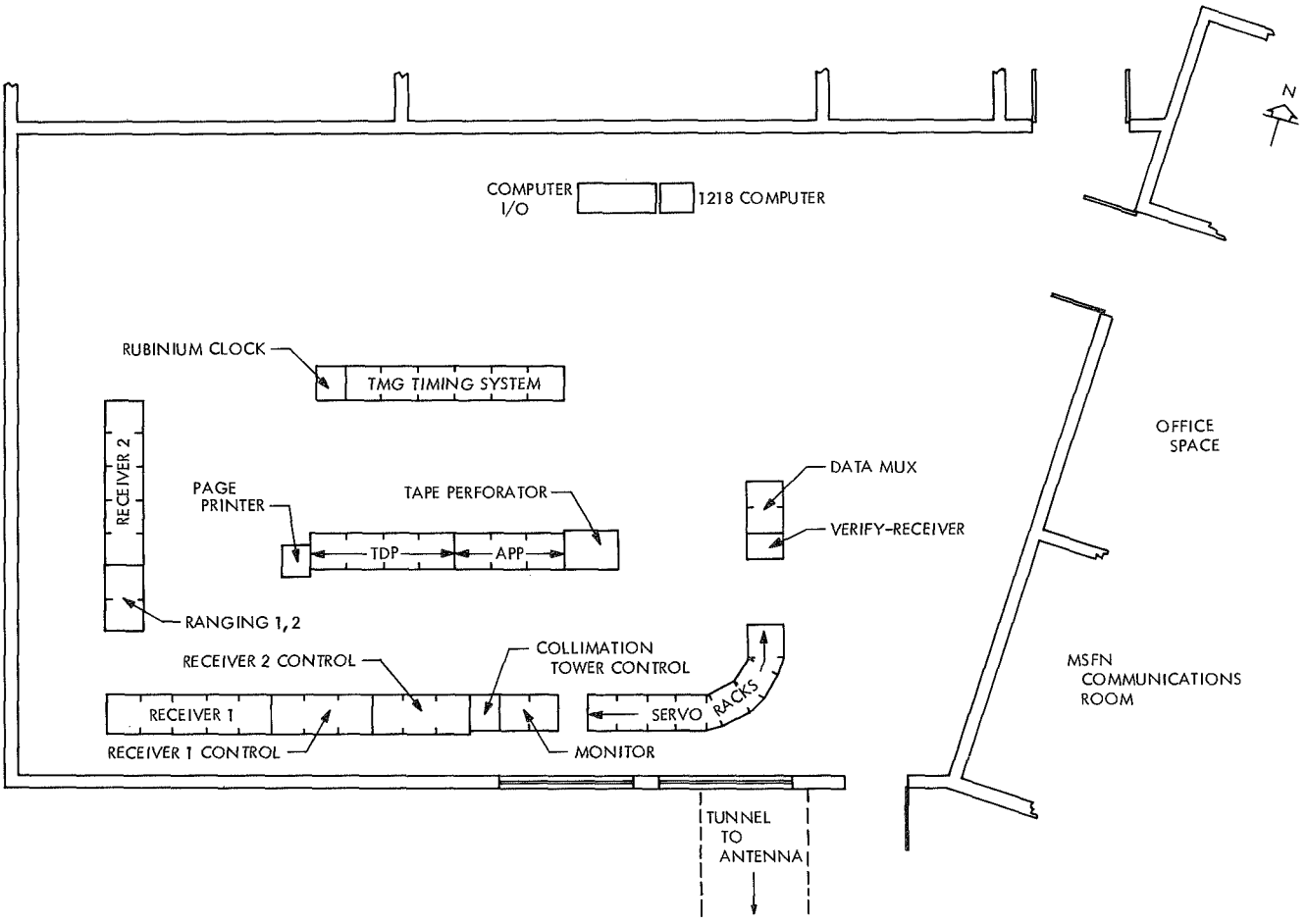

Fig. 1. MSFN/DSS 11 control room

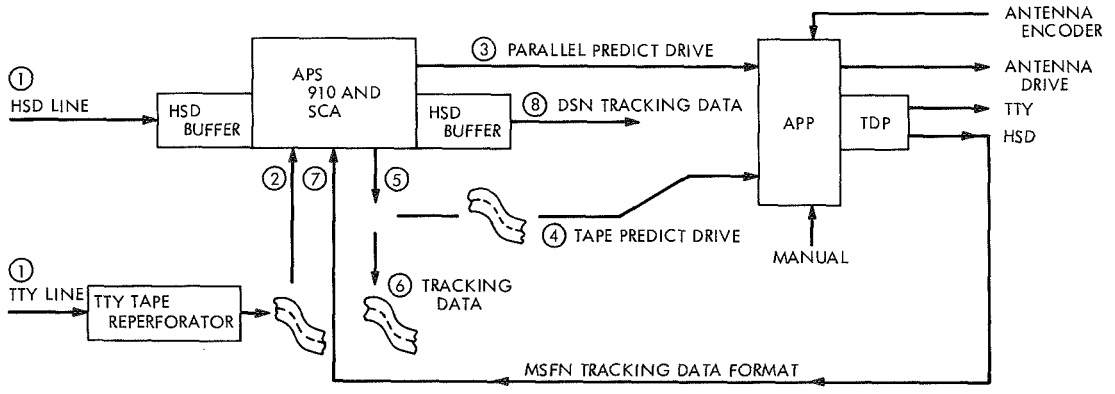

① 29-POINT ACQUISITION MESSAGE, JPL OR DSN
② 5-LEVEL TTY TAPE TO APS-910 OPTICAL READER
③ PARALLEL 5-LEVEL ELECTRICAL DRIVE
④ COMPUTER 7-LEVEL DRIVE TAPE
⑤ 910 HIGH-SPEED TAPE PUNCH
⑥ ORIGINAL DATA RECORD OF TRACKING DATA
⑦ TDP INPUT TO SCA HSD REGISTER
⑧ HSD DSN TRACKING DATA OUTPUT

Fig. 2. Integrated MSFN/DSN configuration

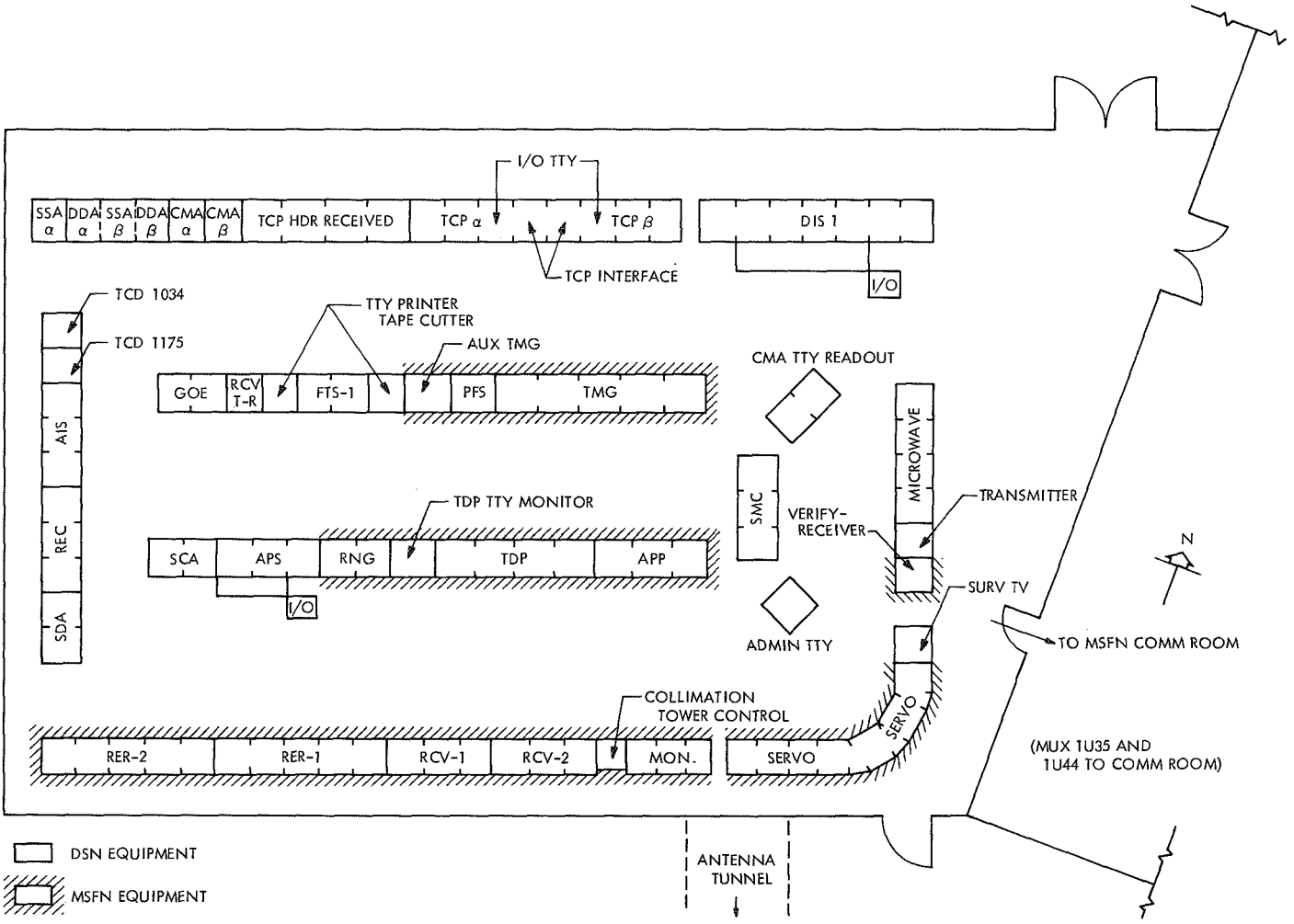

Fig. 3. DSS 11 integrated with MSFN

Implementation of an S-Band Microwave Link for Spacecraft Compatibility Testing

R. Sniffin
DSIF Engineering Section

As a cost-effective and time-effective approach to spacecraft compatibility testing, a microwave link between the Jet Propulsion Laboratory and TRW, Inc., has been installed, and the performance of this link has been evaluated experimentally.

I. Introduction

The Deep Space Network requires that all spacecraft which are to be tracked by its stations receive a compatibility test prior to launch. Two facilities are maintained for this purpose. One of these, DSS 71, is located at Cape Kennedy and is used for pre-launch checkout of the spacecraft. The second facility, CTA 21, is located at the Jet Propulsion Laboratory in Pasadena, California and is used for engineering checkout of spacecraft and spacecraft subsystems before shipment to the launch facility.

The *Pioneers F* and G spacecraft scheduled for launch in March of 1972 and April of 1973 are being designed and constructed for the Ames Research Center by TRW Systems Division of Redondo Beach, California. As a practical alternative to requiring the Pioneer Project to supply a spacecraft to the DSN for testing at CTA 21, it was decided to conduct as many tests as possible using a microwave link between CTA 21 and TRW. The remaining tests would either be performed at CTA 21 on spacecraft subsystems or at DSS 71 on the flight spacecraft. The decision as to which tests could be conducted via the microwave link would be based on the performance of the link.

II. Path Selection

The Jet Propulsion Laboratory lies against the foothills of the San Gabriel Mountains 39 km north, northeast of TRW. Between the two facilities are a group of low mountains called the San Rafael Hills. These hills preclude any single-hop microwave link. It is also doubtful that a single-hop link would be successful due to the low grazing angle of the beam with the terrain and the resulting interference from man-made structures. It is therefore both necessary and desirable to use a passive repeater located on an intervening terrain peak. There

are three peaks in the San Rafael Hills from which line-of-sight transmission to both JPL and TRW are possible. One of these, however, was eliminated due to a JPL building which partially blocks the path from the JPL microwave relay antenna complex. The choice between the remaining two peaks was made on the basis of the ease with which a permit for use of the land could be obtained and the ease with which the antennas could be installed.

The selected location was on an abandoned fire lookout tower owned by the County of Los Angeles. Figure 1 shows the terrain profile along the two portions of the link. A helicopter survey was also made to ensure that no man-made obstructions were present. The line between the terrain and the line-of-sight path represents the boundary of the first Fresnel zone. This zone is normally considered to be the region which must be free of obstructions in order to have free-space propagation conditions apply. Since a considerable amount of terrain lies within the first Fresnel zone, no attempt was made to calculate the effect of this terrain on the performance of the link.

III. Preliminary Performance Predictions

In order to determine the adequacy of the proposed link hardware, a power study was performed based on free-space propagation conditions. Since these conditions are not realized, the predicted link loss only represents an engineering approximation. Table 1 summarizes the items in terms of their contribution to the total link loss.

IV. Link Stability Test Description

The completed microwave link was tested over a 24-h period extending from 04:02 GMT on February 20, 1971 to 04:02 GMT on February 21, 1971. A modified *Mariner C* flight transponder was used to simulate the spacecraft at the TRW end of the link. Analog (strip-chart) recordings of received signal amplitude and phase at CTA 21 were generated. In addition the receiver automatic gain control voltage was sampled at 0.125-s intervals and recorded on digital tape for later data reduction.

V. Link Stability Test Results

Seventeen hours of signal amplitude data were reduced by an XDS-920 computer. The remaining 7 h could not be reduced by this technique because of tape changes falling within the hour and a partial failure of the transponder. Figure 2 shows the distribution of signal amplitudes (histogram) with the mean and standard deviation of the signal level for each of the seventeen hours which were reduced. Three hours of data were converted to the frequency domain by use of the Cooley-Tukey Fast Fourier Transform. The resultant power spectrums are shown in Fig. 3.

A study of the analog recording of received signal phase showed a diurnal phase change of 158 deg at the received frequency. The phase jitter was less than 5 deg.

VI. Conclusions

The S-band microwave link established between JPL and TRW is usable for large signal testing of the *Pioneer F* and *Pioneer G* telecommunications subsystem. The amplitude stability of the link is nominally ± 1.3 dB.

The signal amplitude stability degrades during the afternoon hours with the largest variations being observed near local sunset. All sidebands caused by varying link amplitude are at least 30 dB below the carrier level. The phase stability of the two-way link is also acceptable for such testing.

Table 1. Microwave link power study

Item	Loss contribution, dB
Cable loss (CTA 21 to antenna)	−5.0
Antenna gain (1.8-m antenna)	+30.0
Propagation loss (3.7 km at 2295 MHz)	−111.1
Antenna gain (1.8-m antenna)	+30.0
Cable loss (10.5-m type T-214)	−4.3
Antenna gain (1.8-m antenna)	+30.0
Propagation loss (35.7 km at 2295 MHz)	−131.7
Antenna gain (1.8-m antenna)	+30.0
Cable loss (to measurement point)	−2.6
Total microwave link loss	−134.7

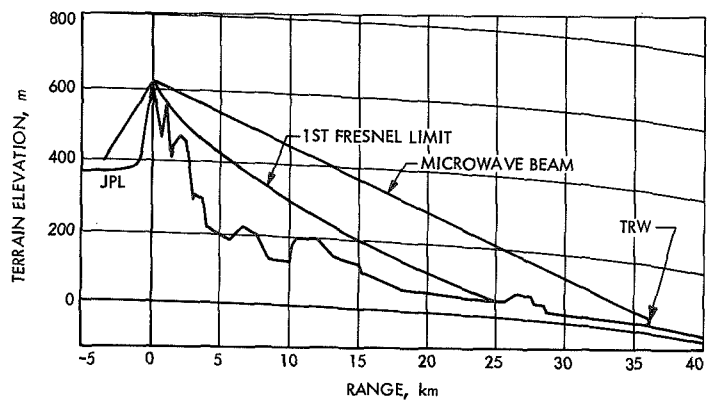

Fig. 1. Terrain profile and first Fresnel zone limit

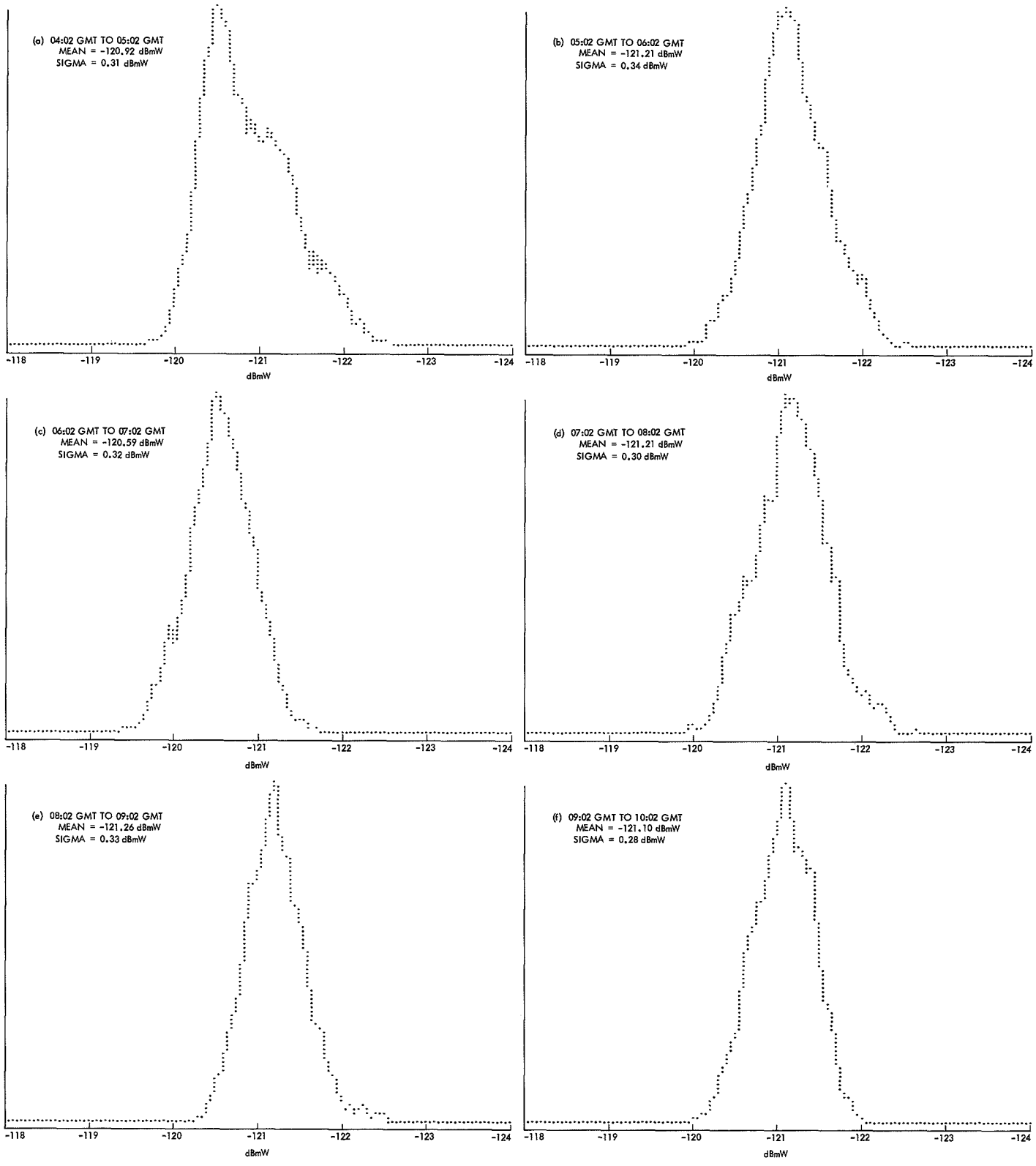

Fig. 2. Distribution of signal amplitudes

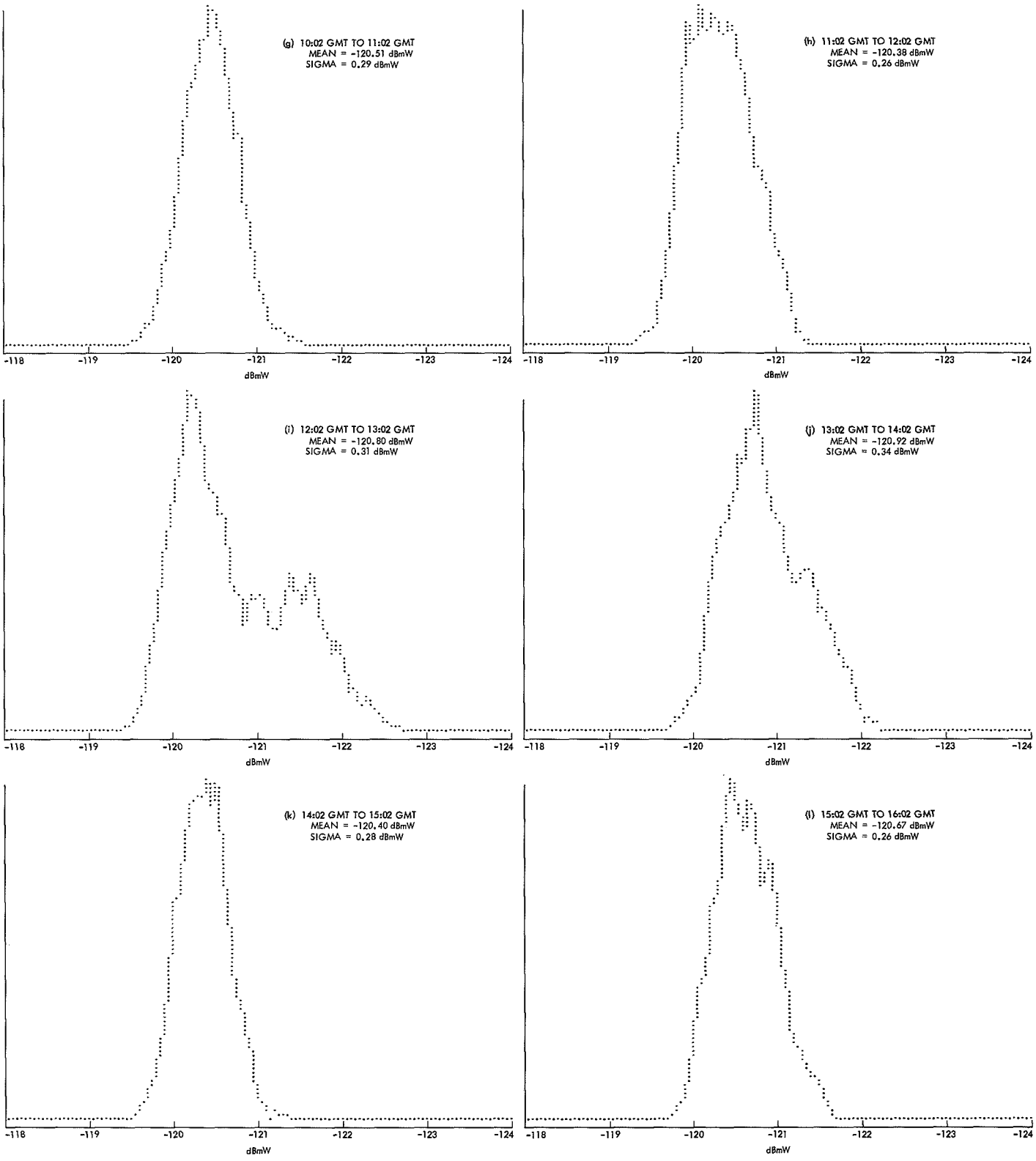
(g) 10:02 GMT TO 11:02 GMT
MEAN = -120.51 dBmW
SIGMA = 0.29 dBmW
(h) 11:02 GMT TO 12:02 GMT
MEAN = -120.38 dBmW
SIGMA = 0.26 dBmW
(i) 12:02 GMT TO 13:02 GMT
MEAN = -120.80 dBmW
SIGMA = 0.31 dBmW
(j) 13:02 GMT TO 14:02 GMT
MEAN = -120.92 dBmW
SIGMA = 0.34 dBmW
(k) 14:02 GMT TO 15:02 GMT
MEAN = -120.40 dBmW
SIGMA = 0.28 dBmW
(l) 15:02 GMT TO 16:02 GMT
MEAN = -120.67 dBmW
SIGMA = 0.26 dBmW
-118
-119
-120
-121
-122
-123
-124
dBmW

Fig. 2. (Contd)

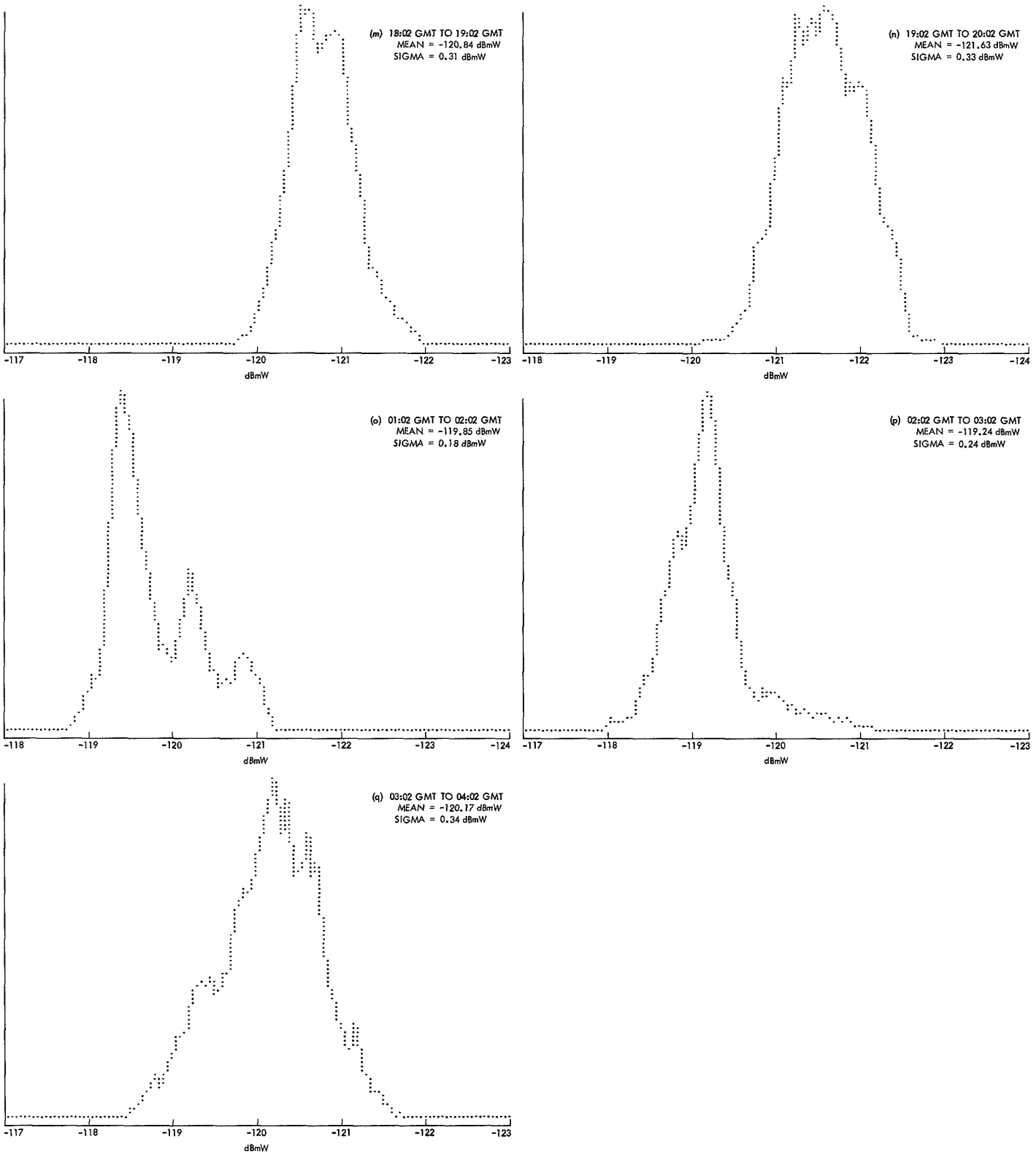
(m) 18:02 GMT TO 19:02 GMT
MEAN = -120.84 dBmW
SIGMA = 0.31 dBmW
-117 -118 -119 -120 -121 -122 -123
dBmW
(n) 19:02 GMT TO 20:02 GMT
MEAN = -121.63 dBmW
SIGMA = 0.33 dBmW
-118 -119 -120 -121 -122 -123 -124
dBmW
(o) 01:02 GMT TO 02:02 GMT
MEAN = -119.85 dBmW
SIGMA = 0.18 dBmW
-118 -119 -120 -121 -122 -123 -124
dBmW
(p) 02:02 GMT TO 03:02 GMT
MEAN = -119.24 dBmW
SIGMA = 0.24 dBmW
-117 -118 -119 -120 -121 -122 -123
dBmW
(q) 03:02 GMT TO 04:02 GMT
MEAN = -120.17 dBmW
SIGMA = 0.34 dBmW
-117 -118 -119 -120 -121 -122 -123
dBmW

Fig. 2. (Contd)

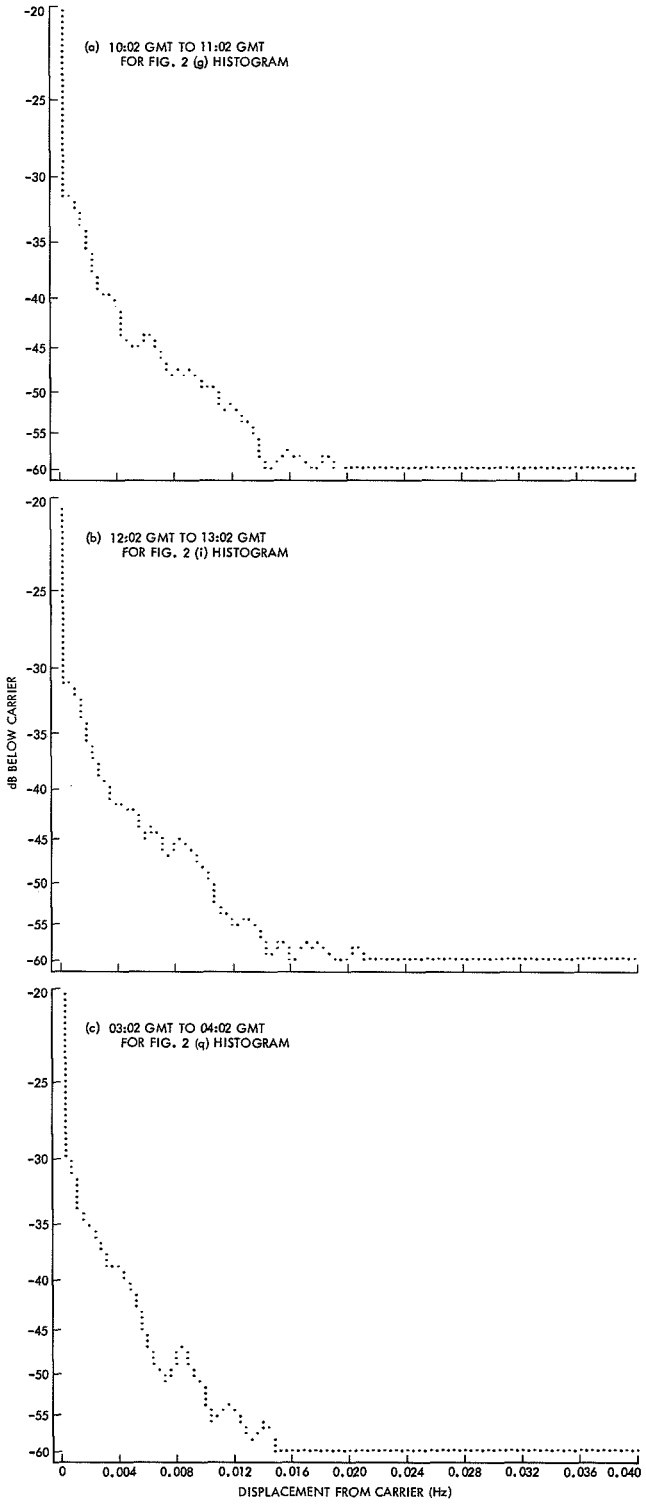

Fig. 3. Power spectrum of received signals

Digital Step Attenuator

E. C. Oakley
R. F. Systems Development Section

A 50-ohm digital step attenuator has been developed having 0.2-dB resolution and 51-dB maximum loss. This device has been tested from dc to 10 MHz, where a ±5-degree maximum differential phase shift was measured. Preliminary tests indicate that the attenuator may operate satisfactorily at frequencies as high as 100 MHz. No signal discontinuity occurs during switching, and positive confirmation of step activation is provided. The attenuator is constructed on a 14.5 by 3.2-cm (5.7 by 1.25-in.) double-sided etched circuit card, and occupies a volume of less than 74 cm³ (4.5 in.³).

A computer-controllable attenuator was required to control the 10-MHz input signal level to the Mark III Ranging Demodulator Assembly (RDA). The requirements called for 8-bit resolution (one part in 256) and a total available 51-dB attenuation range. This yields a least-significant-bit (LSB) weight of 0.2 dB. The attenuator was required to have a 50-ohm characteristic impedance, unbalanced to ground. The computer-controllable requirement also made positive confirmation of step actuation mandatory. Since the RDA is a phase-sensitive demodulation system, the attenuator is called upon to maintain less than ±5 degrees differential phase shift over the 51-dB dynamic range at 10 MHz. It was also desirable to insure that no signal discontinuity occurred during step actuation.

The attenuator design was to be as general purpose as possible, and so can accept input from dc to 10 MHz. Solid-state switching of the attenuator steps was ruled out because of the dc response requirement, and because of the difficulty in isolating the signal from the digital controls and noise which might be superimposed upon them. The switching speed of electromechanical relays is entirely adequate for the application, and the low contact resistance yields a lower pad-out insertion loss at the 50-ohm impedance level than can be achieved with solid-state switches.

The digitally controlled step attenuator takes the form of a multiplying digital-to-analog converter (MDAC); that is, the output signal is the product of the input reference

signal and the binary control word. As such, severe constraints are imposed if the device is to maintain monotonicity at both dc and 10 MHz. Resistors employed in the attenuator pads are of the metal film type, possessing low-temperature coefficient (±5 ppm), having low reactance and small skin-effect factor so that the ratio of dc to RF resistance will be low.

To maintain an overall linearity and accuracy of one-half least-significant bit (½ LSB), a ±0.01-dB, dc accuracy per step was imposed. Although ±5% resistor tolerance would satisfy the ±0.01-dB accuracy requirement for the 0.2-dB step, all ±1.0% resistors were utilized in the 0.2 through 3.2-dB steps, ±0.5% for the 6.4-dB stages, and 0.1% for the three 8.533-dB stages (of the 25.6-dB step). Thus, the worst-case tolerance for the eight steps would be ±0.08 dB, which is less than ½ LSB.

The Pi-pad configuration was chosen over the Tee because of a much greater ease of mechanical layout.

Figures 1 and 2 show conventional switching schemes for Pi and Tee pads, respectively. Both require an additional switch pole for confirmation indication, and both open the signal path during switch time-of-flight. Although this latter limitation could be removed by using shorting-type contacts, this is difficult, at best, to achieve with relays.

A slight re-configuring of the Pi-pad as shown in Fig. 3 will remove the signal-loss limitation without the need for shorting-type contacts. Due to switch-lead inductance, the pad-out phase delay will be greater through the short than through the pad for Figs. 1, 2, and 3. This is reduced somewhat in Fig. 3 by the shunting effect of the pad series element. Note in all three of these schemes that, during pad-out conditions, the signal must pass through two contact resistances in series, which for networks at the 50-ohm impedance level will introduce a pad-out insertion loss of approximately 0.035 dB, assuming 100 milliohm contact resistances.

Figure 4 shows a switched Tee-pad arranged to gain the advantages that were gained for the Pi-pad by going from Fig. 1 to Fig. 3. Additionally, Fig. 4 has only one contact resistance in series with the signal during pad-out conditions, thus halving the insertion loss to 0.017 dB.

Since a double-pole double-throw relay is utilized for switching, the circuit of Fig. 4 halves the lead inductance in series with the signal during pad-out condition, thus reducing the differential delay when the pad is switched in. Of the two contacts which have become available, one can now be used as a confirmation indicator. This contact loses ground when the pad is *in*, shown CON "not" (the complement of CONfirmation). This signal can be inverted, if necessary, by utilizing a suitable pull-up resistor.

If a Pi-pad is introduced into the circuit of Fig. 4, all the previous advantages are retained, and a new one added. The Pi-pad resistors physically group around the relay in a two-dimensional circuit plane, rather than the three dimensions required for the Tee.

Referring to Fig. 5, the intrinsic phase delay for the pad-in condition is greater (that is, more negative) than the pad-out delay, for pad attenuation values less than approximately 11.7 dB. These intrinsic delays will add algebraically when considering an assembly of cascaded attenuation stages. Stages having a design loss greater than 11.7 dB will have less (that is, more positive) phase shift. These intrinsic delays will *not* sum algebraically, and can exhibit a composite differential phase shift many times worse than the sum of the individual delays in a multistage assembly.

It was shown that the phase delay of each pad less than 11.7 dB could be reduced to zero by capacitive compensation of the *series* resistive element of the Pi-pads. Similarly, the phase advance of the pads larger than 11.7 dB could be reduced to zero by capacitive compensation of the *shunt* resistive elements of the Pi-pads. However, the *residual* phase shifts for these compensated larger Pi-pads would not sum algebraically. To overcome this problem, the larger attenuation steps were broken into smaller stages such that no individual stage exceeded 11.7 dB.

A residual differential phase shift of ±0.5-degree maximum per stage was realized by use of ±5% tolerance, ±5% incremental-value fixed capacitors. Thus, the need to employ variable trimmer capacitors to achieve the ideal zero residual was avoided.

Figure 6 shows the resultant compensated stage design which is typical of the eleven cascaded stages. Six individual stages are for the 0.2-, 0.4-, 0.8-, 1.6-, 3.2-, and 6.4-dB steps. The 12.8-dB step consists of two 6.4-dB stages, while the 25.6-dB step is composed of three 8.533-dB stages.

The confirmation signals of the individual stages of the 12.8- and 25.6-dB steps are serially ANDed on a separate logic board so as to provide only one confirmation terminal each, for those steps. The serial ANDing provides an additional benefit in that large output signal

excursions will not occur during the switching time for the two largest steps. This feature, coupled with the no-signal-loss switching scheme, limits the level excursion to less than one-third of the most-significant bit, i.e., less than 8.533 dB.

Figure 7 shows the functional layout of the stages, which are arranged on a double-sided etched circuit board 3.2 cm (1.25 inches) wide by 14.5 cm (5.7 inches) long. Each stage is in a keystone-shaped modular form so as to group alternately in a space-conserving fashion, and to minimize interstage conductor length. The end areas are for connector termination. The signal travels down the long center axis of the board, and signal-carrying conductors assume strip-line dimensions where practical, to minimize VSWR. The complete attenuator occupies a volume of less than 74 cm^3 (4.5 $in.^3$).

This device has been tested from dc to 10 MHz, where a $\pm$5-degree maximum phase shift was measured. Preliminary data indicate that the attenuator may perform satisfactorily at frequencies up to 100 MHz.

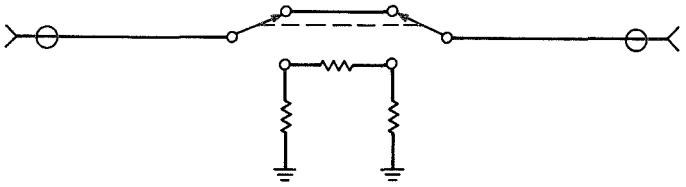

Fig. 1. Pi configuration

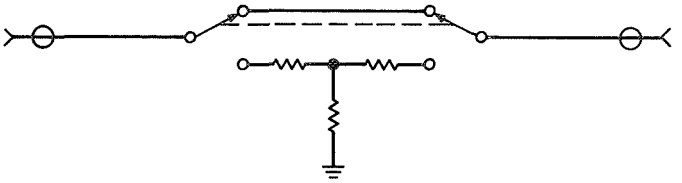

Fig. 2. Tee configuration

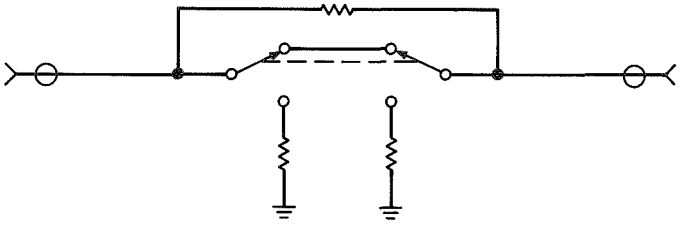

Fig. 3. Modified Pi

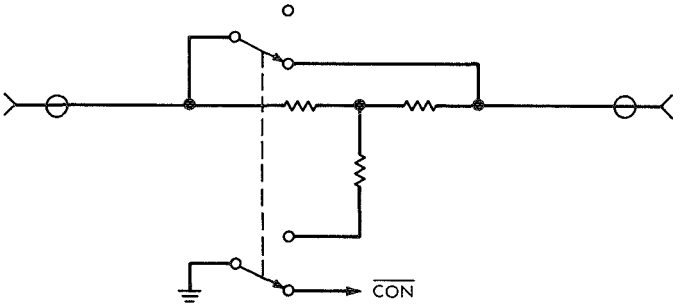

Fig. 4. Tee with confirmation

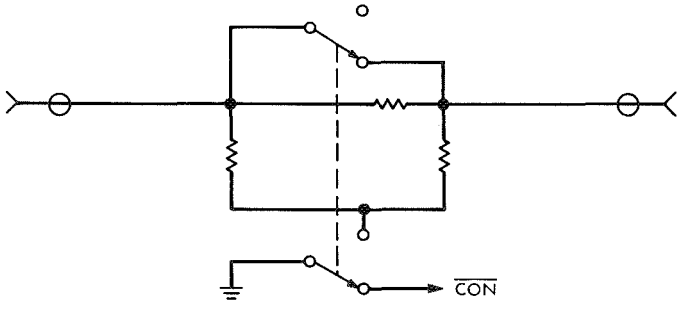

Fig. 5. Pi with confirmation

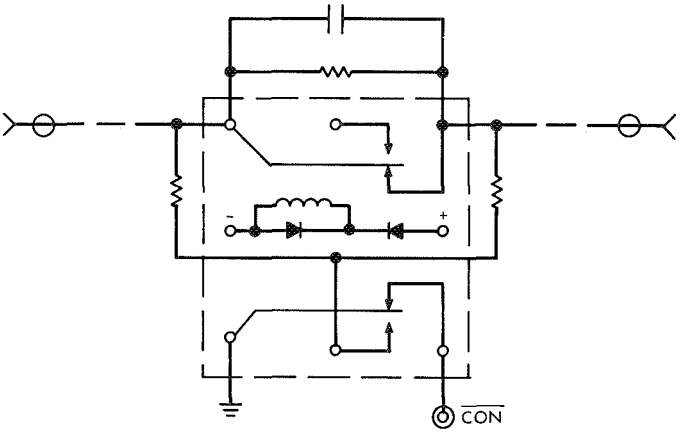

Fig. 6. Compensated Pi with confirmation

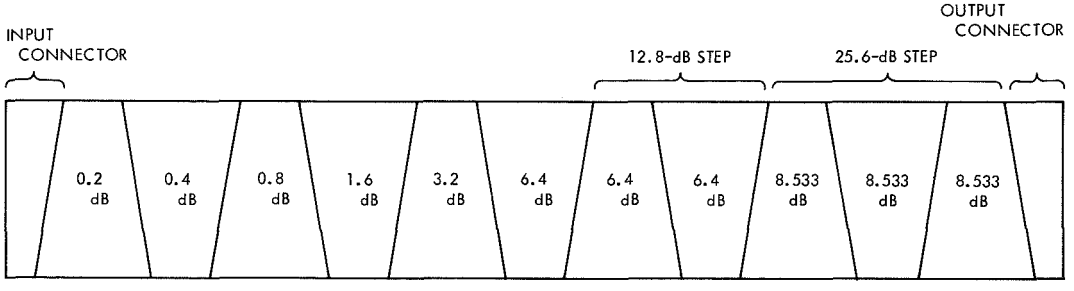

Fig. 7. Functional layout of stages

Rotating Antenna Tests at DSS 12

C. E. Weir
R. F. Systems Development Section

Tests were conducted using a rotating antenna on the collimation tower at DSS 12 (Echo Deep Space Station) to simulate the rotating Pioneer F spacecraft. Specific measurements were taken to determine the degradation in telemetry bit error rate and doppler quality as a result of the rotation and misalignment of the rotating antenna relative to the receiving antenna.

I. Introduction

The *Pioneer F* spacecraft will utilize a conical scan (CONSCAN) system to allow automatic pointing of its antenna at the earth. The spacecraft will rotate continuously about the roll axis during the mission, and will consequently present some characteristics to a ground station not seen on previous missions. A rotating antenna on the collimation tower at DSS 12 was used to simulate the spacecraft so as to allow quantitative measurement of the effect of CONSCAN on telemetry bit error rate and doppler quality.

The useful property of a CONSCAN system is production of an AM signal in any direction of observation not coincident with the axis of rotation. To do so requires that the antenna be offset slightly so that rotation causes the line representing the direction of maximum radiation from the antenna to describe a right circular cone whose vertex is at the antenna and whose apex angle is twice the offset angle. At any point on the axis of rotation, also the axis of the cone, the signal strength remains constant during rotation, while in any other direction the signal strength will change in a manner which can be predicted by analysis of the radiation pattern of the rotating antenna. At any off-axis point the observed signal strength will be a sinusoid at the rotational frequency, expected to be about 4.8 rpm for *Pioneer F*, plus, so long as the observation point sees only the main lobe of the radiation pattern during one rotation, harmonics of relatively low amplitude.

The *Pioneer F* spacecraft, with a CONSCAN antenna system whose axis is the rotational axis, will thus see an AM signal derived from the uplink transmission whenever the antenna is not pointed exactly at the earth. Upon ground command the spacecraft will be able to

point itself at the earth by on-board processing of the AM waveform to produce signals for the orientation jets. Intervals of some days will elapse between such maneuvers so that precession of the inertial attitude between spacecraft and earth will cause an increase in the amplitude of the CONSCAN AM signal. Such a variation in received signal level at a ground station will affect the data quality, in particular that of telemetry bit error rate and doppler phase jitter, neither of which is a simple linear function of signal strength. The rotating antenna tests were undertaken with an idea of measuring such degradations for different values of received signal strength and CONSCAN antenna misalignment.

Conventional techniques should suffice for counting telemetry bit error rates so long as the counting interval is long compared to the CONSCAN rotational rate. Previously employed tests to measure doppler jitter, however, are inappropriate, since they measure only a static value and are inapplicable to a situation of varying signal strength. In addition, previous doppler tests were for zero frequency shift as is normally experienced over the path transmitter-collimation tower-receiver. One circularly polarized antenna rotating relative to another always produces a doppler shift since the polarization vector rotates at the carrier frequency plus or minus, depending upon the relative sense, the frequency of antenna rotation. Doppler count as a function of time should therefore be a straight line with slope proportional to the rotation rate. It was decided the most meaningful analysis of doppler quality would be the standard deviation between data points and a fit of the data to a straight line.

II. Test Procedures

A. Preliminary

A four-foot-diameter antenna with circularly polarized feed was obtained to serve as the rotating antenna. Using the JPL antenna range, the feed was focused by adjusting for the narrowest possible main lobe of radiation. Since the four-foot antenna corresponds in size to neither of the directive antennas that will be on *Pioneer F*, it is necessary to scale all parameters. *Pioneer F* offset of the antennas is 1 dB, which value is caused by skew of 0.3 times the 3-dB beamwidth. The four-foot antenna had an S-band beamwidth of nine degrees, requiring offset of 2.7 degrees. The antenna was bolted to a rotating mount, allowing continuous rotation by means of a rotary joint. Rotation rate was adjustable. A shim was placed between antenna and mount to offset the antenna axis by 2.7 degrees. Handwheels on the mount permitted motion of the rotating antenna in azimuth and elevation. The assembly, consisting of antenna plus rotating mount, was installed near the top of the DSS 12 collimation tower. Cables were run to the room at the base of the tower for antenna feed and rotation control.

B. Station Configuration

The configuration used during the tests is shown in Fig. 1. The *Pioneer* GOE (ground operational equipment) was used to simulate the functions of the spacecraft. Although the GOE characteristics are more that of *Pioneers* previous to *F*, they are quite close to those desired, besides being all that was available. Two-way lock was maintained over the path transmitter—GOE transponder—receiver for all data runs. The doppler data from the extractor was fed into the TDH and then was recorded on magnetic tape at the rate of one sample per second by the DIS computer. The tape was later reduced by data analysis programs. A test bit stream of coded telemetry data was generated by the GOE Data Format Generator at the collimation tower and used to modulate the transponder transmitter. Modulation index was adjusted for 6.9-dB carrier suppression, the same as expected for *Pioneer F*. After being received inside the control room, the telemetry was demodulated by GOE and compared by the TCP computer with a locally generated bit stream. The TCP counted bit errors and output the results on typewriter. The procedure whereby the actual data stream was generated twice was necessary since no cable line to use as a reference was available between collimation tower and control room.

C. Data Collection

Receiver AGC voltage as a function of signal strength was calibrated at the beginning of each day of the test. The rotating antenna was adjusted to produce signals of a particular AM characteristic; values of 0, 2, 4, and 6 dB peak-to-peak were used during the test. These adjustments were made with the ground transmitter turned off, for the safety of the individual on the tower, and were done while receiving a strong signal in the station receiver. In this manner the received signal could be displayed on a chart recorder to aid in adjusting the antenna offset to the desired level. After setting the antenna misalignment, two-way lock was established and the received signal at the transponder attenuated to −110 dBm. Maintaining such a strong level should ensure the preponderance of the jitter seen to be a product of the station receiver and not the transponder. Attenuation was inserted in the transponder transmitter to produce the

desired signal levels at the station receiver. Nominal values of −130, −140, −150, and −160 dBm were used. Digital voltmeter AGC readings, which varied at the CONSCAN rotational frequency rate, were averaged to calculate the mean value at a given attenuator setting. Data runs were typically 15 minutes for a particular CONSCAN amplitude and received signal level.

III. Results

Degradation of doppler quality and of telemetry bit error rate in the presence of CONSCAN was noted. That is, both quantities were worse with CONSCAN at an averaged signal level than at the same signal level in the absence of CONSCAN. More quantitative results must await further analysis and are not yet available. Two interesting factors of importance to operational tracking of *Pioneer F* did appear, however, and will be mentioned here. First, the CONSCAN AM can be determined to no better than 0.1 dB p–p because of the presence of modulation at a frequency approximately 72/minute corresponding to the maser cryogenic pump. This is of consequence principally when atempting to boresight the CONSCAN system. Second, the narrow AGC position of the station receiver will not follow variations at the CONSCAN rate, and either medium or wide AGC must be used with resultant production of noisier data.

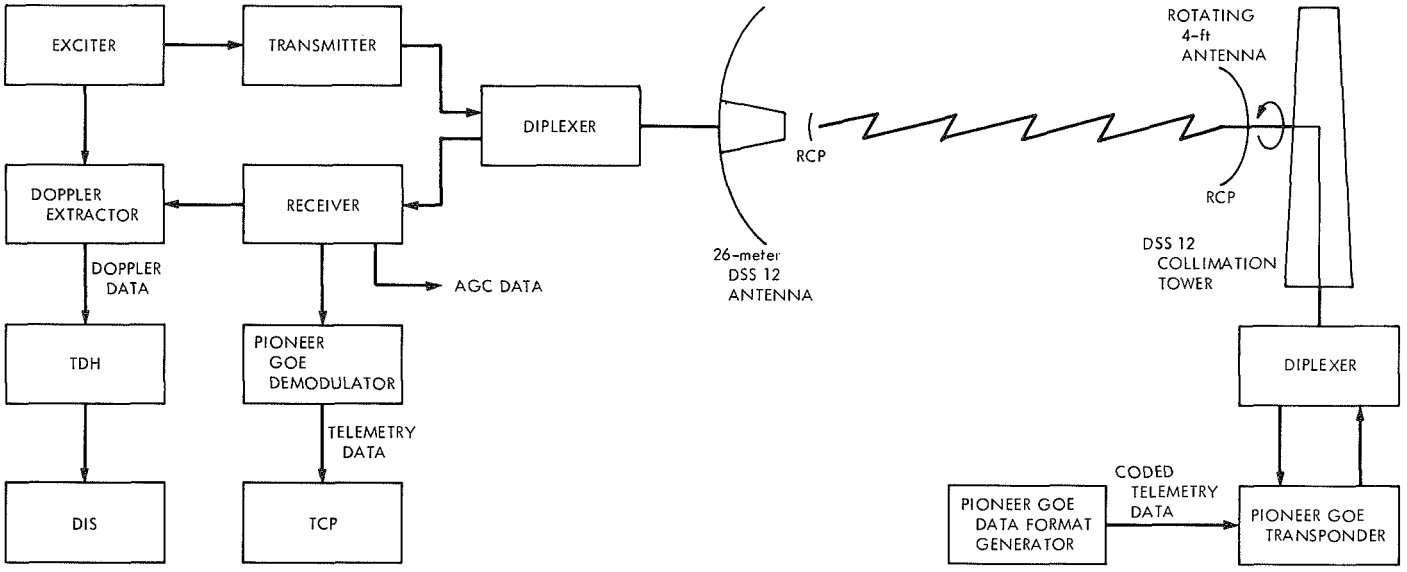

Fig. 1. Configuration used for rotating antenna tests

Radiometric Data Accountability, Validation, and Selection in Real-Time

R. B. Miller
DSN Engineering and Operations

The design goal for providing real-time Tracking Data System accountability, validation, and selection is described.

I. Introduction

A principal responsibility of the DSN Tracking System Analysis Group (TRAG) is to provide a source of validated radiometric data, with all associated information required for processing, for both flight projects and nonreal-time data users (Ref. 1). This article describes the TRAG design goal for providing a complete and validated data source with a minimum of manual intervention. The functions described will be part of the Mark III A 360/75 tracking software subsystem.

II. Goals

Accountability. Be able to detect outages in real-time so that significant outages can be filled prior to comple-

tion of a current tracking pass. Provide with the data a description of the quantity of each data type available.

Validation. Be able to detect bad or marginal data in real time to enable rapid failure isolation. Provide with the data a measure of the data quality.

Selection. Provide a means for a data user to specify the time span, data types, sample rate, and minimum quality of the data passed to the user.

III. Design

The elements of the design are shown in Fig. 1. Principal inputs to the system are the radiometric data itself, tracking predictions of the data, and manual tolerances and limits. Principal output is a central alarm display and summary formats for TRAG personnel, and summary and point-by-point information provided with the data to the user.

A. Accountability

Two sections of the SFOF tracking software subsystem are involved in real time accountability. The first is the Teletype Tracking Data Outage Program (TYDOP) which can be considered to be part of the teletype tracking data input processor (TYDIP). This software element computes the sample rate of the incoming data and places it on to the system data record (SDR) for each point it can be determined. TYDOP will also determine gaps in the incoming data and produce a record of all outstanding outages which can be displayed on request. This outage summary will automatically be updated when a data recall fills an outage. Entries in the outage summary can also be manually deleted if judged to be insignificant. TYDOP will also pass outage and data stoppage alarms on to the tracking alarms processor (TAP).

The second software element is a portion of the master file program (MFP) which computes accountability statistics on a data-type basis for each active stream. It formats this information as pass summaries included with the data on the SDR and will also send this information to TAP for a continually updated real-time display of the pass status.

B. Validation

The principal real-time analytical tool is the pseudoresidual program. The pseudoresidual process involves comparing the incoming metric data with a prediction of the data produced automatically by the tracking predict subsystem. The name "pseudo" references the fact that the residual is computed from an *a priori* predict while a "true" residual is computed from an *a posteriori* fit to the data. The computation starts with a straight difference of observed data minus predict. The resulting "raw" residual is then detrended and a running noise estimate computed on the detrended residual.

There will be three forms of output from pseudoresiduals: listing and plots, alarms, and a quality indication.

The listings and plots were the only output of the 7044 pseudoresidual program. The 360/75 will add additional flexibility in output selection and will make the listing or plots available on DTV. The listings can also be sent to character printers (teletype machines).

The alarms will be computed by comparing the raw residual, the residual mean, and the computed noise to standard or manually entered tolerance limits. Resulting alarms will be sent in text form to a character printer and to TAP to become part of the summary display. The occurrence of an alarm would direct the attention of the real-time tracking system analyst to the residual listing to assist in analyzing the problem.

The quality indicator is desired as an automatic means of labeling obviously bad data and of indicating the relative quality of good data compared to some standard. A prototype doppler quality indicator proposed for the 1971 era is shown in Table 1. Referring to the table, values from 2 to 7 indicate that a doppler point is a blunder point and give its relative size and sign. Values from 8 to 15 give the relative quality of the data, based on noise, compared to some standard. The comparison is the ratio of the calculated estimated noise, based on the last 15 detrended residuals including the current point, over a predicted nominal noise based on a noise model. How useful the 8 through 15 values of the doppler quality indicator will be will depend heavily on the noise model. The noise model is currently under development by DSIF personnel. It will be a function of data sample rate, and uplink and downlink signal level.

The doppler quality indicator will consist of 16 bits accompanying each data point on the system data record and project data files. The first four bits will be the value of K (Table 1), and the last four bits will be a value from Table 1.

C. Selection

Data selection will take place in a software block called the data selector and project file generator which is functionally part of the MFP. Currently the only selection capability is spacecraft, station, and a time span. It is the desire to add selection by sample rate, data type, and quality.

Sample rate selection will involve selecting every *n*th point to arrive at the requested sample rate (the requested rate must be lower than or equal to the rate already on the SDR). Sample rate selection will also require mapping data condition codes and the quality indications on the points in between the selected points. This is so that there will not be a loss of information at the selected sample rate.

The quality selection would cause only data above a certain Quality Indicator value to be passed on to the project data file.

IV. Implementation

It is hoped to have the system described implemented in time to support *Mariner* Mars 1971 orbital operations. This would be with the doppler quality indicator in a prototype R & D basis.

Reference

1. Heller, J., and Miller, R. B., "DSN Tracking System Operations," in *The Deep Space Network*, Space Programs Summary 37-65, Vol. II, pp. 122–125. Jet Propulsion Laboratory, Pasadena, Calif., Sept. 30, 1970.

Table 1. Proposed values for prototype doppler quality indicator

Value	Meaning
0	Not available
1	Receiver or synthesizer out of lock
2	$3K\,\sigma'_{est} \leq R_i$
3	$-3K\,\sigma'_{est} \geq R_i$
4	$2K\,\sigma'_{est} \leq R_i < 3K\,\sigma'_{est}$
5	$-2K\,\sigma'_{est} \geq R_i > -3K\,\sigma'_{est}$
6	$K\,\sigma'_{est} \leq R_i < 2K\,\sigma'_{est}$
7	$-K\,\sigma'_{est} \geq R_i > -2K\,\sigma'_{est}$
8	$\infty > \frac{\sigma_{est}}{N_e} \geq 5.0$
9	$5.0 > \quad \geq 4.0$
10	$4.0 > \quad \geq 3.0$
11	$3.0 > \quad \geq 2.0$
12	$2.0 > \quad \geq 1.5$
13	$1.5 > \quad \geq 1.0$
14	$1.0 > \quad \geq 0.5$
15	$0.5 > \frac{\sigma_{est}}{N_e} \geq 0.0$

K = stored or input constant (usually 3).

R = difference between i^{th} raw residual and a least squares fit to the last N (usually 15) raw residuals.

$\sigma'_{est} \equiv \sigma_{est_{i-1}}$ = calculated noise estimate on last N (usually 15) prior to this point.

$\sigma_{est} \equiv \sigma_{est_i}$ = calculated noise estimate shifted to include current point.

N_e = predicted noise estimate calculated from a noise model.

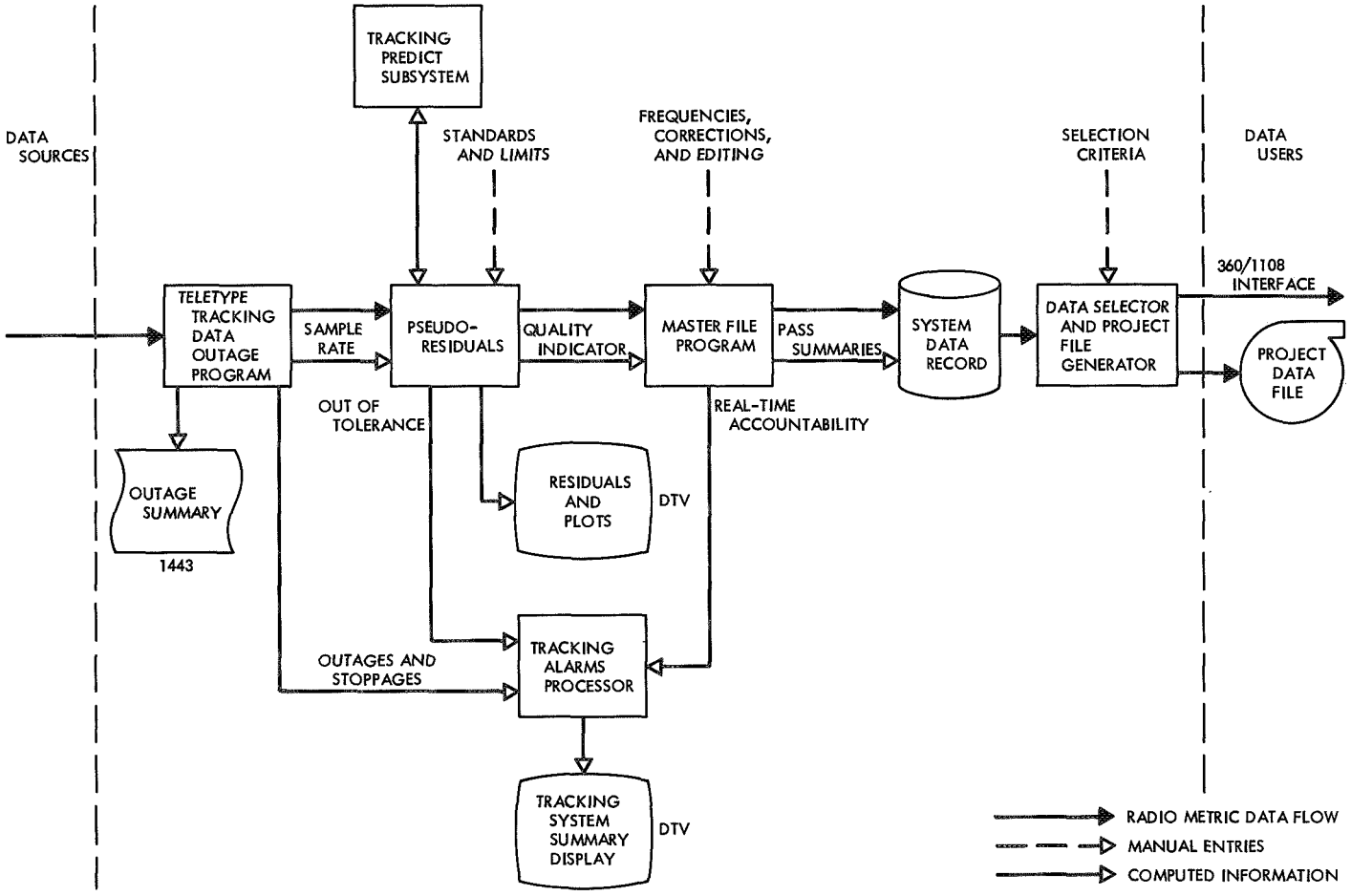

Fig. 1. Tracking system data accountability, validation, and selection

DSN Monitor Analysis System

J. E. Allen
DSN Engineering and Operations Section

This article describes the status of the Deep Space Network Monitor Analysis Group and the progress of the monitor system as it relates to its ability to support flight projects utilizing the Mark III software packages and the 360/75 computer.

I. Introduction

There are some major changes within the Monitor System occurring in both the facilities and the operation group. These changes have necessitated personnel and procedure changes within the Deep Space Network Monitor Group at the SFOF.

The Monitor Group has taken a positive role in the development of the DSN monitor at the SFOF, has become more aware of the monitor system hardware, software, and conceptual design, and the system is developing into a more meaningful and useful activity.

II. Software Status

In assessing the status of the monitor software, "delivered" means that the software is operational. There may be some minor problems, but it is not a major catastrophe if they are not solved.

As of April 19, 1971 the status of the software was as shown in Table 1.

In the Monitor software development, there are two serious problems. Work-around procedures have been

established at this time to accommodate the software slippage.

(1) Ability to produce validated system data record (SDR). The workaround is to require that DSIF monitor Digital Instrumentation Subsystem (DIS) log tapes be retained for a period of not less than 30 days. These tapes may be mailed to the SFOF for analysis and evaluation.

(2) No computer driven alarm processor. The workaround for this is to require that the on-duty monitor personnel keep a watchful eye on the R/T data and to record the data that is questionable, out of limit, or missing. This is a long and laborious process but there is no other way at this time.

III. Testing

The Monitor group has supported all *Mariner* Mars 1971 tests including the DSIF's operation verification tests. Monitor personnel have been able to locate potential problem areas and to define workaround procedures. Supporting the tests has given the group considerable insight as to the internal workings of the DSN and project.

The tests, for the most part, have been very good and the monitor system has operated well without too many problems. The software packages as shown in Table 1 all have operated as designed.

Documentation of the internal operating procedures has been hampered because the final system has not been determined. Consequently the Standard Operating Procedures that have been written have been in a constant state of modification.

The monitor's digital television formats have worked well and it is planned to update digital television formats within 2 days as outlined in DSN Monitor Document 820-4. The only limitation to the 2-day turnaround is getting the change into the computer system. The plan at this time is to have modifications added to the software on a weekly basis.

IV. Training

The monitor system, as part of the Network Analysis Team, adopted a minimum manning concept on Nov. 1, 1970. From Nov. 1, 1970 to March 29, 1971, minimum manning was provided in the Network Analysis area to support the *Pioneer* and *Mariner* Mars '69 Projects. *Mariner* Mars 1971 Project tests, facility tests and MOS training were supported as required.

An internal training program was established to familiarize personnel with the DSN Mark III software. Personnel developed new operating procedures and assisted in the development and testing of the new software packages operating in the IBM 360/75 computer. To date the following have been accomplished:

(1) Training. Approximately 977 student hours of training have been received by 12 monitor personnel. This includes a week's trip to the Goldstone DSCC for tracking site familiarization.

(2) Model II monitor software was accepted Feb. 12, 1971. This included the monitor criteria data (MCD) processor and raw high-speed data dump capability on 1443 line printer. The alarm processor will be implemented in future systems.

(3) Data tables for the monitor criteria data sets have been redefined with realistic modes of operation. Some of the existing monitored parameters were modified, others were deleted or added.

(4) An overlay has been designed for use on the high-speed data status performance block to assist in the identification and decoding of the bits within the blocks.

(5) With the absence of computer driven alarm processors, digital television formats have been designed to support the real-time monitoring function. These formats were designed to easily detect a DSN alarm condition.

(6) A reference library was established for the network analysis area consisting of all project documents and Standard Operating Procedures. These reference materials are being maintained by the data records analysts.

V. Staffing

The normal staffing of the Monitor Group contains one JPL supervisor and twelve contractors. The organization structure is as shown in Fig. 1.

Table 1. Software status

Name	Characteristic	Status
DSIF monitor	Station monitor console display	Delivered
	Alarms	Delivered
	Pseudo-residuals	Future system
	Output to DSN monitor (simultaneous with receipt of high-speed data input)	Delivered
	Original data record	Delivered
GCF monitor	Deep space station comm terminal monitor	Delivered
	SFOF comm terminal monitor	Delivered
	GCF monitor display	
	High-speed data configuration	Delivered
	Voice configuration	Delivered
	Teletype configuration	Delivered
	High-speed data and communication processor status	Delivered
SFOF monitor	Status displays	
	High-speed data input status	Delivered
	User's terminal and display status	In checkout
	System status	Future system
	Interface status (communication processor, 1108)	Future system
DSN monitor	Monitor criteria data sets	
	Monitor criteria data set callup	Delivered
	Real-time modify	Delivered
	Retain modification	Delivered
	Generate alarms on teletype	Future system
	Generate alarms on printer	Future system
DSN monitor	Interface with facility monitor	
	DSIF	Delivered
	GCF	Delivered
	SFOF	Delivered, but limited
	Interface with telemetry	
	DSIF	Delivered
	SFOF	Future system
	Interface with tracking	
	DSIF	Delivered
	SFOF	Future system
	Interface with command	
	DSIF	Delivered
	SFOF	Future system
DSN monitor digital television display	Legibility	Delivered
	Capacity to handle 5 DSS, GCF and SFOF Facility monitor	Delivered
	Initial format assignment	Delivered
	R/T format change	
	2260 Keyboard or card reader	Delivered
	Format request box	Delivered
	Same format, multiple channels	Delivered
	Distribution to operation control team and network analysis team	Delivered

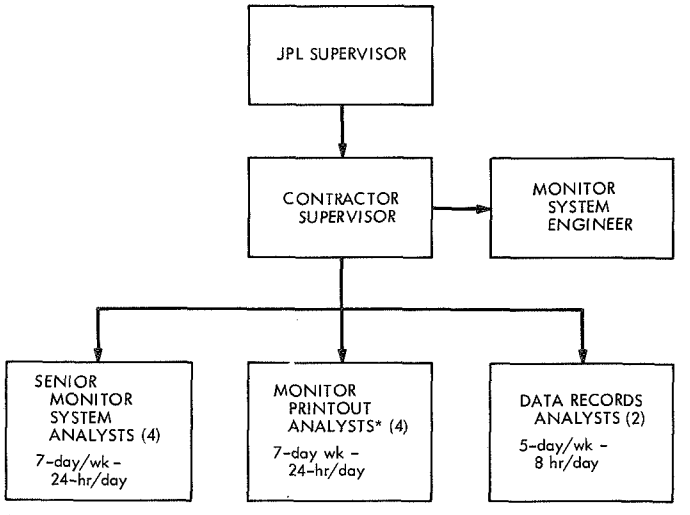

*THE PRINTOUT ANALYSTS WILL ASSIST THE MONITOR, TRACKING, TELEMETRY AND COMMAND SYSTEM ANALYSTS AS REQUIRED

Fig. 1. *Monitor Group organization*

Operational Capabilities of the SFOF Mark IIIA User Terminal and Display Subsystem

J. A. Turner
SFOF/GCF Operations Section

The Space Flight Operations Facility (SFOF) Mark IIIA Central Processing System has been developed to meet requirements for independent and simultaneous operation of multiple missions flown by an array of increasingly complex and sophisticated spacecraft. The Deep Space Network (DSN) Operations and Mission Support Areas must all be supported by the same computer system and therefore have been equipped with identical user input/output devices. The user input/output devices and their capabilities are described with the suggestion that operating techniques be developed and adapted to the improved and more interactive input/output capabilities of the new User Terminal and Display Subsystem.

I. Introduction

The SFOF Mark IIIA Central Processing System (CPS) was developed at JPL to meet the requirements of the DSN and the flight projects it supports. The System Functional Design, 360/75 Computer Configuration, User Device Switching, and Video Image Display were discussed by Willems (Ref. 1), Stiver (Ref. 2), Simon (Ref. 3), Habbal (Ref. 4), and Diem (Ref. 5).

The Digital Television Assembly, Video Image Display Assembly, Simulation Center, Diagnostics, and High-Speed Data Processing were discussed by Singleton (Ref. 6), Volkoff (Ref. 7), Polansky (Ref. 8), Wells (Ref. 9), Mullen (Ref. 10), and McClure (Ref. 11).

II. Subsystem Configuration and Interfaces

The User Terminals and Display Devices of the User Terminal Display Subsystem (UTDS), represented by the column of blocks along the lefthand side of Fig. 1, provide the primary interfaces between the user/controllers and the DSN Mark III Data System and its facilities and subsystems.

Figure 1 is a simplified hardware block diagram of the UTDS. The interfaces between its assemblies are shown as well as the interfaces with the Scientific Computing Facility, and the mission-dependent Mission and Test Video Subsystem. By matching the lines along the right-hand side with Figs. 2 and 3, the interfaces with the Mark III CPS can be seen. Figure 4 illustrates the CPS interface with the remainder of the DSN Mark III Data System (GCF and DSIF). Figure 5 illustrates the major hardware/software interfaces at the SFOF.

III. UTDS Hardware Description

User terminal and display devices may be divided into two categories. The first category includes those devices which directly control or are controlled by elements of the SFOF CPS. The second category includes user

devices located in the user areas but controlled or driven by elements of other facilities or systems.

A. The First Category of User Devices

1. Display Station IBM 2260. This device consists of a cathode-ray tube (CRT) output display and may be equipped with a manual entry keyboard. When equipped with a keyboard, it is designated 2260 WK and when without the keyboard as 2260 WO. Both configurations are commonly referred to as 2260. Manual entry device (MED) requests are entered via the keyboard in fixed field format. The entries are displayed, character by character, as they are entered via the keyboard. By entering the @ character at any point in the MED entry, a display will appear to provide the options available for use in formulating the entry. Administrative messages and alarms functionally related to each MED may also be displayed.

The formats are segregated by subsystem and provide the capability for performing a comprehensive set of functions. The MEDs acceptable from each station are controlled by functional commitment.

The 2260 WO may be provided as an independent display device in which case its displays are determined by its scheduled allocation as an output display, or it may be provided as an adjunct to a 2260 WK, in which case its displays are controlled by local MED inputs.

2. Card Reader IBM 2501. This device provides for rapid input of MED instructions, for input of user data in response to program requests and to enter JPL OS/360 background or job-shop jobs under certain conditions.

Well-planned use of the 2501 can greatly simplify the input/output (I/O) operation. The Simulated Manual Input Messages (SMIM) program can, to some extent, automate the entry of multiple MED instructions and thus reduce the load on the 2260 WK. The use of user data decks in response to program requests augments the interactivity between the user and the software subsystems. The JPLOS/360 JOB capability makes the 360/75 computer available for independent program operation.

3. Line Printer IBM 1443. This device is a 240-line per minute printer provided as an output medium for data from the 360/75 computer. Data may be directed to these printers from the user area manual entry devices or by allocating the device in the Data Processing Control Center (DPCC) as an output writer.

The 1443 is not intended as a bulk printer or logging device but as a medium for receiving alarms, status messages, administrative messages and reports. It is most useful as an adjunct to the digital television display.

4. Format Request Box (FRB). The format request box provides the user with the capability of selecting one of a set of fixed formats for display on a designated channel of the Digital Television Assembly (DTV). This assembly initially provides 60 DTV channels which display data processed and formatted by the 360/75.

The format request is made by entering on six thumbwheels the data ID, format number, and the channel on which the display is desired. A momentary contact pushbutton indicator on the box enters the request into the system. Its acceptance by the system is acknowledged by relighting of the enter button.

The use of the FRB expands the channel display capacity; however, because the DTV channel is available to many users, their requirements must be considered when changing formats.

5. DTV Hard Copy Printers Gould 4800. The DTV hard copy printer provides the user with a permanent record of the image displayed on the digital television monitors. The hardcopy output capability consists of six printers, each of which outputs a 20.3- × 15.2-cm (8- × 6-in.) printed replica of a selected DTV channel's alphanumeric and/or graphic volatile display. Selection is accomplished via one of six copy request units, each of which can select any of the sixty DTV channels for printout on that panel's associated printer. Hardcopy prints are available in about eleven seconds unless that printer is busy servicing prior requests. Requests are queued in the 3100 computer, which inhibits updates to any DTV channel that has hardcopy requests pending. This ensures that the display content at the time of selection will not change before a copy is stored in the Display Image Buffer (DIB) for subsequent printing. The DIB provides simultaneous storage for only one printout at each printer. Therefore, multiple requests at a single printer will delay channel updates, for a multiple of 11 seconds. However, requests from several printers can be processed in an overlap mode.

This capability will be extremely useful for copying plots, or graphic displays. The copy is reproducible on most copiers and is fully storable itself. The device is not useful as a bulk printer but is ideally suited for recording a significant event for more detailed study by recall from system data records.

The printers will be located in various user and operations areas and are user operated with the printer controls and the DTV copy request unit.

6. Digital Television Copy Request Unit—JPL CRU. This device is separately provided to enable channel selection for the DTV hard copy printer. It contains one 12-position and one 10-position thumbwheel and a momentary contact push button indicator. The thumbwheels permit 129 channel selections. The request is entered into the display computer by pressing the push button which extinguishes the ready light. Acceptance of the request is acknowledged by relighting of the ready light.

7. Time Reference Displays. Time reference displays are included in the Mission Display Board (MDB), on SFOF Internal Comm Subsystem (SIC), TVSA monitors, and as ceiling-mounted readouts in the user areas.

The MDB timed displays are controlled from the support chiefs' console and may display time referenced to significant mission events or to the localities of the Deep Space Stations. These time displays are also available on TVSA channels for general or local display.

Event counters driven by the time reference system are also available. These displays are ceiling-mounted and controllable by the user from console- or desk-mounted panels for countup or countdown.

8. Video Image Display (VID) Photo Printers. Initially, two printers will be provided in the user area in order to provide high-quality operational prints of spacecraft-acquired image and image-related data and histogram plots. Additional printers, up to a total of 32, may be added to the assembly as future requirements dictate. Each will be a self-service unit capable of printing images from any VID display channel.

The output will be 20.3- × 20.3-cm (8- × 8-in.) semi-archival positive opaque prints with a resolution of 1536 × 1536 elements in 32 discernible shades of gray.

9. High-Resolution VID Monitors. High-resolution display of the spacecraft pictures on 43.2-cm (17-in.) TV monitors will enable the experiment and science teams to make real-time decisions based on the spacecraft pictures. The high-resolution monitors will display 832 elements per line and 800 lines. They will provide 32 discernible shades of gray with equal resolution of shades over the dynamic range. Six bits per pixel image data will be converted to 64-level video to eliminate quantization contouring. In addition to the image, a 16-shade reference gray-scale will be displayed to the right of the image. Geometric error will be held to 2%. Dynamic focus and gamma correction will be provided. To provide maximum picture definition, digital signals will be fed to the monitors; the conversion to analog video will be performed at each individual monitor. The VID will be capable of updating the entire display in 5 seconds. The basic VID assembly will include two high-resolution channels with capability for expansion to eight channels.

B. The Second Category of User Devices

1. Teletype Printers—Teletype Corp RO Teletypewriter Set (TTY or RO). These devices are provided in two configurations. The normal sets are furnished for the receipt and display of message traffic from the NASCOM network via the West Coast Switching Center. These messages are processed in accordance with NASCOM procedures.

Identical devices are furnished for CPS data printout. These machines have an added 36-button selector box which enables them to be connected to one of 36 teletype distribution channels. They may also be equipped with a different character set depending upon the coding of the data to be displayed.

The CPS data destined for the latter machines is transferred by electrical interface to the GCF SFOF Comm Terminal Subsystem at the rate of 40.8 kilobits per second for storage until it can be switched by the Communications Processor (CP) and transmitted to the teletypewriter sets.

It is important to consider the fact that the maximum printing speed of the RO sets is 100 words per minute or 50 data bits per second. This is a ratio of 816:1, which limits the rate at which the CP can accept data from the CPS for display over a given TTY channel. The switching functions in the CP and the carriage returns and line feeds performed by the printer subtract further from the nominal machine speed of 50 data bits per second. In effect, the output rate of the teletypewriter limits the output rate of the 360/75 to something less than 50 bits per second. Any attempt to output data to the teletypewriters in excess of these speeds will cause a loss of data in the CP due to drum wraparound, a closure of the CPS–CP interface, and a resultant backup of data in the Computation and Storage Subsystem.

2. Television Assembly (TVSA) Monitors. Approximately 400 television monitors, of various types for different purposes, are located throughout the SFOF. Operations consoles are equipped with 23- or 36-cm (9- or 14-in.) monitors with selector keys that permit the user to select available video inputs. Ceiling- and floor-mounted, 58-cm (23-in.) monitors are normally patched to a single preselected camera. It is possible, however, to change the camera to which the 58-cm (23-in.) monitors are patched by making the proper interconnections in the centralized control equipment. Free-standing monitors, either 43- or 28-cm (17- or 11-in.), are installed on tables where close viewing is possible. Selector keys are provided for the 43- or 28-cm (17- and 11-in.) monitors to permit the user to select available video inputs.

The television communications equipment (see Fig. 6) acquires information for display in the following manner:

(1) Surveillance television cameras are mounted in various parts of the SFOF in such a manner as to permit television monitoring of these areas.

(2) A group of television cameras is mounted in a manner that will permit television monitoring of both incoming and outgoing teletype traffic.

(3) Hard copy television cameras are located in various parts of the SFOF and are arranged to permit viewing of status boards, chart recorders, time displays, and handwritten, typed, or other graphical hard copy material.

(4) Data from non-camera sources such as computers are provided as a video signal to a patching assembly which makes it available to test and monitoring equipment, to fixed monitors, and to the solid-state video switching assembly, which makes it available to users by push-button selection.

Digital television display is one of the most significant additions to the SFOF capabilities. It provides the user with real-time display of processed data formatted to his specifications and updated nominally every 4 seconds. Alarm, range and status indicators can be included. Alphanumeric and graphic representation may be used separately or in combination to provide a wide variety of annotated plots and graphs.

3. Scientific Computing Facility (SCF) I/O Devices. SCF I/O devices perform the same relative functions for users of the 1108 computers as the CPS devices do for their users.

The CPS and SCF computers have tape and electrical interfaces for the purposes of transferring data and files common to programs in both computers. The interconnection of I/O devices or transfer of display data between the two systems is not contemplated.

IV. Conclusion

The Mark IIIA User Terminal and Display Subsystem and related user devices provide greatly increased capabilities for interactive control of data processing functions by mission operations and DSN operations controllers.

For the first time both the users and the controllers of the Central Processing System have a direct hands-on capability without intervention of operators. The CPS systems controllers, DSN operations controllers, and the MOS controllers of the various projects use identical I/O hardware and operating techniques.

The common operating techniques combined with the JPLOS/MCUI capability of handling mission peculiar data as modules of a single system provide a highly versatile multi-mission capability.

At this time the system is in full time use, with exceptions, and is in transition from development to operational status. It is being closely evaluated by the *Mariner* Mars 1971 MOS team, by the *Pioneer* operations planning group, and by the DSN Operations Control Team in preparation for support of the *Mariner* Mars 1971 and *Pioneer F* and *G* interplanetary flight projects.

It has already become evident that operating philosophies and efficiencies can be significantly improved by adapting to the improved system capabilities.

References

1. Willems, A. M., "Simulation Center Hardware Development–Programmed Input/Output Serial Data Generators and Receivers," in *The Deep Space Network*, Space Programs Summary 37-66, Vol. II, pp. 70–71. Jet Propulsion Laboratory, Pasadena, Calif., Nov. 30, 1970.

2. Stiver, R. A., "Mark IIIA IBM 360/75 Computer Configuration," in *The Deep Space Network*, Space Programs Summary 37-66, Vol. II, pp. 71–75. Jet Propulsion Laboratory, Pasadena, Calif., Nov. 30, 1970.

3. Simon, H. S., "Functional Design of the Space Flight Operations Facility for the 1970–1972 Era," in *The Deep Space Network*, Space Programs Summary 37-66, Vol. II, pp. 90–94. Jet Propulsion Laboratory, Pasadena, Calif., Nov. 30, 1970.

4. Habbal, N., "SFOF IBM 360/75 User Device Switching Assemblies," in *The Deep Space Network*, Space Programs Summary 37-66, Vol. II, pp. 75–77. Jet Propulsion Laboratory, Pasadena, Calif., Nov. 30, 1970.

5. Diem, W., "Video Image Display Assembly," in *The Deep Space Network*, Space Programs Summary 37-66, Vol. II, pp. 94–96. Jet Propulsion Laboratory, Pasadena, Calif., Nov. 30, 1970.

6. Singleton, F. L., "SFOF Digital Television Assembly," in *The Deep Space Network*, Space Programs Summary 37-65, Vol. II, pp. 86–91. Jet Propulsion Laboratory, Pasadena, Calif., Sept. 30, 1970.

7. Volkoff, J. J., "Contrast Ratio Determination for the SFOF Video Image Display," in *The Deep Space Network*, Space Programs Summary 37-65, Vol. II, pp. 91–93. Jet Propulsion Laboratory, Pasadena, Calif., Sept. 30, 1970.

8. Polansky, R. G., "DSN Mark IIIA Simulation Center Development," in *The Deep Space Network*, Space Programs Summary 37-65, Vol. II, pp. 94–96. Jet Propulsion Laboratory, Pasadena, Calif., Sept. 30, 1970.

9. Wells, R. A., "Diagnostics for the SFOF Mark IIIA Central Processing System: Standalone Acceptance and Maintenance Routines," in *The Deep Space Network*, Space Programs Summary 37-65, Vol. II, pp. 97–99. Jet Propulsion Laboratory, Pasadena, Calif., Sept. 30, 1970.

10. Mullen, P. G., "High-Speed Data, SFOF Outbound Communication," in *The Deep Space Network*, Space Programs Summary 37-65, Vol. II, p. 101. Jet Propulsion Laboratory, Pasadena, Calif., Sept. 30, 1970.

11. McClure, J. P., "GCF Wideband Digital Data System," in *The Deep Space Network*, Space Programs Summary 37-65, Vol. II, pp. 102–103. Jet Propulsion Laboratory, Pasadena, Calif., Sept. 30, 1970.

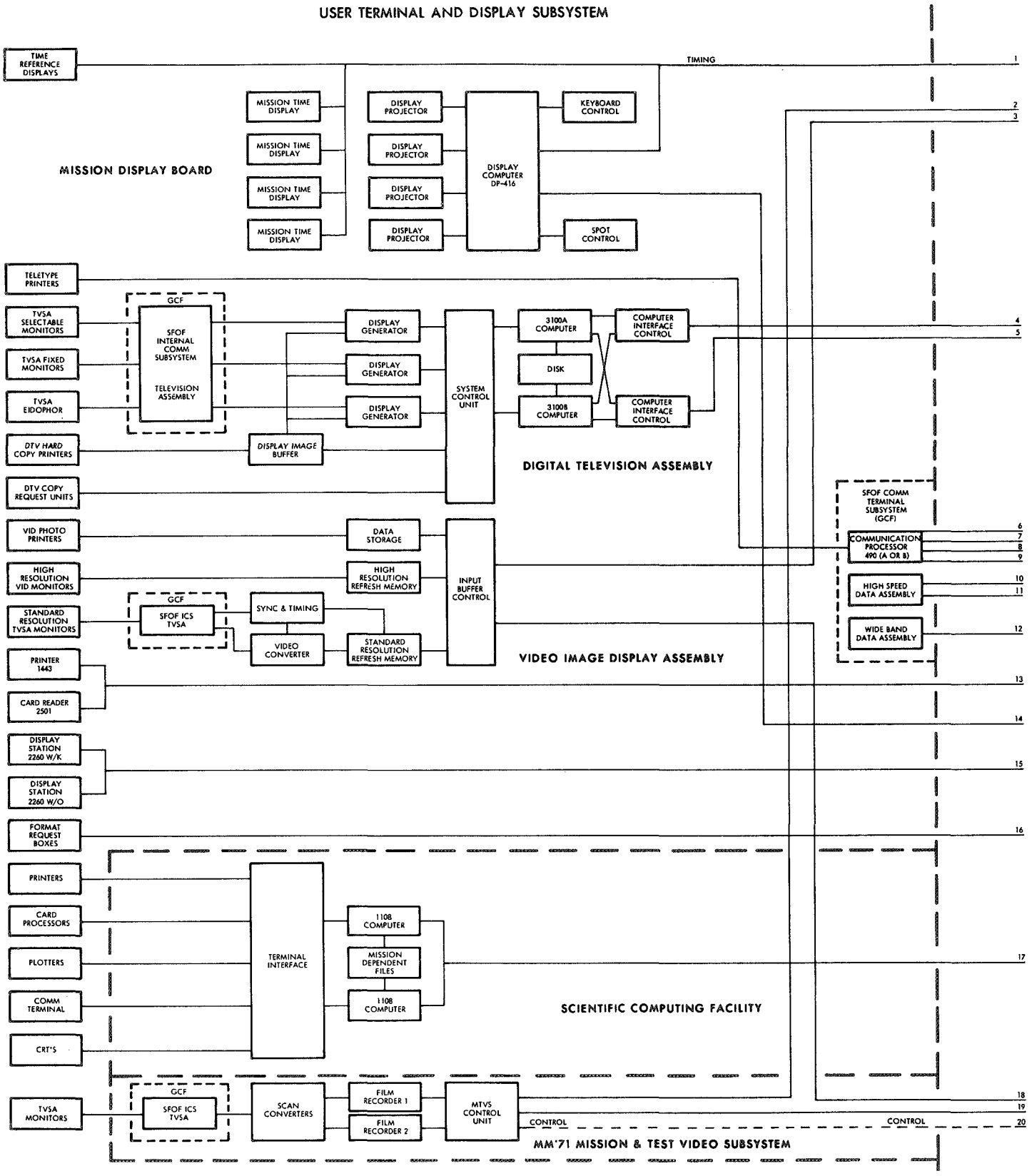

Fig. 1. User terminal and display subsystem

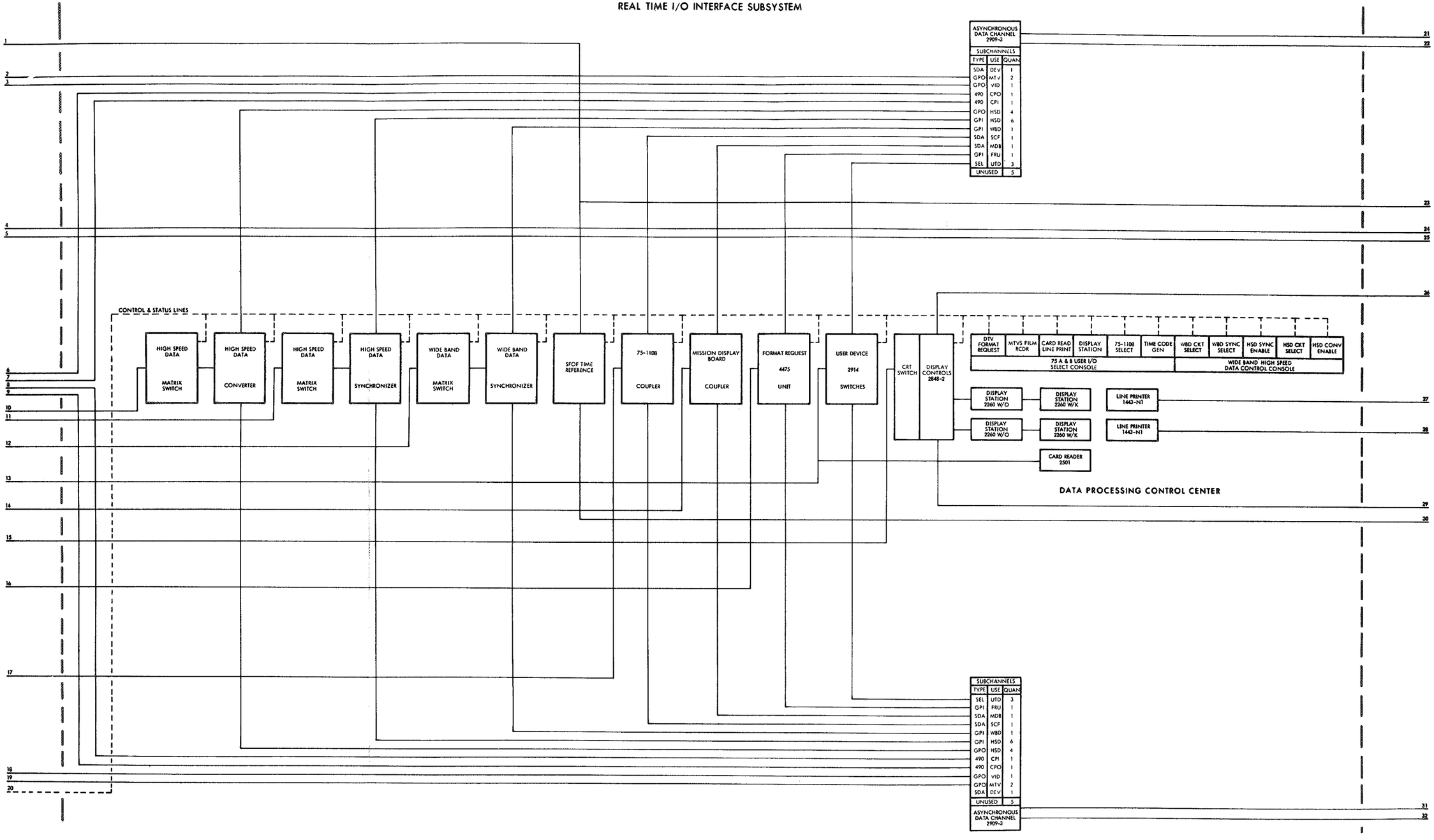

Fig. 2. Real-time I/O interface subsystem

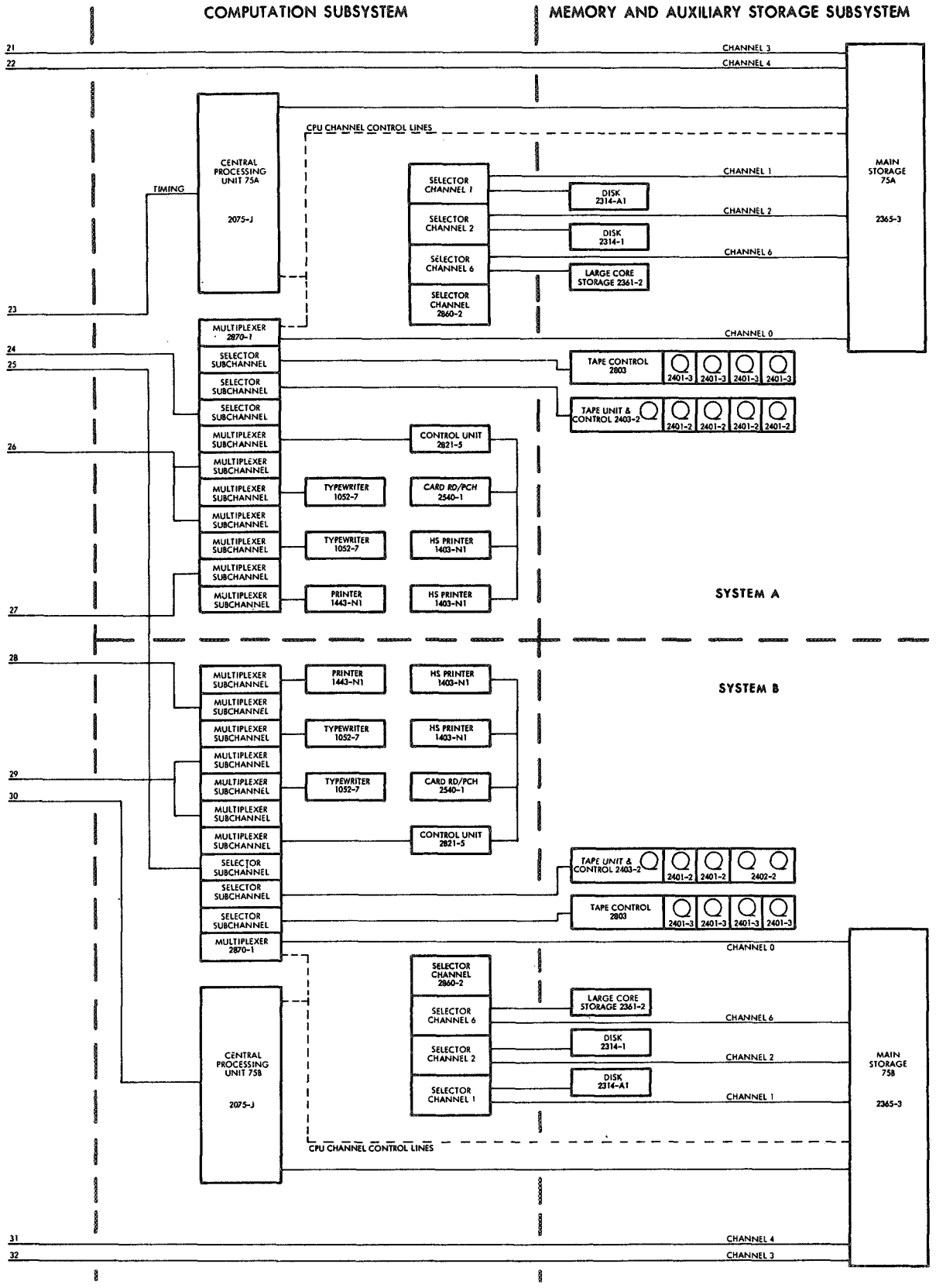

Fig. 3. Computation and memory and auxiliary storage subsystems

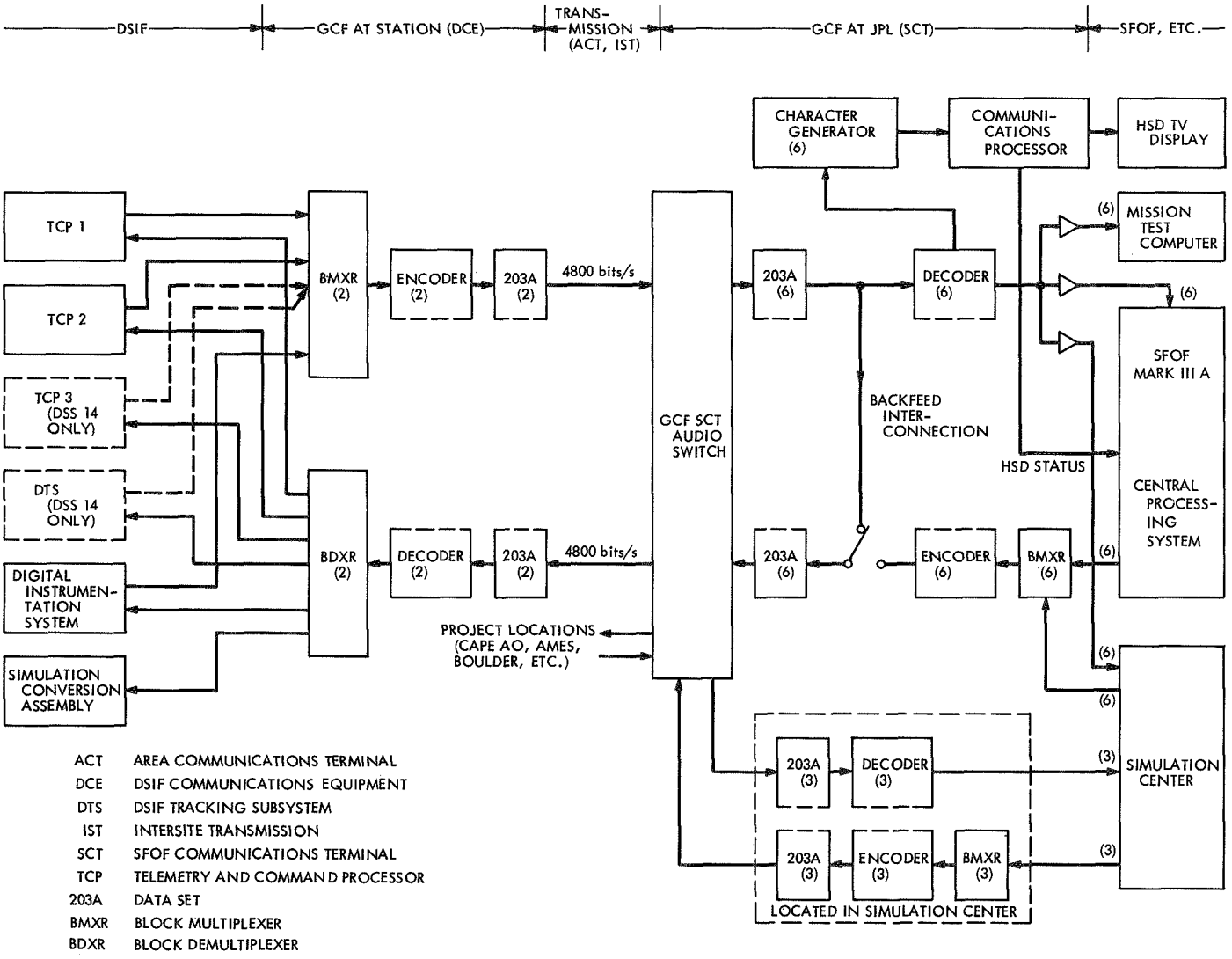

Fig. 4. Ground Communications Facility 1971–1972 High-Speed Data System

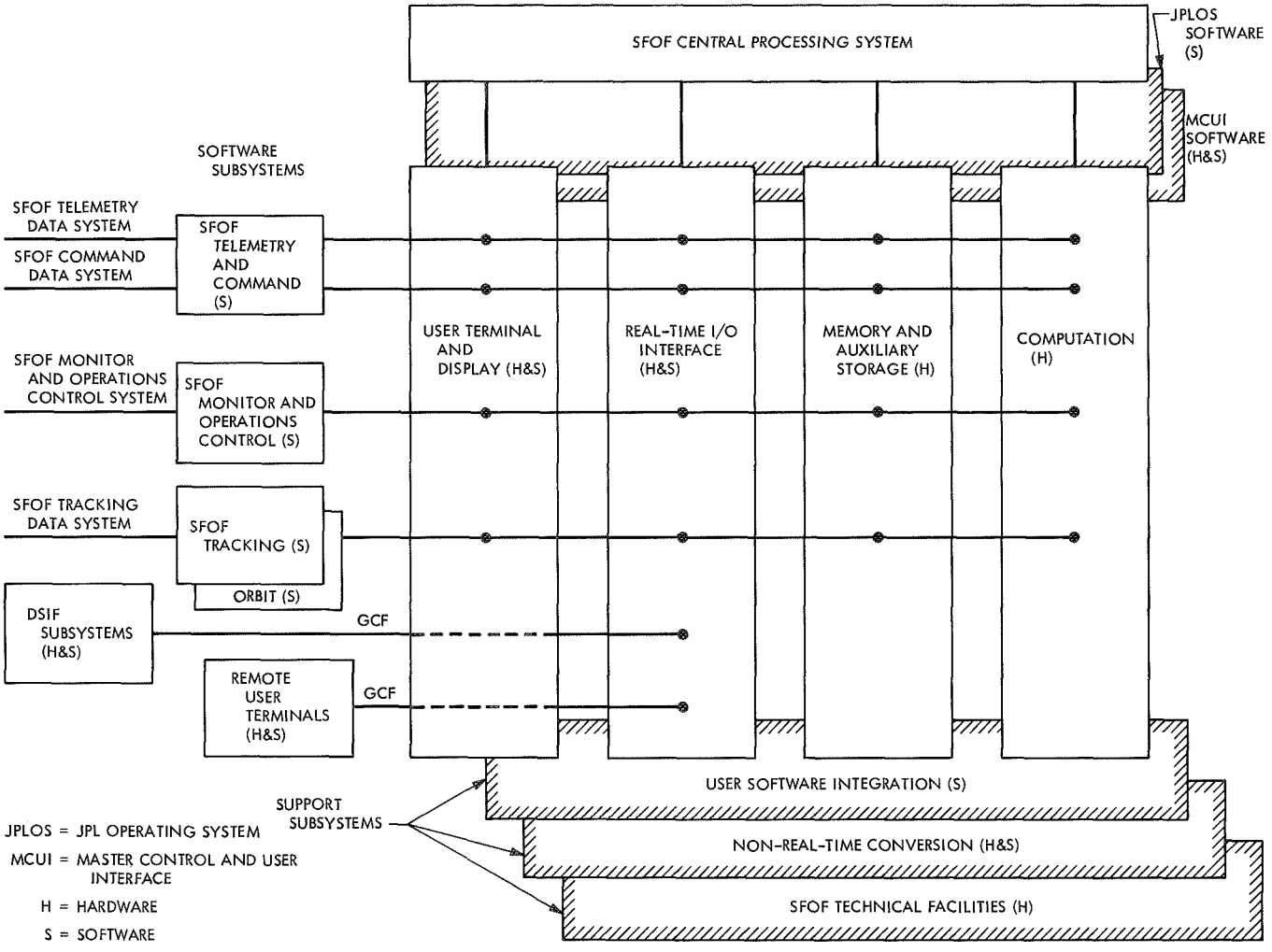

Fig. 5. SFOF Central Processing System hardware/software interfaces

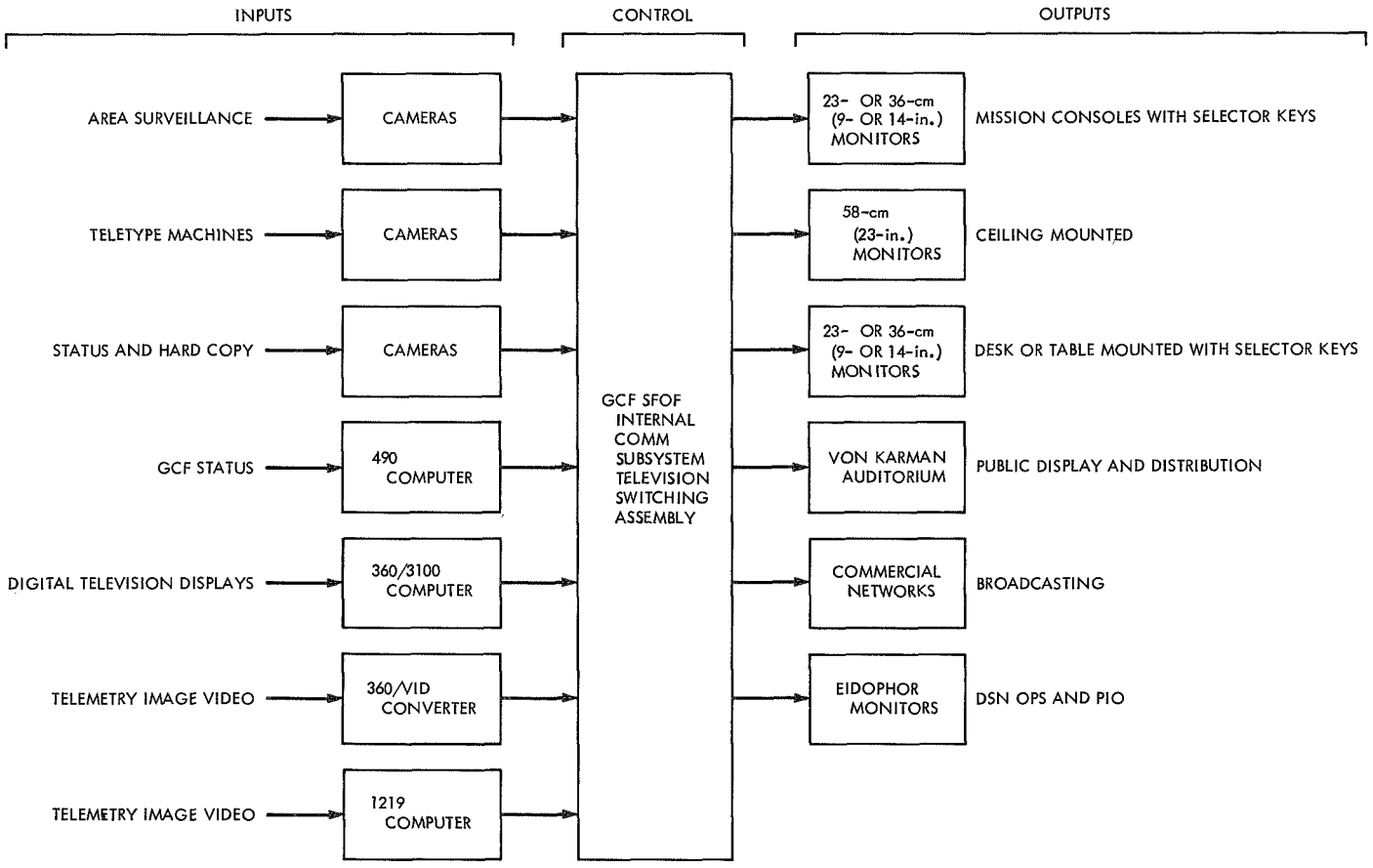

Fig. 6. GCF SFOF television system configuration

Software for the DSN Video Subsystem

J. H. Weidner
Flight Operations and DSN Programming Section

The Deep Space Network (DSN) video subsystem provides the flight projects at JPL with a real-time and near real-time tonal image (picture) processing and display capability. The software of the subsystem controls all components and processes the picture data which it receives from the DSN Telemetry System. The video software is designed to give the flight projects the capability to automatically process, display, and record the picture data as they are received from the spacecraft. Its design also includes an interactive capability for selective picture processing and display.

I. Introduction

As more planetary spacecraft are carrying cameras that will record tonal images (pictures), a decision has been made to develop a video subsystem in the Space Flight Operations Facility (SFOF) to provide real-time and near real-time processing and display of the pictures that are received from the spacecraft. The video subsystem is to be an added capability of the SFOF Telemetry System. The subsystem that is being developed consists of a number of different components. This article will describe the software portion of the video subsystem which controls the entire subsystem and processes the video data for display.

II. System Description

Figure 1 is a block diagram of the total DSN video subsystem. The main components of the subsystem are the digital computer and related software, the Video Image Display (VID) Assembly (Ref. 1), and the interface with the Mission and Test Video System (film recorders) (Ref. 2). Other elements of the subsystem include the following:

(1) The SFOF Closed Circuit TV Assembly for display of the standard resolution images produced by the VID.

(2) The Facility Digital TV Assembly for the display of the picture-related data. These data relate to the pictures being displayed on the high resolution and standard resolution VID subchannels.

(3) User communication with the DSN video system which is provided by the IBM 2260 input/output terminals. A set of input commands for this device is available to the video subsystem user that will allow him to control the video subsystem.

The video software operates under the control of the JPL operating system (JPLOS). This is a specially designed and built system for real-time operations at JPL; it is a multi-jobbing system, which operates in the IBM 360/75 computer. The picture data are provided to the video software by the spacecraft telemetry processor which also resides in the computer. Each line of the picture data is encased in a telemetry data frame. The telemetry software passes the synchronized telemetry frames (picture lines) to the video software where they are collected into complete pictures.

III. Design Goals

The initial design of the DSN video software was pointed toward the *Mariner* Mars 1971 mission, which will send two spacecraft to the vicinity of the planet Mars; each spacecraft will carry tonal image cameras. The design of the software, however, was kept as mission independent as possible so that changes that have to be made to it in order to handle the work of future missions can be kept to a minimum. Design also included the ability to process the data from a number of spacecraft (at least two) concurrently.

As the video subsystem is an advanced engineering effort, specific users' requirements were not available. Therefore, in designing the operating characteristics of the subsystem, it was realized that they must be as flexible to the prospective users' needs as possible. The operating characteristics of the subsystem were therefore designed in a way to give the users the greatest amount of capability. Operating characteristics include a fully automatic mode where the user can initialize the video software to process, display, and record the pictures that are being received from the spacecraft in real time and automatically, according to an initialized format. The initialization includes such items as what processing the computer is to perform on the pictures, and where and how the pictures are to be displayed. The system also will provide an interactive mode where the user can request special display and processing steps for a specified image. The interactive capability will also work in conjunction with the System Data Record that is maintained by the telemetry software. This record system stores all of the telemetry data that have been received from the spacecraft since they were launched. The data are stored on disk or tape. Through the use of this telemetry software, the video subsystem user can retrieve any picture that has been received from a spacecraft. Upon receipt of the picture by the video software, the user can process and display the image through the video system in any manner he desires.

Certain minimum enhancement and picture processing techniques were also included in the design. These include contrast stretch, contouring, and banding. Picture enlargement, or zooming, can also be done by the software on user-specified portions of a picture. Picture-segment averaging, which will fill in missing sections of a picture, is also provided. Other types of picture enhancement can be provided to meet specific project needs.

IV. Software Description

The video software is only one of several systems of software that reside in the IBM 360/75 computer. The system that is closely aligned with the video software is the telemetry system. The telemetry software provides the picture data to the video software. The data are passed, one line at a time, in a standardized format. The format is the same whether the data are being received directly from a spacecraft in real time or from the System Data Record, which is maintained by the telemetry system.

Figure 2 is a block diagram of the video software. The boxes depict program load modules which execute asynchronously from one another. The solid lines and small box depict data that are to be passed between the load modules. The broken lines depict a request to execute (invoke) the resultant load module. Not shown in the block diagram are the system interfaces which are in reality very much present, but would not add anything to the diagram.

Upon receipt of each telemetry frame of data (picture line) from the telemetry processor, the Video Input Control and Processor Module (VICM) will perform the necessary processing on the picture line, and store it on a direct access data set. All lines of the picture (700 in the case of the *Mariner* Mars 1971 spacecraft) are accumulated in the data set. When a complete picture has been received, the VICM will determine whether the picture is being received directly from the spacecraft in real time or has been recalled from the Telemetry System Data Record at the request of the system user. In the case of real-time data, the module will determine whether there is a user-initialized set of automatic processing and display requirements for the spacecraft's pictures. If a set of requirements does exist, they will be placed in a queue, and a system request is made to invoke the Video Output Control Module (VOCM). Pictures recalled from

the Telemetry System Data Record are stored in a uniquely named data set. Upon receipt of the whole picture, the user is notified via the IBM 2260 input/output (I/O) terminal that the picture is ready for display processing. The user can then use his control messages to the 2260 to process and display the recalled picture. The recalled picture will remain in its data set until the user requests that it be removed.

Since the real-time data being received from the spacecraft continues uninterrupted from picture to picture, the VICM will store the lines of the following picture into another data set using a double buffer approach for storage of the pictures received in real time. It requires just over 4.5 minutes to receive all of the lines of a picture from the spacecraft; therefore, all output processing and display of a picture must be carried out within that time limit because the data set will again be required to store the picture that will be received after the following one.

The VOCM can be invoked by either the VICM (as described above) or by the User Input/Output Module. Upon execution, it will interrogate the output request queue that has been set up for it. The requests are for picture output to either the VID equipment or the film recorders in the Mission and Test Video System (MTVS). The output control module will set up the necessary linkages and invoke the appropriate module (see Fig. 2); it will then continue to operate until all of the display requests in the queue have been processed. Simple enhancement transformations which are to be performed on every picture element (pixel) of a picture in an identical manner are performed in this module. An enhancement transformation table is produced which is passed to the relevant output module for transformation of all of the picture elements of the picture. After all display requests in the queue have been satisfied, the VOCM will terminate.

The User Input/Output Control Module (UIOM) allows the video subsystem user to communicate with the video subsystem through the I/O terminal. The user can input a variety of requests to the video software. These requests include the following:

(1) Request that an image stored in a video data set (either a picture received from a spacecraft in real time or a picture recalled from the System Data Record) be processed and output for display or recording on a specified device.

(2) Change the automatic processing and display requirements for the pictures being received from the spacecraft in real time.

(3) Recall a picture from the Telemetry System Data Record for storage in a video data set.

(4) Bring the individual display and recording devices of the VID on or off line with the computer.

Other messages for the general housekeeping of the video subsystem are also provided to the user. As was mentioned above, the UIOM places the display requests into the display request queue and requests the system to invoke the video Output Control Module.

The VID Data Formatter Module (VDFM) and the MTVS Data Formatter Module (MDFM) are invoked to process, format, and output a particular picture. The film recorder appears to the MDFM as an individually addressable tonal grid containing 1024^2 elements. The picture, histogram (the histograms depict quantity of pixels as a function of tonal values), and the gray scales are formatted by the software for this grid, and output via the system software and the hardware. Related alphanumeric data that describe the picture and processing are placed on the alphanumeric field (29 characters by 28 lines) which is adjacent to the grid field. The related data include enhancement and any other special processing information that the software performed on the picture and picture identification data.

The VDFM formats the pictures for output to the Video Image Display Assembly. The problem is considerably different from that of the film recorder since there are a variety of end devices on the VID Assembly, plus a disk storage that is capable of storing up to 34 pictures and their related data. All pictures that are output to the VID Assembly for display and/or printing are stored on this disk file. Any picture that is stored on the disk can be retrieved, at the request of the software, for display or printing. The VDFM provides the VID Assembly with the picture's related alphanumeric data, gray scale data, and histograms. All of these data are output onto the VID printer; however, only picture data are output to the TV subchannels. Data are transferred from the computer to the VID Assembly in records that contain 16 picture lines of data.

The VDFM will also provide the picture-related alphanumeric data and histogram data to the digital television system. The data will relate to the pictures that

are being displayed on the standard-resolution and high-resolution television monitors of the VID Assembly. The user will, therefore, be able to view the related information of the picture being displayed on the television subchannels. These data include a histogram of the tonal image, enhancement, and any other special processing information that the software performed on the picture and picture identifying data.

V. Conclusion

The DSN video software is designed to provide a versatile system to the user. It will process pictures in real time from more than one spacecraft and at the same time allow the user to process and work on selected pictures in a fully interactive manner. The software formats the pictures and related information for display or recording on a number of different types of end devices.

References

1. Diem, W., "Video Image Display Assembly," in *The Deep Space Network,* Space Programs Summary 37-66, Vol. II, pp. 94–96. Jet Propulsion Laboratory, Pasadena, Calif., Nov. 30, 1970.
2. "Mission and Test Video System," in *Flight Projects,* Space Programs Summary 37-64, Vol. I, pp. 3–7. Jet Propulsion Laboratory, Pasadena, Calif., July 31, 1970.

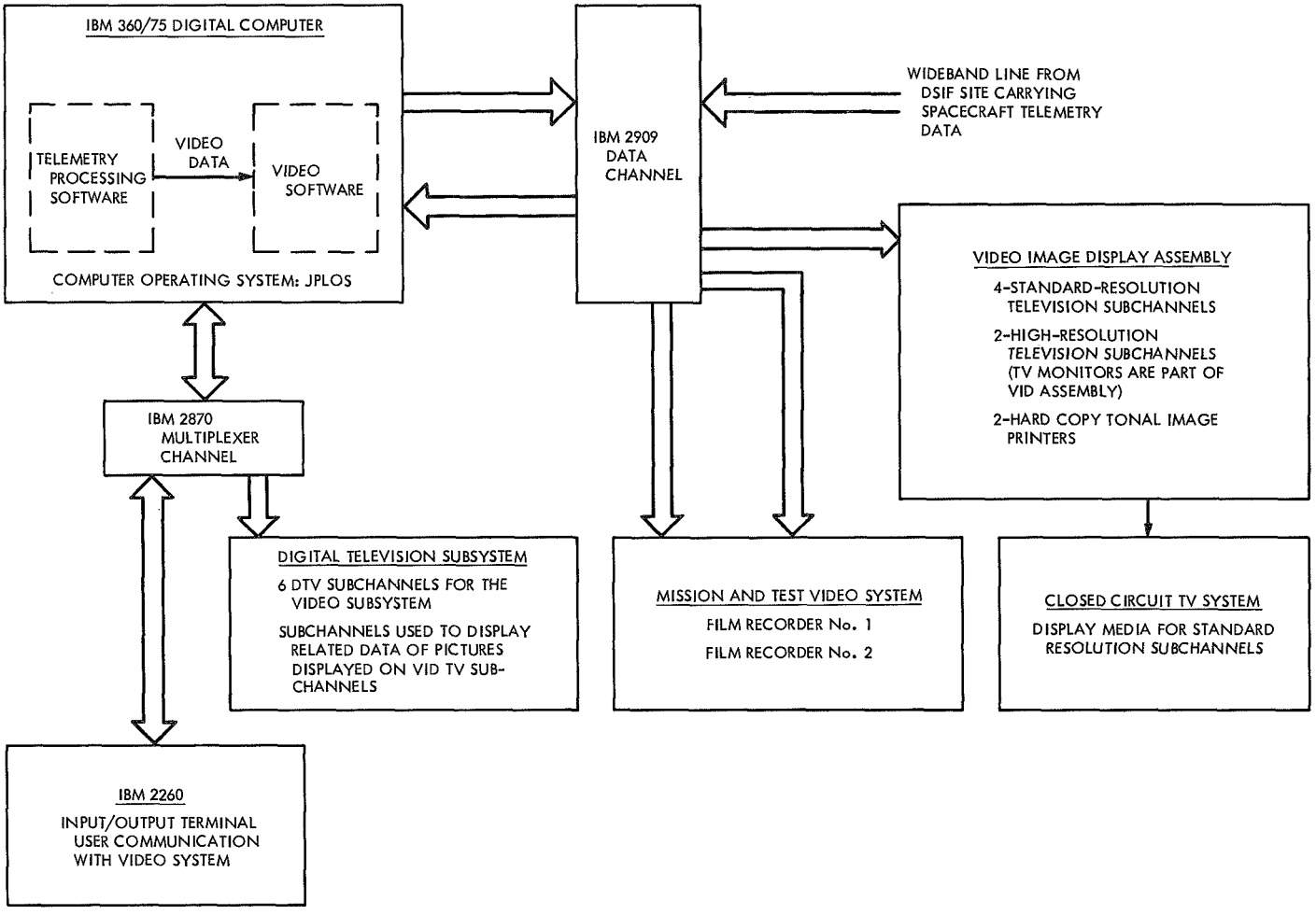

Fig. 1. Block diagram of video subsystem

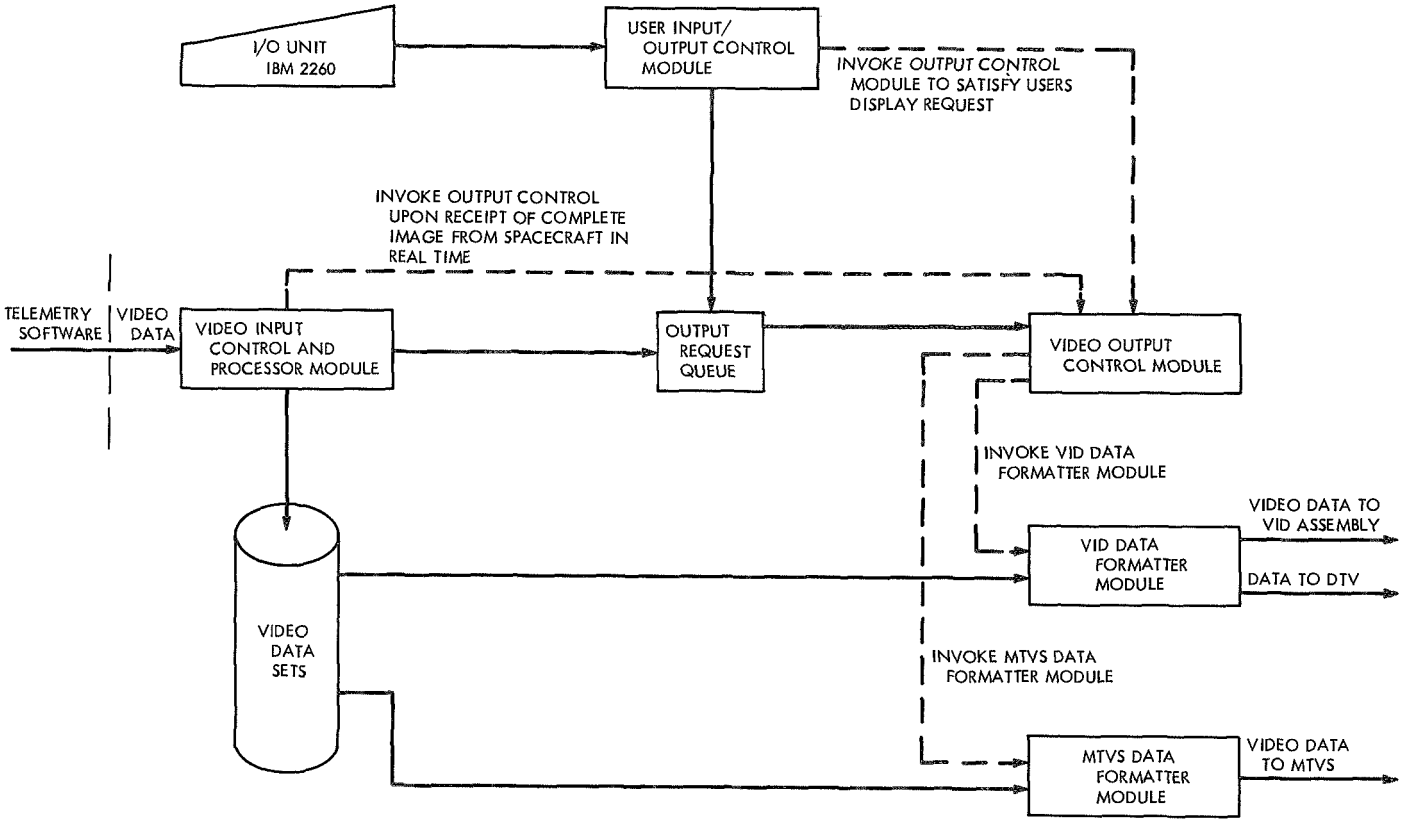

Fig. 2. Video software block diagram

26-m Antenna HA-dec Counter Torque Modifications

F. Menninger
DSIF Engineering Section

This article describes the improvement in tracking performance of a 26-m antenna as a result of changes in the hydraulic circuit of the HA-dec servo subsystem. A discussion of previous problem areas and the results of the new modification are stated.

I. Introduction

A servo hydraulic control system is used to control the motion of the 26-m HA-dec DSIF antennas. Over the past several years improvements have been made in tracking performance; however, several persistent problems have remained. The most persistent of these has been an apparent "hitching" of the drive motor. This article describes a change which will substantially reduce this effect.

All of the improvements to date have been in the area of the control room electronics. However, modifying the electronics alone yielded only partial results. As servo loop gain was increased the gearing backlash became the limiting factor. Therefore attention was directed to the antenna-mounted components.

The drive system for the antenna consists of two separate gear reducers for each axis. This provides two-point drive on each of the bull gears. The two-point drive was utilized to reduce the bull gear load during extreme wind loading condition, in addition it affords a means for providing an anti-backlash gearing arrangement for servo drive.

When the antenna system was first designed, an attempt was made to operate with one gear box driving and one gear box restraining. This is similar to the series arrangement. However the overall system gain was reduced by a factor of two, so this arrangement was dropped for a more suitable arrangement. The current hydraulic circuit is shown in Fig. 1. The subsystem is basically a velocity control system with rate feedback used to close the velocity loop.

Anti-backlash is achieved by driving one hydraulic motor at full load line pressure and the other at a pressure which is reduced by means of a counter balance valve. The motors are geared together and therefore, in theory at least, are operating at the same speed. Because of the reduced pressure across one motor, at light to moderate loads it will be operating as a pump and provide a torque to eliminate gear backlash.

II. Problem

The problem with the present arrangement is that it does not perform well at low speed. The counter balance valves require a minimum flow to develop the reduced pressure. At low velocities the motor flow is less than the required minimum and the drive motors will begin to alternately run across the backlash region. This effect is commonly called hitching.

The minimum flow through the counter balance valve is particularly a problem at zero antenna velocity. Under these conditions the only flow is the leakage to drain through the motor cases. This case leakage tends to vary widely from site to site and causes severe hitching problems at some sites.

The hitching problem has two principal effects. The first is a visual feedback to the operator who observes an unsteady motion and under extreme conditions an increase in the servo tracking error. The second effect is that the rate loop gain is limited by the nonlinear backlash characteristics at low speed. In order to maintain stability the loop gain is so low that the tracking error is increased and the position loop bandwidth limited.

III. Solution

In order to eliminate the hitching, a means for providing a small constant flow across the counter balance valve is required. Fig. 2 shows the addition of two pressure compensated flow control valves, located between each of the driving motors and their counter balance valve and case drain. This provides a constant flow through the counter balance valve to drain. The flow required to assure proper operation of the counter balance valve was found to be approximately 0.1 gal/min.

A prototype installation was made at DSS 11 to prove the validity of the scheme. With the flow control valves blocked out of the circuit, the counter torque pressure was adjusted to 20.7 N/cm^2 ΔP. Smooth manual velocity runs were attempted at the lowest possible antenna rates. Data printouts were made of each run and the antenna rate varied from 0.0004 to 0.0020 deg/s. A visual observation on the antenna revealed that during these runs the drive motors would stop and start alternately as they ran across the backlash. This produces the hitching motion.

The flow control valves were then inserted into the hydraulic circuit and the test repeated. Under the same type of electronic control a somewhat lower rate was obtained of approximately 0.001 deg/s but the variation in rate was only ± 0.0001 deg/s as compared with the previous test of ± 0.0008 deg/s. In addition the visual observation indicated that both motors were running constantly and smoothly together.

Several operational commitments have been satisfied by DSS 11 with the prototype installation. Operational personnel have stated the antenna tracking performance to be significantly improved as a result of this modification.

A permanent installation for all DSIF sites is currently in process for this modification.

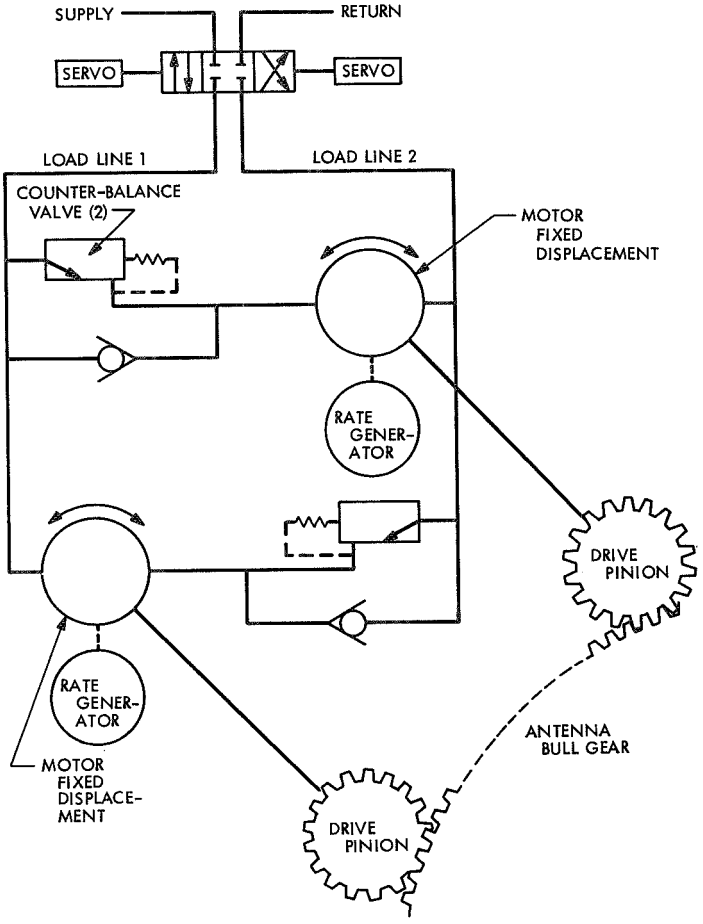

Fig. 1. Hydraulic circuit of HA-dec servo subsystem

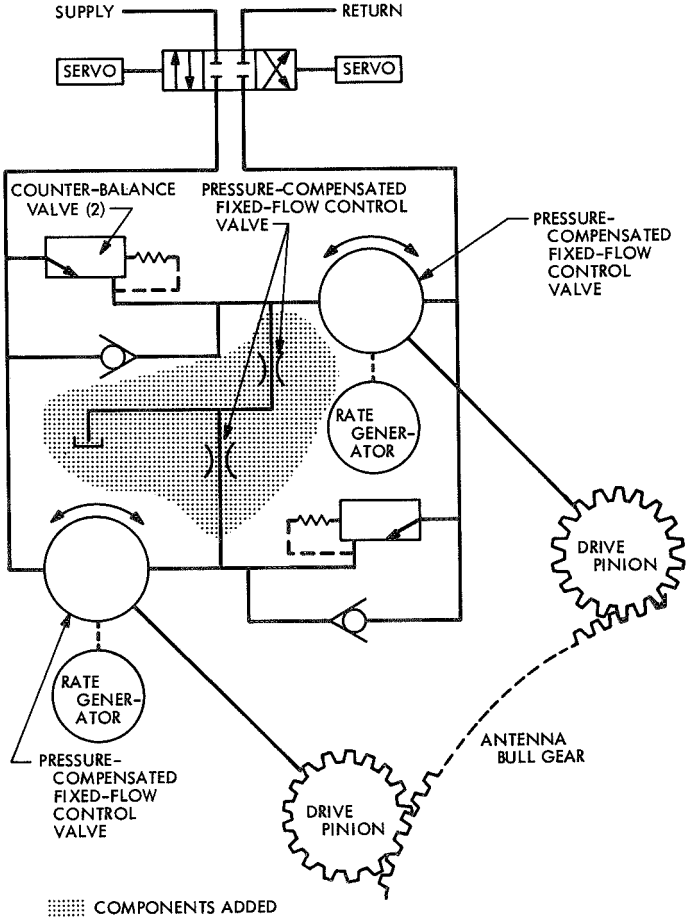

Fig. 2. Pressure-compensated flow control valve

Bibliography

Anderson, J. D., *Determination of the Masses of the Moon and Venus and the Astronomical Unit from Radio Tracking Data of the Mariner II Spacecraft.* Technical Report 32-816. Jet Propulsion Laboratory, Pasadena, Calif., July 1, 1967.

Anderson, J. D., et al., "The Radius of Venus as Determined by Planetary Radar and Mariner V Radio Tracking Data," *J. Atmos. Sci.,* pp. 1171–1174, Sept. 25, 1968.

Berman, A. L., *Tracking System Data Analysis Report, Ranger VII Final Report,* Technical Report 32-719, Jet Propulsion Laboratory, Pasadena, Calif., June 1, 1965.

Berman, A. L., *ABTRAJ—On-Site Tracking Prediction Program for Planetary Spacecraft,* Technical Memorandum 33-391. Jet Propulsion Laboratory, Pasadena, Calif., Aug. 15, 1968.

Cain, D. L., and Hamilton, T. W., *Determination of Tracking Station Locations by Doppler and Range Measurements to an Earth Satellite,* Technical Report 32-534. Jet Propulsion Laboratory, Pasadena, Calif., Feb. 1, 1964.

Carey, C. N., and Sjogren, W. L., "Gravitational Inconsistency, in the Lunar Theory: Confirmation by Radio Tracking," *Science,* Vol. 160, pp. 875, 876, Apr.–June 1968.

Curkendall, D. W., and Stephenson, R. R., "Earthbased Tracking and Orbit Determination—Backbone of the Planetary Navigation System," *Astronaut. Aeronaut.,* Vol. 7, May 1970.

Curkendall, D. W., "Planetary Navigation: The New Challenges," *Astronaut. Aeronaut.,* Vol. 7, May 1970.

Efron, L., and Solloway, C. B., *Proceedings of the Conference on Scientific Applications of Radio and Radar Tracking in the Space Program,* Technical Report 32-1475, Jet Propulsion Laboratory, Pasadena, Calif., July 1970.

Flanagan, F. M., et al., *Deep Space Network Support of the Manned Space Flight Network for Apollo: 1962–1968,* Technical Memorandum 33-452, Vol. I. Jet Propulsion Laboratory, Pasadena, Calif., July, 1970.

Fjeldbo, G., and Eshleman, V. R., "Radio Occultation Measurements and Interpretations," in *The Atmospheres of Venus and Mars,* p. 225. Gordon and Breach, Science Publishers, Inc., New York, N. Y.

Goldstein, R. M., et al., *The Superior Conjunction of Mariner IV,* Technical Report 32-1092. Jet Propulsion Laboratory, Pasadena, Calif., Apr. 1, 1967.

Goldstein, R. M., "Radar Time-of-Flight Measurements to Venus," *Astron. J.,* Vol. 73, No. 9, Aug. 1968.

Goldstein, R. M., and Rumsey, H., Jr., "A Radar Snapshot of Venus," *Science,* Vol. 169, September 1970.

Gordon, H. J., et al., *The Mariner 6 and 7 Flight Paths and Their Determination From Tracking Data,* Technical Memorandum 33-469. Jet Propulsion Laboratory Pasadena, Calif., Dec. 1, 1970.

Bibliography (contd)

Hamilton, T. W., et al., *The Ranger IV Flight Path and Its Determination From Tracking Data,* Technical Report 32-345. Jet Propulsion Laboratory, Pasadena, Calif., Sept. 15, 1962.

Kellermann, K. I., et al., "High Resolution Observations of Compact Radio Sources at 13 Centimeters," *Astrophys. J.*, Vol. 161, pp. 803–809, Sept. 1970.

Labrum, R. G., Wong, S. K., and Reynolds, G. W., *The Surveyor V, VI, and VII Flight Paths and Their Determination from Tracking Data,* Technical Report 32-1302. Jet Propulsion Laboratory, Pasadena, Calif., Dec. 1, 1968.

Levy, G. S., et al., "Pioneer VI Faraday Rotation Solar Occultation Experiment," in *The Deep Space Network,* Space Programs Summary 37-55, Vol. II. Jet Propulsion Laboratory, Pasadena, Calif., Jan. 31, 1969.

Lieske, J. H., and Null, G. W., "Icarus and the Determination of Astronomical Constants," *Astron. J.*, Vol. 74, No. 2, Mar. 1969.

Lorell, J., and Sjogren, W. L., *Lunar Orbiter Data Analysis,* Technical Report 32-1220. Jet Propulsion Laboratory, Pasadena, Calif., Nov. 15, 1967.

Lorell, J., *Lunar Orbiter Gravity Analysis,* Technical Report 32-1387. Jet Propulsion Laboratory, Pasadena, Calif., June 15, 1969.

Lorell, J., et al., "Celestial Mechanics Experiment for *Mariner*," *Icarus,* Vol. 12, January 1970.

McNeal, C. E., *Ranger V Tracking Systems Data Analysis Final Report,* Technical Report 32-702. Jet Propulsion Laboratory, Pasadena, Calif., Apr. 15, 1965.

Melbourne, W. G., et al., *Constants and Related Information for Astrodynamical Calculations,* Technical Report 32-1306. Jet Propulsion Laboratory, Pasadena, Calif., July 15, 1968.

Melbourne, W. G., "Planetary Ephemerides," *Astronaut. Aeronaut.*, Vol. 7, May 1970.

Miller, L., et al., *The Atlas–Centaur VI Flight Path and Its Determination from Tracking Data,* Technical Report 32-911. Jet Propulsion Laboratory, Pasadena, Calif., Apr. 15, 1966.

Mulholland, J. D., and Sjogren, W. L., *Lunar Orbiter Ranging Data,* Technical Report 32-1087. Jet Propulsion Laboratory, Pasadena, Calif., Jan. 6, 1967.

Mulholland, J. D., *Proceedings of the Symposium on Observation, Analysis, and Space Research Applications of the Lunar Motion,* Technical Report 32-1386. Jet Propulsion Laboratory, Pasadena, Calif., Apr. 1969.

Muller, P. M., and Sjogren, W. L., *Consistency of Lunar Orbiter Residuals With Trajectory and Local Gravity Effects,* Technical Report 32-1307. Jet Propulsion Laboratory, Pasadena, Calif., Sept. 1, 1968.

Muller, P. M., and Sjogren, W. L., *Lunar Mass Concentrations,* Technical Report 32-1339. Jet Propulsion Laboratory, Pasadena, Calif., Aug. 16, 1968.

Null, G. W., Gordon, H. J., and Tito, D. A., *Mariner IV Flight Path and its Determination From Tracking Data,* Technical Report 32-1108. Jet Propulsion Laboratory, Pasadena, Calif., Aug. 1, 1967.

Bibliography (contd)

O'Neil, W. J., et al., *The Surveyor III and Surveyor IV Flight Paths and Their Determination From Tracking Data*, Technical Report 32-1292. Jet Propulsion Laboratory, Pasadena, Calif., Aug. 15, 1968.

Pease, G. E., et al., *The Mariner V Flight Path and Its Determination From Tracking Data*, Technical Report 32-1363. Jet Propulsion Laboratory, Pasadena, Calif., July 1, 1969.

Renzetti, N. A., *Tracking and Data Acquisition for Ranger Missions I–V*, Technical Memorandum 33-174. Jet Propulsion Laboratory, Pasadena, Calif., July 1, 1964.

Renzetti, N. A., *Tracking and Data Acquisition for Ranger Missions VI–IX*, Technical Memorandum 33-275. Jet Propulsion Laboratory, Pasadena, Calif., Sept. 15, 1966.

Renzetti, N. A., *Tracking and Data Acquisition Support for the Mariner Venus 1962 Mission*, Technical Memorandum 33-212. Jet Propulsion Laboratory, Pasadena, Calif., July 1, 1965.

Renzetti, N. A., *Tracking and Data Acquisition Report, Mariner Mars 1964 Mission: Near-Earth Trajectory Phase*, Technical Memorandum 33-239, Vol. I. Jet Propulsion Laboratory, Pasadena, Calif., Jan. 1, 1965.

Renzetti, N. A., *Tracking and Data Acquisition Report, Mariner Mars 1964 Mission: Cruise to Post-Encounter Phase*, Technical Memorandum 33-239, Vol. II. Jet Propulsion Laboratory, Pasadena, Calif., Oct. 1, 1967.

Renzetti, N. A., *Tracking and Data Acquisition Report, Mariner Mars 1964 Mission: Extended Mission*, Technical Memorandum 33-239, Vol. III. Jet Propulsion Laboratory, Pasadena, Calif., Dec. 1, 1968.

Renzetti, N. A., *Tracking and Data System Support for Surveyor: Missions I and II*, Technical Memorandum 30-301, Vol. I. Jet Propulsion Laboratory, Pasadena, Calif., July 15, 1969.

Renzetti, N. A., *Tracking and Data System Support for Surveyor: Missions III and IV*, Technical Memorandum 30-301, Vol. II. Jet Propulsion Laboratory, Pasadena, Calif., September 1, 1969.

Renzetti, N. A., *Tracking and Data System Support for Surveyor: Mission V*, Technical Memorandum 30-301, Vol. III. Jet Propulsion Laboratory, Pasadena, Calif., December 1, 1969.

Renzetti, N. A., *Tracking and Data System Support for Surveyor: Mission VI*, Technical Memorandum 30-301, Vol. IV. Jet Propulsion Laboratory, Pasadena, Calif., December 1, 1969.

Renzetti, N. A., *Tracking and Data System Support for Surveyor: Mission VII*, Technical Memorandum 30-301, Vol. V. Jet Propulsion Laboratory, Pasadena, Calif., December 1, 1969.

Renzetti, N. A., *Tracking and Data System Support for the Mariner Venus 67 Mission: Planning Phase Through Midcourse Maneuver*, Technical Memorandum 33-385, Vol. I. Jet Propulsion Laboratory, Pasadena, Calif., September 1, 1969.

Bibliography (contd)

Renzetti, N. A., *Tracking and Data System Support for the Mariner Venus 67 Mission: Midcourse Maneuver Through End of Mission*, Technical Memorandum 33-385, Vol. II. Jet Propulsion Laboratory, Pasadena, Calif., September 1, 1969.

Renzetti, N. A., *Tracking and Data System Support for the Pioneer Project. Pioneer VI. Prelaunch to End of Nominal Mission*, Technical Memorandum 33-426, Vol. I. Jet Propulsion Laboratory, Pasadena, Calif., Feb. 1, 1970.

Renzetti, N. A., *Tracking and Data System Support for the Pioneer Project. Pioneer VII. Prelaunch to End of Nominal Mission*, Technical Memorandum 33-426, Vol. II. Jet Propulsion Laboratory, Pasadena, Calif., Apr. 15, 1970.

Renzetti, N. A., *Tracking and Data System Support for the Pioneer Project. Pioneer VIII. Prelaunch Through May 1968*, Technical Memorandum 33-426, Vol. III. Jet Propulsion Laboratory, Pasadena, Calif., July 15, 1970.

Renzetti, N. A., *Tracking and Data System Support for the Pioneer Project. Pioneer IX. Prelaunch Through June 1969*, Technical Memorandum 33-426, Vol. IV. Jet Propulsion Laboratory, Pasadena, Calif., Nov. 15, 1970.

Sjogren, W. L., *The Ranger III Flight Path and Its Determination From Tracking Data*, Technical Report 32-563. Jet Propulsion Laboratory, Pasadena, Calif., Sept. 15, 1965.

Sjogren, W. L., et al., *Physical Constants as Determined From Radio Tracking of the Ranger Lunar Probes*, Technical Report 32-1057. Jet Propulsion Laboratory, Pasadena, Calif., Dec. 30, 1966.

Sjogren, W. L., et al., *The Ranger VI Flight Path and Its Determination From Tracking Data*, Technical Report 32-605. Jet Propulsion Laboratory, Pasadena, Calif., Dec. 15, 1964.

Sjogren, W. L., et al., *The Ranger V Flight Path and Its Determination From Tracking Data*, Technical Report 32-562. Jet Propulsion Laboratory, Pasadena, Calif., Dec. 6, 1963.

Sjogren, W. L., and Trask, D. W., *Physical Constants as Determined From Radio Tracking of the Ranger Lunar Probes*, Technical Report 32-1057. Jet Propulsion Laboratory, Pasadena, Calif., Dec. 30, 1966.

Sjogren, W. L., *Proceedings of the JPL Seminar on Uncertainties in the Lunar Ephemeris*, Technical Report 32-1247. Jet Propulsion Laboratory, Pasadena, Calif., May 1, 1968.

Stelzried, C. T., *A Faraday Rotation Measurement of a 13-cm Signal in the Solar Corona*, Technical Report 32-1401. Jet Propulsion Laboratory, Pasadena, Calif., July 15, 1970.

Thornton, J. H., Jr., *The Surveyor I and Surveyor II Flight Paths and Their Determination From Tracking Data*, Technical Report 32-1285. Jet Propulsion Laboratory, Pasadena, Calif., Aug. 1, 1968.

Vegos, C. J., et al., *The Ranger VIII Flight and Its Determination From Tracking Data*, Technical Report 32-766. Jet Propulsion Laboratory, Pasadena, Calif. (to be published).

Bibliography (contd)

Vegos, C. J., et al., *The Ranger IX Flight Path and Its Determination From Tracking Data*, Technical Report 32-767. Jet Propulsion Laboratory, Pasadena, Calif., Nov. 1, 1968.

Winn, F. B., *Selenographic Location of Surveyor VI, Surveyor VI Mission Report: Part II. Science Results*, Technical Report 32-1262. Jet Propulsion Laboratory, Pasadena, Calif., Jan. 10, 1968.

Winn, F. B., "Post Landing Tracking Data Analysis," in *Surveyor VII Mission Report: Part II. Science Results*, Technical Report 32-1264. Jet Propulsion Laboratory, Pasadena, Calif., Mar. 15, 1968.

Winn, F. B., "Post Lunar Touchdown Tracking Data Analysis," in *Surveyor Project Final Report: Part II. Science Results*, Technical Report 32-1265. Jet Propulsion Laboratory, Pasadena, Calif., June 15, 1968.

Winn, F. B., *Surveyor Posttouchdown Analyses of Tracking Data*, NASA SP-184. National Aeronautics and Space Administration, Washington, D.C., p. 369.

NASA — JPL — Coml., L.A., Calif.